

# Auxetic Structures in Cardiovascular Stent Design

Ebba Montgomery Liljeroth

Department of Mechanical Engineering  
University College London

Primary Supervisor:  
Prof. Gaetano Burriesci

Secondary Supervisor:  
Prof. Silvia Schievano

# UCL Research Paper Declaration Form

## referencing the doctoral candidate's own published work(s)

Please use this form to declare if parts of your thesis are already available in another format, e.g. if data, text, or figures:

- have been uploaded to a preprint server;
- are in submission to a peer-reviewed publication;
- have been published in a peer-reviewed publication, e.g. journal, textbook.

*This form should be completed as many times as necessary. For instance, if you have seven thesis chapters, two of which containing material that has already been published, you would complete this form twice.*

<b>1. For a research manuscript that has already been published</b> (if not yet published, please skip to section 2):		
<b>a) Where was the work published?</b> (e.g. journal name)	Click or tap here to enter text.	
<b>b) Who published the work?</b> (e.g. Elsevier/Oxford University Press):	Click or tap here to enter text.	
<b>c) When was the work published?</b>	Click or tap to enter a date.	
<b>d) Was the work subject to academic peer review?</b>	Please select.	
<b>e) Have you retained the copyright for the work?</b>	Please select.	
[If no, please seek permission from the relevant publisher and check the box next to the below statement]:		
<input type="checkbox"/> <i>I acknowledge permission of the publisher named under 1b to include in this thesis portions of the publication named as included in 1a.</i>		
<b>2. For a research manuscript prepared for publication but that has not yet been published</b> (if already published, please skip to section 3):		
<b>a) Has the manuscript been uploaded to a preprint server?</b> (e.g. medRxiv):	No	<b>If yes, which server?</b> Click or tap here to enter text.
<b>b) Where is the work intended to be published?</b> (e.g. names of journals that you are planning to submit to)	Applied Materials Today	
<b>c) List the manuscript's authors in the intended authorship order:</b>	Ebba Montgomery-Liljeroth; Silvia Schievano, Gaetano Burriesci	

<b>d) Stage of publication</b>		Submitted	
<b>3. For multi-authored work, please give a statement of contribution covering all authors</b> (if single-author, please skip to section 4):			
Ebba Montgomery Liljeroth: Data collection, Writing, Editing; Silvia Schievano: Editing, Formatting, Supervision; Gaetano Burriesci: Refinement of equations and text, Images, Editing, Formatting, Supervision			
<b>4. In which chapter(s) of your thesis can this material be found?</b>			
Chapter 3. Introduction to Auxetics			
<b>5. e-Signatures confirming that the information above is accurate</b> (this form should be co-signed by the supervisor/ senior author unless this is not appropriate, e.g. if the paper was a single-author work):			
<b>Candidate:</b>	Ebba Montgomery Liljeroth	<b>Date:</b>	05/10/2022
<b>Supervisor/ Senior Author</b> (where appropriate):	Click or tap here to enter text.	<b>Date:</b>	Click or tap to enter a date.

## Declaration of originality

I, Ebba Montgomery Liljeroth, confirm that the work presented in this thesis is my own. I gratefully acknowledge the continuous help and guidance by my supervisors and their respective teams of researchers and students. When information has been derived from other sources; I confirm that this has been indicated in the thesis.



## Impact statement

With an ageing population, necessarily associated with growing healthcare demands and rising costs to provide it, it is essential to optimise current treatments and continuously implement more effective sustainable solutions.

Medical device innovation goes hand in hand with advancements in other fields such as engineering and material science. New clinical demands provide a stimulus for engineering innovation, whilst innovative technological advancements open new opportunities in medicine.

The implementation of transformative solutions typically requires an initial stage where different disciplines, initially far from each other, are brought together. The aim of this project has been to fill the gap between theoretical knowledge of auxetic structures and materials behaviour and the requirements allowing to expand their unique features to cardiovascular stent applications.

This has primarily led to significant impact in expanding the current theoretical knowledge and understanding of auxetics applications in tubular configurations. For the first time, in this work are derived and validated comprehensive analytical models describing the mechanical response of double arrowhead structures, which exhibit extreme negative Poisson's ratios.

Secondly, from a translational perspective, this project has sought to simplify the design process of cardiovascular stents leveraging auxetic behaviours, with strong impact for the biomedical industry and medical device researchers. In particular, the thesis provides guidance in the selection of the most appropriate auxetic structures, based on the intended purpose and functional requirements

A similar contribution is hoped to be made in enabling the exploitation of the properties offered by auxetics in more general contexts where tubular configurations are used, such as oesophageal stents, cannulation devices or other fields where similar structures may be of advantage. The overall thesis is intended to contribute to navigate the auxetic parameter options and possibilities that exist for those that may not come from a specific background on negative Poisson's ratio materials and help lower the initial threshold for anyone contemplating using auxetic structures for any design purposes.

## Abstract

Deformations of the great vessels during the cardiac cycle are characterised by simultaneous dilatation and elongation. Congenital conditions, vascular diseases or natural ageing often affect the great vessels, and stents and stent-graft devices are required to restore the proper cardiovascular function. However, these devices are generally highly stiff and not designed to replicate the physiological dynamics of healthy vessels.

This PhD project aims at investigating the properties of auxetic structures to design stents that can mimic the great vessels' physiological deformations. These structures differ from standard materials and provide unusual mechanical properties thanks to their negative Poisson's ratios.

The project focused on three different auxetic cellular configurations that are suitable for adaptation to tubular cellular structures and are reported to exhibit highly negative Poisson's ratios: re-entrant hexagonal honeycomb, double-arrowhead shape and hexachiral shape. This has required the derivation and validation of new analytical models, filling the gaps in the current description. The effect of the possible changes in the characteristic geometric parameters defining each auxetic configuration over the mechanical response of the tubular structure to circumferential expansion, axial tension and twisting was analysed analytically and by finite element modelling. The different ranges of Poisson's ratios, Young's moduli and shear moduli for all three configurations are presented in a consistent unified nomenclature. This allows a direct comparison between the available options, simplifying the selection on the most suitable auxetic structure. Comparison to clinical data confirms that auxetic configurations can be leveraged to mimic the range of physiological dynamics of the great vessels. In the context of stents and stent-grafts, this may contribute to enhance their physiological behaviour and long-term outcomes, by restoring more natural vessel dynamics and reducing late complications.

# Table of Contents

UCL Research Paper Declaration Form .....	1
Declaration of originality .....	3
Impact statement .....	4
Abstract.....	5
List of abbreviations .....	9
List of figures .....	10
List of tables.....	15
1. Introduction .....	16
1.1 Introduction.....	16
1.2 Scope of PhD, research question, aims, .....	16
1.3 Outline of this thesis .....	17
2. Background: Clinical Problem .....	19
2.1 Heart and great vessels.....	19
2.2 Treatments for cardiovascular diseases: Open heart surgery vs transcatheter .....	24
2.3 Stents: Different types, materials and design considerations .....	24
2.3.1 The importance of stent-design: Structure of existing stents, stent-grafts and percutaneous pulmonary valve implantation (PPVI) .....	26
2.4 Summary and Conclusion.....	27
3. Auxetic structures and materials – background, review and selection .....	28
3.1 Introduction to auxetics.....	28
3.2 Re-entrant structures .....	31
3.2.1 Inverted or re-entrant hexagonal honeycomb .....	31
3.2.2 Double arrowhead.....	39
3.2.3 Other re-entrant shapes .....	43
3.3 Chiral structures .....	44
3.4 Rotating plates.....	57
3.4.1 Rotating quadrangular plates .....	58
3.4.2 Rotating triangular plates .....	65
3.5 Others .....	67
3.6 Summary/Discussion: Options and Suitability for cardiovascular stents.....	67
3.7 Conclusion: Choice of which auxetic structures to study further in this specific study .....	69
4. Development of analytical method for Double Arrowhead .....	70
4.1 Introduction to analytical method .....	70
4.2 Flexure model.....	72
4.2.2 Uniaxial loading of double arrowhead cell in direction 2 .....	74

4.2.3 Flexural response of double arrowhead cell in shear loading .....	75
4.2.4 Calculating the elastic properties for pure flexure deformation .....	81
4.2.5 Rewritten in the format $la = L$ and $lb = L\sin\alpha\sin\beta$ .....	82
4.3 Stretching model.....	83
4.3.1 Shear .....	83
4.3.2 Rewritten in the format $la = L$ and $lb = L\sin\alpha\sin\beta$ .....	84
4.4 Combining flexure and stretching to a complete shear model .....	85
4.4.1 Rewritten in the format $la = L$ and $lb = L\sin\alpha\sin\beta$ .....	85
4.5 Conclusion.....	85
5. Analytical Method.....	86
5.1 Re-entrant Hexagonal: Selection of analytical model, conversion to tubes .....	86
5.2 Double arrowhead: Development of analytical model, conversion to tubes .....	88
5.3 Hexachiral: Selection of analytical model, conversion to tubes .....	90
6. Numerical Method .....	93
6.1 Nominal tubes – For comparison between analytical and numerical .....	93
Reference configurations .....	95
6.2 Finite Element Analysis: Details.....	98
6.2.1 Beam models, Beam types, Analysis type etc .....	98
6.3 Modes of deformation and associated boundary conditions.....	99
6.3.1 Circumferential expansion .....	100
6.3.2 Longitudinal expansion.....	101
6.3.3 Twist – Shear .....	102
7. Results: Tubular structures .....	104
7.1 Re-entrant hexagonal .....	104
7.1.1 Poisson's ratio.....	104
7.1.2 Young's modulus.....	106
7.1.3 Shear modulus.....	108
7.2 Double arrowhead .....	109
7.2.1 Poisson's ratio.....	109
7.2.2 Young's modulus.....	111
7.2.3 Shear modulus.....	113
7.3 Hexachiral .....	114
7.3.1 Poisson's ratio.....	115
7.3.2 Young's modulus.....	116
7.3.3 Shear modulus.....	117
7.4 Difference between analytical and numerical models .....	118
7.5 Summary results.....	119

8. Discussion .....	120
8.1 Discussion of study of tubular structures.....	120
8.1.1 General behaviour of the auxetic tubular structures .....	120
8.1.2 Comparison and suitability for different types of applications.....	122
8.1.3 Difference between analytical and numerical predictions – impact on design considerations, limitations, and further questions .....	123
8.1.4 Summary tubular structures .....	124
9. Specific issues in practical stent design .....	125
9.1 Manufacturing and deployment discussion .....	125
9.2 Membranes .....	125
9.2.1 Membrane modelling methodology.....	126
9.2.2 Membrane elastic strain and stress results.....	130
9.3 Examples of cardiovascular applications possibly suitable for auxetic stents and design suggestions.....	135
9.4 Case study: Design of auxetic stent graft for ascending aorta using re-entrant hexagonal honeycombs.....	136
9.4.1 Introduction to Design Process.....	136
9.4.2 Analytical design process.....	137
9.4.3 Numerical modelling process .....	139
9.4.4 Resulting design.....	141
9.4.5 General afternotes and concluding remarks .....	143
10. Conclusion and future works .....	144
Bibliography .....	146
Appendix.....	157

## List of abbreviations

*AV* – Aortic Valve

*CAD* – Computer Aided Drawing

*CT* – Computer Tomography

*DAH* – Double-Arrowhead

*FEA* – Finite Element Analysis

*HC* – Hexachiral

*LA* – Left Atrium

*LV* – Left Ventricle

*LVOT* - Left Ventricular Outflow Tract

*MRI* – Magnetic Resonance Imaging

*NPR* – Negative Poisson's Ratio

*PA* - Pulmonary Artery

*PET* - Polyethylene terephthalate

*PPVI* - Percutaneous Pulmonary Valve Implantation

*PTFE* - Polytetrafluoroethylene

*PV* - Pulmonary Valve

*RA* – Right Atrium

*REH* – Re-entrant hexagonal honeycomb

*RV* – Right Ventricle

*RVOT* – Right Ventricular Outflow Tract

*TAVI/TAVR* – Transcatheter Aortic Valve Implantation/Transcatheter Aortic Valve Replacement

## List of figures

Figure 1: Anatomy of the heart [6] .....	20
Figure 2: The aorta subdivided into the main parts. [7].....	21
Figure 3: Left: Pulmonary Artery with the planes indicating A. sub-valve: through the 3 hinge points of the valve in the RVOT; B. supra-valve: through the 3 commissural points at the end of the valvular sinuses; C. pre-bifurcation: below the bifurcation with only 1 point of intersection with plane R and with plane L; D. mid-valve: at the mid-point between the sub-valve and the supra-valve planes; E. mid-trunk: at the mid-point between the supra-valve and pre-bifurcation planes; R. orthogonal to the right pulmonary artery centreline, 1 mm above the bifurcation; L. orthogonal to the left pulmonary artery centreline, 1 mm above the bifurcation; Right: Movement of plane E (and pulmonary trunk) during the cardiac cycle [29] .....	23
Figure 4: The different steps of inserting a coronary stent with a balloon catheter: i) The insertion of catheter guiding wire, (ii) The positioning of collapsed stent and balloon, (iii) the placement and expansion of stent by expansion of balloon, (iv) the removal of the balloon and catheter, with the expanded stent left in place [36] .....	25
Figure 5: Aortic aneurism repair with open heart surgery versus with a non-invasively placed stent [37] .....	25
Figure 6: Examples of different Transcatheter Aortic Valve Replacements [43].....	26
Figure 7: Examples of different commercially available stent-grafts [44] .....	26
Figure 8: The behaviour of (left) regular positive Poisson's ratio materials and (right) auxetic negative Poisson's ratio materials and structures under deformation, with the original shape in dark and the deformed shape in lighter grey, under uniaxial loading in the direction of the arrows.....	29
Figure 9: Example of re-entrant hexagonal honeycomb before (left) and after (right) uniaxial compressive deformation. ....	32
Figure 10: Schematic nominal stress – nominal strain diagram for cellular hexagonal structures subjected to in-plane compressive load. ....	33
Figure 11: Comparison of the in-plane Poisson's ratios, Young's moduli and shear modulus determined with the different models proposed for the analysis of hexagonal honeycombs (see Table 1) in conventional and auxetic configurations. The parameters used as defined above is $t = 0.05$ , $d = 0.5$ and $B \times H = 1 \times 1$ unit lengths, resulting in $l = B/(2 * \sin\phi) = 0.5/\sin\phi$ and $h = H/2 + l * \cos\phi = 0.5 + l * \cos\phi$ .....	38
Figure 12: Example of double arrowhead structure before (left) and after (right) uniaxial compressive deformation. ....	40
Figure 13: Diagrams of the in-plane Poisson's ratios and Young's moduli determined with the equations for the analysis of double arrowhead structures (see Table 2) in conventional and auxetic configurations. The parameters used as defined above is $t = 0.05$ , $d = 0.5$ and	

$B \times H = 1 \times 1$  unit lengths, resulting in  $l = B/(2 * \cos\theta) = 0.5/\cos\theta$ . As defined above,  
 $\varphi = \arctan(2 H/B + \tan\vartheta) = \arctan(2 + \tan\vartheta)$ ..... 42

Figure 14: Common STAR-n systems labelled as (a) STAR-3, (b) STAR-4 and (c) STAR-6 configurations..... 43

Figure 15: Schematic representation of a Milton lattice and description of the identified mechanism providing internally auxetic behaviour. .... 44

Figure 16: Trichiral (a), tetrachiral (b) and hexachiral (c) structures, and description of the mechanism responsible for the auxetic behaviour. .... 46

Figure 17: Anti-Trichiral (a) and anti-tetrachiral (b) structures, and description of the mechanism responsible for the auxetic behaviour. .... 47

Figure 18: Comparison of the in-plane Poisson's ratio, Young's modulus and shear modulus determined with the different models proposed for the analysis of hexachiral honeycombs (see Table 3). The parameters used are as defined above  $D = 1$  unit length,  $t = 0.05$  and  $d = 0.5$ . For Bacigalupo & Gambarotta,  $\varphi = 0.85$ . .... 51

Figure 19: Comparison of the in-plane Poisson's ratio and Young's modulus determined for the different chiral and anti-chiral configurations summarised in Table 4. For all  $t=0.05$ ,  $D=1$  (in case  $H=B$ ,  $H=B=D=1$ ), and  $\vartheta = \sin^{-1}\left(\frac{2r}{D}\right)$ . For the tetra-, tri- and anti-trichiral,  $l = \frac{D}{2} * \cos\vartheta$ , and for the anti-tetrachiral  $l = \frac{D}{2} = 0.5$ . .... 54

Figure 20: Deformation mechanism of chiral (a) and anti-chiral (b) missing rib structure. .... 56

Figure 21: Deformation mechanism of rotating plates. .... 57

Figure 22: Deformation mechanism of rotating rectangular plates, connected with Type I (a) and Type II (b) arrangements. .... 59

Figure 23: Deformation mechanism of rotating rhombohedral plates, connected with Type  $\alpha$  (a) and Type  $\beta$  (b) arrangements. .... 59

Figure 24: Deformation mechanism of rotating parallelograms, connected with Type I  $\alpha$  (a), Type II  $\alpha$  (b), Type I  $\beta$  (c) and Type II  $\beta$  (d) arrangements. .... 60

Figure 25: Diagrams of the in-plane Poisson's ratios and Young's moduli determined with the equations for the analysis of rotating quadrangular rigid plates (see Table 7) in conventional and auxetic configurations, the parameters used as defined above  $l = 1$ ,  $a = 1.5$ ,  $b = 0.666$  unit length,  $\varphi = 60^\circ$  and  $K_h = 1.0 \cdot 10^{-6}$  unit force. .... 64

Figure 26: Deformation mechanism of equilateral (a) and irregular (b) rotating triangular plates. .... 65

Figure 27: Example of a re-entrant trichiral honeycomb structure (a) and of a two-level hierarchical rotating squares structure (b) ..... 67

Figure 28: a) Uniaxial loading in 1-direction and resulting b) long beam and c) short beam free body diagram, respectively. .... 72



Figure 29: a) Uniaxial loading in 2-direction and resulting b) long beam and c) short beam free body diagram, respectively. ....	74
Figure 30: Flexural response of double arrowhead cell subjected to shearing.....	75
Figure 31: Free body diagram of the left-side longer beam of length $l_a$ , referred to as beam $A_l$ .....	76
Figure 32: Free body diagram of the right-side longer beam of length $l_a$ , referred to as beam $A_r$ .....	77
Figure 33: Free body diagram of the left-side shorter beam of length $l_b$ , referred to as beam $B_l$ .....	78
Figure 34: Free body diagram of the right-side longer beam of length $l_b$ , referred to as beam $B_r$ .....	78
Figure 35: Shear deflection us as a combination of the deformation of the individual beams .....	80
Figure 36: Shear stretching model of double arrowhead cell.....	83
Figure 37: Schematic of geometric parameters for the re-entrant hexagonal unit cell and the tube used in the equations below, where $\theta = 90 - \varphi$ .....	87
Figure 38: Schematic of geometric parameters for the double arrowhead unit cell and the tube used in the equations below .....	89
Figure 39: Schematic of the geometric parameters of the hexachiral configuration in relation to the tube. Node distance $R$ , node radius $r$ , ligament length $L$ , ligament thickness $t$ and angle of chirality $\beta$ .....	90
Figure 40: Schematic of nominal tube under (a) longitudinal nominal stress, (b) circumferential nominal stress and (c) under nominal shear stress. [49] .....	93
Figure 41: The standard configuration tube for a) REH b) DAH and c) HC.....	98
Figure 42: Symmetry evaluation of the different configurations, from the left: hexachiral, double arrowhead and re-entrant hexagonal honeycombs.....	99
Figure 43: Matching boundary links: The red lines mark the connection between the node on the bottom and top of the tube. The pictures below are of the bottom ends of the tubes. ..	100
Figure 44: The circumferential expansion of an inner tubular surface expands the auxetic structure. For those cases where possible, a symmetry plane is added (see rectangle behind).....	101
Figure 45: Longitudinal expansion of the tubular structure with the aid of a moving plane (moving line on top). ....	101
Figure 46: Twisting of tubular structure with the aid of rotating planes. ....	102

Figure 47: Re-entrant hexagonal geometric parameters referred to in results .....	104
Figure 48: Poisson's ratio in relation to four different geometric parameters for the Re-entrant hexagonal honeycomb configuration, where M&E indicates analytical method derived by Masters & Evans and G&A Gibson & Ashby. Angle Theta ( $\Theta$ ) is given in degrees.....	105
Figure 49: Nominal Young's Modulus $E/E_s$ in relation to four different geometric parameters for the Re-entrant hexagonal honeycomb configuration .....	107
Figure 50: Nominal shear modulus for Re-entrant Hexagonal honeycombs .....	109
Figure 51: Double arrowhead geometric parameters referred to in results .....	109
Figure 52: Poisson's ratio for the double arrowhead.....	111
Figure 53: Nominal Young's moduli for the double arrowhead.....	112
Figure 54: Young's moduli for double arrowhead .....	112
Figure 55: Shear moduli for the double arrowhead.....	113
Figure 56: Double arrowhead shearing - comparing modes of deformation (flexure, stretching and a combination of both). .....	114
Figure 57: Hexachiral geometric parameters referred to in results, with R being the distance between the centre of two unit-cells and L the beam length of the connecting ligament....	115
Figure 58: Poisson's ratio for the hexachiral configurations.....	115
Figure 59: Nominal Young's moduli for hexachiral.....	116
Figure 60: Micropolar constants with two values of ligament aspect ratio $t/L = [1/100 \text{ and } 1/20]$ with rigid nodes (black lines, +, x symbols) and deformable nodes (red lines, $\square$ , $\Delta$ symbols) for Nominal Young's Modulus and Poisson's ratio by Spadoni and Ruzzene for comparison. [106] .....	117
Figure 61: Nominal shear moduli for the hexachiral configurations.....	117
Figure 62: Micropolar constants with two values of ligament aspect ratio $t/L = [1/100 \text{ and } 1/20]$ with rigid nodes (black lines, +, x symbols) and deformable nodes (red lines, $\square$ , $\Delta$ symbols) for Nominal Shear Modulus by Spadoni and Ruzzene for comparison. [106] .....	118
Figure 63: Direct quantitative comparison of the different ranges achievable for the different configurations without altering thickness of struts, for the circumferential (c) and the axial (z) directions for anisotropic parameters, with each dot representing the numerical result from one analysis for the reference $d/D=0.02$ . Higher concentrations of dots indicate the property intervals more commonly achieved while outliers highlight extreme cases achieved only for a very small range of values for a parameter. ....	122
Figure 64: Re-entrant hexagonal membrane model, where the thin black lines represent the beams, the blue the membrane, and the pink and green the matching boundaries (where the pink side is tied to the mirrored green side, vertically and horizontally respectively).....	127

Figure 65: Double arrowhead membrane model, where the thin black lines represent the beams, the blue the membrane, and the pink and green the matching boundaries (where the pink side is tied to the mirrored green side, vertically and horizontally respectively).....	128
Figure 66: Hexachiral membrane model, where the thin black lines represent the beams, the blue the membrane, and the pink and green the matching boundaries. ....	129
Figure 67: Re-entrant hexagonal membrane stresses and strains .....	131
Figure 68: Double arrowhead membrane strain and stresses .....	132
Figure 69: Top: Equivalent von Mises stress for the hexachiral configuration with membrane, Middle: Equivalent von Mises stress with threshold excluding beam stresses, Bottom: Equivalent elastic strain .....	134
Figure 70: Instability of hexachiral membrane with struts of equivalent thickness to those for the double arrowhead and re-entrant hexagonal, with indications of out-of-plane deformations. To the left, in-plane view, to the right, out of plane view. At the top, the auxetic structure's struts were allowed to move out of plane, at the bottom the struts were restricted to in-plane movement (range of displacement shown in color narrowed for clarity). ....	135
Figure 71: To the left, the pattern cut out from the tube; to the right, the unfolded pattern. ....	139
Figure 72: One cell cut out from the structure with the aid of symmetry plans to mark the presence of the other cells in the grid: cell marked in pattern on the left, isolated cell on the right.....	140
Figure 73: The cell flanked by symmetry planes marking the existence of the other cells, here around the circumference of the cylinder .....	140
Figure 74: Expansion in the radial direction, symmetry planes shown, accounting for the rest of the cells around the circumference of the tube .....	142
Figure 75: Expansion in the radial direction, view on cell showing expansion in both radial and longitudinal direction. ....	142
Figure 76: Shape of cell during the diastolic versus systolic phase of the cycle.....	142
Figure 77: Final device in full.....	143
Figure 78: a) Uniaxial loading in 1-direction and resulting b) long beam and c) short beam free body diagram, respectively .....	157
Figure 79: a) Uniaxial loading in 2-direction and resulting b) long beam and c) short beam free body diagram, respectively .....	159

## List of tables

Table 1: Equations derived by the different research groups for the determination of the Poisson's ratios, elastic moduli and, where available, shear modulus, in the two in-plane directions of orthotropy of hexagonal honeycombs. ....	36
Table 2: Equations of the in-plane Poisson's ratios and elastic moduli for double arrowhead structures. ....	41
Table 3: Equations derived by the different research groups for the determination of the in-plane Poisson's ratio, elastic modulus and, where available, shear modulus, for hexachiral honeycombs. ....	50
Table 4: Equations derived by Mousanezhad et al. [82] for the determination of the in-plane Poisson's ratio, elastic modulus and, where available, shear modulus, for tetrachiral, anti-tetrachiral, trichiral and anti-trichiral honeycombs.....	53
Table 5: Schematic representation of different orthotropic chiral configurations and equations derived by different groups for the determination of the Poisson's ratios and, where available, elastic moduli for the two in-plane directions of orthotropy. ....	55
Table 6. Equations derived for the determination of the in-plane Poisson's ratio and elastic modulus for missing rib structures.....	57
Table 7. Equations derived for the determination of the in-plane Poisson's ratio, elastic modulus and, where available, shear modulus, for different quadrangular plate configurations described in the literature. ....	62
Table 8. Equations derived for the determination of the in-plane Poisson's ratio, elastic modulus shear modulus, for triangular plate configurations.....	66
Table 9: Geometric parameters used for Re-entrant Hexagonal Honeycombs .....	95
Table 10: Geometric parameters used for the Double Arrowhead configuration .....	96
Table 11: Geometric parameters used for the Hexachiral configuration .....	96
Table 12: Membrane model parameters.....	130
Table 13: Re-entrant hexagonal membrane results.....	130
Table 14: Double arrowhead membrane results.....	131
Table 15: Hexachiral membrane results .....	133
Table 16: Anatomical data .....	141
Table 17: Analytical design .....	141
Table 18: Comparison analytical design and numerical model .....	141

# 1. Introduction

## 1.1 Introduction

Biomedical engineering is a rapidly growing field where new technologies are constantly developing to answer challenges in modern medicine. One of these big challenges is cardiovascular disease, the leading cause of mortality and morbidity globally [1]. Ageing, congenital conditions and vascular disease resulting in decreased cardiac capacity and health complications affect large proportions of the population, and the cardiovascular burden is likely to increase further in the future. Widely used devices to treat the most common cardiovascular diseases are stents, metallic wire-meshes that act like scaffolds to maintain the vessels open. Despite their several applications, stents are generally not designed to restore the dynamic patterns of the vessels, which in normal healthy conditions can exhibit quite large motions with simultaneous elongation and circumferential expansion, especially in the case of the great vessels. Most common materials and structures do not replicate this behaviour; instead, elongation in one direction causes contraction in the other. Auxetic materials and structures have emerged over the last few decades as a novel material class that exhibits the unusual property of simultaneous elongation in two or more orthogonal directions when stretched along one of the directions. Attempts at designing stents that leverage auxetic structures have been made, but the gap of knowledge in auxetics structure behaviour for cardiovascular applications remains wide. To help bridge this gap, this PhD project provides guidance on auxetics structures from the stent design perspective, whilst enhancing our knowledge on the general mechanical behaviour of these structures. It has so far resulted in one publication, “Elastic Properties of 2D Auxetic Honeycomb Structures—A Review” in *Applied Materials Today* from Chapter 3, and one further in process with the working title “Models for the elastic deformation of auxetic double arrowhead honeycombs for planar and tubular structures” from Chapter 4, as well as the potential of a publication covering the membrane investigation in Chapter 9. It has also resulted in two presentations on the topics so far, one at the 10<sup>th</sup> International Conference Auxetics and other materials and models with “negative” characteristics and 15<sup>th</sup> International Workshop Auxetics and related systems, September 2019 in Poznan, titled “*Using auxetic structures for stents*”, and one at the 9<sup>th</sup> World Congress of Biomechanics, July 2022 Taipei, titled “*Auxetic structural properties for use in cardiovascular stents*”.

## 1.2 Scope of PhD, research question, aims,

The aim of this thesis is to explore the use of auxetic structures in cardiovascular stent design. These structures could be used to improve the dynamic performance of

cardiovascular stents, resulting in better hemodynamics and long-term outcomes to the benefit of the patients.

The main objectives of this project can be summarised as follows:

- **To review the literature and identify which auxetic structures may be suitable for use in the design of cardiovascular stents**

Among previously described auxetic structures, to identify those theoretical elastic properties warranting further investigation for their behaviour in tubular, stent-like configurations.

- **To develop analytical expressions to investigate the elastic mechanical behaviour of auxetic structures of interest that lack current comprehensive equations**

In particular, the double arrowhead structure has no derived expressions for shear modulus that can be readily found in the literature.

- **To undertake a numerical analysis of the effect of the geometric parameters on the main auxetic structures in order to compare their features in the context of tubular structures for practical applications**

To test different configurations and assess the resulting elastic properties in order to increase the information available for stent design applications.

- **To identify exemplar practical applications and suggestions for the development of a stent design**, by leveraging suitable auxetic structures.

### 1.3 Outline of this thesis

Here in **Chapter 1: Introduction**, we present the remainder of this thesis which is organised as follows:

**Chapter 2: Clinical Background**, provides a general overview of the project background, from the clinical perspective, by introducing cardiovascular disease, and the anatomy, physiology and common pathologies of the heart, with focus on relevant mechanisms. Further insight into available types of treatment and in particular stents is provided. Finally stent design is discussed to provide a framework for the following chapters.

**Chapter 3: Introduction to Auxetics**, provides an introduction to auxetics, together with an in-depth analysis of available auxetic configurations and the selection of those that may find potential use in cardiovascular stent design, to be further studied.

**Chapter 4: New analytical model**, introduces the development of a new analytical method for examining the elastic mechanical behaviour of the double-arrowhead structure, presenting expressions for the Poisson's ratio, Young's moduli and shear modulus.

**Chapter 5: Analytical Method**, introduces the analytical method used for analysis of tubular structures, comparing three selected auxetic structures, implemented from literature or developed in the previous chapter and converted for tubular structures.

**Chapter 6: Numerical Method**, introduces the numerical method used for analysis of the tubular structures of Chapter 5, discussing finite element modelling, boundary conditions and deformation mechanisms.

**Chapter 7: Results**, shows the results obtained from the analysis of the tubular structures, both from the analytical and numerical investigations.

**Chapter 8: Discussion**, discusses the results obtained above and analyses the limitations of the study: both the differences between analytical and numerical results, and the limitations to consider when trying to implement this in practical device design are examined.

**Chapter 9: Comments on Practical Stent Design**, relates to the intended clinical applications, and how the knowledge obtained can result in stent designs using auxetic structures, demonstrating the implementation of the acquired knowledge.

**Chapter 10: Conclusion**, summarises the work done in this thesis and outlines interesting research avenues for the future.

## 2. Background: Clinical Problem

Cardiovascular disease is one of the leading causes of death in the modern world [1], and, together with a decrease in life expectancy, is often the cause for a reduction in the quality of life for patients affected by this disease and their family, bearing important social costs. The source of cardiovascular disease ranges from congenital malformations to lifestyle related diseases and ageing, with a multitude of other different possible factors and triggers. With the increase in medical knowledge and technology available to the health care system, conditions that previously were fatal can now be treated. This means that people now live with an increasing range of diseases for a longer time and improving their quality of life is imperative to advancing modern health care. In the U.K. alone, 7.6 million people are living with heart and circulatory diseases [2]. Globally, it is estimated that 550 million people worldwide are living with heart and circulatory diseases, and 34% of global death can be attributed to these [3]. 16% of the world's total deaths are related with ischaemic, or coronary, heart disease [4]. Stroke or cerebrovascular disease is the second most common cause for death worldwide, with 11% of total deaths, followed by chronic pulmonary disease with approximately 6% [4]. In the U.K. an average of 13 babies per day are diagnosed with a congenital heart defect [2], and globally an average of 3 300 per day, causing at least 220 000 deaths globally each year, the majority before the first birthday [3]. Cardiovascular disease is also associated with highly increased risk of vascular cognitive impairment and vascular dementia, caused by ischaemic damage to the blood vessels of the brain, with people with a family history of coronary disease significantly more likely to develop vascular dementia [2]. This manifests differently depending on the region where the damage is located and its severity. In the U.K., vascular dementia is recognised to be the second most common type of dementia after Alzheimer's, reported in up to 1 in 5 cases, and it is also suspected to be underdiagnosed due to difficulties diagnosing its different forms [2].

### 2.1 Heart and great vessels

The heart,

Figure 1, can be divided into the right and left side, where the right side collects the de-oxygenized blood from the body via the superior and inferior vena cava in the right atrium. It is then transported via the tricuspid valve into the right ventricle where it is pumped through the pulmonary valve and through the pulmonary artery to the lungs. The oxygenated blood from the lungs is then collected through the pulmonary veins in the left atrium and then let through the bicuspid, or mitral, valve into the left ventricle where it pumped out through the aortic valve to the aorta and the rest of the body. The heart beats approximately 72 beats



per minute for an average human, resulting in the heart and the large vessels experiencing about 40 million cycles per year [5].

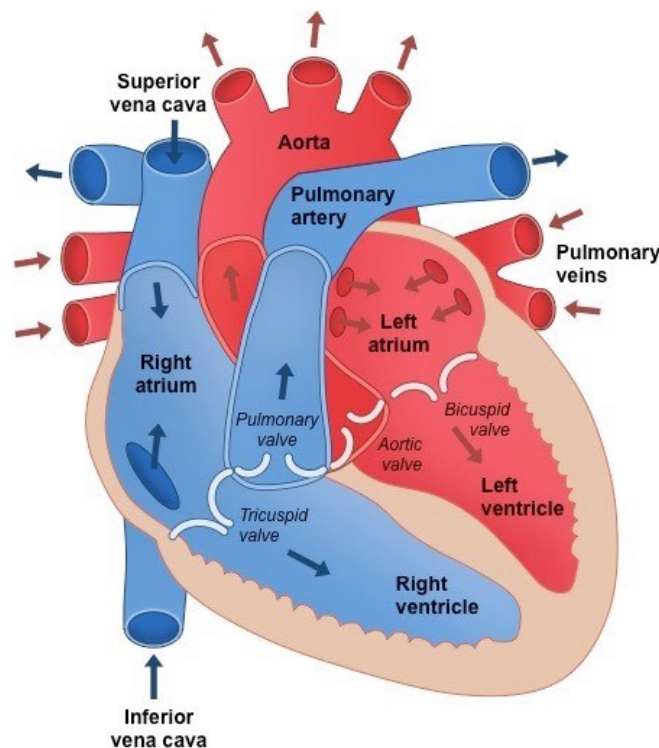


Figure 1: Anatomy of the heart [6]

The cardiac cycle can be divided into systole, or contraction of the heart muscles, where the contraction of the ventricles pushes the blood into the arteries (the pulmonary and aorta), and diastole, the relaxation of the heart muscles, which allows the ventricles to fill up again with blood from the atriums.

The heart pumping function is regulated by four valves: the atrioventricular valves (tricuspid and mitral valve), and the semilunar valves (pulmonary and aortic valve) located between the ventricles and the great vessels (aorta and pulmonary artery).

The aorta, Figure 2, delivers oxygenated blood to the entire body. It is made of the aortic root, the ascending aorta, the aortic arch and the descending aorta, going further down into the abdominal aorta [7]. The ascending aorta is commonly measured from the sinotubular junction to the first artery of the aortic arch, the innominate or brachiocephalic artery. The dynamics of the ascending aorta during the cardiac cycle has been studied and, during systole, longitudinal extension with a downwards displacement of the aortic root has been noted together with partially simultaneous dilation of the diameter[8]. The aortic movement is mostly passive and is due to the combination of the movement of the heart muscle and the aortic blood flow. During the ventricular systole, the ventricle contracts to eject the blood

from the heart and push it into the aorta, pulling down the annulus attached to the aortic root. As a result, the aorta is forced to stretch axially, while expanding circumferentially due to the blood volume ejected from the ventricle. The motion of the aortic root makes it difficult to measure the diameters along the length of the aortic root and ascending aorta, as they do not remain in the same plane [9]–[11]. However, diameter measurements over the cardiac cycle are linked to cardiovascular disease, both when aortic stiffening has led to a reduction in the motion of the heart and when aortic elongation precedes aortic dissection [11], [12].

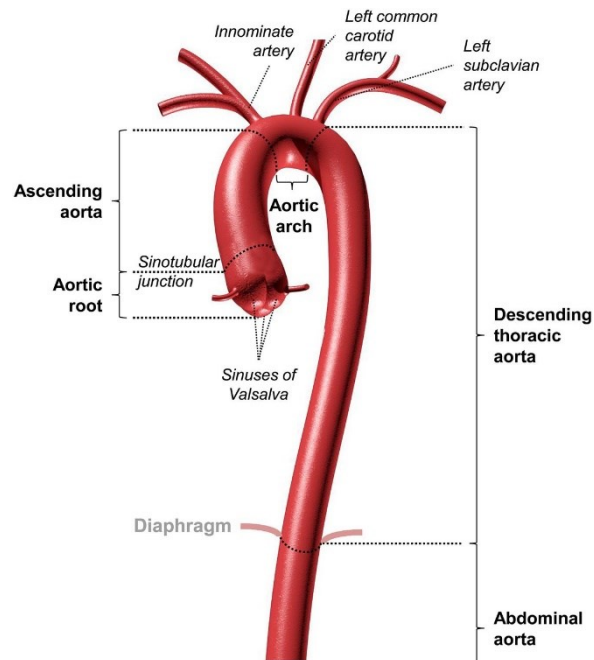


Figure 2: The aorta subdivided into the main parts. [7]

The downward displacement of the aortic root during systole is on average 8.9 mm axial downward motion and six degrees clockwise axial twist. [13] Cardiac patients with aortic insufficiency are likely to experience enhanced longitudinal stress in the ascending aorta due to increased aortic root movement. [13] Patients with aortic insufficiency and large aortic root displacement may be at considerable risk of mechanical damage to their aorta through acute (rupture) or chronic (fatigue related) events [13]. The role of aortic motion has been further linked to reducing the wall stress of the vessel [14]. The longitudinal strains of the ascending aorta have been suggested to be around 6.7-8.5% and the circumferential strains 7.9-8.1% [15], suggesting approximately equal elongation and dilation during the cardiac cycle.

Both the inner diameter and wall thickness of the aorta vary along the vessel and changes during the cardiac cycle [16], [17]. The aortic wall consists of three layers, the adventitia, the media and the intima, which cannot be distinguished by normal echocardiography [18], [19].

The adventitia is the thin, outermost layer and is composed mainly of collagen. It has the greatest tensile strength of the three layers. In aortic dissection it becomes separated from the intimal layer and in aneurysms it expands in diameter [18]. The media is the thick middle layer which accounts for up to 80% of the wall thickness. It consists of intertwining sheets of elastic tissue and muscle fibres [18]. The intima is the thin inner layer of the aorta, that consist of a membrane lined with endothelial cells in direct contact with the blood. It is the layer which is the most susceptible to injury and the site for atherosclerosis and calcification becoming thickened, calcified, or ulcerated. [18]

There have been attempts to analyse the elastic properties of each individual layer and their combination, but due to the varied nature of the three and their interactions with each other this have been difficult [20]–[22]

The aortic wall has been found to exhibit a nonlinear behaviour over finite strains [21], [23] which in part can be attributed to the interaction between the collagen and elastin in the walls [24]. This further complicates ex-vivo testing conditions, as the degradation of the organic components after extraction affects the mechanical response [24].

Studies on bovine aortas have found that the collagen fibre orientation changes in the media, where the fibre orientation is predominantly axial near the intima but changes to a largely circumferential orientation towards the adventitia [25]. The preferred fibre angle also differs depending on the direction and type of deformation applied to the specimen, when subjected to ex-vivo testing; with indications that the fibres tend to realign in the direction of the strain [25]. There have been suggestions that the thin inner layer of the median closer to the intima is arranged to support loads in the axial direction, like the axial wall shear stresses arising from blood flow, while the thicker part with circumferentially arranges fibres deeper in the vascular wall bear the load of the pulse pressure waves during the cardiac cycle [25]. For axial and biaxial loading tension load, the wall thickness decreases, but during circumferential loading the wall has been reported to becomes thicker, indicating a possible auxetic behaviour [25]. Another study found the resulting axial stress from the axial extension of the artery to be shared between the elastic fibres in the media and the axial and diagonal collagen fibres in the adventitia [22].

Uniaxial tensile testing of healthy human aortic tissue confirmed higher circumferential strength in comparison to longitudinal strength for the abdominal aorta [26]. There are also reports of different properties for different regions of the aorta, with the ascending aorta found to be more compliant than the aortic sinuses, and with biaxial tests indicating a roughly equal stiffness for the ascending aorta for the circumferential and longitudinal directions [27].

There have been promising attempts to compare findings from in vivo speckle tracking echocardiography and ex-vivo tissue measurement findings for aortic stiffness [28].

The pulmonary artery, Figure 3, is the vessel transporting the blood from the right ventricle to the lungs. The pulmonary valve is situated proximal to the heart, between plane A and B in Figure 3. The pulmonary trunk from plane B branches out at plane C into the right and left pulmonary artery, and then further out into smaller branching into the lungs. [29]. The normal reference values for the pulmonary trunk diameters have been suggested for healthy subjects to be around 27 mm for females and 29 mm for males [30]. The dynamics of the pulmonary artery during the cardiac cycle has been noted to change considerably the location of the planes relative to both their initial placement and each other [29]. The diameters along the trunk also vary during the cardiac cycle, and the pulmonary annulus was found in many cases to be not circular but elliptical in shape. Looking at patients having pulmonary valve repair, not only the diameters differ between the subjects, but the entire shape of the pulmonary artery varies greatly [29], [31].

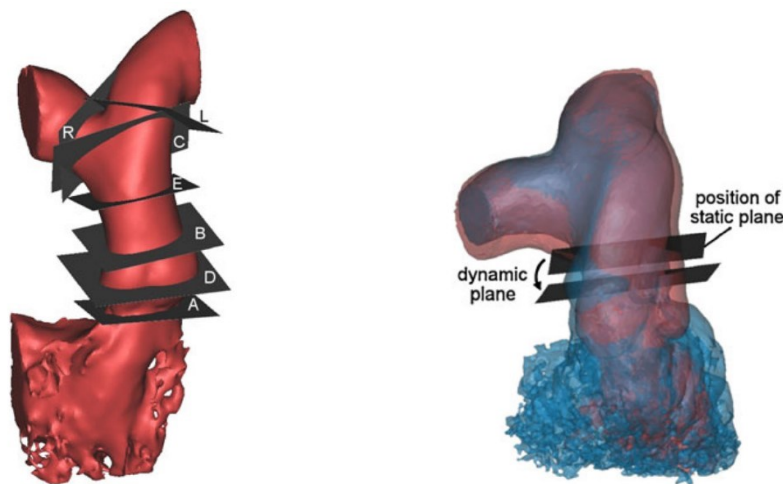


Figure 3: Left: Pulmonary Artery with the planes indicating A. sub-valve: through the 3 hinge points of the valve in the RVOT; B. supra-valve: through the 3 commissural points at the end of the valvular sinuses; C. pre-bifurcation: below the bifurcation with only 1 point of intersection with plane R and with plane L; D. mid-valve: at the mid-point between the sub-valve and the supra-valve planes; E. mid-trunk: at the mid-point between the supra-valve and pre-bifurcation planes; R. orthogonal to the right pulmonary artery centreline, 1 mm above the bifurcation; L. orthogonal to the left pulmonary artery centreline, 1 mm above the bifurcation; Right: Movement of plane E (and pulmonary trunk) during the cardiac cycle [29]

For all blood vessels, an abnormal dilation of the vessel is referred to as an aneurysm, which if left untreated can result in rupture, a life-threatening event requiring immediate medical attention. There are several different causes that may lead to abnormal vessel dilation, from connective tissue disorders to loss of vessel wall elasticity due to infections or ageing. An abnormal narrowing of a blood vessel is referred to as a stenosis. Stenosis can also refer to

valves that cannot open fully, usually due to calcification. This can lead to insufficient blood flow through the stenotic vessel, or even complete blockage, which can be life-threatening. There can be several different causes for stenosis; when of congenital nature, it often demands corrective surgery soon after birth, whilst most cases are due to aging and the development of calcifications. Age is also related to stiffening of the vessels and can hamper the dynamics of the heart and of the ascending aorta [32]–[34].

## 2.2 Treatments for cardiovascular diseases: Open heart surgery vs transcatheter

Open heart surgery remains the standard of care for most cardiovascular diseases, still superior to other approaches when it comes to versatility and precision. However, the trauma it causes to the body and the longer intensive care and hospital stays associated with it, makes it unviable in some cases, especially for patients who have an overall fragile state of health for example due to age or those suffering from more than one severe condition [35], as well as those who have congenital conditions that forces them to undergo repeated procedures with regular intervals for many years. Recent advancements in treating cardiovascular disease rely on the development of minimally invasive procedures that aim to decrease the risks associated with open heart surgery.

Minimally invasive procedures rely on the use of new technologies and techniques based on catheters / balloons and stents. Balloon angioplasty was the first of such techniques to be widely employed in cardiovascular treatments. A balloon is inserted with a catheter through a larger peripheral vessel and then guided to the correct position in the cardiovascular system where it is inflated to widen a stenotic vessel or valve in the case of balloon valvuloplasty. The intention of this is to improve blood flow through the vessel or valve. Balloons have been subsequently used as a delivery method for stents, stent grafts or even replacement heart valves for more permanent solutions.

## 2.3 Stents: Different types, materials and design considerations

Stents are metallic scaffolds designed to restore the lumen of vessels, usually created from biocompatible materials such as stainless steel, cobalt-chromium, platinum iridium, nitinol, etc. They can be covered by fabric (commonly polyethylene terephthalate (PET) or polytetrafluoroethylene (PTFE)), called stent-grafts, or used as an anchoring system for transcatheter heart valve replacement.

The most common example of this application is coronary stents, used to widen the coronary arteries affected by stenosis, allowing blood to flow to pass unobstructed, Figure 4.

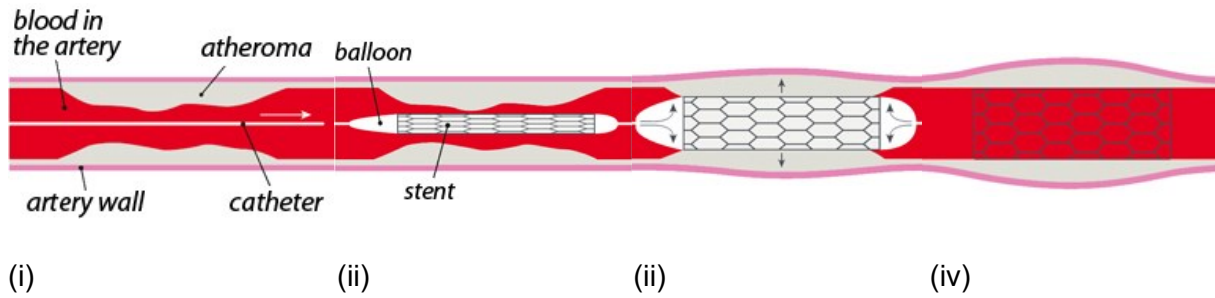


Figure 4: The different steps of inserting a coronary stent with a balloon catheter: i) The insertion of catheter guiding wire, (ii) The positioning of collapsed stent and balloon, (iii) the placement and expansion of stent by expansion of balloon, (iv) the removal of the balloon and catheter, with the expanded stent left in place [36]

An example of large stent grafts is aortic stent grafts, used to repair aneurysms in the descending aorta, as an alternative to open heart surgery.

During open-heart surgery for aortic aneurysm, the diseased part of the aorta is fully removed, and a sleeve is stitched in place instead. When a stent-graft is used, instead, the native vessel is preserved, but the blood flows through the stent-graft, see Figure 5, avoiding further stresses in the diseased part of the vessel. This approach also reduces the disruption in the blood flow in the treated region. [37]

Aortic stent grafts are usually made of nitinol self-expandable stent structures. Nitinol is an alloy of nickel and titanium which exhibits super-elastic

behaviour, allowing recoverable strains of the order of 7-9% (about 20 times larger than for stainless steel) [38]–[40]. Hence, the prosthesis is collapsed into a sheath, delivered through the vasculature to the anatomical region, and then unsheathed to allow its elastic (or pseudo-elastic as it involves a phase transformation), re-expansion.

A final example of stent use is Transcatheter Aortic Valve Replacement (TAVR), also known as Transcatheter Aortic Valve Implantation (TAVI), see Figure 6. Balloon expandable TAVR valves like the original SAPIEN (Edwards Lifesciences, Irvine, CA, U.S.A.) family have a frame made from cobalt-chromium alloy or stainless steel, and are balloon expanded, providing high radial strength. Self-expandable valves like the CoreValve (Medtronic Inc., Minneapolis, MN, U.S.A) are made from nitinol and conform to the native annulus in the attempt to recover their unstressed expanded configuration [41]. Studies suggest that there is no significant difference in post-procedure mortality between self-expandable or balloon-

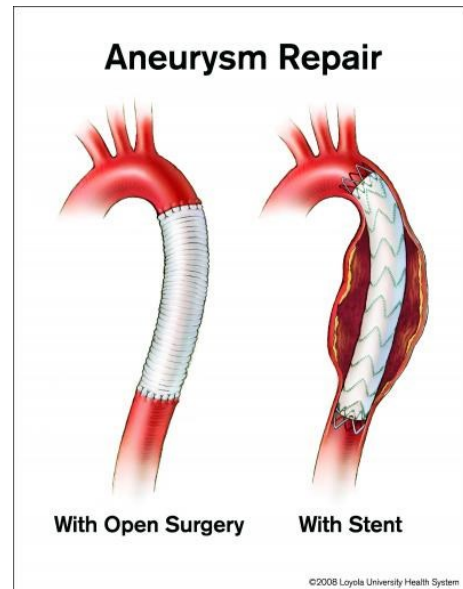


Figure 5: Aortic aneurysm repair with open heart surgery versus with a non-invasively placed stent [37]



expandable valves; however other factors might act as an indication to which might be the preferred option [42], [43].

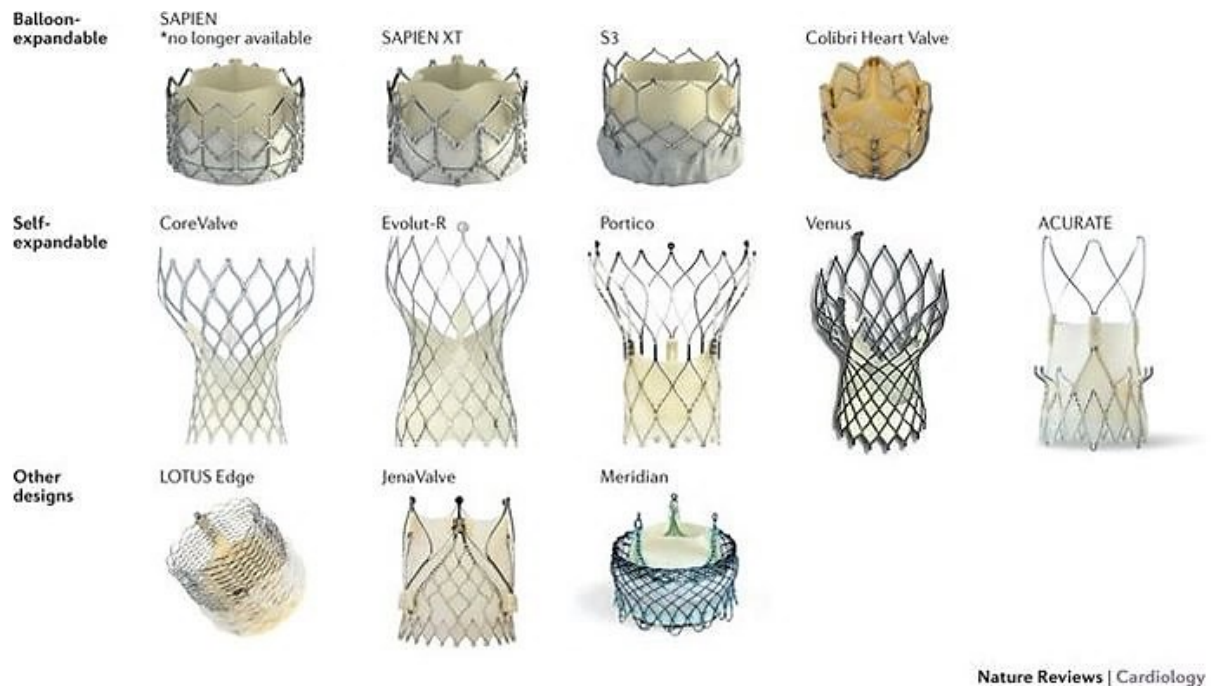


Figure 6: Examples of different Transcatheter Aortic Valve Replacements [43]

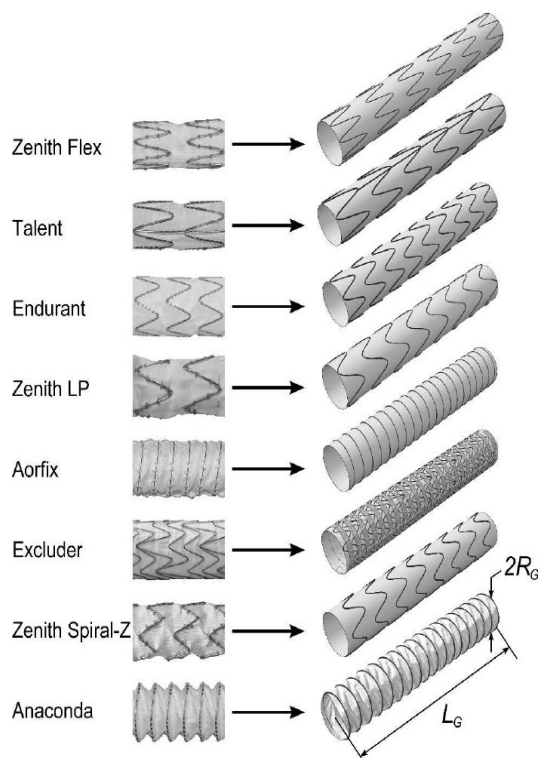


Figure 7: Examples of different commercially available stent-grafts [44]

### 2.3.1 The importance of stent-design: Structure of existing stents, stent-grafts and percutaneous pulmonary valve implantation (PPVI)

There are a wide range of different stent and stent-graft designs available, see Figure 7, and it is well accepted that the stent design strongly influences its mechanical behaviour and biomedical performance [44]. For coronary stents for example, there are several studies looking at the impact of the geometrical features of the different stent designs as well as the metallic composition of them. [45].

Stent designs are categorised in different ways, with further differences in the designs and properties between stents and stent grafts, based on the analysis of cell design, like open or closed cell structure, z-rings (like Zenit) or oval (like

Anaconda) rigid part of the stent, and the number of and type of connection between the rings, which for stent grafts can be just fabric coating.

There is a trade-off between several geometrical and mechanical requirements in stent design. For example, stents with less connections in the axial direction provide higher flexibility but lower scaffolding compared to tubular stents with a more uniform distribution of struts on the stent design. Stents with more connections tend to foreshorten more during radial expansion than their flexible counterparts, whilst more open structures can have more protrusion of intimal tissue into the vessel lumen. The shortening of stents can be an issue both in placement and for cases where the length of the stent is critical [46]. Intimal tissue protrusion can be a problem not only for bare stents, but also in stent-grafts where the lack of axial connections can make them more prone to kinking at the curvature of the vessel [44].

One way to approach these contradictory requirements and try to minimise the trade-offs between flexibility and scaffolding support could be the use of auxetic structures, especially when it comes to shortening of the stents as auxetic structures, by nature, do the opposite. This property could also allow for more control of the dynamic behaviour of the stents, as well as a means to mimic the natural dynamics of healthy vessels that during systole dilate and elongate simultaneously.

There are both theoretical auxetic stent designs and more well investigated patented systems available in literature, however few of these delve into their design selection criteria.

There are several types of auxetic structures and materials in use in medical engineering [47], and for stents there are several different auxetic designs explored. There have also been studies of more general character of auxetics in tubular structures and more specific for intended use in stents [48]–[51], using chiral structures[52]–[55], rotating plates/holes, and specific proposed designs such as the origami TiNi alloy stent graft [56] and, for non-cardiovascular applications, oesophageal stents[57] and tracheal stents[55]. Stents specifically designed for cardiovascular use, like coronary stents [58] and more advanced potentially biodegradable shape memory polymer vascular stents [59], [60] have also been explored, no extensive rationale is provided on the selected auxetic configuration. This makes difficult to assess the soundness of the design and transfer the knowledge to other medical applications.

## 2.4 Summary and Conclusion

The dynamics of the great vessels has been well documented and changes in the natural dynamics have been linked to cardiovascular disease. For example, in the ascending aorta, the specific dynamic behaviour is important in allowing correct function and reduce stress on the vessel wall. The longitudinal strains of the ascending aorta have been reported to be around 6.7-8.5% and the circumferential strains 7.9-8.1% [15], suggesting approximately



equal elongation and dilation during the cardiac cycle. However, current stent designs used to treat cardiovascular diseases do not take this dynamic behaviour into account. It would be desirable to have a solution to integrate these considerations in the design of appropriate cardiovascular devices to attempt to restore the natural motion in diseased vessels.

### 3. Auxetic structures and materials – background, review and selection

The behaviour of conventional materials and structures is that they oppose any change in volume, so they respond to an elongation in one direction by contracting in the other, and when compressed in one direction they expand in the other. Regarding stent design, this implies issues with increase in length and shortening when they are loaded into the delivery system and then expanded during implantation [61]–[63]. This also becomes a problem if the tubular structure should allow simultaneously elongation and diametrical expansion, as each of these forms of deformation opposes the other. Auxetic structures can overcome these limitations and have therefore been proposed for applications in cardiovascular stenting [49]. However, although the understanding and modelling of their mechanical properties is relatively mature for planar structures, with exception of few potentially relevant typologies, these applications require a readaptation of the current knowledge to tubular configurations. This chapter aims to describes the auxetic structures that have currently been identified and designed, identifying the different approaches utilised to define their mechanical behaviour and analysing their structural properties, limitations, and potential field of application. In particular, the focus lies on the major works within the field, discussing their limitations and addressing works done to complement them.

#### 3.1 Introduction to auxetics

Auxetics are defined as materials or structures with the elastic property of negative Poisson's ratio (NPR): when the material is stretched in one direction, it expands in one or more transverse directions as well. This differs from most materials and structures which, when stretched in one direction, typically react to the resulting increase of size in that direction by contracting transversally, see Figure 8. Hence the term auxetic, first suggested by Evans et al in 1991 [64], from the Greek word '*auxetos*' meaning 'what tends to increase'.

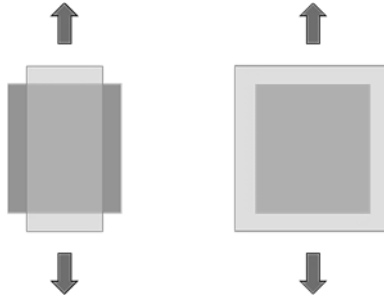


Figure 8: The behaviour of (left) regular positive Poisson's ratio materials and (right) auxetic negative Poisson's ratio materials and structures under deformation, with the original shape in dark and the deformed shape in lighter grey, under uniaxial loading in the direction of the arrows.

This behaviour emerges at the level of the internal structure of the material or stems from the structural micro and macro architecture. In the case of auxetic 'materials', the phenomenon typically depends on the molecular patterns that, when subjected to a negative stress, can occupy the intrinsic free volume between them to contract also in the lateral direction by allowing a substantial increase in the material density [64]. Another example of auxetic mechanisms is behind molecular structures like the rigid 'free' molecules described by Wojciechowski [65]. Similar mechanisms can be exploited configuring structures at micro scale and macro scale levels, like in the case of polymeric foams [66] or mainly macro scale like sandwich panels or stents [49], [67]. For many auxetic structures, the auxetic behaviour derives from the geometry and deformation mechanisms of an auxetic unit cell, and is scaled up by repetition cells [68]. Cellular structures can be divided into two categories – 2D structures, usually referred to as honeycomb structures (or 'honeycombs') and 3D structures referred to as foams [69].

Auxetic materials and structures have received strong attention as they exhibit properties, such as higher indentation resistance, thermal impact resistance, higher shear moduli as well as higher fracture toughness [64], [70], [71] that can be leveraged in a number of applications. Their acoustic properties are very interesting as the Poisson's ratio influences the speed of wave propagation in materials [72]. Another advantage of auxetic materials is the ability to assume a synclastic or dome-shaped curvature under out-of-plane bending – conversely to regular materials which assume an anti-clastic or saddle shaped curvature [67], [70] – a useful feature when manufacturing doubly curved sandwich panels, as explained by Evans [67]. When an auxetic sandwich panel is bent out-of-plane, on the compressed side, the auxetic behaviour results in a contraction also in the other in-plane direction. Conversely, on the tension side, it results in expansion also in the other in-plane direction. Overall, one side of the panel expands in both directions and the other contracts in both directions, turning the panel into a dome shape as an effect of the negative Poisson's ratio. Moreover, auxetic cellular macrostructures maintain the same advantage as ordinary

cellular material, with a lower density, making them highly appropriate for the aerospace industry among others [70]. Other applications where auxetic materials are becoming more and more popular include packaging, filters, piezo-electric composite sensors and sound insulation [71], with fields where they provide improved performance are the textile [73], [74], medical devices [48] and sport equipment industries [75].

To select the most appropriate structures for further study, the review of auxetic structures will focus on the mechanical properties of 2D auxetic cellular structures, so called auxetic honeycombs. These can be easily adapted to a large range of different applications where a change of the micro / macro structure is the basis for the auxetic behaviour as well as the basis for many of the 3D adaptations. In fact, 2D honeycombs provide a simplified model that can be extended to 3D cellular structures, [68].

In our case, the 2D structures can easily be adapted into tubular stenting structures by wrapping the plane like a sheet being wrapped into a hollow tube.

The auxetic honeycombs will be presented into three main groups, depending on the main mechanism controlling deformation:

- re-entrant honeycomb structures;
- chiral structures; and
- rotating plate structures.

For each group, the most typical structures and their common variations will be reviewed. Focus will be on the mechanical properties of the structures, without details of other properties associated with auxetic materials [76]. In particular, together with the Poisson's ratio, the nominal Young's modulus and shear modulus will be examined, and a unified and consistent formulation will be provided for all the different structures examined in this review, thus allowing direct comparison to help select the best options to proceed for cardiovascular stent designs.

To allow for direct comparison, the equations are rewritten adopting the same nomenclature and dimensional parameters between the different models, namely the horizontal and vertical cell dimensions ( $B$  and  $H$  respectively) or in case of circular unit cells like the hexachiral the unit diameter  $D$ , the cell wall thickness  $t$ , and the depth of the cell structure  $d$ . The horizontal in-plane direction of orthotropy was indicated as direction 1, the vertical as direction 2 of orthotropy, and the out-of-plane direction as direction 3. The derived equations estimate, for the two in-plane directions of orthotropy, the Poisson's ratios  $\nu_{12}$  and  $\nu_{21}$ , the elastic moduli  $E_1$  and  $E_2$  and, where available, the shear modulus  $G_{12}$ , with the subscripts defined as in the usual notation adopted for orthotropic materials.

A comparison of the responses predicted from the different equations summarised for the most investigated cases is represented graphically. These were derived assuming a unit cell of dimensions  $B \times H = 1 \times 1$  unit lengths or  $D = 1$  unit length, with a uniform wall thickness  $t = 0.05$  unit lengths, wall depth  $d = 0.5$  unit lengths and Poisson's ratio of the wall material  $\nu_s = 0.3$ .

By narrowing the scope of this review to 2D auxetic structures and their mechanical properties, the result does not only provide an in-depth overview of the different methods that have been reported in the literature to evaluate the auxetic behaviours, but also facilitate comparison between different structures. The standardised nomenclature can guide the choice on the most suitable auxetic structure for each different application, according to the required elastic behaviour, range of Poisson's ratio and sensitivity to realistic manufacturing challenges.

### 3.2 Re-entrant structures

One of the earliest re-entrant structures identified for its auxetic behaviour and intentionally exploited in a structural design by Gibson et al in 1982 [77] is the re-entrant hexagonal honeycomb structure. This is also one of the first auxetic structures where a 3D adaptation of the 2D structure was first attempted in the configuration proposed by Almgren in 1985 that offered a Poisson's ratio of -1 in all three dimensions [78]. Later, other re-entrant systems were identified and introduced, such as the double arrowhead shape [79] and the STAR-systems [80], [81].

The auxetic behaviour of re-entrant structures mostly depends on the angles between the ribs defining the cells, which change with the cells' deformation. Thus, the Poisson's ratio generally varies non-linearly with the nominal strain [72]. However, Grima *et al* investigated different ways to achieve linear negative compressibility through constrained angle stretching instead of the more commonly studied modes of deformation like flexure and hinging [82], though stretching has previously been studied without exploring compressibility by Masters and Evans [83].

#### 3.2.1 Inverted or re-entrant hexagonal honeycomb

The most extensively investigated auxetic re-entrant structure is the inverted hexagonal honeycomb, represented in Figure 9.

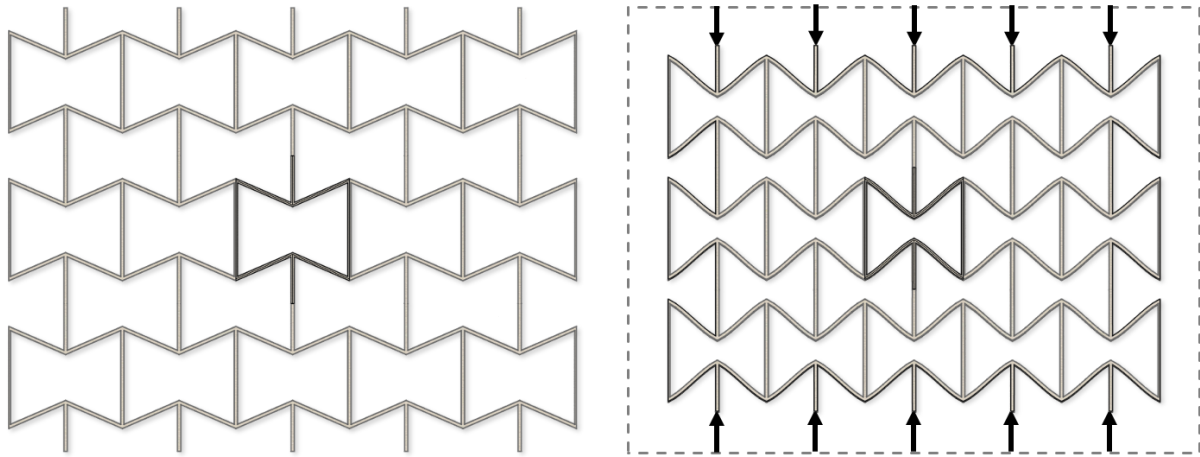


Figure 9: Example of re-entrant hexagonal honeycomb before (left) and after (right) uniaxial compressive deformation.

The structure exhibits orthotropic behaviour, and both the in-plane and out-of-plane properties have been studied extensively using different analytical approaches, as well as numerically and experimentally. The first systematic study on this class of materials was published by Gibson *et al* [77] in 1982 and analysed the mechanical response of two-dimensional cellular materials, including re-entrant hexagonal honeycombs, proposing basic equations for the prediction of their behaviour, validated by experimental models. Later, Gibson and Ashby dedicated a chapter in their book ‘Cellular Solids’ [68] to the analytical study of honeycombs, particularly the hexagonal honeycomb structure including the auxetic variation. This work investigated both the elastic in-plane and out-of-plane deformations of honeycomb structures, as well as their failure mechanisms. The approach proposed by Gibson and Ashby identifies an initial response of honeycomb structures to in-plane compression led by bending of the cell walls. This is analysed by applying the conventional beam theory to determine expressions of the nominal in-plane Poisson’s ratios, Young’s moduli and shear modulus. Hence, the mechanical response is assumed linear elastic up to the cell collapse, which, depending on the dimensions and material of the structure, occur by elastic failure (i.e., buckling of compressed walls), ductile failure (i.e., plastic collapse due to plastic hinge formation) or brittle failure (fracture). Compressive collapse is associated with a plateau in the nominal stress level, eventually lost when the material densification caused by the phenomenon results in a substantial increase in the stiffness of the structure (see Figure 10).

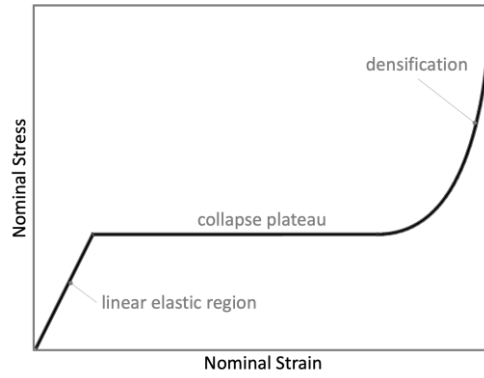


Figure 10: Schematic nominal stress – nominal strain diagram for cellular hexagonal structures subjected to in-plane compressive load.

The expression of the shear modulus from the model proposed by Gibson and Ashby appears to underestimate the value observed experimentally [68], [84]. Moreover, it becomes inaccurate for configurations characterised by slanted walls about orthogonal to the longitudinal walls, for which unacceptable values of the nominal Poisson's ratios and Young's moduli tending to infinity may be determined. This problem was addressed by an expanded version of the model proposed by Masters and Evans [83] that includes the description of other modes of elastic deformation of the honeycomb beyond bending such as hinging and stretching. The latter takes over as principal mode of deformation when the angle between the longitudinal and slanted walls tends to  $90^\circ$  when the force is in the vertical direction. Despite being accurate for modelling honeycombs with a smaller thickness compared to the wall lengths, in the case of the model by Gibson and Ashby up to  $t/l = 0.25$  [68], these models do not take into account the effect of the shape of the ligaments and the mode of connection on the deformation, which becomes significant as the ratio of the wall thickness to the wall in-plane lengths increases. In order to address this limitation, Grima, Gatt, Ellul and Attard (2011) [85] have recently proposed a set of adjusted equations using the results from numerical analyses. A number of other studies include further details in the modelling of the connections between the walls. However, they are limited to periodic hexagonal honeycomb structures, and do not investigate their reliability in the case of re-entrant auxetic configurations. These include the work from Balawi and Abot (2008) [86] that takes into account the curved intersections of the honeycomb walls commonly present in commercially manufactured honeycombs [87] (although Gibson and Ashby had already introduced a model with double wall thickness in the vertical direction [68], this model neglected the deformation in the vertical walls). Also, compared to the description from Masters and Evans, this model introduces the presence of curvature in the cell walls beyond the hinging region. This allows better description of the reduction in in-plane nominal moduli observed numerically as the radius of curvature at the wall joints increases. Another study worth mentioning, although validated only for regular hexagonal

honeycombs, was recently published by Malek and Gibson (2015) [84]: the authors introduce a beam model taking into account the effective bending length of the cell walls, which provides better alignment with both numerical and experimental results found in earlier works by Gibson at high relative densities [88].

The studies described above model the mechanical response of honeycombs by applying beam theory, but other approaches have been used as well, based on homogenisation to analyse the structure as an equivalent continuum, or on energy methods [89].

Gonella and Ruzzene (2008) [89] derived equations equivalent to those determined by Gibson and Ashby [77], but obtained through partial differential equations associated with the homogenised continuum models of the hexagonal and re-entrant hexagonal honeycomb lattices. Their model was also developed further to study the wave propagation in the structure analytically.

Berinskii (2018) [90] also used homogenisation to derive analytically the Poisson's ratios and elastic constants for the re-entrant honeycomb structure. This model takes into account the elastic deformation of the ribs, including deformation from flexure, stretching and shearing. Although the derived equations are relatively simple, the model leads to a behaviour very similar to that predicted by Masters and Evans [83]. Berinskii also established a framework to extend the same approach to the estimation of the elastic constants for a few different auxetic structures, although he did not provide in-depth validation in the manuscript.

An alternative approach to model the mechanical response of honeycombs, based on empirical models using dummy atoms (EMUDA), was proposed by Grima *et al* (2005) [91]. This force-field based molecular mechanics approach was specifically applied to re-entrant hexagonal honeycomb structures due to the broad availability of data suitable for validation.

The equations derived by the various research groups to describe the in-plane mechanical behaviour of hexagonal honeycombs are summarised in Table 1. Using the standardized nomenclature defined above, adding the angle  $\varphi$  between vertical and inclined struts. The plane of the common wall of the neighbouring cells was aligned vertically and defined as direction 2 of orthotropy. The horizontal in-plane direction of orthotropy was indicated as direction 1-

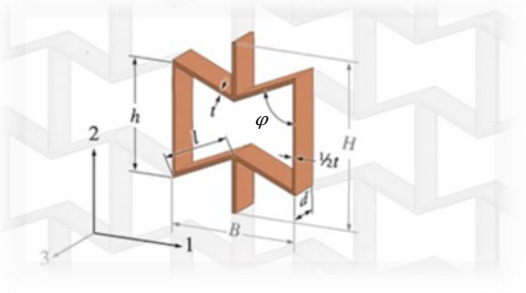
Diagrams are represented in Figure 11 for a range of the angle  $\varphi$  between vertical and inclined struts changing from  $45^\circ$  to  $135^\circ$ , thus covering the case of conventional ( $\varphi \geq 90^\circ$ ) and auxetic honeycombs ( $\varphi < 90^\circ$ ). The diagrams confirm that all models provide close predictions of the Poisson's ratio  $\nu_{12}$  for angles between vertical and inclined struts far from  $90^\circ$ . When  $\varphi$  approaches this value, the model proposed by Gibson and Ashby [68] leads to

unacceptable values of  $\nu_{12}$  (indeterminate for configurations characterised by slanted walls about orthogonal to the longitudinal walls, for which unacceptable values of the nominal Poisson's ratios and Young's moduli tending to infinity may be determined).



Table 1: Equations derived by the different research groups for the determination of the Poisson's ratios, elastic moduli and, where available, shear modulus, in the two in-plane directions of orthotropy of hexagonal honeycombs.

**HEXAGONAL HONEYCOMB**

	<p>Dimensions:</p> <p><math>h</math>: length of vertical wall (aligned with direction 2)</p> <p><math>l</math>: length of inclined wall</p> <p><math>\varphi</math>: angle between vertical and inclined walls</p> <p><math>t</math>: cell wall thickness</p> <p><math>d</math>: depth of cell structure</p> <p><math>B</math>: horizontal dimension of unit cell (along direction 1)</p> <p><math>H</math>: vertical dimension of unit cell (along direction 2)</p> <p>Material Properties of cell wall material:</p> <p><math>E_s</math>: Young's modulus</p> <p><math>\nu_s</math>: Poisson's ratio</p> <p><math>G_s</math>: Shear modulus (for isotropic materials <math>G_s = E_s/2(1 + \nu_s)</math>)</p> <p><math>\rho_s</math>: density</p> <p>Relative density: <math>\rho = \rho_s t \frac{(H \sin \varphi + B \cos \varphi + 2B)}{BH \sin \varphi}</math></p>
<b>Gibson &amp; Ashby (confirmed by Gonella &amp; Ruzzene) [68], [69][89]</b>	
Poisson's ratios:	
$\nu_{12} = -\frac{B}{H} \cot \varphi$	$\nu_{21} = -\frac{H}{B} \tan \varphi$
Young's moduli:	
$E_1 = 8 \frac{E_s t^3}{B^2 H} \cdot \frac{\sin \varphi}{\cot^2 \varphi}$	$E_2 = 8 \frac{E_s t^3 H}{B^4} \sin \varphi$
Shear modulus:	
$G_{12} = \frac{H}{B} \cdot \frac{8 E_s t^3 \sin^3 \varphi}{(H \sin \varphi - B \cos \varphi)^2 (B + 2H \sin \varphi - 2B \cos \varphi)}$	
Notes: Based on beam bending deformation. Validated experimentally: inaccurate when $\varphi \rightarrow 0$ (which leads to $\nu_{12}$ and $E_2 \rightarrow \infty$ )	
<b>Masters &amp; Evans [83]</b>	
Poisson's ratios:	
$\nu_{12} = -\frac{B}{H} \cdot \frac{\frac{B^2}{4t^2 d \sin^2 \varphi} + 2\nu_s + 1}{\frac{B^2 \cos \varphi}{4t^2 \sin^2 \varphi} + 2(1 + \nu_s) \cot \varphi + \sin \varphi \cos \varphi}$	$\nu_{21} = -\frac{H}{B} \cdot \frac{\frac{B^2}{4t^2 \sin^2 \varphi} + 2\nu_s + 1}{\frac{B^2}{4t^2 \sin \varphi \cos \varphi} + 2(1 + \nu_s) \tan \varphi + \cot \varphi + \frac{2H}{B \cos \varphi} - \frac{2}{\sin \varphi}}$
Young's moduli:	
$E_1 = \frac{2E_s t}{H} \cdot \frac{1}{\frac{B^2 \cos^2 \varphi}{4t^2 \sin^2 \varphi} + 2(1 + \nu_s) \frac{\cos^2 \varphi}{\sin \varphi} + \sin \varphi}$	$E_2 = \frac{B^2}{2HE_s t} \cdot \frac{1}{\frac{B^2}{4t^2 \sin \varphi} + 2(1 + \nu_s) \sin \varphi + 2\frac{H}{B} + \frac{\cos^2 \varphi - 2 \cos \varphi}{\varphi}}$
Shear Modulus:	
$G_{12} = \frac{2E_s t}{B} \cdot \frac{1}{\frac{(H - B \cot \varphi)^2 (B + 2H \sin \varphi - 2B \cos \varphi)}{4t^2 H \sin \varphi} + \frac{E_s}{G_s} \cdot \left[ \frac{\sin \varphi}{HB} (H - B \cot \varphi)^2 + \frac{2}{H} \cdot (H - B \cot \varphi) \right] + \frac{B + H \cot \varphi}{2} \left( \frac{2 \sin \varphi}{H} + \cot \varphi \right)}$	
Notes: Includes tension and hinging deformations in previous model. Validated experimentally with data from Gibson & Ashby.	
<b>Grima et al. [85]</b>	
Poisson's ratios:	
$\nu_{12} = -\frac{B}{H} \cdot \frac{\left\{ \left[ \frac{B}{2t \sin \varphi} - \frac{1}{2} \left( \tan \frac{\varphi}{2} - \cot \varphi \right) \right]^2 + 1 + 2\nu_s \right\} \sin \varphi \cos \varphi}{\left[ \frac{B}{2t \sin \varphi} - \frac{1}{2} \left( \tan \frac{\varphi}{2} - \cot \varphi \right) \sin \varphi \right]^2 + 2(1 + \nu_s) \cos^2 \varphi + \sin^2 \varphi}$	
$\nu_{21} = -\frac{H}{B} \cdot \frac{\left\{ 1 + 2\nu_s + \left[ \frac{B}{2t \sin \varphi} - \frac{1}{2} \left( \tan \frac{\varphi}{2} - \cot \varphi \right) \right]^2 \right\} \sin \varphi \cos \varphi}{\frac{H + B \cot \varphi + \frac{t}{2} \tan \frac{\varphi}{2}}{2 \sin \varphi} + \frac{t}{2} \left( \tan \frac{\varphi}{2} - \cot \varphi \right) + \cos^2 \varphi + 2(1 + \nu_s) \sin^2 \varphi + \left[ \frac{B}{2t} - \frac{1}{2} \left( \tan \frac{\varphi}{2} - \cot \varphi \right) \sin \varphi \right]^2}$	

Young's moduli:

$$E_1 = \frac{B E_s t}{H} \cdot \frac{1}{\left[ \frac{B}{2 \sin \varphi} - \frac{t}{2} \left( \tan \frac{\varphi}{2} - \cot \varphi \right) \right] \left\{ \left[ \frac{B}{2t} \cot \varphi - \frac{1}{2} \left( \tan \frac{\varphi}{2} - \cot \varphi \right) \cos \varphi \right]^2 + 2(1 + \nu_s) \cos^2 \varphi + \sin^2 \varphi \right\}}$$

$$E_2 = \frac{H E_s t}{B} \cdot \frac{1}{\left[ \frac{B}{2 \sin \varphi} - \frac{t}{2} \left( \tan \frac{\varphi}{2} + \cot \varphi \right) \right] \left\{ \left( \frac{\frac{B}{\sin \varphi} - t \left( \tan \frac{\varphi}{2} + \cot \varphi \right)}{\left( \frac{H}{2} - \frac{B}{2} \cot \varphi \right) - \frac{t}{4} \tan \frac{\varphi}{2}} + \cos^2 \varphi \right) + \left[ \frac{B}{2t} - \frac{1}{2} \left( \tan \frac{\varphi}{2} + \cot \varphi \right) \sin \varphi \right]^2 + 2(1 + \nu_s) \sin^2 \varphi \right\}}$$

Shear Modulus: *Not calculated*

Notes: Beam analysis modelling bending, tension and hinging deformations (more suitable when wall thickness is relevant). Validated numerically.

**Berinskii [90]**

Poisson's ratios:

$$\nu_{12} = \frac{B}{H} \cdot \frac{2 \left[ 1 - \left( \frac{2t \sin \varphi}{B} \right)^2 \right] \sin \varphi \cos \varphi}{1 + \left( \frac{2t \sin \varphi}{B} \right)^2 + \left[ 1 - \left( \frac{2t \sin \varphi}{B} \right)^2 \right] \cos 2\varphi}$$

$$\nu_{21} = \frac{H}{B} \cdot \frac{2 \left[ 1 - \left( \frac{2t \cos \varphi}{B} \right)^2 \right] \sin \varphi \cos \varphi}{1 + 5 \left( \frac{2t \cos \varphi}{B} \right)^2 - \left[ 1 - \left( \frac{2t \cos \varphi}{B} \right)^2 \right] \cos 2\varphi}$$

Young's moduli:

$$E_1 = \frac{2B E_s}{H} \cdot \frac{\left( \frac{2t \sin \varphi}{B} \right)^3}{1 + \left( \frac{2t \sin \varphi}{B} \right)^2 + \left[ 1 - \left( \frac{2t \sin \varphi}{B} \right)^2 \right] \cos 2\varphi}$$

$$E_2 = \frac{2H E_s}{B} \cdot \frac{\left( \frac{2t \sin \varphi}{B} \right)^3}{1 + 5 \left( \frac{2t \sin \varphi}{B} \right)^2 - \left[ 1 - \left( \frac{2t \sin \varphi}{B} \right)^2 \right] \cos 2\varphi}$$

Shear Modulus: *Not calculated*

Notes: Homogenisation model of simple formulation, providing similar results to previous models.

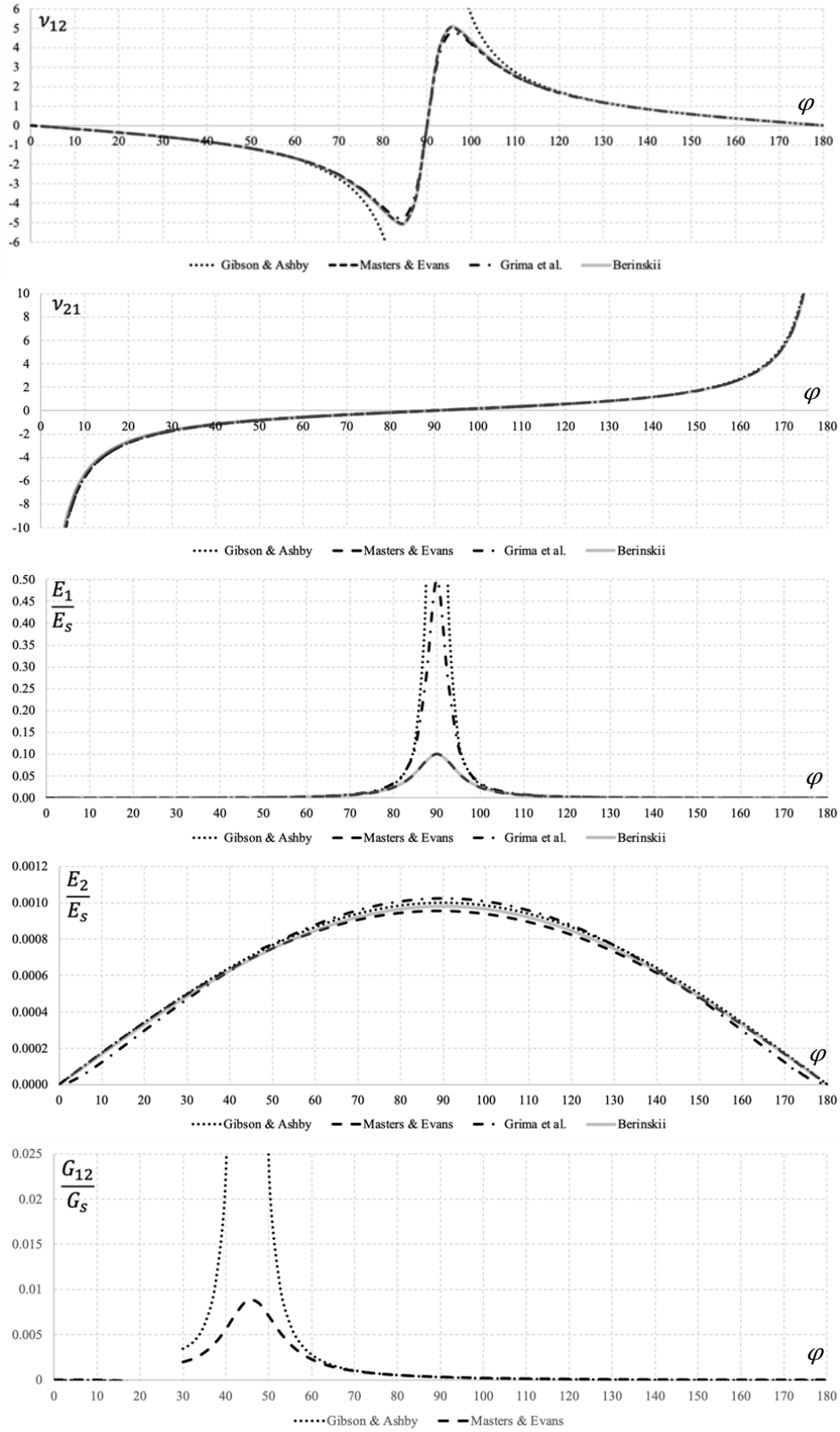


Figure 11: Comparison of the in-plane Poisson's ratios, Young's moduli and shear modulus determined with the different models proposed for the analysis of hexagonal honeycombs (see Table 1) in conventional and auxetic configurations. The parameters used as defined above is  $t = 0.05$ ,  $d = 0.5$  and  $B \times H = 1 \times 1$  unit lengths, resulting in  $l = B/(2 * \sin\varphi) = 0.5/\sin\varphi$  and  $h = H/2 + l * \cos\varphi = 0.5 + l * \cos\varphi$ .

Although the studies described above assume, for simplicity, uniformity of the walls defining the hexagonal honeycomb, different models have been developed to deal with variations, such as the use of ribs with different mechanical properties [82]. Also, a number of re-entrant hexagonal honeycomb structures based on rounded walls has been investigated [92].

A main limitation of the described analytical models is their inability to correctly predict the non-linear behaviour associated with potentially large deformations. An analytical attempt to address this issue was proposed by Wan *et al.* (2003) [93]. Another important aspect to consider when adopting these models to predict the behaviour of real cases, or when validating them versus experimental data and numerical simulations, is the fact that they do not account for the effect of the size of specimen nor, in most cases, of its depth [94]. In reality, due to the presence of stress-free cut cell edges at borders of the surface of a specimen, as well as constraints applied at the boundaries, the behaviour of physical specimens is expected to depart from that described by analytical models, that are derived for single cells or infinite size specimens. However, as the size of the sample increases, a plateau is typically observed, and the properties of the specimen converge to those of an infinite specimen. In the case where numerical models are used for validation, implementing periodic boundary conditions has been suggested as a possible approach to model the properties of infinite plates [95].

The out-of-plane properties have been generally studied less than the in-plane properties for the re-entrant hexagonal honeycomb. Main studies include the work from Gibson and Ashby [68] and Zhang and Ashby [96], that provide some description of the out-of-plane behaviour of the honeycomb lattices and the associated failure mechanisms, essentially consisting of linear buckling and fracture [96]. Smith *et al* (2002) [76] and Scarpa *et al* (2003) [97] report increased out-of-plane elastic and shear moduli and larger collapse stresses for auxetic configurations, when compared with analogous hexagonal honeycombs with the same relative density.

### 3.2.2 Double arrowhead

Another common auxetic structure based on the unfolding of re-entrant cells was first identified by Larsen *et al* (1997) [79], and is represented in Figure 12. This can be found in literature under different names, such as *double-headed arrow* [73], *double arrow* [98] or *double arrowhead* structure [90], here preferred because more commonly used.

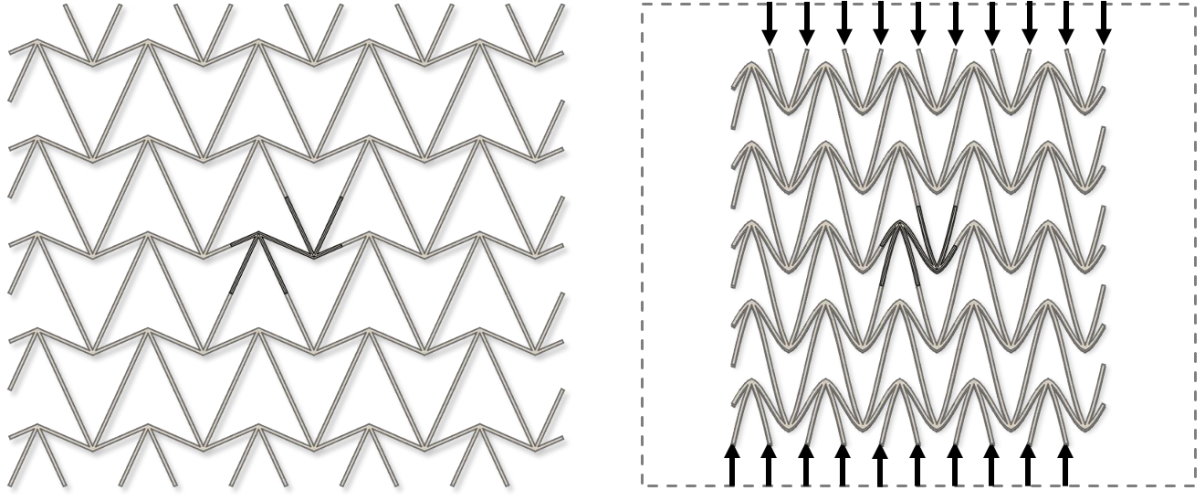
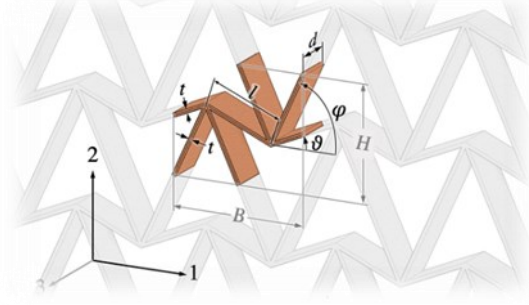


Figure 12: Example of double arrowhead structure before (left) and after (right) uniaxial compressive deformation.

Although the double arrowhead configurations can be adapted to a number of practical applications, such as knitted fabrics [74], their mechanical properties have been investigated far less than the re-entrant hexagonal honeycomb structure. The analytical continuum model proposed by Berinskii [90], derived as a part of a generalised study for comparison with other auxetic structures, provides one of the most complete analytical predictions of the in-plane mechanical response of double arrowhead structures. As described in the previous section, this model uses homogenisation and takes into account the elastic deformation of the ribs, including deformation from flexure, stretching and shearing. The resulting equations are summarised in Table 2, using the standardized nomenclature defined above, adding the angles  $\vartheta$  and  $\varphi$  between the direction 1 of orthotropy and the short and long walls, respectively. Direction 1 of orthotropy is defined as the in-plane direction orthogonal to the in-plane axis of symmetry of the cells, which is the direction 2 of orthotropy. Diagrams are represented in Figure 13 for the possible range of the angle  $\vartheta$  between the direction of orthotropy 1 and the short walls. The angle  $\varphi$  between the direction 1 of orthotropy and the long walls is univocally defined from the previous parameters, as  $\varphi = \arctan(2H/B + \tan \vartheta)$ .

Table 2: Equations of the in-plane Poisson's ratios and elastic moduli for double arrowhead structures.

DOUBLE ARROWHEAD HONEYCOMB



Dimensions:

$l$ : length of short wall

$\theta$ : angle between direction 1 and short wall

$\varphi$ : angle between direction 1 and long wall

$t$ : cell wall thickness

$d$ : depth of cell structure

$B$ : horizontal dimension of unit cell (along direction 1)

$H$ : vertical dimension of unit cell (along direction 2)

Length of long wall can be calculated as  $L = l \cdot \frac{\cos \theta}{\cos \varphi}$

Material Properties of cell wall material:

$E_s$ : Young's modulus

$\nu_s$ : Poisson's ratio

$G_s$ : Shear modulus (for isotropic materials  $G_s = E_s/2(1 + \nu_s)$ )

$\rho_s$ : density

Relative density:  $\rho = \rho_s \frac{2t(\cos \varphi + \cos \theta)}{B \sin \varphi \sin \theta}$

**Berinskii [90]**

Poisson's ratios:

$$\nu_{12} = -\frac{4 \left[ 1 - \left( \frac{t}{l} \right)^2 \right] \cos^2 \theta \cdot \cos^2 \varphi \left[ \tan \theta \cdot \tan \varphi - \left( \frac{2t \cos \theta}{B} \right)^2 \right]}{\left\{ 1 + \left( \frac{2t \cos \theta}{B} \right)^2 - \left[ 1 - \left( \frac{2t \cos \theta}{B} \right)^2 \right] \cos 2\theta \right\} \cdot \left\{ 1 + \left( \frac{2t \cos \theta}{B} \right)^2 - \left[ 1 - \left( \frac{2t \cos \theta}{B} \right)^2 \right] \cos 2\varphi \right\}}$$

$$\nu_{21} = -\frac{2 \left[ 1 - \left( \frac{2t \cos \theta}{B} \right)^2 \right] \sin^2(\varphi - \theta) \left[ \tan \theta \cdot \left( 2 \frac{H}{B} + \tan \theta \right) - \left( \frac{2t \cos \theta}{B} \right)^2 \right]}{1 + 6 \left( \frac{2t \cos \theta}{B} \right)^2 + \left( \frac{2t \cos \theta}{B} \right)^4 - \left[ 1 - \left( \frac{2t \cos \theta}{B} \right)^2 \right]^2 \cos 2(\varphi - \theta)}$$

Young's moduli:

$$E_1 = E_s \frac{2 \left( \frac{2t \cos \theta}{B} \right)^3 \cos \theta \cos \varphi \left[ 2 \left[ 1 + \left( \frac{2t \cos \theta}{B} \right)^2 \right] - \left[ 1 - \left( \frac{2t \cos \theta}{B} \right)^2 \right] (\cos 2\theta + \cos 2\varphi) \right]}{\sin(\varphi - \theta) \left( 1 + \left( \frac{2t \cos \theta}{B} \right)^2 - \left( 1 - \left( \frac{2t \cos \theta}{B} \right)^2 \right) \cos 2\theta \right) \left( 1 + \left( \frac{2t \cos \theta}{B} \right)^2 - \left( 1 - \left( \frac{2t \cos \theta}{B} \right)^2 \right) \cos 2\varphi \right)}$$

$$E_2 = E_s \frac{\left( \frac{2t \cos \theta}{B} \right)^3 \sin(\varphi - \theta) \left\{ 2 \left[ 1 + \left( \frac{2t \cos \theta}{B} \right)^2 \right] - \left[ 1 - \left( \frac{2t \cos \theta}{B} \right)^2 \right] (\cos 2\theta + \cos 2\varphi) \right\}}{\cos \theta \cdot \cos \varphi \left\{ 1 + 6 \left( \frac{2t \cos \theta}{B} \right)^2 + \left( \frac{2t \cos \theta}{B} \right)^4 + \left[ 1 - \left( \frac{2t \cos \theta}{B} \right)^2 \right]^2 \cos 2(\varphi - \theta) \right\}}$$

Shear Modulus: *Not calculated*

Notes: Homogenisation model of simple formulation, providing similar results to previous models.

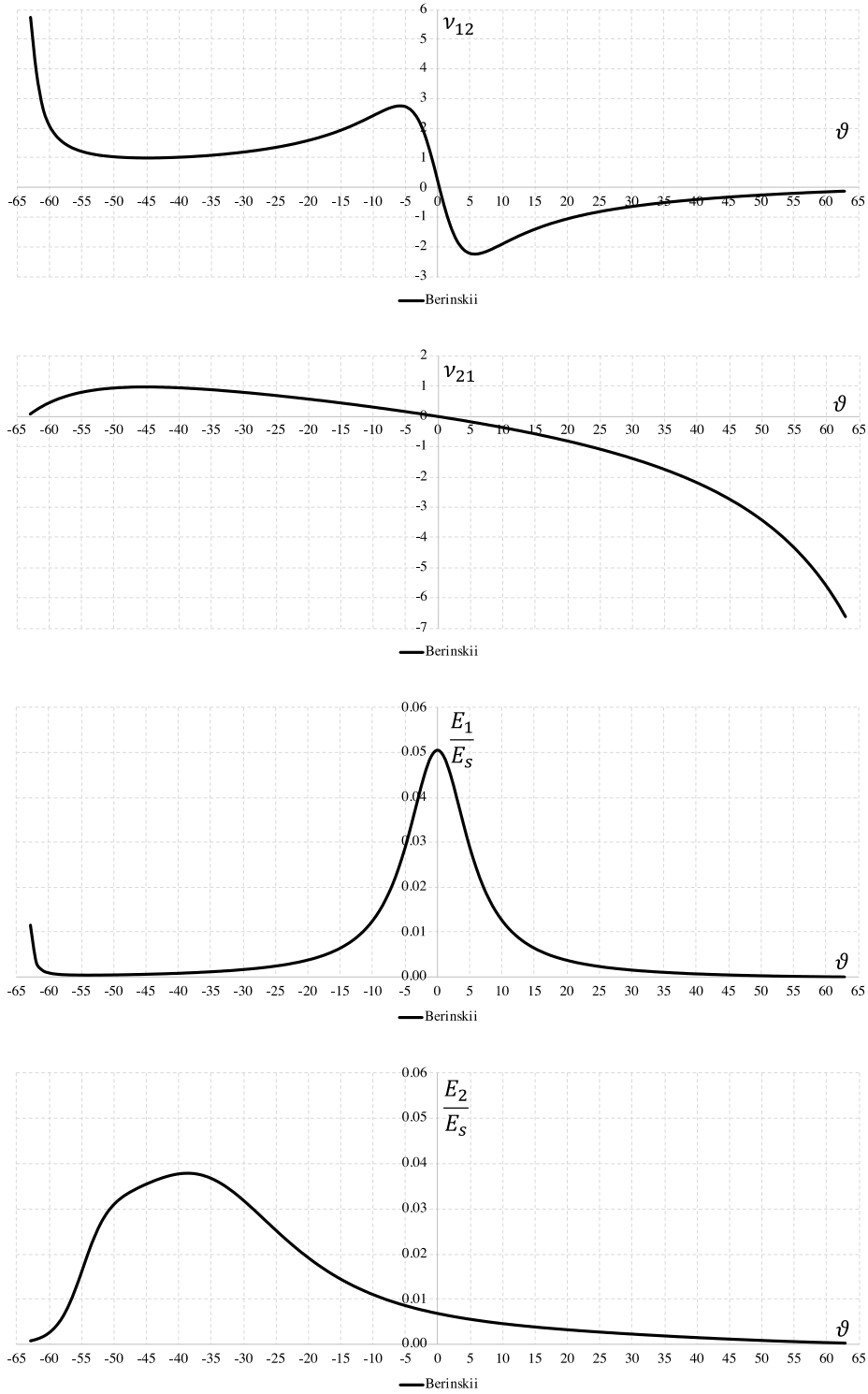


Figure 13: Diagrams of the in-plane Poisson's ratios and Young's moduli determined with the equations for the analysis of double arrowhead structures (see Table 2) in conventional and auxetic configurations. The parameters used as defined above is  $t = 0.05$ ,  $d = 0.5$  and  $B \times H = 1 \times 1$  unit lengths, resulting in  $l = B/(2 * \cos\theta) = 0.5/\cos\theta$ . As defined above,  $\varphi = \arctan(2 H/B + \tan\vartheta) = \arctan(2 + \tan\vartheta)$ .

### 3.2.3 Other re-entrant shapes

#### 3.2.3.1 Star-shapes

Star configurations were identified as potentially auxetic by Theocaris *et al.* in 1997 [81], and more recently described and expanded in terms of configurations by Grima *et al.* (2005) [80]. As in the inverted honeycomb and double arrowhead structures, their main principle of deformation consists in the unfolding of re-entrant cells. Grima *et al.* [80] applied empirical modelling using dummy atoms (EMUDA) to investigate the mechanical response of STAR-3, STAR-4 and STAR-6 configurations (these are described in Figure 14). Their analysis indicates that the STAR-3 configuration displays auxetic behaviour only for a few combinations of hinging force constants, while the STAR-4 and STAR-6 configurations are auxetic for most of them. The STAR-4 configurations are generally characterised by higher negative Poisson's ratios than STAR-6 (for corresponding values of the hinging force constants) [80], but still present less auxetic behaviour than re-entrant hexagonal honeycombs. The STAR-4 configuration was also studied numerically by Theocaris *et al.*, using homogenisation, examining it as a beam structure as well as star shaped inclusions in a continuum [81]. The use of star-shaped pores to achieve auxetic behaviour was further investigated by Mizzi *et al* [99].

Other variations of the connected star configurations were analytically analysed by Ai and Gao [100] using Castigliano's theorem.

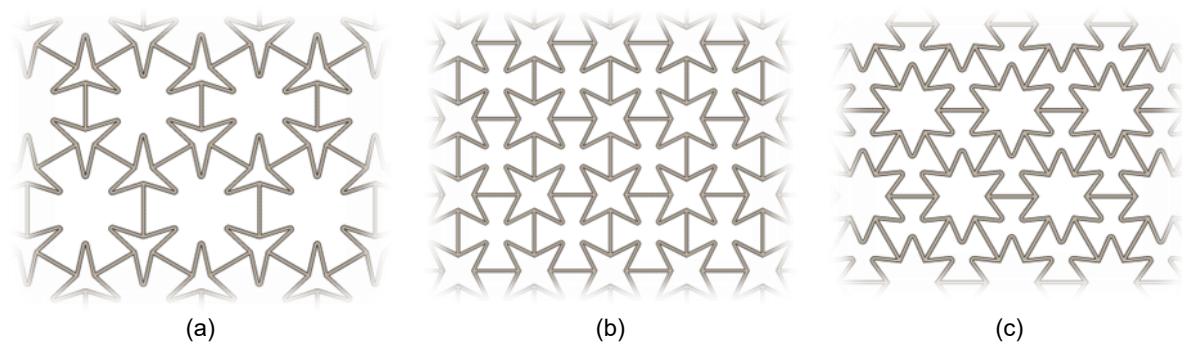


Figure 14: Common STAR-n systems labelled as (a) STAR-3, (b) STAR-4 and (c) STAR-6 configurations.

Another auxetic structure investigated in the literature and based on the unfolding deformation mechanism with similarities to the double arrowhead configuration, is the Milton lattice [101] represented in Figure 15. This was developed to explain the mechanism of a laminate showing a negative Poisson's ratio.



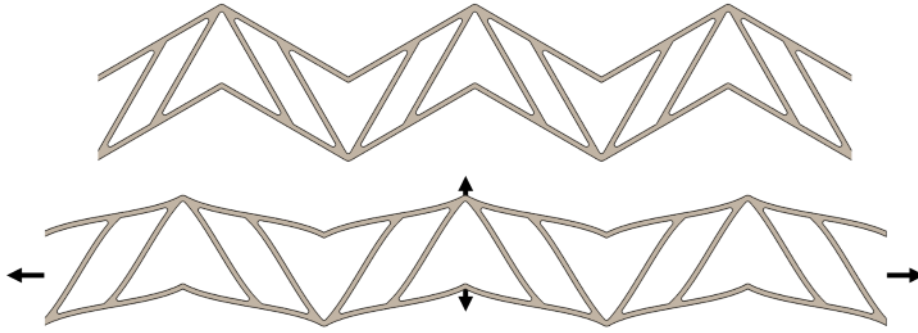


Figure 15: Schematic representation of a Milton lattice and description of the identified mechanism providing internally auxetic behaviour.

### 3.3 Chiral structures

A different approach to achieve structural auxetic behaviour consists of enforcing the wrapping and unwrapping of ligaments around specific nodes. Structures exploiting this principle are called auxetic chiral structures, referring to the chiral property of their asymmetry - that their structure and their mirror image are not superimposable, and are classified based on the number of ligaments (e.g., trichiral, tetrachiral, hexachiral, etc. as shown in Figure 16) and on the way each ligament wraps around the nodes at its ends. In particular, if ligaments are fastened on the same side of both nodes at their ends, thus forcing these to rotate in opposite orientations during the deformation, anti-chiral configurations are obtained, as shown in Figure 17 (denoted by the prefix 'anti-').

The use of chiral configurations as potential auxetic structures was first suggested by Lakes in 1991 [102], [103], who described a hexachiral configuration. These structures exhibit hexagonal symmetry, which results in mechanical in-plane isotropy [103], and are reported to offer high shear rigidity and a deformation mechanism which allows high strains in the elastic range of the wall material [104].

Numerical and experimental investigations of the hexachiral configuration suggested by Lakes, as well as of tetrachiral, anti-tetrachiral, trichiral and anti-trichiral configurations presented by Alderson *et al* [105] indicate that the in-plane deformation of chiral and anti-chiral structures is predominantly led by cylinder rotation and ligament bending. The Poisson's ratio is close to -1 for the analysed hexachiral, tetrachiral and anti-tetrachiral configurations, and does not appear to be affected by ligament length. However, the auxetic behaviour decreases with the increasing ligament thickness, especially for the hexachiral model. On the contrary, the anti-trichiral model displays negative Poisson's ratios only for shorter ligaments, and the trichiral model does not show auxetic behaviour. This was

explained by the presence of competing deformation mechanisms, between the bending of the ligaments due to the rotation of the nodes and the direct bending of off-axis ligaments.

Hexachiral and tetrachiral models exhibit higher Young's moduli than the trichiral models, and chiral models has a higher in-plane compressive modulus than the anti-chiral equivalents, for any given number of ligaments. This was realistically attributed to the fact that ligaments of chiral structures bend producing two buckles, with a change of curvature at their midspan, while in anti-chiral structures they deform in a single buckle. This appears clearer when comparing the deformed configurations in Figure 16 and Figure 17. To correctly interpret the results described by Alderson *et al.* [105], we need to consider the fact that they applied 1-2% compressive strain to their specimen, which also had much thicker walls than those previously tested by Prall and Lakes.

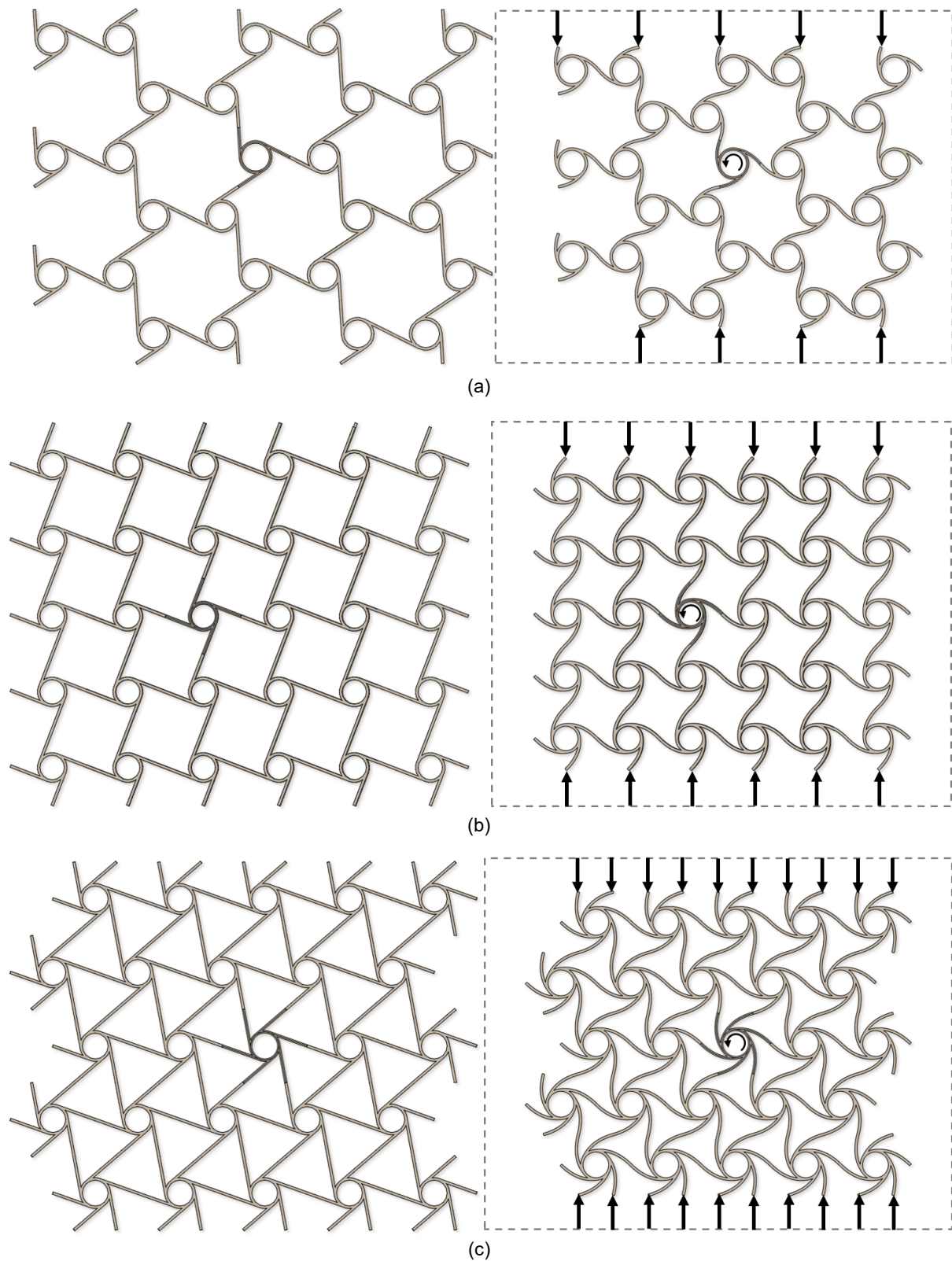


Figure 16: Trichiral (a), tetrachiral (b) and hexachiral (c) structures, and description of the mechanism responsible for the auxetic behaviour.

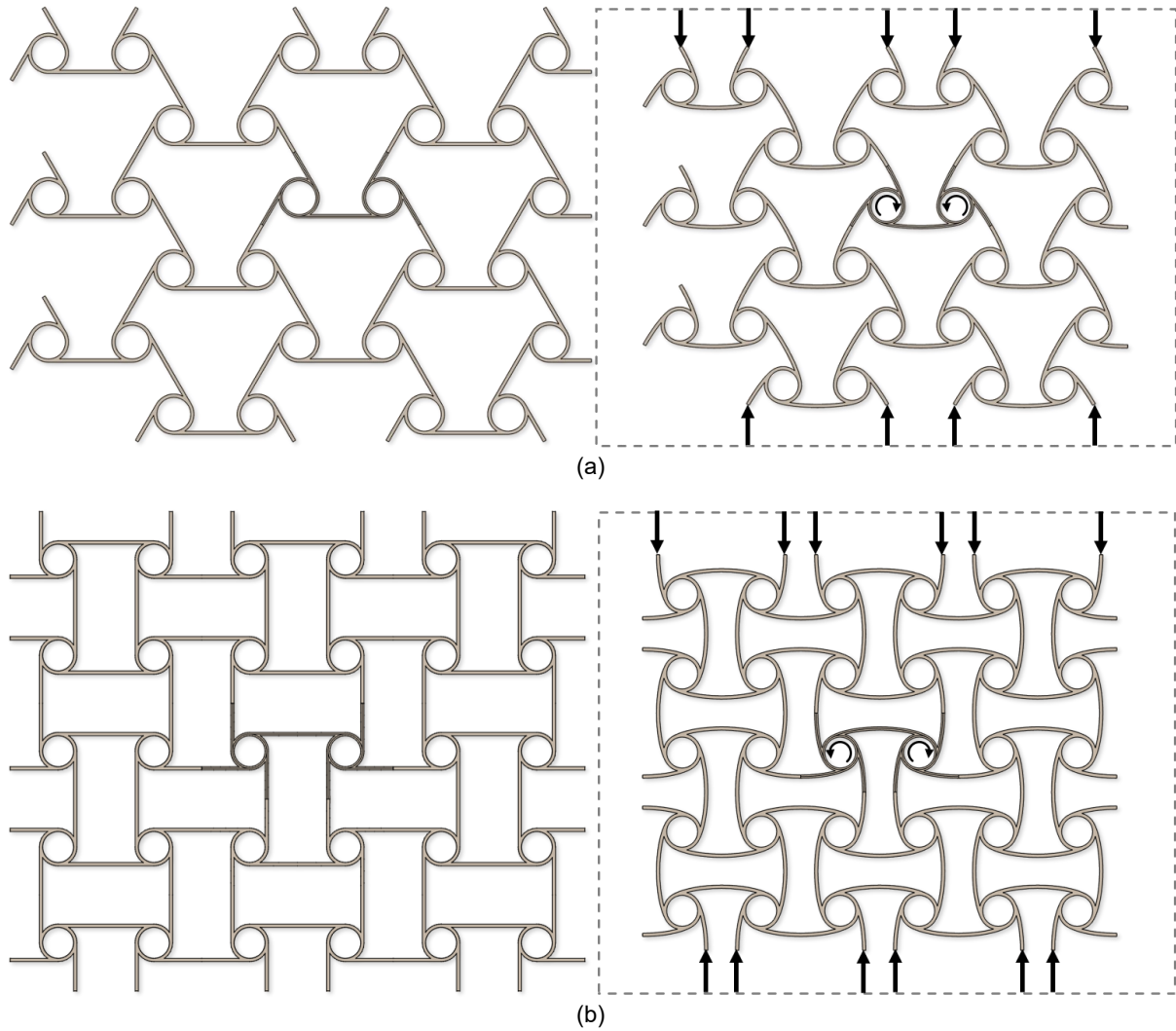


Figure 17: Anti-Trichiral (a) and anti-tetrachiral (b) structures, and description of the mechanism responsible for the auxetic behaviour.

The majority of analytical studies of the elastic constants for chiral configurations focuses on hexachiral configurations. The first attempt to describe their in-plane elastic properties was presented by Prall and Lakes, who applied the beam theory and an energy approach to predict a constant in-plane Poisson's ratio of -1 [103]. This approach, similarly to Gibson and Ashby's analysis on the re-entrant hexagonal honeycomb, assumes that deformations are small, the main deformation mode is bending of the cell walls, and axial deformation and shear within the ligaments can be neglected. The bending of the cell walls and the equal rotation of all cell nodes were confirmed and validated with experimental tests, although the node wall thickness in the physical specimens was larger than the ligament thickness, contributing to the validity of a rigid node model. Tests also confirmed that the structures maintained the predicted Poisson's ratio of about -1 up to 25% of nominal strain [103].

However, this analytical approach is reported to be valid only for slender beams with a reference value of the relative density of the structure below 0.29 [68], [103]. Moreover, the predicted Poisson's ratio, which is constant for any change in geometric parameters and equal to -1, results in a structure with a theoretically infinite shear modulus [103], [106], [107]. In an attempt to remove this indeterminacy, Spadoni and Ruzzene [106] used micropolar continuum methods with both rigid and deformable nodes to calculate the elastic constants of a hexachiral auxetic structure. The rigid node model leads to a Poisson's ratio dependent on the ligament thickness, and equal to -1 only for the ideal and unattainable condition that the ligament thickness is zero. The deformable node analysis relies on numerical simulations by means of finite element analysis. Comparison of the rigid node analytical model with the deformable node numerical model shows substantial discrepancies in the estimated Young's modulus. Importantly, with the analytical approach suggested by Spadoni and Ruzzene, the estimated shear modulus, indeterminate (infinite) in Prall and Lakes model, becomes finite and determinable. Their analysis indicates that the shear modulus is equivalent to that of a lattice consisting of regular triangles, and much lower if the contribution of deformable rings is considered. In parallel, Liu *et al* [108] applied a similar approach, still based on the micropolar theory through a continuum theory model with reinterpretation of in-plane isotropic tensors. Their results matched the exact solution of corresponding discrete models.

A more recent study presented by Bacigalupo and Gambarotta [109] applies a micropolar homogenisation derived from Spadoni and Ruzzene [106] and Liu *et al*. [108], while introducing an additional parameter defining the deformable portion of the ligaments. In the same work, they propose a second approach based on a second gradient homogenisation developed to study periodic cells consisting of deformable portions like the ligaments, nodes, and eventual filling material in between the ligaments and in the nodes. Interestingly, the study indicates that the presence of filling material between the walls of the auxetic structure (even if very soft) strongly reduces and eventually reverses the auxetic behaviour [109].

The equations derived by the various research groups to describe the in-plane mechanical behaviour of hexachiral honeycombs are summarised in Table 3. The standardized nomenclature presented above is used, with the addition of the angle  $\vartheta$  between radial direction and the inclined struts.

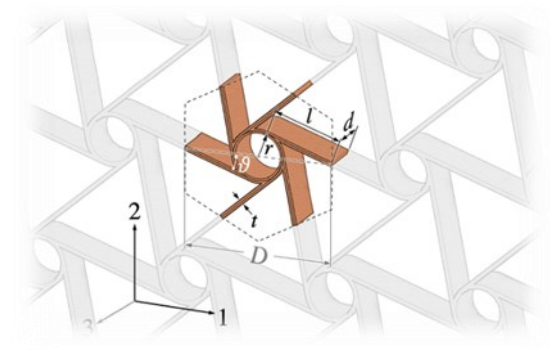
The responses predicted from the different equations summarised in Table 3 is represented in

Figure 18 according to the standardized unit diameters presented above. Diagrams are

represented for the theoretical range of the angle  $\vartheta$  between  $0^\circ$ , corresponding to the case where the circles at the nodes degenerate into points and the structure becomes made of triangles, and  $90^\circ$ , where the circles at the nodes occupy the entire cell diameter and the structure become made of circles. The diagrams confirm that the Poisson's ratio of -1 predicted by Prall and Lakes is a theoretical limit practically unattainable and approached for an angle  $\vartheta = 45^\circ$ . In fact, the auxetic behaviour reduces at smaller and larger angles, reverting at angles close to  $0^\circ$  and  $90^\circ$ . All three models based on micropolar homogenisation predict a similar behaviour, with the descriptions of Spadoni and Ruzzene [106] and Liu *et al.* [108] providing practically identical results for both Poisson's ratio and Young's modulus. All models fail to give realistic estimates of the structure moduli at large values of  $\vartheta$ , as the models assumed them to tend to infinity while in literature the extreme case of a lattice of connected circles have been evaluated to finite values [110].

Table 3: Equations derived by the different research groups for the determination of the in-plane Poisson's ratio, elastic modulus and, where available, shear modulus, for hexachiral honeycombs.

**HEXACHIRAL HONEYCOMB**



Dimensions:

$l$ : half length of ligaments

$\vartheta$ : angle between radial direction and ligaments

$t$ : ligament wall thickness

$d$ : depth of cell structure

$r$ : radius of circle at node

$D$ : width of unit cell

Material Properties of cell wall material:

$E_s$ : Young's modulus

$\nu_s$ : Poisson's ratio

$G_s$ : Shear modulus (for isotropic materials  $G_s = E_s/2(1 + \nu_s)$ )

$\rho_s$ : density

Relative density:  $\rho = \rho_s 2t \frac{(3 \cos \vartheta + \pi \sin \vartheta)}{\sqrt{3}D}$

**Prall & Lakes [103]**

Poisson's ratios:

$$\nu_{12} = \nu_{21} = -1$$

Young's moduli:

$$E_{1,2} = E_s \sqrt{3} \frac{t^3}{2l r^2} = E_s \frac{4\sqrt{3}t^3}{D^3 \sin^2 \vartheta \cos \vartheta}$$

Shear modulus:

$$G_{12} = \infty$$

Notes: Based on beam bending deformation. Inaccurate when  $\vartheta \rightarrow 0$  (which leads to  $E_{1,2} \rightarrow \infty$ ) and for the calculation of  $G_{12}$

**Spadoni & Ruzzene [106]**

Poisson's ratios:

$$\nu_{12} = \nu_{21} = \frac{4 \left( \frac{t}{D \cos \vartheta} \right)^2}{\left[ \left( \frac{t}{D \cos \vartheta} \right)^4 \cos^2 \vartheta + 1 - \cos^2 \vartheta + 3 \left( \frac{t}{D \cos \vartheta} \right)^2 \right]} - 1$$

Young's moduli:

$$E_{1,2} = E_s \frac{4\sqrt{3} \left[ 1 + \left( \frac{t}{D \cos \vartheta} \right)^2 \right]}{\left[ 2 \left( \frac{t}{D \cos \vartheta} \right)^4 \cos^2 \vartheta + 2 \sin^2 \vartheta + 6 \left( \frac{t}{D \cos \vartheta} \right)^2 \right]} \left( \frac{t}{D \cos \vartheta} \right)^3$$

Shear Modulus:

$$G_{12} = E_s \left[ \frac{\sqrt{3}}{4} \left( \frac{t}{D \cos \vartheta} \right) + \frac{\sqrt{3}}{4} \left( \frac{t}{D \cos \vartheta} \right)^3 \right]$$

Notes: Micropolar continuum model, removing the indeterminant of  $\nu = -1$ , with the assumption of rigid rings

**Liu et al. [108]**

Poisson's ratios:

$$\nu_{12} = \nu_{21} = \frac{1 - \left( \frac{t}{D} \right)^2 - \left( \frac{D \cos \vartheta \sin \vartheta}{t} \right)^2}{3 + \left( \frac{t}{D} \right)^2 + \left( \frac{D \cos \vartheta \sin \vartheta}{t} \right)^2}$$

Young's moduli:

$$E_1 = E_2 = E_s 2\sqrt{3} \left( \frac{t}{D} \right)^3 \frac{\sec^2 \vartheta \left( \left( \frac{t}{D} \right)^2 + \cos^2 \vartheta \right)}{3 \left( \frac{t}{D} \right)^2 + \frac{1}{8} \left( \frac{t}{D} \right)^4 + \cos^2 \vartheta \sin^2 \vartheta}$$

Shear Modulus: *Not calculated*

Notes: Based on micropolar continuum method. Verified by comparison to the exact solution of the corresponding discrete models.

Poisson's ratios:

$$\nu_{12} = \nu_{21} = \frac{\left(\left(\frac{t}{D \cos \vartheta}\right)^2 \cos^2 \vartheta - \varphi^2 \sin^2 \vartheta\right) \left(\varphi^2 - \left(\frac{t}{D \cos \vartheta}\right)^2\right)}{3\varphi^2 \left(\frac{t}{D \cos \vartheta}\right)^2 + \left(\frac{t}{D \cos \vartheta}\right)^4 \cos^2 \vartheta + \varphi^4 \sin^2 \vartheta}$$

Young's moduli:

$$E_1 = E_2 = E_s \frac{2\sqrt{3} \left(\frac{t}{D \cos \vartheta}\right)^3 \left(\varphi^2 + \left(\frac{t}{D \cos \vartheta}\right)^2\right)}{\left(3\varphi^2 \left(\frac{t}{D \cos \vartheta}\right)^2 + \left(\frac{t}{D \cos \vartheta}\right)^4 \cos^2 \vartheta + \varphi^4 \sin^2 \vartheta\right) \varphi}$$

Shear Modulus:

$$G_{12} = E_s \frac{\sqrt{3}}{4} \frac{t}{D \cos \vartheta} \frac{\left(\varphi^2 + \left(\frac{t}{D \cos \vartheta}\right)^2\right)}{\varphi^3}$$

Notes: Based on micropolar continuum method introducing the concept of effective beam length for the ligaments, where  $\varphi$  is the ratio between effective length and actual length  $l$ .

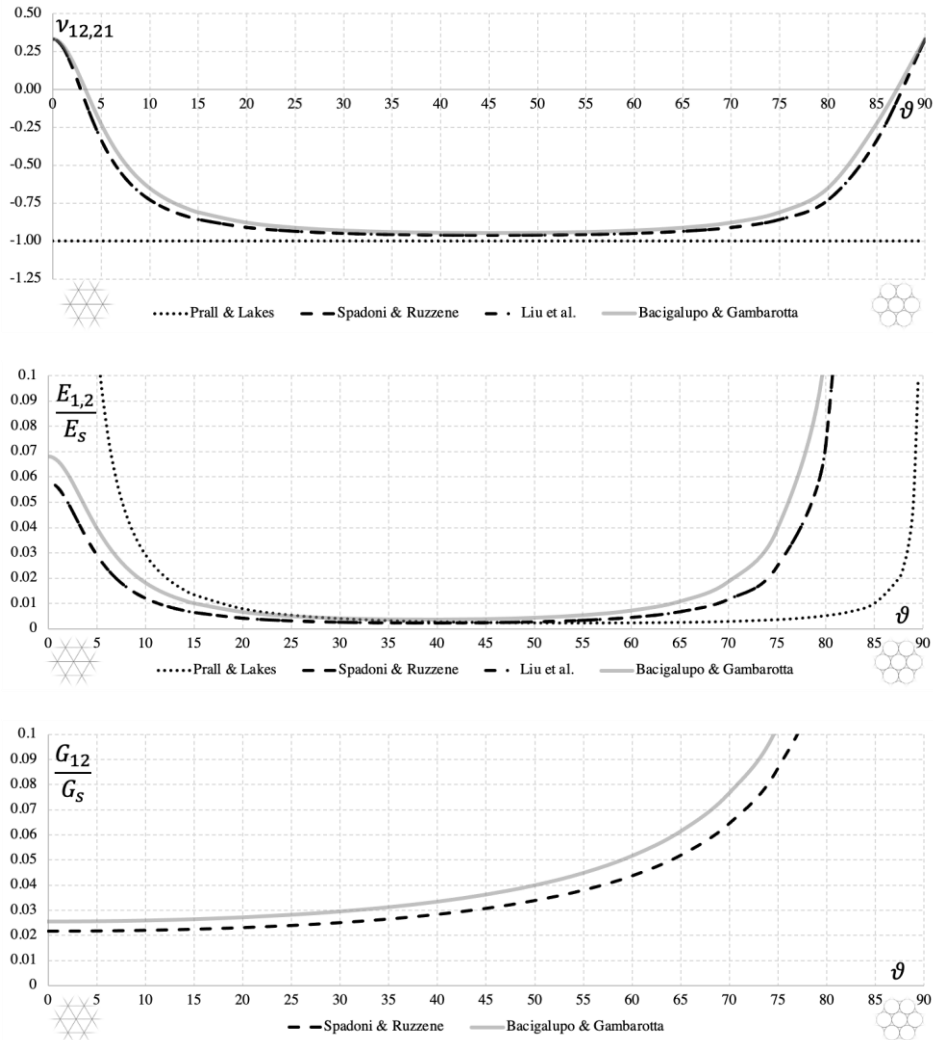


Figure 18: Comparison of the in-plane Poisson's ratio, Young's modulus and shear modulus determined with the different models proposed for the analysis of hexachiral honeycombs (see Table 3). The parameters used are as defined above  $D = 1$  unit length,  $t = 0.05$  and  $d = 0.5$ . For Bacigalupo & Gambarotta,  $\varphi = 0.85$ .

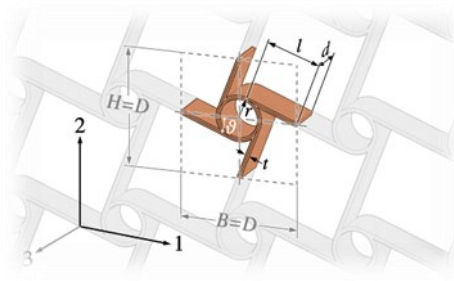
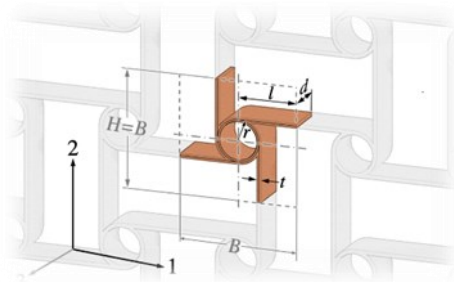
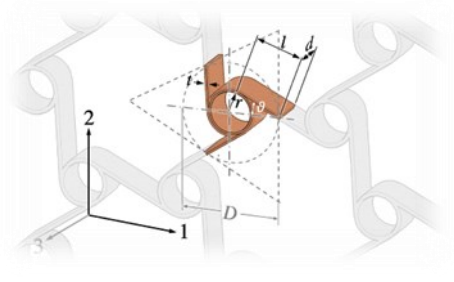
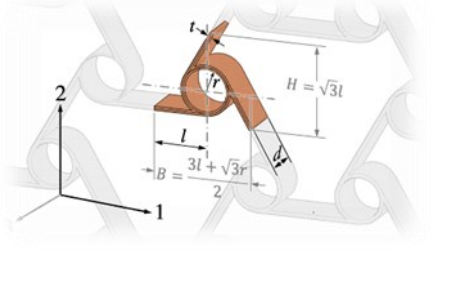


Other chiral configurations have received less attention in terms of analytical description. Recently, Mousanezhad *et al.* [111] applied energy-methods based on Castigliano's second theorem to derive analytical expressions for the in-plane mechanical response of tetrachiral, anti-tetrachiral, trichiral and anti-trichiral configurations. Since the tetrachiral and anti-tetrachiral systems are stretching dominated, both the stretching and the bending terms of Castigliano's theorem were included, whilst, in the case of trichiral and anti-trichiral, structures were assumed to deform in a bending dominated manner, their study only included the bending terms.

Comparison of the analytical predictions with numerical solutions revealed a number of discrepancies. In particular, the tetrachiral and trichiral configurations did not exhibit a negative Poisson's ratio in the computational models. This behaviour, in the case of tetrachiral model, is in contrast with that described by Alderson *et al.* [105], and is attributed by Mousanezhad *et al.* to the different boundary conditions imposed in the two analyses. In the case of trichiral configuration, the different behaviour between the analytical and numerical predictions is attributed by the authors to the fact that, in the numerical case, the major form of deformation shifted from the ligaments to the nodes, assumed rigid in the equations. This also justifies the Young's modulus estimated analytically.

The equations derived by Mousanezhad *et al.* for the different configurations are summarised in Table 4, using the notations reported in the figures represented in the table. The responses predicted for the different configurations in Table 4 are represented in Figure 19. All geometric parameters and the Poisson's ratio of the wall material are kept consistent with previous studies. Diagrams are represented for ratios between the radius of the node and the dimension  $B$  of the unit cell ranging from zero (ligaments only) to 1 (node circles only). The diagrams confirm that the trichiral and anti-trichiral structures can exhibit auxetic behaviour only for a limited range of geometrical configurations.

Table 4: Equations derived by Mousanezhad et al. [111] for the determination of the in-plane Poisson's ratio, elastic modulus and, where available, shear modulus, for tetrachiral, anti-tetrachiral, trichiral and anti-trichiral honeycombs.

<p><b>Tetrachiral</b></p> 	<p>Poisson's ratios:</p> $\nu_{12} = \nu_{21} = -1^*$ <p>Young's moduli:</p> $E_{1,2} = \frac{E_s t^3}{B \cos^3 \vartheta} \cdot \frac{1}{t^2 + \sin^2 \vartheta B^2}$ <p>Shear modulus:</p> $G_{12} = \frac{E_s t^3}{2B \cos^3 \vartheta} \cdot \frac{1}{B^2 \cos^2 \vartheta + t^2 \tan^2 \vartheta}$ <p>* in Mousanezhad et al. [111] the Poisson's ratio is indicated as equal to zero, but it is here assumed that it was a typographical error.</p>
<p><b>Anti-Tetrachiral</b></p> 	<p>Poisson's ratios:</p> $\nu_{12} = \nu_{21} = \frac{-6 \left(\frac{r}{B}\right)^2}{6 \left(\frac{r}{B}\right)^2 + \left(\frac{t}{B}\right)^2}$ <p>Young's moduli:</p> $E_{1,2} = E_s \frac{\left(\frac{t}{B}\right)^3}{\left(\frac{t}{B}\right)^2 + 6 \left(\frac{r}{B}\right)^2}$ <p>Shear Modulus:</p> $G_{12} = E_s \frac{1}{2} \left(\frac{t}{B}\right)^3$
<p><b>Trichiral</b></p> 	<p>Poisson's ratios:</p> $\nu_{12} = \nu_{21} = \nu = \sqrt{3} \frac{\sin\left(\frac{\pi}{6} - \vartheta\right) \cdot \cos\left(\frac{\pi}{6} - \vartheta\right) + \sin\left(\frac{\pi}{6} + \vartheta\right) \cdot \cos\left(\frac{\pi}{6} + \vartheta\right)}{\cos^2\left(\frac{\pi}{6} - \vartheta\right) + 4 \sin^2 \vartheta + \cos^2\left(\frac{\pi}{6} + \vartheta\right)}$ <p>Young's moduli:</p> $E_1 = E_2 = E_s 2\sqrt{3} \left(\frac{t}{D}\right)^2 \frac{\sec^2 \vartheta \left(\left(\frac{t}{D}\right)^2 + \cos^2 \vartheta\right)}{3 \left(\frac{t}{D}\right)^2 + \frac{1}{8} \left(\frac{t}{D}\right)^4 + \cos^2 \vartheta \cdot \sin^2 \vartheta}$ <p>Shear Modulus: <i>Not reported</i></p>
<p><b>Anti-Trichiral</b></p> 	<p>Poisson's ratios:</p> $\nu_{12} = \nu_{21} = \frac{1 - 6 \left(\frac{r}{l}\right)^2}{1 + 6 \left(\frac{r}{l}\right)^2}$ <p>Young's moduli:</p> $E_1 = E_2 = E_s \frac{\frac{1}{2\sqrt{3}} \left(\frac{t}{l}\right)^3}{1 + 6 \left(\frac{r}{l}\right)^2}$ <p>Shear Modulus: <i>Not reported</i></p>

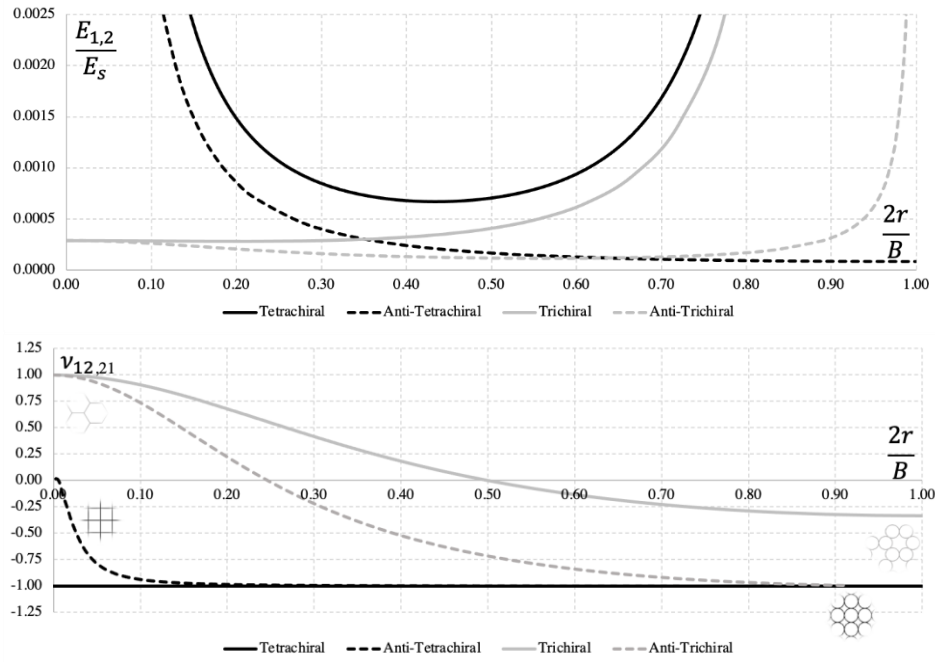
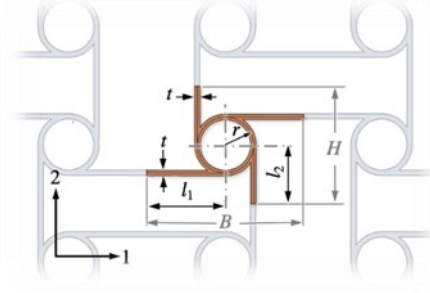
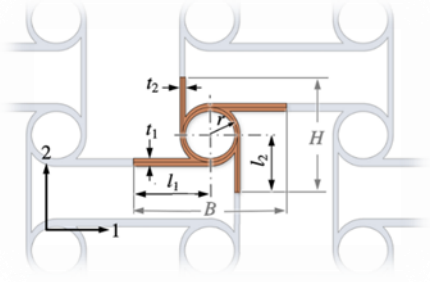
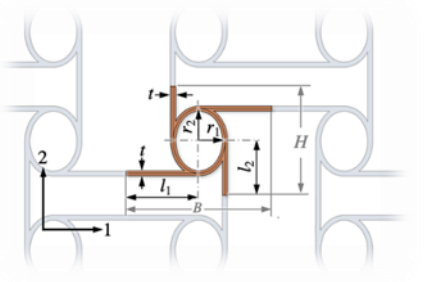
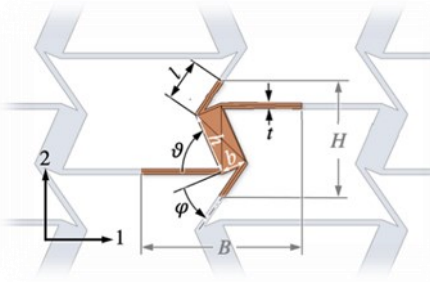


Figure 19: Comparison of the in-plane Poisson's ratio and Young's modulus determined for the different chiral and anti-chiral configurations summarised in Table 4. For all  $t=0.05$ ,  $D=1$  (in case  $H=B$ ,  $H=B=D=1$ ), and  $\vartheta = \sin^{-1}\left(\frac{2r}{D}\right)$ . For the tetra-, tri- and anti-trichiral,  $l = \frac{D}{2} * \cos\vartheta$ , and for the anti-tetrachiral  $l = \frac{D}{2} = 0.5$ .

As described above, one of the main features of chiral structures is their ability to offer the same mechanical characteristics in the different in-plane directions. However, chiral configurations can be readapted to provide orthotropic responses. In particular, the anti-tetrachiral structure is the most suitable for this application, and a range of variations on this structure have been suggested and analysed, that differentiate the responses in the two directions of orthotropy by allowing for different length of the ligaments (Chen *et al.*, 2013) [56]; for different length and thickness of the ligaments (Gatt *et al.*, 2013) [57]; for different length of the ligaments and elliptical nodes (Wu *et al.*, 2017) [52]. Also, hybrid tetrachiral – anti-tetrachiral structures with rectangular nodes have been suggested and analysed (Grima *et al.*, 2008) [114]. Recently, attempts have been made to adapt similar approaches to hexachiral structures, by introducing irregularities [115].

The anti-tetrachiral orthotropic configurations described above and the analytical expressions of the derived mechanical properties are summarised in Table 5

Table 5: Schematic representation of different orthotropic anti-tetrachiral configurations and equations derived by different groups for the determination of the Poisson's ratios and, where available, elastic moduli for the two in-plane directions of orthotropy.

<p>Chen et al. [112]</p> 	<p>Poisson's ratios:</p> $\nu_{12} = -\frac{B}{H}; \quad \nu_{21} = -\frac{H}{B}$ <p>Young's moduli:</p> $E_1 = E_s \frac{\left(\frac{t}{r}\right)^3 \frac{B}{r}}{12 \left(1 - \frac{t}{2r}\right)^2 \frac{H}{r}} \left( \frac{1}{\frac{B}{r} - 2\sqrt{2\frac{t}{r} - \left(\frac{t}{r}\right)^2}} + \frac{1}{\frac{H}{r} - 2\sqrt{2\frac{t}{r} - \left(\frac{t}{r}\right)^2}} \right)$ $E_2 = E_s \frac{\left(\frac{t}{r}\right)^3 \frac{H}{r}}{12 \left(1 - \frac{t}{2r}\right)^2 \frac{B}{r}} \left( \frac{1}{\frac{H}{r} - 2\sqrt{2\frac{t}{r} - \left(\frac{t}{r}\right)^2}} + \frac{1}{\frac{B}{r} - 2\sqrt{2\frac{t}{r} - \left(\frac{t}{r}\right)^2}} \right)$ <p>Shear modulus: <i>Not reported</i></p>
<p>Gatt et al. [113]</p> 	<p>Poisson's ratios:</p> $\nu_{12} = -\frac{(2r + t_2)B}{(2r + t_1)H}; \quad \nu_{21} = -\frac{(2r + t_1)H}{(2r + t_2)B}$ <p>Young's moduli:</p> $E_1 = \frac{1}{3(2r + t_1)^2} \frac{l_1}{l_2} \left( \frac{E_{s1} t_1^3}{l_1} + \frac{E_{s2} t_2^3}{l_2} \right)$ $E_2 = \frac{1}{3(2r + t_2)^2} \frac{l_2}{l_1} \left( \frac{E_{s1} t_1^3}{l_1} + \frac{E_{s2} t_2^3}{l_2} \right)$ <p>Shear modulus: <i>Not reported</i></p>
<p>Wu et al. [52]</p> 	<p>Poisson's ratios:</p> $\nu_{12} = (\nu_{21})^{-1} = -\frac{B \left( \gamma_1 - \frac{t}{2} \right)}{H \left( \gamma_2 - \frac{t}{2} \right)}$ <p>Young's moduli:</p> $E_1 = \frac{E_s t^3}{3(2r_2 - t)^2} \cdot \frac{B}{H} \left( \frac{1}{B - 2r_1 \sqrt{2\frac{t}{r_2} - \left(\frac{t}{r_2}\right)^2}} + \frac{1}{H - 2r_2 \sqrt{2\frac{t}{r_1} - \left(\frac{t}{r_1}\right)^2}} \right)$ $E_2 = \frac{E_s t^3}{3(2r_1 - t)^2} \cdot \frac{H}{B} \left( \frac{1}{B - 2r_1 \sqrt{2\frac{t}{r_2} - \left(\frac{t}{r_2}\right)^2}} + \frac{1}{H - 2r_2 \sqrt{2\frac{t}{r_1} - \left(\frac{t}{r_1}\right)^2}} \right)$ <p>Shear Modulus: <i>Not reported</i></p>
<p>Grima et al. [114]</p> 	<p>Poisson's ratios:</p> $\nu_{12} = (\nu_{21})^{-1} = -\frac{H \cos(\varphi - \arctan \frac{b}{h})}{2 \sin(\vartheta + \arctan \frac{b}{h}) [2l + \sqrt{h^2 + b^2} \sin(\varphi - \arctan \frac{b}{h})]}$ <p>Young's moduli: <i>Not reported</i></p> <p>Shear Modulus: <i>Not reported</i></p>

The out-of-plane behaviour of chiral structures has been analysed for hexachiral honeycombs by Spadoni *et al.* [104], who studied the problem with analytical approaches based on linear buckling for thin plates, as well as shells and bifurcation numerical simulations by means of finite element analysis. This article identifies the geometric parameters defining the structure that can be altered to increase the flat-wise buckling response, such as diameter to length ratio for the cylinder nodes or the wall thickness, which increases the global and local buckling loads. On the contrary, the ratio between the ligament's length and the cylinder nodes diameter (or the angle between the radial direction and the ligaments), defining the level of chirality, decreases the buckling load even when normalised for relative density. Scarpa *et al.* [116] studied the same configuration by means of finite element analyses and experimental tests. Flat-wise buckling and the anelastic buckling behaviour of the hexachiral structure was further explored by Miller *et al.* [117], by means of numerical and experimental approaches, and expanded to tetrachiral and anti-tetrachiral structures. Lorato *et al.* [118] studied the out-of-plane properties of the hexachiral, tetrachiral, anti-tetrachiral, trichiral and anti-tetrachiral configurations applying analytical, numerical and experimental approaches. Both the transverse Young's modulus and the transverse shear modulus were studied: the transversal nominal Young's modulus was reported to increase when moving from the trichiral to the anti-trichiral, to the tetrachiral, to the anti-tetrachiral and finally to the hexachiral configurations, although some minor changes in this order were observed in experiments with thicker ligaments.

Another interesting configuration, proposed in 2000 by Smith *et al.* [119] to describe the behaviour of auxetic foams, is represented by the missing rib model. This is based on a lozenge grid with missing rib portions, which results in a configuration which shares the features of both tetrachiral and re-entrant structures (see Figure 20.a). In fact, the deformation of missing rib models is associated with rotations of the hub of crossed-ligaments, as well as hinging at the ligaments joints. As for the chiral configurations previously described, anti-chiral missing rib arrangements can also be designed (see Figure 20.b), which would still retain auxetic behaviour [120].

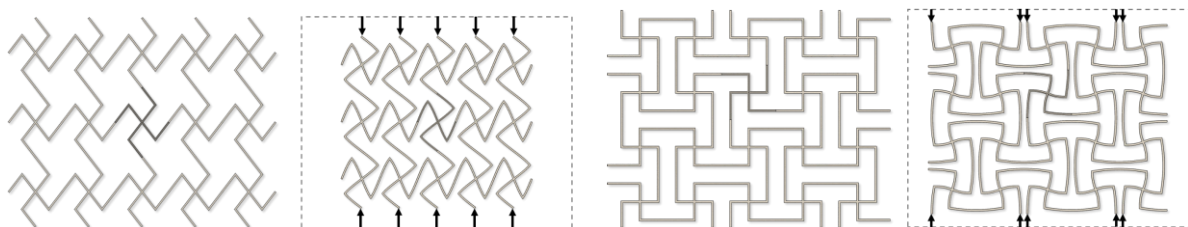
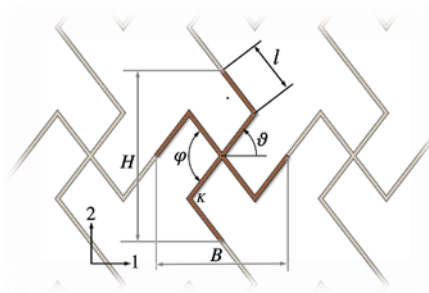


Figure 20: Deformation mechanism of chiral (a) and anti-chiral (b) missing rib structure.

Analytical models of this type of structures are still highly simplified, and mostly referred to chiral missing rib configurations. The equations derived by Smith *et al.* (2000) [119] to describe the in-plane mechanical behaviour of these structures are summarised in Table 6. The reference dimensions used in the equations are described in the figure in the table, and the joints with angle  $\vartheta$  are spring hinges, with spring constant equal to  $k$ .

Table 6. Equations derived for the determination of the in-plane Poisson's ratio and elastic modulus for missing rib structures

Chiral Missing Rib [119]	
	Poisson's ratios:
	$\nu_{21} = (\nu_{12})^{-1} = \tan^2\left(\frac{\varphi}{2}\right)$
	Young's moduli:
	$E_1 = k \frac{1}{4l^2} \frac{\cot(\varphi - \vartheta)}{\sin \vartheta \sin(\varphi - \vartheta)}$
	$E_2 = k \frac{1}{4l^2} \frac{\tan \vartheta}{\cos \vartheta \cos(\varphi - \vartheta)}$
	Shear Modulus:
Not reported	

### 3.4 Rotating plates

At the beginning of the new millennium, various research groups identified auxetic behaviour in the rotational degree of freedom of plates or crystals, interconnected through hinges at their vertices in such a way that, when they are compressed / expanded in one direction, they rotate the plates so that they compress / expand in the other direction as well, thus producing a negative Poisson's ratio. An example of this mechanism is described in Figure 21.

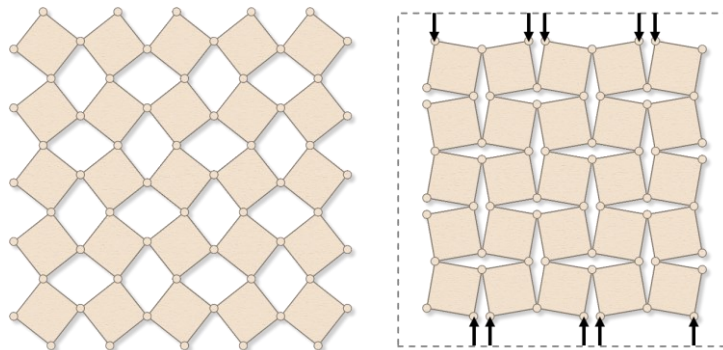


Figure 21: Deformation mechanism of rotating plates.

Grima and Evans investigated the auxetic behaviour of rigid rotating squares and triangular plates, showing that in idealised settings with rigid components, their Poisson's ratio is equal to -1 [121]. They later expanded their investigation into rotating triangles [122], rectangles with different connectivity [123], [124], rhombi [125], [126], parallelograms [126] and non-regular plates. As these rigid models, being highly idealised structures, typically overestimate the auxeticity of the systems [127], semi-rigid and stretching connected plates were also investigated [128]. The same main deformation mechanism was shown to be applicable to crystal structures [129], [130] and justify the natural negative Poisson's observed in materials such as some silicates like  $\alpha$ -cristobalite [131], [132] and zeolites like natrolite [133].

### 3.4.1 Rotating quadrangular plates

The idealised structure of rotating rigid squares has been found isotropic and to have a Poisson's ratio of -1 [121], independently of the strain level, for any angle characterising the configuration [127]. The Young's modulus is dependent on the stiffness of the hinges and on the strain, approaching infinity when the structure becomes fully closed and open [128] (given the assumption of perfectly rigid squares and hinges). Similarly, the shear modulus is constant and equal to infinite for any configuration. In reality, the Poisson's ratio would be dependent on whether hinging or deformation of the plates would be the dominant type of deformation; hence, it would be dependent on the relative rigidity of the squares with respect to the rigidity of the hinges [123].

When considering real semi-rigid structures, the Poisson's ratio is expected to be less negative than the ideal value of -1 estimated for rigid units, with some further reduction also deriving from misalignment of deformation with the major axes of the plane. The nominal shear modulus also becomes finite, an effect of the hinges, compliance and the material shear modulus, which also results in shape changes in the single plates, that depart from the perfectly square shape to become rhombohedral, rectangular or parallelogram shapes. To account for these changes, a model was introduced by Grima *et al.* [127] allowing the diagonals of the squares to deform independently. This, together with the expected increase in Poisson's ratio compared to theoretical ideal value of -1, shows a loss of the properties of isotropy, independency on the scale and on the nominal strain. Similarly, the Young's and shear moduli return finite (although the latter still appears to approach infinity when the structure is fully open).

When using rectangular plates, two alternative connectivity arrangements can be achieved, usually indicated as *Type I*, which defines two orthogonal axes of symmetry (resulting in rhombic empty shapes), and *Type II*, where symmetry is lost (and the empty shapes appear as parallelograms). These are described in Figure 22.



Rectangular *Type I* configurations exhibit anisotropic mechanical behaviour and Poisson's ratios variable with the level of strain, controlled by the proportions of the sides of the plates. Otherwise, *Type II* configurations are characterised by isotropy, with a constant Poisson's ratio of -1, similar to the rotating squares system [124].

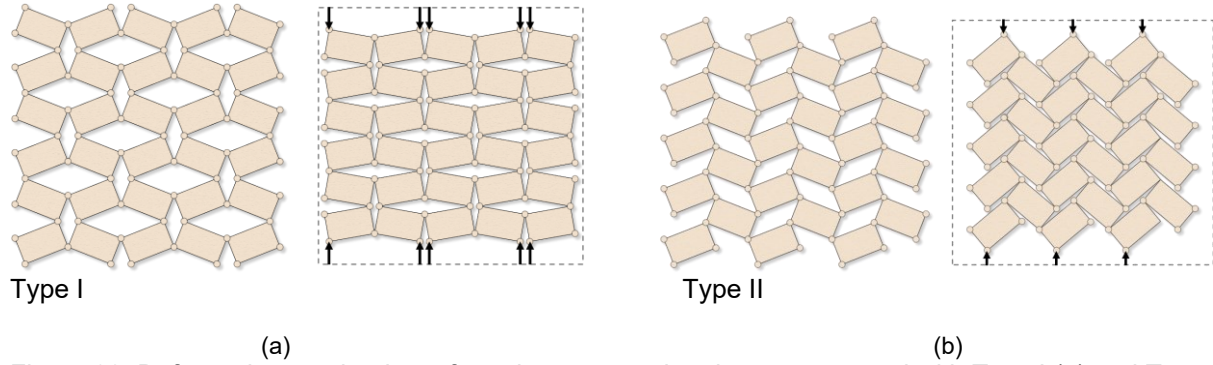


Figure 22: Deformation mechanism of rotating rectangular plates, connected with Type I (a) and Type II (b) arrangements.

Rotating rhombohedral plate configurations were presented as an alternative to rotating squares and as a way to generalise the model further, see Figure 23. Similarly to rectangular plates, two different connecting arrangements can be used, usually indicated as *Type  $\alpha$* , where the obtuse angle of one rhombus is connected to the acute angle of its adjacent plate, and *Type  $\beta$* , where the connecting angles of the rhombi at the same connection are the same. *Type  $\alpha$*  is a space filling means to connect the rhombi, while *Type  $\beta$*  leaves gaps even when fully compressed. The mechanical behaviour of the two arrangements is substantially different, with *Type  $\alpha$*  being highly anisotropic and exhibiting both positive and negative Poisson's ratios, depending on the shape of the rhombi and on the strain (it is dependent on the angles between the plates). *Type  $\beta$*  configurations, instead, are isotropic with a constant Poisson's ratio of -1, independently of the strain, and cannot shear [125].

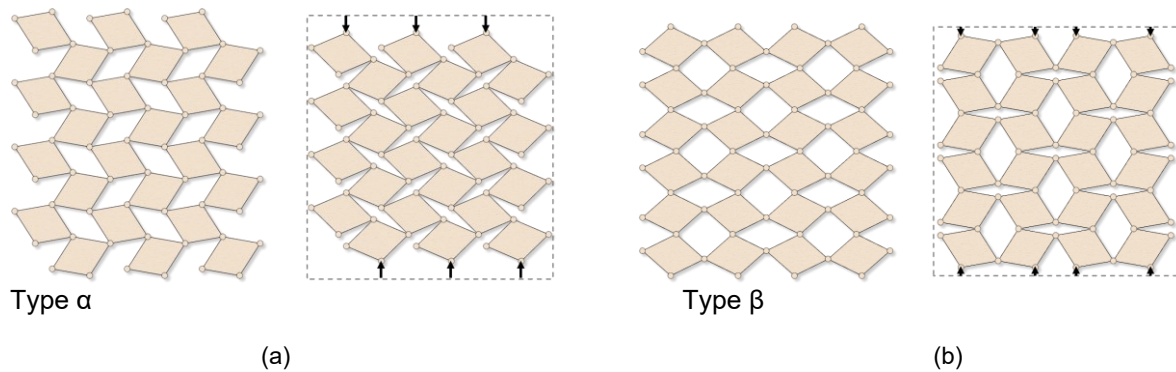


Figure 23: Deformation mechanism of rotating rhombohedral plates, connected with Type  $\alpha$  (a) and Type  $\beta$  (b) arrangements.



These concepts can be further generalised by expanding into parallelograms, which can combine the connection arrangements described for rhombohedral and rectangular plates, resulting into four potential configurations *Type I  $\alpha$* , *Type II  $\alpha$* , *Type I  $\beta$*  and *Type II  $\beta$* , as described in Figure 24 [126].

*Type II  $\alpha$*  configuration has been studied in depth by Grima *et al.* [126], who found that the Poisson's ratio varies with the nominal strain level and can be either positive or negative. Interestingly, this behaviour is very different from that observed for *Type II* rectangular plates (that exhibits a constant negative Poisson's ratio equal to -1), of which *Type II  $\alpha$*  can be regarded as a generalisation. Instead, the variation of the Poisson's ratio with the nominal strain is actually very close to that observed in *Type I* rectangular plate systems and *Type  $\alpha$*  rhombohedral plates.

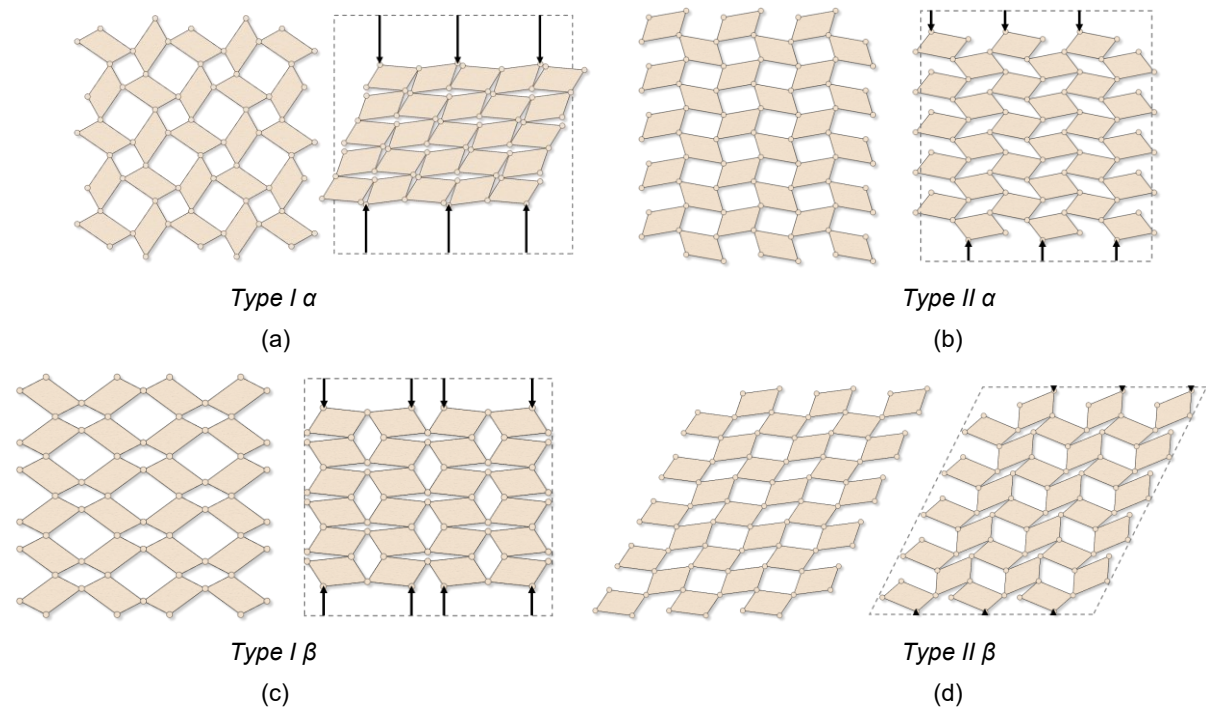


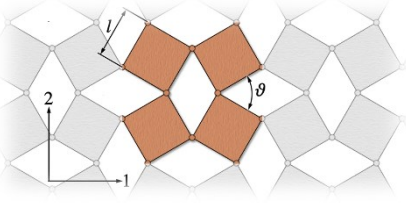
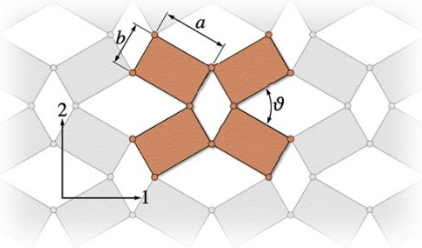
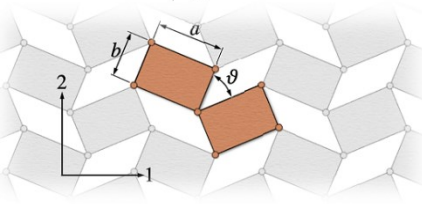
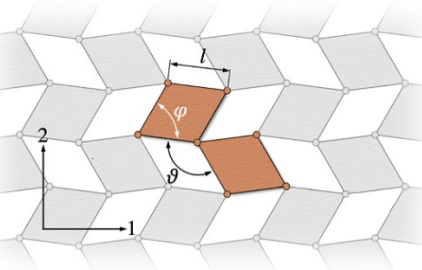
Figure 24: Deformation mechanism of rotating parallelograms, connected with Type I  $\alpha$  (a), Type II  $\alpha$  (b), Type I  $\beta$  (c) and Type II  $\beta$  (d) arrangements.

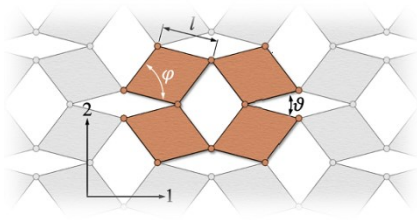
The equations derived by Grima and collaborators [121], [123]–[126] to describe the in-plane mechanical behaviour of different quadrangular *rigid* plate configurations are summarised in Table 7. A figure describing the reference dimensions used in the equations is included on the left side of each set of equations.

For all cases,  $K_h$  is the stiffness constant of the hinges. The notation adopted for the directions of orthotropy, the Poisson's ratios, the elastic moduli and, where available, the shear modulus, are the same as in previous tables.

A comparison of the responses predicted from the different equations summarised in Table 7 is represented in Figure 25. These were derived assuming plates of area  $l \times l = 1 \times 1$  square unit lengths for the square and rhombohedral configurations,  $a \times b = 1.5 \times 0.666 = 1$  square unit lengths for the rectangular and parallelogram plates, and an angle  $\varphi = 60^\circ$  for the rhombohedral and parallelogram plates. Diagrams are represented for a range of the angle  $\vartheta$  changing from 0 to  $90^\circ$ . For the unit stiffness constant,  $K_h = 1.0 \times 10^{-6}$  was used. The diagrams confirm the mentioned similarity between the behaviour of *Type I* rectangular, *Type α* rhombohedral and *Type II α* parallelepiped plate systems. In particular, equations provide equivalent values for *Type α* rhombohedral and *Type II α* parallelepiped plate systems, while the similarity is only qualitative for the case of *Type I* rectangular plates.

Table 7. Equations derived for the determination of the in-plane Poisson's ratio, elastic modulus and, where available, shear modulus, for different quadrangular plate configurations described in the literature.

Rotating Square Plates [121]	
	Poisson's ratios: $\nu_{12} = \nu_{21} = -1$
	Young's moduli: $E_{1,2} = K_h \frac{8}{l^2} \frac{1}{(1 - \sin \theta)}$
	Shear modulus: $G_{12} = \infty$
Rotating Rectangular Plates [123], [124]	
<p><i>Type I</i></p> 	Poisson's ratios: $\nu_{21} = (\nu_{12})^{-1} = \frac{a^2 \sin^2(\frac{\theta}{2}) - b^2 \cos^2(\frac{\theta}{2})}{a^2 \cos^2(\frac{\theta}{2}) - b^2 \sin^2(\frac{\theta}{2})}$
	Young's moduli: $E_1 = 8K_h \frac{a \cos(\frac{\theta}{2}) + b \sin(\frac{\theta}{2})}{[a \sin(\frac{\theta}{2}) + b \cos(\frac{\theta}{2})] [-a \sin(\frac{\theta}{2}) + b \cos(\frac{\theta}{2})]^2}$ $E_2 = 8K_h \frac{a \sin(\frac{\theta}{2}) + b \cos(\frac{\theta}{2})}{[a \cos(\frac{\theta}{2}) + b \sin(\frac{\theta}{2})] [a \cos(\frac{\theta}{2}) - b \sin(\frac{\theta}{2})]^2}$
	Shear Modulus: $G_{12} = \infty$
	<hr/> Poisson's ratios: $\nu_{12} = \nu_{21} = -1$
<p><i>Type II</i></p> 	Young's moduli: $E_1 = E_2 = \frac{8K_h}{ab(1 - \sin \theta)}$
	Shear modulus: $G_{12} = \infty$
Rotating Rhombohedral Plates [125], [126]	
<p><i>Type α</i></p> 	Poisson's ratios: $\nu_{12} = (\nu_{21})^{-1} = \tan\left(\frac{\theta - \varphi}{2}\right) \cdot \tan\left(\frac{\theta + \varphi}{2}\right)$
	Young's moduli*: $E_1 = \frac{4K_h \sin(\frac{\theta + \varphi}{2})}{l^2 \cos(\frac{\theta - \varphi}{2}) \cdot \cos^2(\frac{\theta + \varphi}{2})}$ $E_2 = \frac{4K_h \cos(\frac{\theta - \varphi}{2})}{l^2 \sin(\frac{\theta - \varphi}{2}) \cdot \sin^2(\frac{\theta + \varphi}{2})}$
	Shear modulus: $G_{12} = \infty$
	<hr/> Poisson's ratios: $\nu_{12} = \nu_{21} = -1$
<p><i>Type β</i></p>	Young's moduli*:



$$E_1 = E_2 = \frac{4K_h}{l^2 \sin^2\left(\frac{\vartheta - \varphi}{2}\right) \cdot \sin\varphi}$$

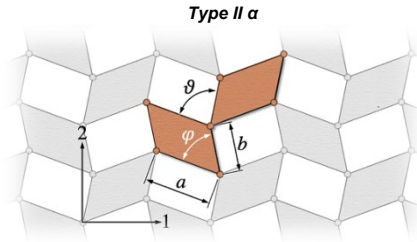
Shear modulus:

$$G_{12} = \infty$$

---

### Rotating Parallelograms [126]

---



Poisson's ratios:

$$\nu_{12} = (\nu_{21})^{-1} = \tan\left(\frac{\vartheta - \varphi}{2}\right) \tan\left(\frac{\vartheta + \varphi}{2}\right)$$

Young's moduli\*:

$$E_1 = \frac{4K_h \sin\left(\frac{\vartheta + \varphi}{2}\right)}{a b \cdot \cos\left(\frac{\vartheta - \varphi}{2}\right) \cdot \cos^2\left(\frac{\vartheta + \varphi}{2}\right)}$$

$$E_2 = \frac{4K_h \cos\left(\frac{\vartheta - \varphi}{2}\right)}{a b \cdot \sin\left(\frac{\vartheta + \varphi}{2}\right) \cdot \sin^2\left(\frac{\vartheta - \varphi}{2}\right)}$$

Shear Modulus:

$$G_{12} = \infty$$


---

\* In the original equations of these Young's moduli, the denominators are multiplied by the plate depth, here removed for units' consistency.

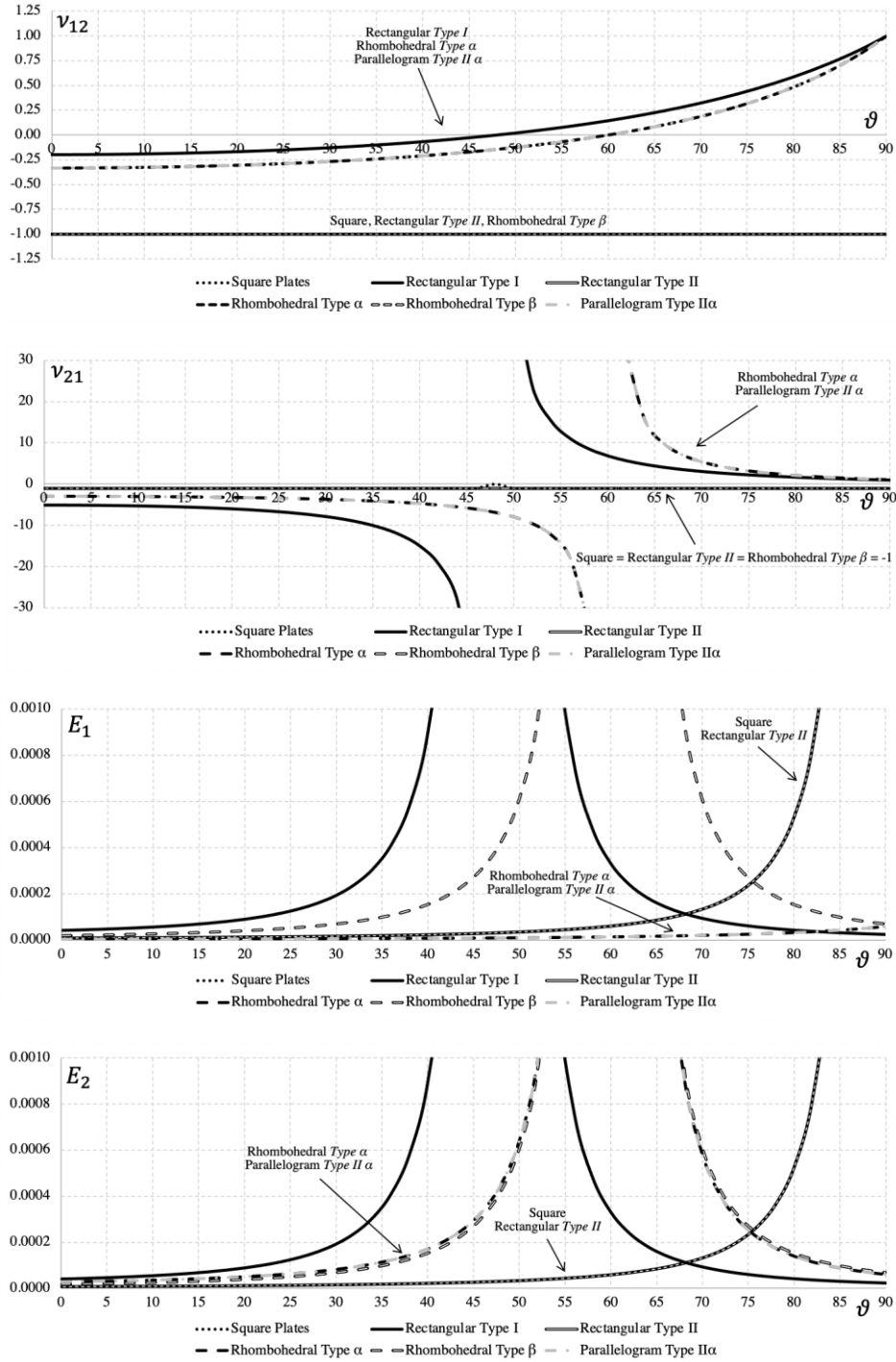


Figure 25: Diagrams of the in-plane Poisson's ratios and Young's moduli determined with the equations for the analysis of rotating quadrangular rigid plates (see Table 7) in conventional and auxetic configurations, the parameters used as defined above  $l = 1$ ,  $a = 1.5$ ,  $b = 0.666$  unit length,  $\varphi = 60^\circ$  and  $K_h = 1.0 \cdot 10^{-6}$  unit force.

### 3.4.2 Rotating triangular plates

The first proposed rotating triangular plate system was based on equilateral triangles which are connected and deform as described in Figure 26.a. For an ideal structure with perfectly rigid plates and hinges, where all deformations are due to rotation of the triangles, the system is isotropic with constant negative Poisson's equal to -1. The Young's modulus approaches infinity when the structure is fully collapsed and fully expanded, and the shear modulus is infinite for any configuration [122].

Pairs of irregular triangles have also been studied for applications in rotating plate auxetic structures (see Figure 26.b). In this case, the system highlights behaviours that are closer to those observed in honeycomb auxetic systems, which exhibit anisotropy and Poisson's ratios depending on the nominal strain, that can be negative at small strains, but return positive at larger deformations [134].

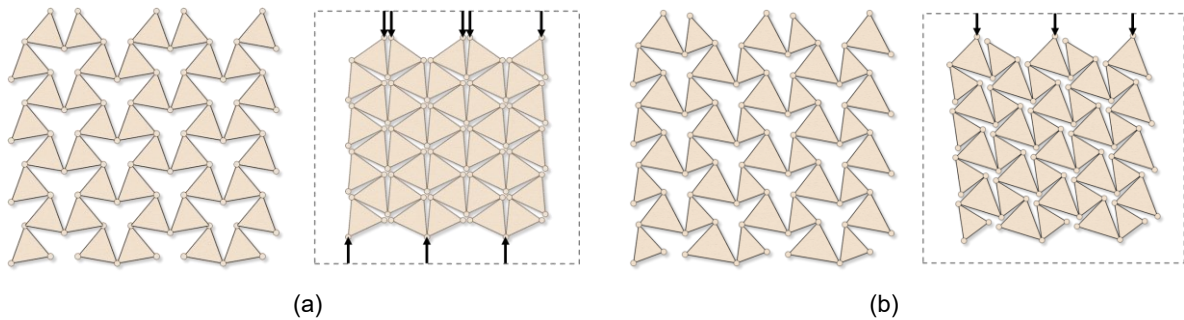
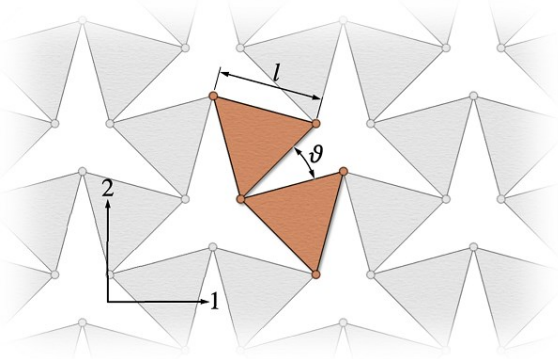
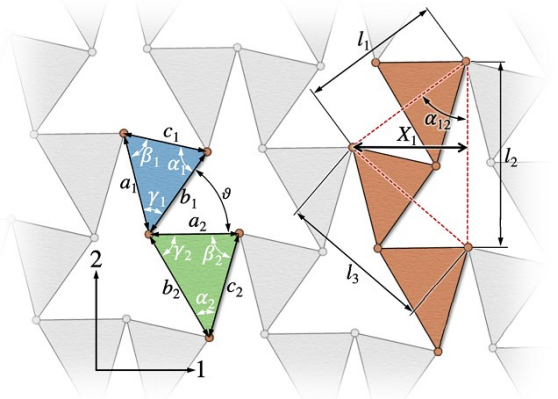


Figure 26: Deformation mechanism of equilateral (a) and irregular (b) rotating triangular plates.

The equations derived by Grima et al [122], [134] to describe the in-plane mechanical behaviour of equilateral and irregular triangular rotating *rigid* plate configurations are summarised in Table 8. A figure describing the reference dimensions used in the equations is included on the left side of each set of equations.

Table 8. Equations derived for the determination of the in-plane Poisson's ratio, elastic modulus shear modulus, for triangular plate configurations.

Rotating Triangular Plates [122]	Poisson's ratios:
<p><b>Equilateral</b></p> 	$\nu_{12} = \nu_{21} = -1$
<p><b>Pairs of Irregular Triangles [134]</b></p> 	<p>Geometric Parameters:</p>
	$l_1 = \sqrt{c_1^2 + c_2^2 + 2c_1c_2\cos(\vartheta - \alpha_1 - \beta_2)}$
	$l_2 = \sqrt{b_1^2 + b_2^2 - 2b_1b_2\cos(\vartheta + \gamma_2)}$
	$l_3 = \sqrt{a_1^2 + a_2^2 - 2a_1a_2\cos(\vartheta + \gamma_1)}$
	$X_1 = \frac{\sqrt{4l_1^2l_2^2 - (l_1^2 + l_2^2 - l_3^2)^2}}{2l_2}$
<p>Poisson's ratios:</p>	$\nu_{12} = (\nu_{21})^{-1} = -\frac{2a_1a_2l_2^2(l_1^2 + l_2^2 - l_3^2) \cdot \sin(\vartheta + \gamma_1) + b_1b_2(l_1^2 + l_2^2 - l_3^2)(l_1^2 - l_2^2 - l_3^2) \cdot \sin(\vartheta + \gamma_2) + 2c_1c_2l_2^2(l_1^2 - l_2^2 - l_3^2) \cdot \sin(\vartheta - \alpha_1 - \beta_2)}{4X_1^2l_2^2b_1b_2 \cdot \sin(\vartheta + \gamma_2)}$
<p>Young's moduli:</p>	$E_1 = \frac{48K_hl_2^7X_1^3}{d[2a_1a_2l_2^2(l_1^2 + l_2^2 - l_3^2) \cdot \sin(\vartheta + \gamma_1) + b_1b_2(l_1^2 + l_2^2 - l_3^2)(l_1^2 - l_2^2 - l_3^2) \cdot \sin(\vartheta + \gamma_2) + 2c_1c_2l_2^2(l_1^2 - l_2^2 - l_3^2) \cdot \sin(\vartheta - \alpha_1 - \beta_2)]^2}$ $E_2 = \frac{3K_hl_2^3}{b_1^2b_2^2X_1d \cdot \sin^2(\vartheta + \gamma_2)}$
<p>Shear Modulus:</p>	$G_{12} = \frac{3K_hl_2^5X_1}{d[a_1a_2l_2^2 \cdot \sin(\vartheta + \gamma_1) + b_1b_2(l_1^2 - l_3^2) \cdot \sin(\vartheta + \gamma_2) + c_1c_2l_2^2 \cdot \sin(\vartheta - \alpha_1 - \beta_2)]^2}$



### 3.5 Others

The configurations above describe the most common basic structures analysed in the literature. A number of hybrid structures, based on combinations of different auxetic configurations, are also possible and have been proposed, such as hybrids between re-entrant and chiral structures [135], [136] (see Figure 27.a). Additionally, hybrid configurations based on hierarchical structures, where the auxetic pattern is 'layered', have been presented [52], [137], as the multi-level hierarchical rotating squares structure described in Figure 27.b. This allows for further tailoring of properties, either to combine advantages for two type of structures, reinforcing one with advantages from another or circumvent a drawback of the primary structure used – like the re-entrant trichiral structure adding the out-of-plane reinforcements of the cylinders of the chiral structures to the higher auxeticity and synclastic out of plane behaviour of the re-entrant hexagonal structure [135], or enhance the possibilities for a specific use like the two-level hierarchical structure in Figure 27.b could be used in a filter for filtering two different particle sizes.

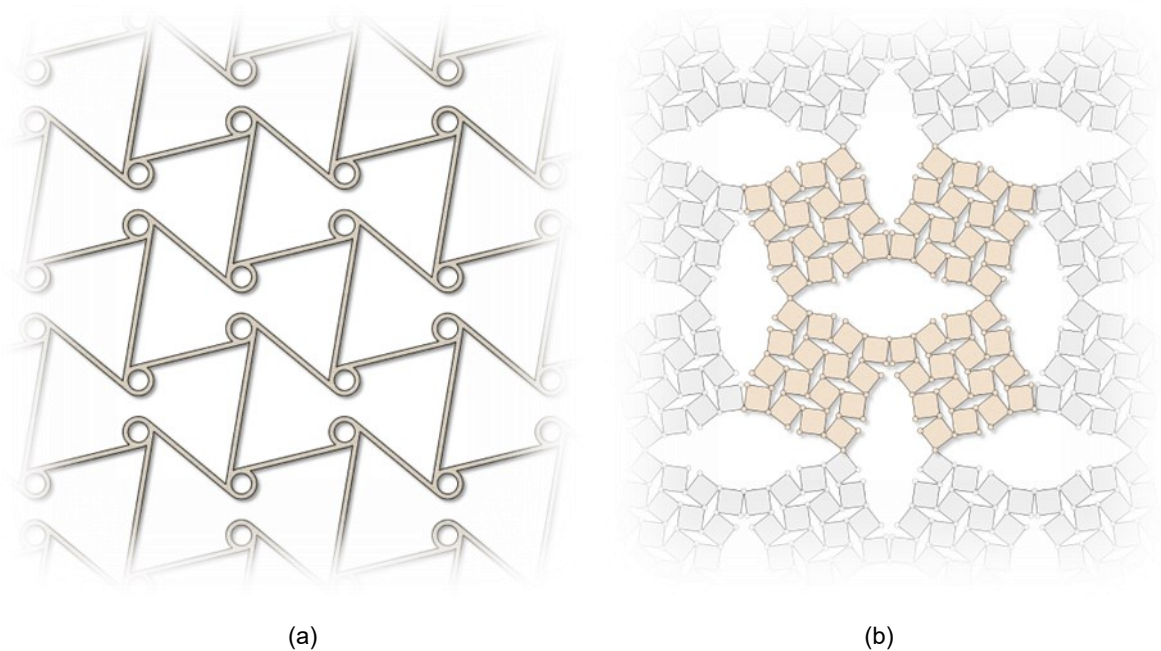


Figure 27: Example of a re-entrant trichiral honeycomb structure (a) and of a two-level hierarchical rotating squares structure (b)

### 3.6 Summary/Discussion: Options and Suitability for cardiovascular stents

There is a large number of two-dimensional auxetic structures that can provide a range of different auxetic behaviours. Several of these structures have been investigated thoroughly in the literature, providing indications on the elastic behaviours, ranges of Poisson's ratio



theoretically achievable with each of the designs, as well as the sensitivity to more realistic manufacturing and usage circumstances. However, no clear comparisons have been made that provides a more direct indication on which structures would be more suited to each specific practical application. There are a few papers that mention the implications of exploiting auxetic configurations, stressing the fact that auxetic solutions require design considerations that may not be present in more conventional manufacturing approaches. For example, Ren *et al* [138] report [109] a practical investigation of designing and testing a nail using auxetic structures. Comparison with normal nails showed several unexpected limitations with the auxetic configuration, such as the need for more specific requirements for the nail's surface roughness (stemming from the surface holes of the auxetic pattern) on the push-in and pull-out performance. Although some of the problems encountered by Ren *et al* in creating an auxetic might not be as prominent for cases that already use cellular structures, it is worth to remember that most of the studies published on the topic have been mainly theoretical or involve models.

The unification of nomenclature, as far as possible, and partial evaluation with standardised parameters provided here, is intended to offer guidance on which elastic behaviours to expect for each auxetic configuration in comparison to others. For example, if a stable Poisson's ratio is required over large deformations, the hexachiral is shown to retain it for deformations up to 25%, in comparison to the rapidly changing Poisson's ratio for the re-entrant structures where the structure angles change largely with deformation. Some of the structures suitable for cases where a larger NPR would be desirable would be the double arrowhead or the re-entrant hexagonal.

For isotropic continuous materials, the Poisson's ratio is equal in all directions and is limited to the range  $-1 < \nu < 0.5$  (expanded to  $-1 < \nu < 1$  for two-dimensional isotropic systems [123], [139]) while for anisotropic structures no such limits exist [64]. Therefore, isotropic systems like the hexachiral system and some of the rotating plates have a limit on maximum NPR achievable in any direction. For anisotropic systems like some of the re-entrant systems it can be observed that although they can achieve higher NPR's in one direction, this is counterbalanced by a lower NPR in the other in-plane direction. So even though re-entrant systems like the re-entrant hexagonal or double arrowhead systems can achieve quite high NPR in one direction, there is a trade-off in the other.

For the purpose of this project, the comparative study of the auxetic structures available in literature has been essential to identify the most suitable options for cardiovascular stenting.

### 3.7 Conclusion: Choice of which auxetic structures to study further in this specific study

As observed in the clinical background, for the major vessels the healthy deformations are large and of the same sign in both the longitudinal and circumferential directions (For the ascending aorta, around 6.7-8.5% and 7.9-8.1% respectively [15]), and it would be optimal to have structures that could restore that motion in a controlled way.

Rotating plates, despite being able to offer the required Poisson's ratios, are not ideal for these applications, due to the need to introduce hinges of controlled properties. These may be obtained by including frictional components, or by exploiting the material elasticity at the joints between the rotating plates. In both cases, as large vessels experience about 40 million cycles per year [5], wearing or crack propagation would represent a major potential risk. Hence, cellular wall structures, similar to those already successfully employed in common angioplasty stents were preferred. Three candidate configurations were selected, characterised by the three largest ranges of negative Poisson's ratio:

- The re-entrant hexagonal, has a large potential range for the negative Poisson's ratio and has been studied extensively, so it is easy to evaluate with the information from the literature and can provide a good benchmark.
- The double arrowhead, which is indicated to have possibly the largest range of achievable negative Poisson's ratios, but it has not been sufficiently analysed in the literature, so it requires further investigation to be evaluated in the light of cardiovascular stenting for the major vessels.
- The hexachiral, which is different to the two above as it depends on a different deformation mechanism and is not re-entrant. It offers isotropic behaviour over a larger range of strain. It is well compared with anti-tetrachiral structures, which are the other interesting chiral structure for these types of applications and is widely studied in the literature with well-developed modelling.

## 4. Development of analytical method for Double Arrowhead

### 4.1 Introduction to analytical method

The double arrowhead (DAH) structure, first introduced by Larsen *et al.* in 1997 [79], is a very interesting configuration, due to its potential to produce a highly anisotropic behaviour with much higher NPRs than the majority of the other auxetic shapes. However, its application is partially limited by the lack of comprehensive analytical equations predicting the effect of its geometric parameters on the achieved mechanical behaviour. In fact, due to the highly anisotropic behaviour of the cellular structure, direct derivation of the shear modulus expression from the Poisson's ratio and Young's modulus is inapplicable. Thus, the aim of this study is to provide an analytical framework for the DAH structure consistent with previous studies on the re-entrant honeycomb, deriving simple equations for the Poisson's ratios, Young's moduli and for the shear modulus, easy to apply to biaxial and tubular structures.

Multiple analytical expressions have been derived to describe the deformation behaviour of the double arrowhead. Brighenti *et al.* [98] started from a kinematic analysis and then adopted a statically indeterminate structural scheme, which accounts for the deformation of the unit cell; Berinskii [90] used a homogenisation method to find the components of the stiffness tensor of the effective continuum analytically, Qiao *et al.* [140] used a beam approach but only considered the deformation in one direction and Li *et al.* [141] used strain energy for a representative volume element to derive both the Poisson's ratio and the Young's modulus. However, all these studies provide only partial analyses, and a comprehensive model, including for example the prediction of the shear modulus is still missing in the literature for the double arrowhead configuration.

For the analytical study, the two-dimensional double arrowhead cell shown in Figure 28 a is considered. To standardise the analytical expressions to current literature, a similar approach to that of Gibson & Ashby [69], and Masters & Evans [83] for the first elastic models of the re-entrant hexagonal honeycomb was adopted.

Expressions for the Poisson's ratio, Young's modulus and shear modulus are derived considering the deformation of the beams by flexural and stretching mechanisms.

For flexure, the bending of the cell walls follows the approach proposed by Gibson & Ashby [68], [77], [88], and later built on by Masters & Evans [83], that considers a cell wall of length  $l$  as a cantilever beam fixed at one end and guided at the other [68], [83], [142], resulting in the relationship for the deformation [143]:

$$\delta = \frac{Ml^2}{12E_sI} = \frac{Fl^3}{12E_sI} \quad (4.1)$$

where  $M = Fl$  is the moment applied to the guided end,  $E_s$  is the Young's modulus of the cell wall material, and  $I$  is the second moment of area of the cell wall.

In the case of shearing, after initially using the flexural analytical approach to shear, it was discovered that stretching becomes the dominant deformation mechanism, requiring some changes in the analytical approach, which is presented below as the stretching approach to shear. This is evident when comparing the equations obtained by applying the flexural and stretching modes with the results from the numerical models for both planar and tubular structures, as further seen in the results in *Chapter 7*. The stretching model appears far more appropriate for the prediction of the shearing of the structure. For completion, stretching equations of the normal deformation in 1- and 2-direction are also included in the *Appendix*. The model is based on the same approach proposed by Masters & Evans for the complementary analysis of the re-entrant hexagonal structure [83] while the shear approach is different to avoid the resulting infinite shear stiffness when using the rigid angles in Masters & Evans, both where the extension of the cell wall of length  $l$  due to the axial force  $F$  is calculated using standard beam theory

$$\delta = \frac{Fl}{E_sA} \quad (4.2)$$

with  $A$  = area of the cell wall cross-section and  $E_s$  = Young's modulus of the cell wall material. The stretching approach used to analyse shearing could be applied to the normal deformation in 1- and 2-direction, but it would result in a basic slider-crank mechanism, with stretching only acting for the two extreme cases (when the shorter beam becomes horizontal, for horizontal tensile loads; and when both beams – the longer and the shorter – align vertically, for vertical tensile loads).

## 4.2 Flexure model

The model is based on a similar approach to that of Gibson & Ashby's [69] uniaxial bending model for the regular and re-entrant hexagonal honeycombs.

### 4.2.1 Uniaxial loading of double arrowhead cell in the 1-direction

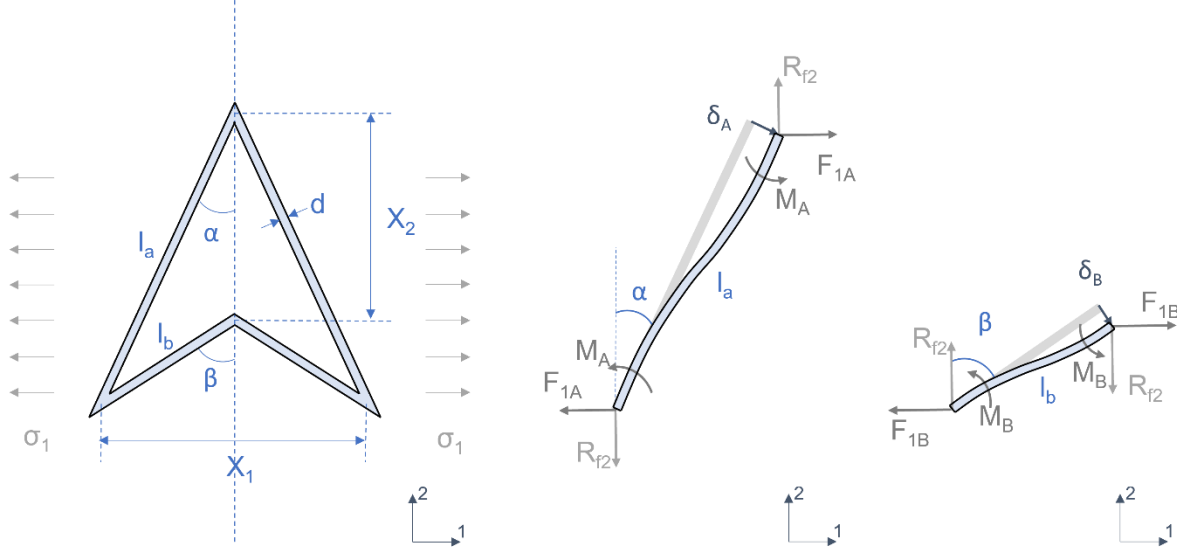


Figure 28: a) Uniaxial loading in 1-direction and resulting b) long beam and c) short beam free body diagram, respectively.

When the double arrowhead cell is subjected to uniaxial loading by a far field nominal stress  $\sigma_1$  (Figure 28 a), the force in the direction of 1 can be expressed as

$$F_1 = \sigma_1 (l_a \cos \alpha - l_b \cos \beta) b \quad (4.3)$$

where  $l_a$  and  $l_b$  are the lengths of the longer and shorter beam respectively;  $\alpha$  and  $\beta$  the angles between the longer and shorter beams to the horizontal direction, respectively; and  $b$  is the out of plane width of the beams.

To maintain equilibrium,  $R_{f2} = 0$ .

For the longer beam (Figure 28 b), the moment  $M_A$  can be calculated as

$$M_A = \frac{F_{1A} l_a \cos \alpha}{2} \quad (4.4)$$

And the displacement  $\delta_A$  as

$$\delta_A = \frac{M_A l_a^2}{6 E_s I} = \frac{F_{1A} l_a^3 \cos \alpha}{12 E_s I} \quad (4.5)$$

Where the component of deformation along the 1-axis is

$$\delta_{A1} = \frac{F_{1A} l_a^3 \cos^2 \alpha}{12 E_s I} \quad (4.6)$$

And the component of deformation along the 2-axis is

$$\delta_{A2} = \frac{F_{1A} l_a^3 \sin \alpha \cos \alpha}{12 E_s I} \quad (4.7)$$

For the shorter beam (Figure 28 c), the moment  $M_B$  can be calculated as

$$M_B = \frac{F_{1B} l_b \cos \beta}{2} \quad (4.8)$$

And the displacement  $\delta_B$  as

$$\delta_B = \frac{M_B l_b^2}{6 E_s I} = \frac{F_{1B} l_b^3 \cos \beta}{12 E_s I} \quad (4.9)$$

Where the component of deformation along the 1-axis is

$$\delta_{B1} = \frac{F_{1B} l_b^3 \cos^2 \beta}{12 E_s I} \quad (4.10)$$

And the component of deformation along the 2-axis is

$$\delta_{B2} = \frac{F_{1B} l_b^3 \sin \beta \cos \beta}{12 E_s I} \quad (4.11)$$

Due to the geometry constrain,  $\delta_{A1} = \delta_{B1}$ , the relation between  $F_{1A}$  and  $F_{1B}$  can be determined as

$$\begin{aligned} \frac{F_{1A} l_a^3 \cos^2 \alpha}{12 E_s I} &= \frac{F_{1B} l_b^3 \cos^2 \beta}{12 E_s I} \\ F_{1B} &= F_{1A} \frac{l_a^3}{l_b^3} \cdot \frac{\cos^2 \alpha}{\cos^2 \beta} \end{aligned}$$

Since:

$$F_1 = F_{1A} + F_{1B} = F_{1A} \left( 1 + \frac{l_a^3}{l_b^3} \cdot \frac{\cos^2 \alpha}{\cos^2 \beta} \right)$$

$$F_{1A} = \frac{F_1}{\left( 1 + \frac{l_a^3}{l_b^3} \cdot \frac{\cos^2 \alpha}{\cos^2 \beta} \right)} = \frac{F_1 l_b^3 \cos^2 \beta}{(l_a^3 \cos^2 \alpha + l_b^3 \cos^2 \beta)} \quad (4.12)$$

$$F_{1B} = \frac{F_1}{\left( 1 + \frac{l_a^3}{l_b^3} \cdot \frac{\cos^2 \beta}{\cos^2 \alpha} \right)} = \frac{F_1 l_a^3 \cos^2 \alpha}{(l_a^3 \cos^2 \alpha + l_b^3 \cos^2 \beta)} \quad (4.13)$$

#### 4.2.2 Uniaxial loading of double arrowhead cell in direction 2

When the double arrowhead cell is subjected to uniaxial loading by a far field nominal stress  $\sigma_2$

(Figure 29 a), the force  $F_2$  in the direction of the stress can be expressed as

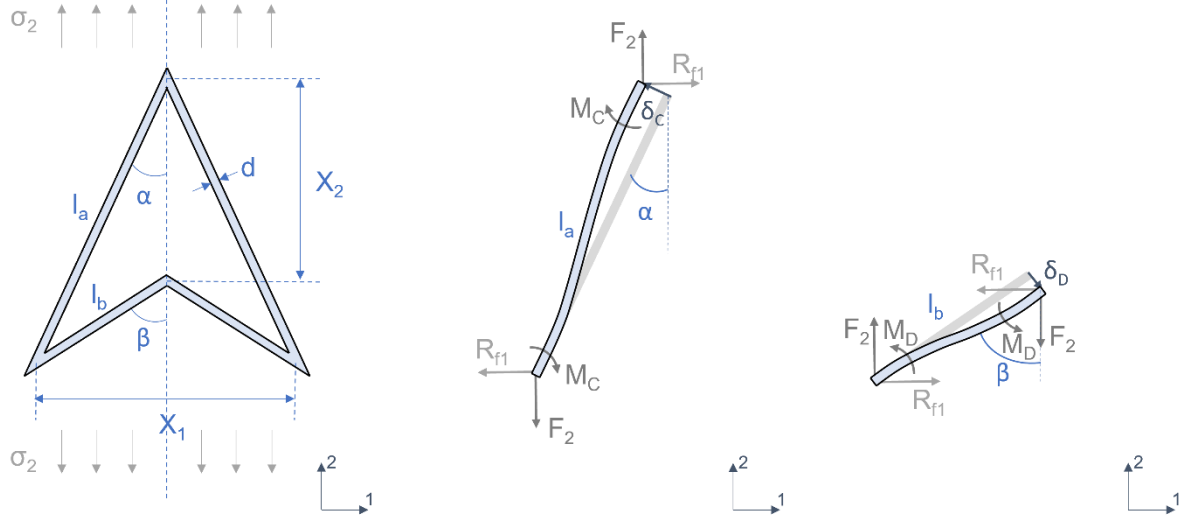


Figure 29: a) Uniaxial loading in 2-direction and resulting b) long beam and c) short beam free body diagram, respectively.

$$F_2 = \sigma_2 b l_a \sin \alpha = \sigma_2 b l_b \sin \beta \quad (4.14)$$

For the longer beam (Figure 29 b), the moment  $M_C$  can be calculated as

$$M_C = \frac{R_{f1} l_a \cos \alpha + F_2 l_a \sin \alpha}{2} \quad (4.15)$$

And the displacement  $\delta_C$  as

$$\delta_C = \frac{M_C l_a^2}{6E_s I} = \frac{(R_{f1} \cos \alpha + F_2 \sin \alpha) l_a^3}{12E_s I} \quad (4.16)$$

Where the component of deformation along the 1-axis is

$$\delta_{C1} = \frac{R_{f1} \cos \alpha + F_2 \sin \alpha}{12E_s I} l_a^3 \cos \alpha \quad (4.17)$$

And the component of deformation along the 2-axis is

$$\delta_{C2} = \frac{R_{f1} \cos \alpha + F_2 \sin \alpha}{12E_s I} l_a^3 \sin \alpha \quad (4.18)$$

For the shorter beam (Figure 29 c), the moment  $M_D$  can be calculated as

$$M_D = \frac{-F_2 l_b \sin \beta - R_{f1} l_b \cos \beta}{2} \quad (4.19)$$

And the displacement  $\delta_D$  as

$$\delta_D = \frac{M_D l_b^2}{6E_s I} = \frac{(-F_2 \sin \beta - R_{f1} \cos \beta) l_b^3}{12E_s I} \quad (4.20)$$

Where the component of deformation along the 1-axis is

$$\delta_{D1} = -\frac{F_2 \sin \beta + R_{f1} \cos \beta}{12E_s I} l_b^3 \cos \beta \quad (4.21)$$

And the component of deformation along the 2-axis is

$$\delta_{D2} = -\frac{F_2 \sin \beta + R_{f1} \cos \beta}{12E_s I} l_b^3 \sin \beta \quad (4.22)$$

Due to the geometrical constraint  $\delta_{C1} = \delta_{D1}$ , an expression for  $R_{f1}$  can be developed

$$\frac{R_{f1} \cos \alpha + F_2 \sin \alpha}{12E_s I} l_a^3 \sin \alpha = -\frac{F_2 \sin \beta + R_{f1} \cos \beta}{12E_s I} l_b^3 \sin \beta$$

$$R_{f1} = -F_2 \frac{l_a^3 \sin \alpha \cos \alpha + l_b^3 \sin \beta \cos \beta}{l_a^3 \cos^2 \alpha + l_b^3 \cos^2 \beta} \quad (4.23)$$

#### 4.2.3 Flexural response of double arrowhead cell in shear loading

When the double arrow cell is subjected to shear loading by a far field nominal stress  $\tau$  (Figure 30), the forces on the beams can be expressed as

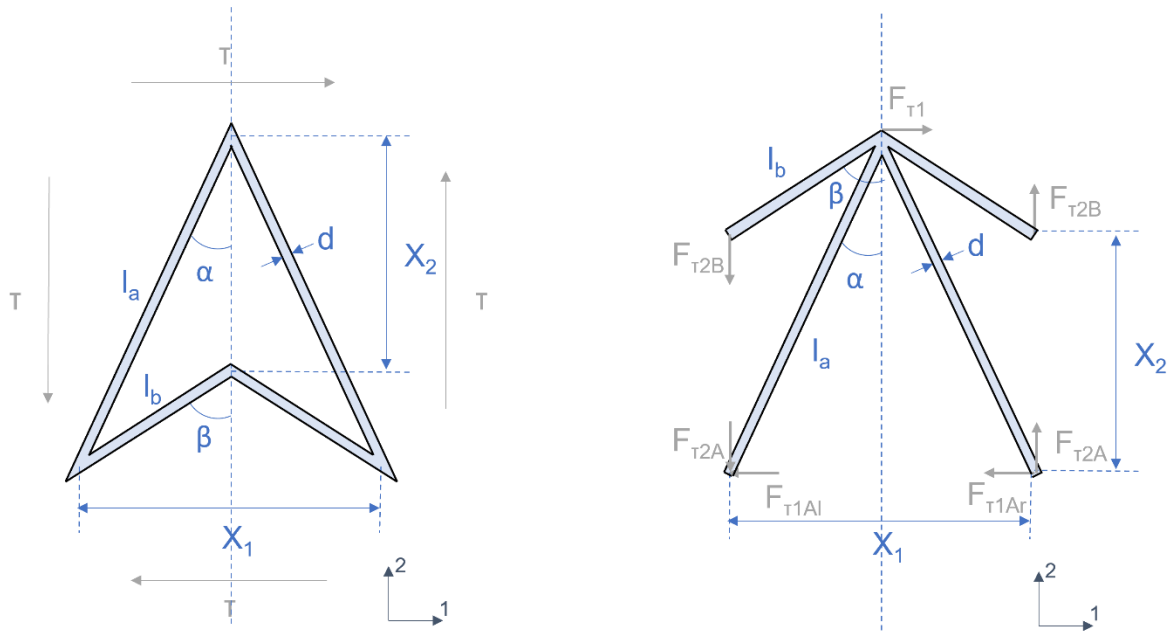


Figure 30: Flexural response of double arrowhead cell subjected to shearing



To maintain equilibrium,  $F_{\tau 1A} = F_{\tau 1Al} + F_{\tau 1Ar} = F_{\tau 1}$  and  $F_{\tau 1B} = 0$ .

It is also:

$$\tau_{12} = -\tau_{21} = \tau \quad (4.24)$$

with:

$$\tau_{12} = \tau = \frac{F_{\tau 1}}{2 l_a b \sin \alpha} \quad (4.25)$$

Then,

$$F_{\tau 1} = 2 \tau l_a b \sin \alpha = 2 \tau l_b b \sin \beta \quad (4.26)$$

Similarly,

$$\tau_{21} = -\tau = -\frac{F_{\tau 2}}{(l_a \cos \alpha - l_b \cos \beta) b} = -\frac{F_{\tau 2A} + F_{\tau 2B}}{(l_a \cos \alpha - l_b \cos \beta) b} \quad (4.27)$$

$$F_{\tau 2} = F_{\tau 2A} + F_{\tau 2B} = \tau (l_a \cos \alpha - l_b \cos \beta) b \quad (4.28)$$

Where  $\tau$  is the far field nominal shear stress and  $b$  the out of plane width of the beams.

To calculate the deformation of beam  $A_l$  (Figure 31):

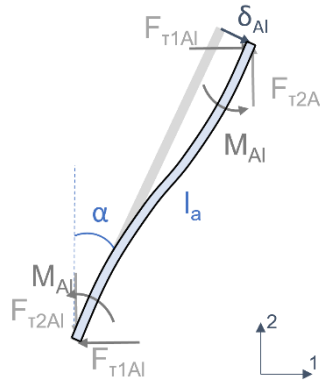


Figure 31: Free body diagram of the left-side longer beam of length  $l_a$ , referred to as beam  $A_l$

For the left-side longer beam with the length  $l_a$ , the moment  $M_{Al}$  can be calculated as

$$M_{Al} = \frac{F_{\tau 1Al} l_a \cos \alpha + F_{\tau 2A} l_a \sin \alpha}{2} \quad (4.29)$$

And the displacement  $\delta_{Al}$  as

$$\delta_{Al} = \frac{M_{AS} l_a^2}{6 E_s I} = \frac{(F_{\tau 1Al} \cos \alpha + F_{\tau 2A} \sin \alpha) l_a^3}{12 E_s I} \quad (4.30)$$

Where the component of deformation along the X1 axis is

$$\delta_{Al1} = \frac{(F_{\tau 1Al} \cos \alpha + F_{\tau 2A} \sin \alpha) l_a^3}{12 E_s I} \cos \alpha \quad (4.31)$$

And the component of deformation along the X2 axis is

$$\delta_{Al2} = \frac{(F_{t1Al} \cos \alpha + F_{t2A} \sin \alpha) l_a^3}{12 E_s I} \sin \alpha \quad (4.32)$$

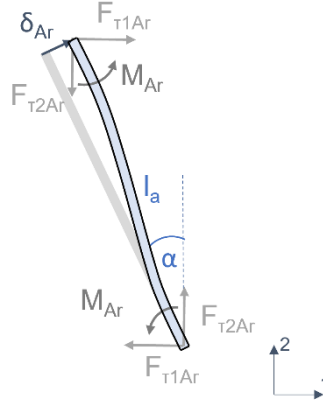


Figure 32: Free body diagram of the right-side longer beam of length  $l_a$ , referred to as beam  $A_r$

To calculate the deformation of beam  $A_r$  (Figure 32):

For the right-side longer beam with the length  $l_a$ , the moment  $M_{Ar}$  can be calculated as

$$M_{Ar} = \frac{F_{t1Ar} l_a \cos \alpha - F_{t2A} l_a \sin \alpha}{2} \quad (4.33)$$

And the displacement  $\delta_{Ar}$  as

$$\delta_{Ar} = \frac{M_{Ar} l_a^2}{6 E_s I} = \frac{(F_{t1Ar} \cos \alpha - F_{t2A} \sin \alpha) l_a^3}{12 E_s I} \quad (4.34)$$

Where the component of deformation along the 1-axis is

$$\delta_{Ar1} = \frac{(F_{t1Ar} \cos \alpha - F_{t2A} \sin \alpha) l_a^3}{12 E_s I} \cos \alpha \quad (4.35)$$

And the component of deformation along the 2-axis is

$$\delta_{Ar2} = \frac{(F_{t1Ar} \cos \alpha - F_{t2A} \sin \alpha) l_a^3}{12 E_s I} \sin \alpha \quad (4.36)$$

To calculate the deformation of beam  $B_l$  (Figure 33):

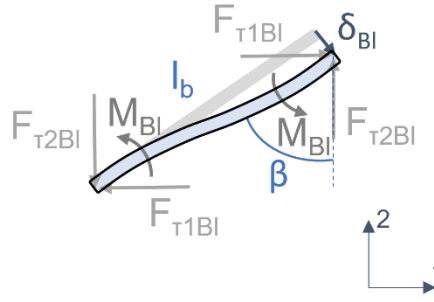


Figure 33: Free body diagram of the left-side shorter beam of length  $l_b$ , referred to as beam  $B_l$

For the left-side shorter beam with the length  $l_b$ , the moment  $M_{Bl}$  can be calculated as

$$M_{Bl} = \frac{F_{T2Bl} l_b \sin \beta}{2} \quad (4.37)$$

And the displacement  $\delta_{Bl}$  as

$$\delta_{Bl} = \frac{M_{Bl} l_b^2}{6E_s I} = \frac{F_{T2Bl} l_b^3 \sin \beta}{12E_s I} \quad (4.38)$$

Where the component of deformation along the 1-axis is

$$\delta_{Bl1} = \frac{F_{T2Bl} l_b^3}{12E_s I} \sin \beta \cos \beta \quad (4.39)$$

And the component of deformation along the 2-axis is

$$\delta_{Bl2} = \frac{F_{T2Bl} l_b^3}{12E_s I} \sin^2 \beta \quad (4.40)$$

To calculate the deformation of beam  $B_r$  (Figure 34):

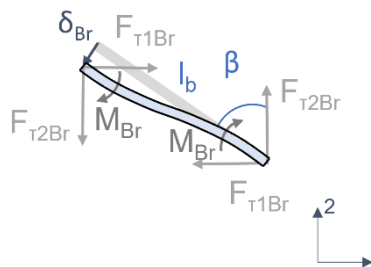


Figure 34: Free body diagram of the right-side longer beam of length  $l_b$ , referred to as beam  $B_r$

For the right-side shorter beam with the length  $l_b$ , the moment  $M_{Br}$  can be calculated as

$$M_{Br} = \frac{-F_{T2Bl} l_b \sin \beta}{2} \quad (4.41)$$

And the displacement  $\delta_{Br}$  as

$$\delta_{Br} = \frac{M_{BS} l_b^2}{6E_s I} = \frac{-F_{\tau 2B} l_b^3 \sin \beta}{12E_s I} \quad (4.42)$$

Where the component of deformation along the 1-axis is

$$\delta_{Br1} = \frac{-F_{\tau 2B} l_b^3}{12E_s I} \sin \beta \cos \beta \quad (4.43)$$

And the component of deformation along the 2-axis is

$$\delta_{Br2} = \frac{-F_{\tau 2B} l_b^3}{12E_s I} \sin^2 \beta \quad (4.44)$$

Due to geometry,  $\delta_{Al2} = \delta_{Ar2}$  (same as/resulting in that  $M_{Al} = M_{Ar}$  and  $\delta_{Al1} = \delta_{Ar1}$ )

$$\frac{(F_{\tau 1Al} \cos \alpha + F_{\tau 2A} \sin \alpha) l_a^3}{12E_s I} \sin \alpha = \frac{(F_{\tau 1Ar} \cos \alpha - F_{\tau 2A} \sin \alpha) l_a^3}{12E_s I} \sin \alpha$$

$$F_{\tau 1Al} \cos \alpha + F_{\tau 2A} \sin \alpha = F_{\tau 1Ar} \cos \alpha - F_{\tau 2A} \sin \alpha$$

$$F_{\tau 1Ar} - F_{\tau 1Al} = 2F_{\tau 2A} \tan \alpha$$

Since  $F_{\tau 1} = F_{\tau 1Al} + F_{\tau 1Ar} \Rightarrow F_{\tau 1Al} = F_{\tau 1} - F_{\tau 1Ar}$

Then:

$$2F_{\tau 1Ar} - F_{\tau 1} = 2F_{\tau 2A} \tan \alpha$$

$$F_{\tau 1Ar} = \frac{F_{\tau 1}}{2} + F_{\tau 2A} \tan \alpha \quad (4.45)$$

and

$$F_{\tau 1Al} = \frac{F_{\tau 1}}{2} - F_{\tau 2A} \tan \alpha \quad (4.46)$$

For equilibrium,  $\Sigma M = 0$  about the node O

$$M_{Br} = -M_{Ar}$$

$$-\frac{F_{\tau 2B} l_b \sin \beta}{2} = -\frac{F_{\tau 1Ar} l_a \cos \alpha - F_{\tau 2A} l_a \sin \alpha}{2}$$

Since  $F_{\tau 2} = F_{\tau 2A} + F_{\tau 2B}$

$$(F_{\tau 2} - F_{\tau 2A}) l_b \sin \beta = F_{\tau 1Ar} l_a \cos \alpha - F_{\tau 2A} l_a \sin \alpha$$

$$F_{\tau 2A} l_a \sin \alpha - F_{\tau 2A} l_b \sin \beta = F_{\tau 1Ar} l_a \cos \alpha - F_{\tau 2} l_b \sin \beta$$

hence

$$F_{\tau 2A} = \frac{F_{\tau 1Ar} l_a \cos \alpha - F_{\tau 2} l_b \sin \beta}{l_b \sin \beta - l_a \sin \alpha} \quad (4.47)$$

Combining with the above expression for  $F_{\tau 1Ar}$  (see eq. 4.45)

$$F_{\tau 2A} l_a \sin \alpha - F_{\tau 2A} l_b \sin \beta = \left( \frac{F_{\tau 1}}{2} + F_{\tau 2A} \tan \alpha \right) l_a \cos \alpha - F_{\tau 2} l_b \sin \beta$$

$$F_{\tau 2A} l_b \sin \beta - F_{\tau 2A} l_a \sin \alpha + F_{\tau 2A} l_a \sin \alpha = F_{\tau 2} l_b \sin \beta - \frac{F_{\tau 1}}{2} l_a \cos \alpha$$

$$F_{\tau 2A} = F_{\tau 2} - \frac{F_{\tau 1} l_a \cos \alpha}{2 l_b \sin \beta} \quad (4.48)$$

Since  $F_{\tau 2} = F_{\tau 2A} + F_{\tau 2B}$

$$F_{\tau 2B} = \frac{F_{\tau 1} l_a \cos \alpha}{2 l_b \sin \beta} \quad (4.49)$$

Defining the shear deflection  $u_s$  (Figure 35) as

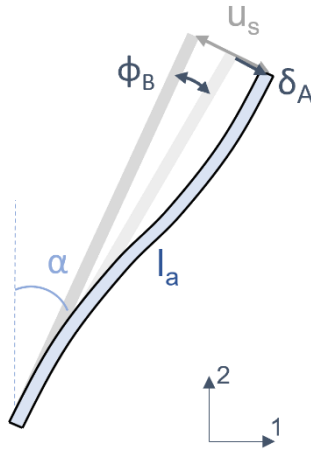


Figure 35: Shear deflection  $u_s$  as a combination of the deformation of the individual beams

$$u_s = \text{rotation at node } O \text{ from moment affecting beam } B \text{ and flexure of beam } A$$

$$= \varphi_B l_a + \delta_{AS} \quad (4.50)$$

$$\varphi_B = \frac{\delta_{BS}}{l_b} = \frac{F_{\tau 2B} \sin \beta l_b^2}{12 E_s I} \quad (4.51)$$

$$u_{s1} = \varphi_{B1} l_a + \delta_{AS1}$$

$$= 2 \frac{F_{\tau 2B} \sin^2 \beta l_b^2 l_a}{12 E_s I} + \frac{(F_{\tau 1Ar} \cos \alpha - F_{\tau 2A} \sin \alpha) l_a^3 \sin \alpha}{12 E_s I} + \frac{(F_{\tau 1Al} \cos \alpha + F_{\tau 2A} \sin \alpha) l_a^3 \sin \alpha}{12 E_s I} \quad (4.52)$$

$$u_{s2} = \varphi_{B2} l_a + \delta_{AS2} = \frac{F_{\tau 2B} \sin \beta \cos \beta l_b^2 l_a}{12 E_s I} + \frac{(F_{\tau 1Ar} \cos \alpha - F_{\tau 2A} \sin \alpha) \cos \alpha l_a^3}{12 E_s I} \quad (4.53)$$

#### 4.2.4 Calculating the elastic properties for pure flexure deformation

For expansion in 1-direction

$$\varepsilon_{1f} = \frac{\delta_{A1}}{X_1} = \frac{\delta_{B1}}{X_1} = \frac{F_{1A} l_a^3 \cos^2 \alpha}{12 E_s I l_a \sin \alpha} = \frac{F_{1A} l_a^2 \cos^2 \alpha}{12 E_s I \sin \alpha} \quad (4.54)$$

$$\varepsilon_{2f} = \frac{\delta_{A2} - \delta_{B2}}{X_2} = \frac{-F_{1A} l_a^3 \sin \alpha \cos \alpha + F_{1B} l_b^3 \sin \beta \cos \beta}{12 E_s I (l_a \cos \alpha - l_b \cos \beta)} \quad (4.55)$$

$$E_{1flexure} = \frac{\sigma_1}{\varepsilon_{1f}} = \frac{12 E_s I \sin \alpha l_a \left( \frac{1}{\cos^2 \alpha l_a^3} + \frac{1}{\cos^2 \beta l_b^3} \right)}{(l_a \cos \alpha - l_b \cos \beta) b} \quad (4.56)$$

$$\nu_{12flexure} = -\frac{\varepsilon_{2f}}{\varepsilon_{1f}} = \frac{\sin \alpha l_a (\tan \alpha - \tan \beta)}{l_a \cos \alpha - l_b \cos \beta} \quad (4.57)$$

For expansion in 2-direction

$$\varepsilon_{1f} = \frac{\delta_{C1}}{X_1} = \frac{\delta_{D1}}{X_1} = \frac{(R_{f1} \cos \alpha + F_2 \sin \alpha) l_a^3 \cos \alpha}{12 E_s I l_a \sin \alpha} = \frac{(R_f \cos \alpha + F_2 \sin \alpha) l_a^2 \cos \alpha}{12 E_s I \sin \alpha} \quad (4.58)$$

$$\varepsilon_{2f} = \frac{\delta_{C2} - \delta_{D2}}{X_2} = \frac{(R_{f1} \cos \alpha + F_2 \sin \alpha) l_a^3 \sin \alpha - (-F_2 \sin \beta - R_{f1} \cos \beta) l_b^3 \sin \beta}{12 E_s I (l_a \cos \alpha - l_b \cos \beta)} \quad (4.59)$$

$$E_{2flexure} = \frac{\sigma_2}{\varepsilon_{2f}} = \frac{12 E_s I (l_a \cos \alpha - l_b \cos \beta)}{b l_a \sin \alpha \left\{ l_a^3 \sin^2 \alpha + l_b^3 \sin^2 \beta - \frac{(\sin \alpha \cos \alpha l_a^3 + \sin \beta \cos \beta l_b^3)^2}{(\cos^2 \alpha l_a^3 + \cos^2 \beta l_b^3)} \right\}} \quad (4.60)$$

$$\nu_{21flexure} = -\frac{\varepsilon_{1f}}{\varepsilon_{2f}} = -\frac{\cot \alpha l_a^2 (l_a \cos \alpha - l_b \cos \beta) \left[ \frac{(\sin \alpha \cos \alpha l_a^3 + \sin \beta \cos \beta l_b^3)}{(\cos^2 \alpha l_a^3 + \cos^2 \beta l_b^3)} \cos \alpha - \sin \alpha \right]}{\left\{ l_a^3 \sin^2 \alpha + l_b^3 \sin^2 \beta - \frac{(\sin \alpha \cos \alpha l_a^3 + \sin \beta \cos \beta l_b^3)^2}{(\cos^2 \alpha l_a^3 + \cos^2 \beta l_b^3)} \right\}} \quad (4.61)$$

For shear

$$\gamma_{1f} = \frac{u_{s1}}{X_2} = \frac{2 F_{\tau 2B} \sin^2 \beta l_b^2 l_a + (F_{\tau 1Ar} \cos \alpha - F_{\tau 2A} \sin \alpha) l_a^3 \sin \alpha + (F_{\tau 1Al} \cos \alpha + F_{\tau 2A} \sin \alpha) l_a^3 \sin \alpha}{12 E_s I (l_a \cos \alpha - l_b \cos \beta)} \quad (4.62)$$

$$\gamma_{2f} = \frac{u_{s2}}{X_1} = \frac{F_{\tau 2B} \sin \beta \cos \beta l_b^2 l_a + (F_{\tau 1Ar} \cos \alpha - F_{\tau 2A} \sin \alpha) \cos \alpha l_a^3}{12 E_s I l_a \sin \alpha} \quad (4.63)$$

$$G_{12flexure} = \frac{\tau}{\gamma_f} = \frac{\tau_2 12E_s I}{\frac{2F_{\tau 2B} \sin^2 \beta l_b^2 l_a + (F_{\tau 1A} r \cos \alpha - F_{\tau 2A} \sin \alpha) l_a^3 \sin \alpha + (F_{\tau 1A} l \cos \alpha + F_{\tau 2A} \sin \alpha) l_a^3 \sin \alpha}{(l_a \cos \alpha - l_b \cos \beta)} + \frac{F_{\tau 2B} \sin \beta \cos \beta l_b^2 l_a + (F_{\tau 1A} r \cos \alpha - F_{\tau 2A} \sin \alpha) \cos}{l_a \sin \alpha}} \cdot \frac{12E_s I}{\frac{b 2 \sin \alpha \cos \alpha l_a^3 \left[ l_b \sin \beta + \left( 1 - 2 \frac{l_a \sin \alpha}{l_b \sin \beta} \right) l_a \sin \alpha \right]}{(l_a \cos \alpha - l_b \cos \beta)} + \frac{b l_a^3 \sin \alpha \cos \alpha [l_b \cos \beta + l_a]}{l_a \sin \alpha}} \quad (4.64)$$

4.2.5 Rewritten in the format  $l_a = L$  and  $l_b = L \frac{\sin \alpha}{\sin \beta}$

$$E_{1flexure} = \frac{12E_s I \left( \frac{1}{\cos^2 \alpha} + \frac{1}{\cos^2 \beta \frac{\sin^3 \alpha}{\sin^3 \beta}} \right)}{b L^3 (\cot \alpha - \cot \beta)} = \frac{12E_s I \left( \frac{1}{\cos^2 \alpha} + \frac{\sin^3 \beta}{\cos^2 \beta \sin^3 \alpha} \right)}{b L^3 (\cot \alpha - \cot \beta)} \quad (4.65)$$

$$\nu_{12flexure} = \frac{\sin \alpha (\tan \alpha - \tan \beta)}{(\cos \alpha - \cot \beta \sin \alpha)} = -\tan \alpha \tan \beta \quad (4.66)$$

$$E_{2flexure} = \frac{12E_s I (\cot \alpha - \cot \beta)}{b L^3 \sin^2 \alpha \left[ 1 + \frac{\sin \alpha}{\sin \beta} \frac{\left( \cos \alpha + \frac{\sin^2 \alpha}{\sin^2 \beta} \cos \beta \right)^2}{\left( \cos^2 \alpha + \frac{\sin^3 \alpha}{\sin^3 \beta} \cos^2 \beta \right)} \right]} = \frac{12E_s I (\cot^2 \alpha \frac{\sin \beta}{\sin \alpha} + \cot^2 \beta)}{b L^3 \sin^2 \alpha (\cot \alpha - \cot \beta)} \quad (4.67)$$

$$\nu_{21flexure} = - \frac{\cot \alpha (\cot \alpha - \cot \beta) \left[ \frac{\left( \cos \alpha + \frac{\sin^2 \alpha}{\sin^2 \beta} \cos \beta \right)}{\left( \cos^2 \alpha + \frac{\sin^3 \alpha}{\sin^3 \beta} \cos^2 \beta \right)} \cos \alpha - 1 \right]}{\left[ 1 + \frac{\sin \alpha}{\sin \beta} \frac{\left( \cos \alpha + \frac{\sin^2 \alpha}{\sin^2 \beta} \cos \beta \right)^2}{\left( \cos^2 \alpha + \frac{\sin^3 \alpha}{\sin^3 \beta} \cos^2 \beta \right)} \right]} = -\cot \alpha \cot \beta \quad (4.68)$$

$$G_{12flexure} = \frac{12E_s I}{b L^3 \cos \alpha \left[ \frac{\sin \alpha}{\sin \beta} \cos \beta + 1 \right]} \quad (4.69)$$

### 4.3 Stretching model

The idea to use a stretching model used is based on Master and Evans' [83] work on the re-entrant hexagonal structure:

#### 4.3.1 Shear

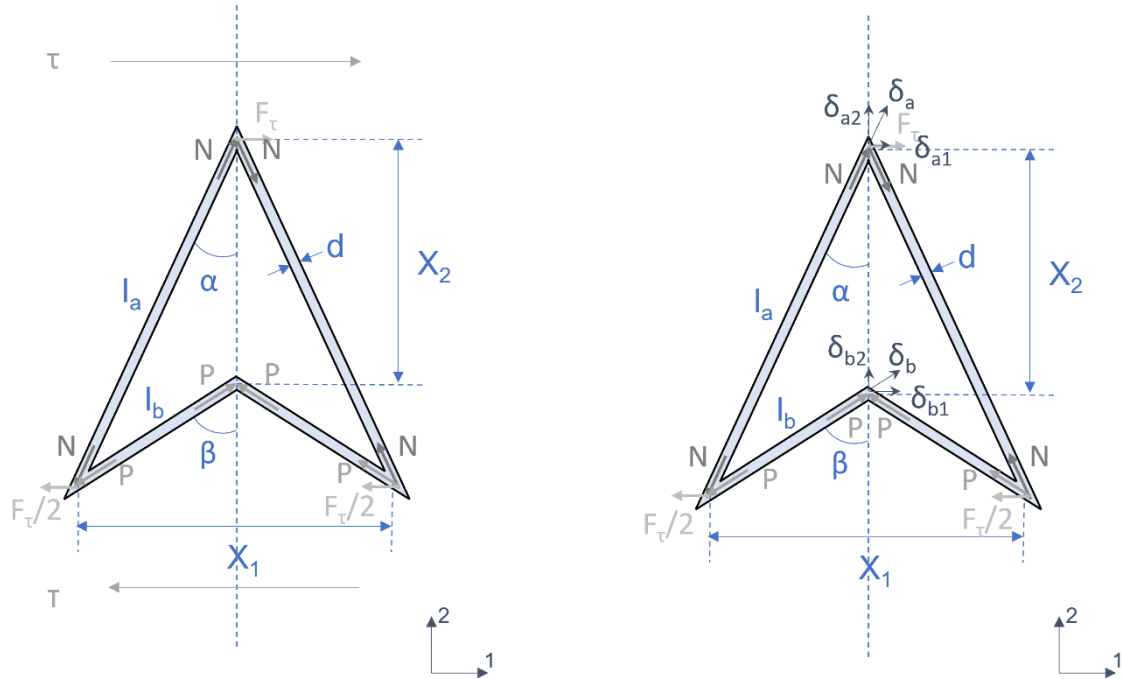


Figure 36: Shear stretching model of double arrowhead cell



To calculate the stretching response under shear loading, the angles were not constrained as in Masters and Evans due to the resulting infinite shear stress, instead the resultant force  $F$  of the two normal forces of the long beams  $N$  was used (Figure 36).

For the long beam  $l_a$

$$F_\tau = 2N \sin \alpha \rightarrow N = \frac{F_\tau}{2 \sin \alpha} \quad (4.70)$$

$$\sigma = \frac{N}{A} \text{ and } \varepsilon_a = \frac{\sigma}{E_s} \rightarrow \varepsilon_a = \frac{F_\tau}{2E_s A \sin \alpha} \quad (4.71)$$

$$\delta_a = \frac{\varepsilon_a l_a}{\sin \alpha} = \frac{F_\tau l_a}{2E_s A \sin^2 \alpha} \quad (4.72)$$

For the short beam  $l_b$

$$F_\tau = 2P \sin \beta \rightarrow P = \frac{F_\tau}{2 \sin \beta} \quad (4.73)$$

$$\sigma = \frac{P}{A} \text{ and } \varepsilon_b = \frac{\sigma}{E_s} \rightarrow \varepsilon_b = \frac{F_\tau}{2E_s A \sin \beta} \quad (4.74)$$

$$\delta_b = \frac{\varepsilon_b l_b}{\sin \beta} = \frac{F_\tau l_b}{2E_s A \sin^2 \beta} \quad (4.75)$$

Angular deformation

$$\gamma_s = \frac{\delta_a + \delta_b}{(l_a \cos \alpha - l_b \cos \beta)} = \frac{\frac{F_\tau l_a}{2E_s A \sin^2 \alpha} + \frac{F_\tau l_b}{2E_s A \sin^2 \beta}}{(l_a \cos \alpha - l_b \cos \beta)} = \frac{F_\tau \left( \frac{l_a}{\sin^2 \alpha} + \frac{l_b}{\sin^2 \beta} \right)}{2E_s A (l_a \cos \alpha - l_b \cos \beta)} \quad (4.76)$$

Shear stress

$$\tau = \frac{F_\tau}{2l_a \sin \alpha b} \quad (4.77)$$

Shear modulus

$$G_{12} = \frac{\tau}{\gamma_s} = \frac{\frac{F_\tau}{2l_a \sin \alpha b}}{\frac{F_\tau \left( \frac{l_a}{\sin^2 \alpha} + \frac{l_b}{\sin^2 \beta} \right)}{2E_s A (l_a \cos \alpha - l_b \cos \beta)}} = \frac{E_s A (l_a \cos \alpha - l_b \cos \beta)}{l_a \sin \alpha b \left( \frac{l_a}{\sin^2 \alpha} + \frac{l_b}{\sin^2 \beta} \right)} \quad (4.78)$$

4.3.2 Rewritten in the format  $l_a = L$  and  $l_b = L \frac{\sin \alpha}{\sin \beta}$

$$G_{12} = \frac{E_s A (\cot \alpha - \cot \beta)}{L b \left( \frac{1}{\sin^2 \alpha} + \frac{\sin \alpha}{\sin^3 \beta} \right)} \quad (4.79)$$

#### 4.4 Combining flexure and stretching to a complete shear model

$$\gamma_{1f} = \frac{u_{s1}}{X_2} = \frac{2F_{\tau 2B} \sin^2 \beta l_b^2 l_a + (F_{\tau 1Ar} \cos \alpha - F_{\tau 2A} \sin \alpha) l_a^3 \sin \alpha + (F_{\tau 1Al} \cos \alpha + F_{\tau 2A} \sin \alpha) l_a^3 \sin \alpha}{12E_s I (l_a \cos \alpha - l_b \cos \beta)} \quad (\text{see 4.62})$$

$$\gamma_{2f} = \frac{u_{s2}}{X_1} = \frac{F_{\tau 2B} \sin \beta \cos \beta l_b^2 l_a + (F_{\tau 1Ar} \cos \alpha - F_{\tau 2A} \sin \alpha) \cos \alpha l_a^3}{12E_s I l_a \sin \alpha} \quad (\text{see 4.63})$$

$$\gamma_s = \frac{\delta_a + \delta_b}{(l_a \cos \alpha - l_b \cos \beta)} = \frac{F_{\tau} \left( \frac{l_a}{\sin^2 \alpha} + \frac{l_b}{\sin^2 \beta} \right)}{2E_s A (l_a \cos \alpha - l_b \cos \beta)} \quad (\text{see 4.79})$$

$$\gamma^T = \gamma_{1f} + \gamma_{2f} + \gamma_s \quad (4.80)$$

$$G_{12} = \frac{\tau}{\gamma^T} = \frac{\tau}{\frac{2F_{\tau 2B} \sin^2 \beta l_b^2 l_a + (F_{\tau 1Ar} \cos \alpha l_a^3 \sin \alpha + F_{\tau 1Al} \cos \alpha l_a^3 \sin \alpha)}{12E_s I (l_a \cos \alpha - l_b \cos \beta)} + \frac{F_{\tau 2B} \sin \beta \cos \beta l_b^2 l_a + (F_{\tau 1Ar} \cos \alpha - F_{\tau 2A} \sin \alpha) \cos \alpha l_a^3}{12E_s I l_a \sin \alpha} + \frac{F_{\tau} \left( \frac{l_a}{\sin^2 \alpha} + \frac{l_b}{\sin^2 \beta} \right)}{2E_s A (l_a \cos \alpha - l_b \cos \beta)}} \quad (4.81)$$

##### 4.4.1 Rewritten in the format $l_a = L$ and $l_b = L \frac{\sin \alpha}{\sin \beta}$

$$G_{12} = \frac{\tau}{\gamma^T} = \frac{E_s}{\frac{bL^3 \cos \alpha \left( \frac{\sin \alpha}{\sin \beta} \cos \beta + 1 \right)}{12I} + \frac{bL}{A(\cot \alpha - \cot \beta)} \left( \frac{1}{\sin^2 \alpha} + \frac{\sin \alpha}{\sin^3 \beta} \right)} \quad (4.82)$$

#### 4.5 Conclusion

The double arrowhead configuration is highly anisotropic in most cases, but there are a few combinations of geometric parameters that can create an on-axis isotropic behaviour for small strains. The analytical models only take small strains into account. Up to which point the current model is accurate and beyond what point a large strain model would be necessary, needs to be investigated further.

Resulting equations above provides the equivalent level of information for the double arrowhead as can be found in the literature for the other structures that will be investigated, but the equations for all three will need to be converted into tubular structures.

## 5. Analytical Method

### 5.1 Re-entrant Hexagonal: Selection of analytical model, conversion to tubes

For the re-entrant hexagonal honeycomb, the model created by Gibson & Ashby in *Cellular solids- Structure and properties* [69], [144] has been widely used for several studies, where the configuration was investigated using beam theory, with flexure as the principal form of deformation. As discussed in the literature review, this leads to a problem with extreme angles. Masters & Evans[83] expanded on this, incorporating stretching and hinging as additional modes of deformation. They however concluded that in most cases, flexure is the largest contributor to deformation, followed by stretching and then hinging, allowing for the use of only the Gibson & Ashby flexure model when not approaching the extreme angles [83]. Other methods have been explored in the literature, like micropolar homogenization as seen in Table 1, but for this study a combination of the approaches by Gibson & Ashby and Masters & Evans were used as a foundation for the rewritten equations adapted for tubular instead of plane structures. Tubular structures have been investigated in a similar way before for the re-entrant hexagonal honeycomb, by Karnessi & Burriesci [49], but were included in the scope of this study due to a slightly different approach to the numerical investigation. Both Gibson & Ashby and Masters & Evans use a beam with a moment of inertia for rectangular cross-sections  $I = bt^3/12$  to calculate the equations for the elastic deformation of hexagonal honeycombs. Since in this case a circular cross-section is used in the numerical models, this has been replaced with the moment of inertia of  $I = \pi d^4/64$  for the following re-adaptations of the equations.

The Gibson & Ashby model was chosen as a framework to calculate the parameters for the axial elongation of the structure, the  $E_z$  and the  $\nu_{zc}$ , as well as the shear modulus,  $G_{cz}$ , of the model. For the parameters stemming from the circumferential expansion of the structure, the Young's modulus  $E_c$  and the Poisson's ratio  $\nu_{cz}$ , the model by Masters & Evans was used as the angles would most likely approach the extreme cases where the Gibson & Ashby model have been proven to be less reliable.

Starting with relating the unit cell dimensions to the dimensions for the tubular structure, with

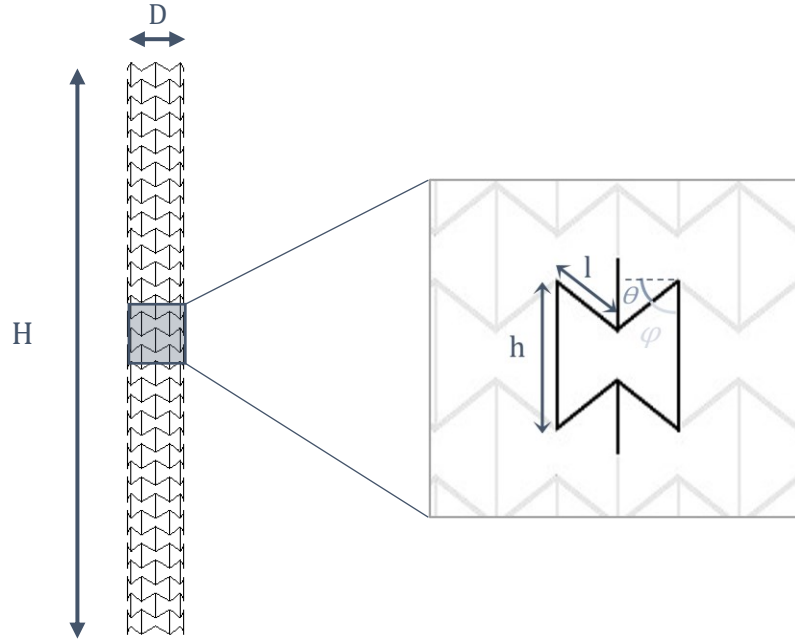


Figure 37: Schematic of geometric parameters for the re-entrant hexagonal unit cell and the tube used in the equations below, where  $\theta = 90 - \varphi$

$D$  being the tube diameter and  $N_c$  the number of unit cells making up the tubular structure in the circumferential direction, for the orientation of the unit cell with regards to the tube as pictured in Figure 37.

$$l = \frac{\pi D}{2N_c \cos \theta} \quad (5.1) \text{ from [49]}$$

The relative density,  $\rho/\rho_s$  where  $\rho_s$  is the density of the solid, of the re-entrant hexagonal honeycomb, is calculated by

$$\frac{\rho}{\rho_s} = \frac{\frac{t(h+2)}{l}}{2 \cos \theta \left( \frac{h}{l} - \sin \theta \right)} \quad (5.2)$$

where  $t$  is the in-plane thickness of the rib.

For the case of linear elastic deformation from uniaxial loading, the equations for the Poisson's ratios for the tube are:

$$\nu_{cz} = -\frac{\varepsilon_z}{\varepsilon_c} = -\frac{\sin \theta}{\left( \frac{h}{l} - \sin \theta \right)} \times \frac{(\pi D)^2 - 3(dN_c \cos \theta)^2}{(\pi D \tan \theta)^2 + 3(dN_c \cos \theta)^2} \quad (5.3) \text{ from [49]}$$

and

$$\nu_{zc} = -\frac{\varepsilon_c}{\varepsilon_z} = -\frac{\left( \frac{h}{l} - \sin \theta \right) \tan \theta}{\cos \theta} \quad (5.4) \text{ from [49]}$$

The Young's modulus for the two directions in-plane:

$$\frac{E_c}{E_s} = \frac{\sigma_c}{\varepsilon_c} = \frac{3(dN_c)^3 \cos^2 \theta}{2D \left( \frac{h}{l} - \sin \theta \right) ((\pi D \tan \theta)^2 + 3(dN_c \cos \theta)^2)} \quad (5.5) [49]$$

and

$$\frac{E_z}{E_s} = \frac{\sigma_z}{\varepsilon_z} = \frac{12 I \left( \frac{h}{l} - \sin \theta \right)}{d l^3 \cos^3 \theta} = \frac{3 \left( \frac{h}{l} - \sin \theta \right)}{2\pi^2} \left( \frac{d N_c}{D} \right)^3 \quad (5.6) [49]$$

The equations for shear:

$$\frac{G_{cz}}{E_s} = \frac{\tau}{\gamma} = \frac{12 I \left( \frac{h}{l} - \sin \theta \right)}{d h^2 (l + 2h) \cos \theta} = \frac{3 \left( \frac{h}{l} - \sin \theta \right) \cos^2 \theta}{2\pi^2 \left( \frac{h}{l} \right)^2 \left( 1 + 2 \frac{h}{l} \right)} \left( \frac{d N_c}{D} \right)^3 \quad (5.7) [49]$$

## 5.2 Double arrowhead: Development of analytical model, conversion to tubes

For the double-arrowhead honeycomb, very few studies were found in literature that focused solely on this. One study focused solely on the double-arrowhead, or double arrow as they denote it, was done by Brighenti et al [98] where the analytical derivation start from a kinematic analysis and then adopts a statically indeterminate structural scheme which accounts for the deformation of the unit cell. A few used homogenizations along with investigating other configurations like Berinskii [90]. However, for consistency with the re-entrant hexagonal honeycomb, as both structures auxeticity stems from the same deformation mechanisms of the unfolding of re-entrant cells, for this study it was chosen to specifically derive new equations for the double-arrowhead unit cell by using a similar approach to the one chosen by Gibson & Ashby and Masters & Evans [68], [83]. As this approach has not been used in the previous literature for the double-arrowhead, the guidance of the above models was not always applicable. Still, they provided a good framework. As they are usually the standard analytical solution used in literature for the REH, this comparable framework for the DAH structure might be useful for creating a similar standard option for the double-arrowhead structure.

All derivations of the equations below for the double arrowhead cell can be found above in chapter 4. The geometric parameters used to derive the equations for the cell can be seen in Figure 38.

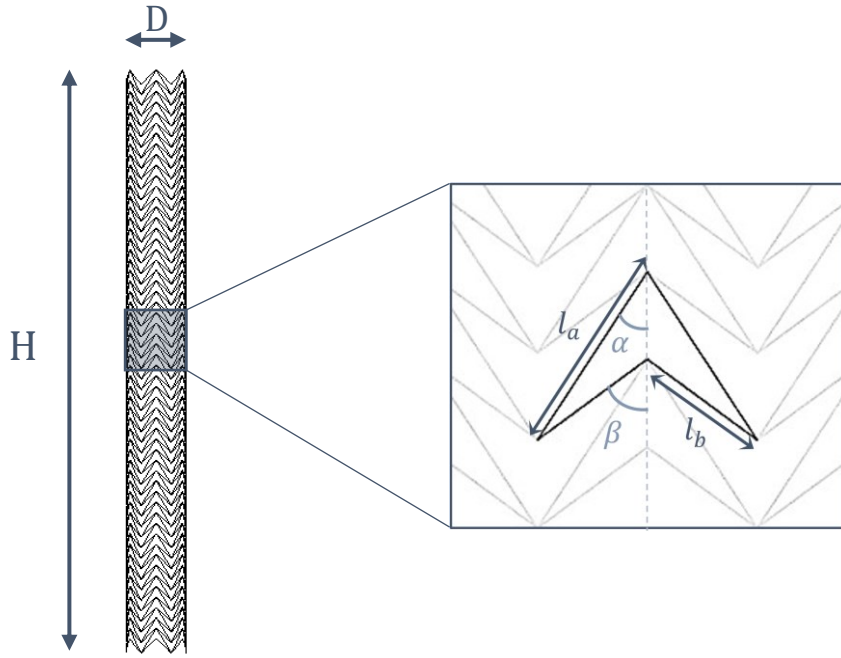


Figure 38: Schematic of geometric parameters for the double arrowhead unit cell and the tube used in the equations below

Again, starting with relating the cell dimensions to the dimensions for the tubular structure, with  $D$  being the tube diameter and  $N_c$  the number of cells making up the tubular structure in the circumferential direction, for the orientation of the cell with regards to the tube as pictured in Figure 38.

$$l_a = \frac{\pi D}{2N_c \sin \alpha} \quad (5.8)$$

For the relative density of the structure

$$\frac{\rho}{\rho_s} = \frac{t(l_a + l_b)}{2l_a \sin \alpha (l_a \cos \alpha - l_b \cos \beta)} \quad (5.9)$$

For the Poisson's ratio, this equals eq. 4.66 and 4.68

$$\nu_{cz} = -\frac{\varepsilon_z^T}{\varepsilon_c^T} = -\tan \alpha \tan \beta \quad (5.10)$$

and

$$\nu_{zc} = -\frac{\varepsilon_c^T}{\varepsilon_z^T} = -\cot \alpha \cot \beta \quad (5.11)$$

For the Young's modulus this is derived from eq. 4.67 and 4.69

$$\frac{E_c}{E_s} = \frac{\sigma_c}{\varepsilon_c^T} = \frac{12I \left( \frac{1}{\cos^2 \alpha} + \frac{\sin^3 \beta}{\cos^2 \beta \sin^3 \alpha} \right)}{b \left( \frac{\pi D}{2N_c \sin \alpha} \right)^3 (\cot \alpha - \cot \beta)} \quad (5.12)$$

and

$$\frac{E_z}{E_s} = \frac{\sigma_z}{\varepsilon_z^T} = \frac{12I(\cot^2 \alpha \frac{\sin \beta}{\sin \alpha} + \cot^2 \beta)}{b \left( \frac{\pi D}{2N_c \sin \alpha} \right)^3 \sin^2 \alpha (\cot \alpha - \cot \beta)} \quad (5.13)$$

For the Shear Modulus, the pure stretching equation is derived from 4.78

$$\frac{G_{cz}}{E_s} = \frac{\tau}{\gamma^T} = \frac{A(\cot \alpha - \cot \beta)}{\left( \frac{\pi D}{2N_c \sin \alpha} \right) b \left( \frac{1}{\sin^2 \alpha} + \frac{\sin \alpha}{\sin^3 \beta} \right)} \quad (5.14)$$

### 5.3 Hexachiral: Selection of analytical model, conversion to tubes

For the hexachiral configuration, Figure 39, Prall & Lakes [103] used a similar approach of beam bending and energy to derive the equations for the elastic properties of the hexachiral structure as the Gibson & Ashby model for the re-entrant hexagonal honeycomb. However, since it was concluded that the hexachiral configuration exhibits a constant Poisson's ratio of -1, it becomes difficult to look at the shear modulus of the structure since the isotropic nature of the hexachiral configuration a Poisson's ratio of -1 gives an infinite shear modulus. This is also stated by Spadoni & Ruzzene [106], who instead developed a method using micropolar homogenization. A similar model was developed by Bacigalupo & Gambarotta [109], but this time adding effective beam length as a factor. Since they do not include a model for calculating the effective beam length, Spadoni & Ruzzene's model was used here as a basis

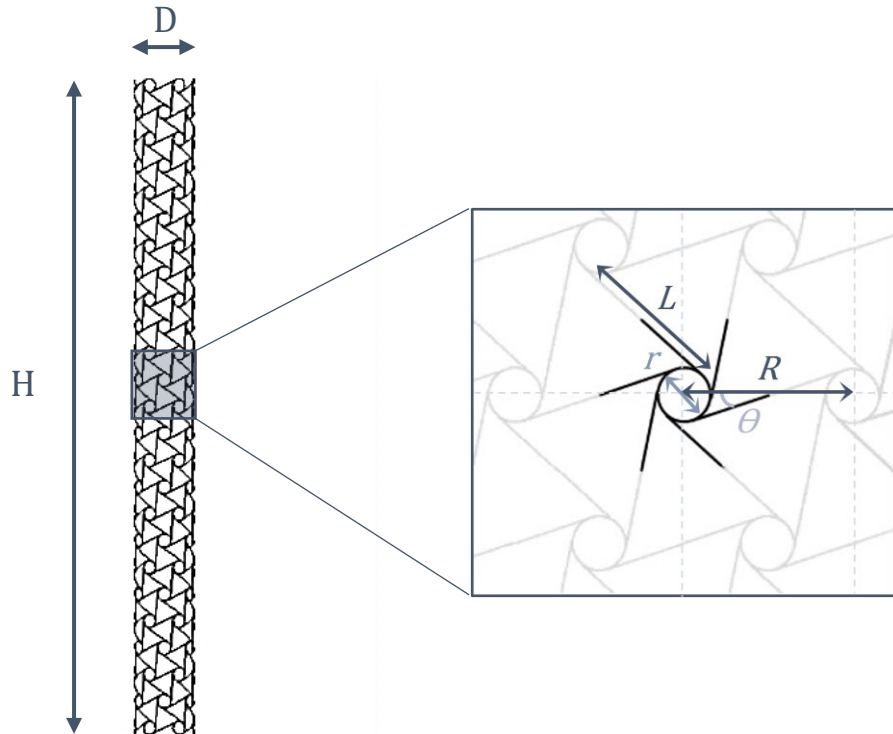


Figure 39: Schematic of the geometric parameters of the hexachiral configuration in relation to the tube. Node distance  $R$ , node radius  $r$ , ligament length  $L$ , ligament thickness  $t$  and angle of chirality  $\beta$ .

for the equations for the analytical analysis of tubular structures constructed of hexachiral honeycombs, with the geometric parameters marked in Figure 39.

The angle for the ligament spacing,  $\theta$ , is for regular hexachiral cells always 60 degrees. The node distance  $R$ , the node radius  $r$ , the angle of chirality  $\beta$  and the ligament length  $L$  are geometrically interdependent, where

$$\sin \beta = \frac{2r}{R} \quad (5.15)$$

and

$$\cos \beta = \frac{L}{R} \quad (5.16)$$

Then relating the unit cell dimensions to the dimensions for the tubular structure, with  $D$  being the tube diameter and  $N_c$  the number of unit cells making up the tubular structure in the circumferential direction, for the orientation of the unit cell with regards to the tube as pictured in Figure 39.

$$R = \frac{\pi D}{N_c} \rightarrow L = \frac{\pi D \cos \beta}{N_c} \quad (5.17)$$

The relative density,  $\rho/\rho_s$  where  $\rho_s$  is the density of the solid, of the hexachiral honeycomb structure according to Spadoni & Ruzzene [106], is calculated as

$$\frac{\rho}{\rho_s} = \frac{t(4\pi r + 6L)}{(4\pi r^2 + 3L^2 \sin \beta)} \quad (5.18)$$

Since the hexachiral structure is theoretically isotropic, only one Young's modulus and one Poisson's ratio is needed. The elastic constants are then, re-adapted from the model by Spadoni & Ruzzene [106] to that of this tubular model, as following with the Poisson's ratio calculated by

$$\nu = \frac{4\left(\frac{t}{D} \frac{N_c}{\pi \cos \beta}\right)^2}{\left(\frac{t}{D} \frac{N_c}{\pi}\right)^4 \frac{1}{\cos^2 \beta} + 1 - \cos^2 \beta + 3\left(\frac{t}{D} \frac{N_c}{\pi \cos \beta}\right)^2} - 1 \quad (5.19)$$

the Young's modulus

$$E^* = \frac{E}{E_s} = \frac{2\sqrt{3}\left[1 + \left(\frac{t}{D} \frac{N_c}{\pi \cos \beta}\right)^2\right]}{\left[\left(\frac{t}{D} \frac{N_c}{\pi}\right)^4 \frac{1}{\cos^2 \beta} + 1 - \cos^2 \beta + 3\left(\frac{t}{D} \frac{N_c}{\pi \cos \beta}\right)^2\right]} \left(\frac{t}{D} \frac{N_c}{\pi \cos \beta}\right)^3 \quad (5.20)$$

and for the shear modulus

$$G^* = \frac{G}{E_s} = \frac{\sqrt{3}}{4} \left[ \left(\frac{t}{D} \frac{N_c}{\pi \cos \beta}\right) + \left(\frac{t}{D} \frac{N_c}{\pi \cos \beta}\right)^3 \right] \quad (5.21)$$



It is important to note that Spadoni & Ruzzene [106] clearly states that the analytical micropolar continuum model is using the assumption of rigid nodes, and that for numerical modelling of cases with deformable nodes the result differs. As they state that any analytical model fully taking into account the deformability of the nodes would be too complex, a simpler model is the best currently available, however they do provide graphs of the results from the second numerical-based deformable node-model as a mean of comparison. This also highlights the importance of using numerical validation for these kinds of complex structures.

## 6. Numerical Method

### 6.1 Nominal tubes – For comparison between analytical and numerical

To compare numerical and analytical results, the same method as the one described by Karnesis and Burriesci [49] was used. For each of the numerical models, nominal elastic properties were calculated.

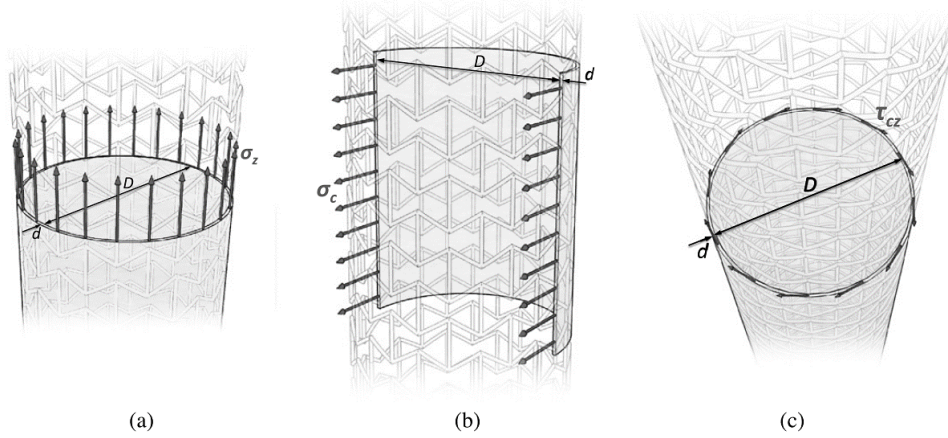


Figure 40: Schematic of nominal tube under (a) longitudinal nominal stress, (b) circumferential nominal stress and (c) under nominal shear stress. [49]

The nominal moduli for the structure were calculated using a nominal tube defined as having a diameter  $D$  equal to the diameter of the tubular structure, wall thickness  $d$  equal to the diameter of the struts, and length  $H$  equal to the axial length of the auxetic structure, as seen in Figure 40.

The nominal longitudinal stress  $\sigma_z$  is the ratio between the resulting axial load on the tube and the resisting nominal cross section calculated  $D * \pi * d$  (Figure 40 (a)), the nominal circumferential stress  $\sigma_c$  is the ratio between the resulting hoop load on the tube and the resisting nominal cross section calculated  $2 * H * d$  (Figure 40 (b)), and the nominal shear stress  $\tau_{cz}$  is the ratio between the resulting axial torque on the tube and the resisting nominal cross section calculated  $D * \pi * d$  (Figure 40 (c)) [49].

To analytically calculate the nominal diameter of the tube  $D$  and the nominal length of the tube  $H$ , simple approximate equations can be derived for each shape from the geometry of the unit cell and their orientation along the nominal tube, represented by a hollow cylinder.

$$D = \frac{N_c l_c}{\pi} \quad (6.1) \quad H = N_z l_z \quad (6.2)$$

Where  $N_c$  is the number of cells in the circumferential direction,  $l_c$  is the cell length in the direction enveloped circumferentially around the tube,  $N_z$  is the number of cells along the length of the tube and  $l_z$  is the cell length in the direction along the length of the tube.

Applying this for each of the different cell geometries:

For the re-entrant hexagonal honeycomb

$$D = \frac{N_c 2 l \cos \theta}{\pi} \quad (6.3)$$

$$H = N_z (h - l \sin \theta) \quad (6.4)$$

For the double arrowhead configuration

$$D = \frac{N_c 2 l_a \sin \alpha}{\pi} = \frac{N_c 2 L \sin \alpha}{\pi} \quad (6.5)$$

$$H = N_z (l_a \cos \alpha - l_b \cos \beta) = N_z L \left( \cos \alpha - \frac{\sin \alpha}{\sin \beta} \cos \beta \right) = N_z L (\cot \alpha - \cot \beta) \sin \alpha \quad (6.6)$$

For the hexachiral configuration

$$D = \frac{N_c * R}{\pi} \quad (6.7)$$

$$H = N_z * R * \sin \theta \quad (6.8)$$

The nominal longitudinal strain  $\varepsilon_z$ , the nominal circumferential strain  $\varepsilon_c$  and the nominal shear strain  $\gamma_{cz}$  are then defined as

$$\varepsilon_c = \frac{\pi D^* - \pi D}{\pi D} = \frac{D^* - D}{D} \quad (6.9)$$

$$\varepsilon_z = \frac{H^* - H}{H} \quad (6.10)$$

$$\gamma_{cz} = \frac{D\varphi}{2H} \quad (6.11)$$

where  $\varphi$  is the relative angular rotation occurring between the cross-sections at the two ends of the tube,  $D^*$  is the expanded diameter of the tubular structure and  $H^*$  is the elongated length of the tubular structure.

The nominal Poisson's ratio  $\nu_{cz}$  is defined as the longitudinal expansion or contraction of the tube in response to a circumferential load; whilst the nominal Poisson's ratio  $\nu_{zc}$  is defined as the circumferential expansion or contraction of the tube in response to a load along the longitudinal axis. The nominal Young's Modulus  $E_c$  is defined as the ratio between the nominal circumferential stress  $\sigma_c$  and the corresponding circumferential strain  $\varepsilon_c$ ; the

nominal Young's Modulus  $E_z$  is defined as the ratio between the nominal longitudinal stress  $\sigma_z$  and the corresponding longitudinal strain  $\varepsilon_z$ ; and the nominal shear Modulus  $G_{cz}$  of the tube is defined as the ratio between the nominal shear stress  $\tau_{cz}$  and the nominal shear strain  $\gamma_{cz}$ , resulting in:

$$\nu_{cz} = -\frac{\varepsilon_z}{\varepsilon_c} = \frac{(H^*-H)D}{H(D^*-D)} \quad (6.12)$$

$$\nu_{zc} = -\frac{\varepsilon_c}{\varepsilon_z} = \frac{H(D^*-D)}{(H^*-H)D} \quad (6.13)$$

$$E_c = \frac{\sigma_c}{\varepsilon_c} = \frac{\sigma_c D}{(D^*-D)} \quad (6.14)$$

$$E_z = \frac{\sigma_z}{\varepsilon_z} = \frac{\sigma_z H}{(H^*-H)} \quad (6.15)$$

$$G_{cz} = \frac{\tau_{cz}}{\gamma_{cz}} = \frac{\tau_{cz} 2H}{D\phi} \quad (6.16)$$

### Reference configurations

For each of the three different unit cells used, models were built to study the effect of varying each geometric variable. To compare with Karnesis & Burriesci [49], the same number of unit cells in the circumferential direction ( $N_c$ ) was used as default, and the same range was used to study the effect of varying the number of cells in the circumferential direction.

Table 9: Geometric parameters used for re-entrant hexagonal honeycombs

<i>REH</i>	<i>Values of parameters</i>	<i>Default parameter</i>
$N_c$	4, 6, 8, 10, 12	12
$\theta$	10°, 20°, 30°, 40°	30°
$h/l$	1.25, 1.5, 1.75, 2	1.5

Table 10: Geometric parameters used for the double arrowhead configuration

<i>DAH</i>	<i>Values of parameters</i>	<i>Default parameter</i>
$N_c$	4, 6, 8, 10, 12	12
$\alpha$	10°, 20°, 30°, 40°	30°
$\beta/\alpha$	1.25, 1.5, 1.75, 2	1.5

Table 11: Geometric parameters used for the hexachiral configuration

<i>HC</i>	<i>Values of parameters</i>	<i>Default parameter</i>
$N_c$	4, 6, 8, 10, 12	12
$L/R$	0.7, 0.8, 0.9, 0.95	0.9

This creates in total  $35 \times 3$  different geometrical configurations for each of the three modes of deformation considered. To be able to compare the different auxetic structures, the ranges of the geometric parameters were kept as consistent as possible across the different structures. For each structure, there were geometric constraints of the possible range that needed to be considered. For the REH the angle  $\theta$  has to be smaller than  $\arcsin(2h/l)$  to avoid co-penetration of the structure and larger than 0 to keep a negative Poisson's ratio, for the DAH the angle  $\beta$  has to be larger than the angle  $\alpha$  for the smaller 'arrow' to fit within the larger 'arrow' and  $\beta$  has to be smaller than 90 degrees, and for the HC the level of chirality  $L/R$  has to be smaller than 1 ( $L/R=1$  is a equilateral triangle) and larger than 0 ( $L/R=0$  is a lattice consisting of directly connected circles), where the most interesting configurations for stents undergoing larger deformations is above  $L/R = 0.7$ , to keep the main form of deformation to flexure of the struts and rotation of the unit cells.

For the number of cells in the circumferential direction,  $N_c$ , the decision was taken to investigate even numbered structures to reduce the number of models, with a minimum of be 4 cells (2 would be too low to be considered a cellular structure and would have extreme cell curvatures). The maximum number of cells in the circumferential direction was chosen to be 12, as more would create a too high relative density in a more realistic setting with a larger  $d/D$ . This results in a relative fine cell density in the circumferential direction, facilitating the comparison to the analytical flat two-dimensional models due to the lower curvature of the individual cell, where examples like Karnesis and Burriesci show that this produces results close to the analytically predicted behaviours that have been verified for the REH both numerically and experimentally for flat planes.

The length of the tubes was chosen as  $H = 10D$ , resulting in a different number of units in the longitudinal direction  $N_z$  depending on cell size for each individual configuration. As periodic boundary conditions were used, this parameter has negligible significance in the present study. In fact, when doing convergence testing the difference in Young's modulus between  $H = 5D$  and  $H = 15D$  is about 0.08% for the REH circumferential expansion, while it is slightly larger but in this case still negligible of 0.6% for Poisson's ratio and 0.7% for Young's Modulus for  $H = 10D$  and  $H = 15D$  for longitudinal expansion. This convergence testing indicates that a shorter tube could be used, however due to the large differences in number of cells in the longitudinal direction with the fewest being 15 and the most being 179 (due to the differences in unit cell size, dependent on factors like number of cells in the circumferential direction), it was decided to keep the tube a bit longer to negate any effect of that difference.

For the diameter  $d$ , there was the choice to make, as this a non-dimensional parameter relating to the individual strut length (like  $d/l$  for the REH for example). This is a common issue in most studies in the literature. As the goal of the project is to facilitate the comparison between the three different types of structures with the aim of find a practicable application, the decision was taken to use the same range of  $d$  for all structures. Hence the non-dimensional parameter chosen for investigating the effect of increasing the strut diameter was  $d/D$ . This still allows for analysis of the non-dimensional equivalents for each structure, while keeping the relationship between the diameter of the strut and the diameter of the tube consistent for all three types of structures. This also better reflects the constraints in practical applications. A maximum parameter  $d/D = 0.02$  was chosen to attempt to maintain the ratios of  $d/l$  within a range where the assumptions in the equations are acceptable, guaranteeing at the same time dimensions consistent with realistic stent designs. This results into values in the range of 0.025-0.1 for  $d/l_a$  for DAH, 0.04-0.15 for  $d/l$  for REH and 0.028-0.15 for  $d/L$  for HC. For an aortic stent of  $D = 26$  mm,  $d = 0.52$  mm, which is a reasonable value and would likely be at the thicker strut end. The models were also investigated for a  $d/D = 0.01$  and  $d/D = 0.005$ . The latter is too thin to be realistic for most practical applications but is intended for the purpose to identify a trend towards the idealised analytical predictions with a more theoretically reasonable maximum  $d/L = 0.035$ . The standard configurations can be seen in Figure 41.

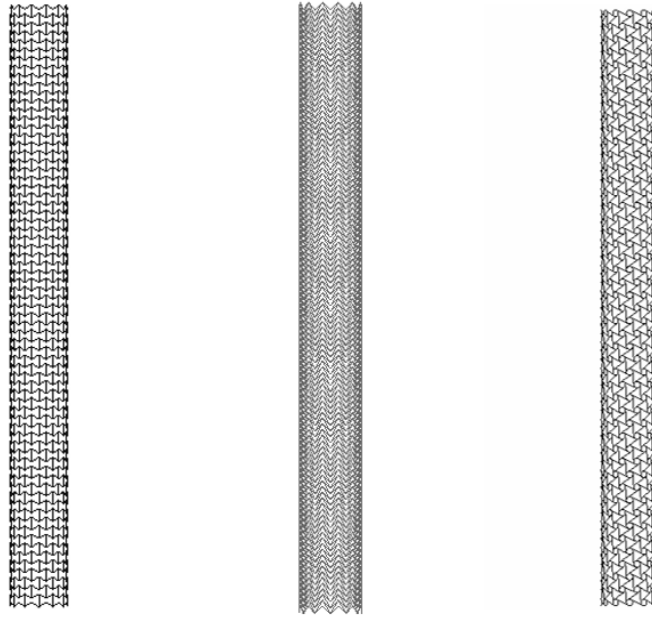


Figure 41: The standard configuration tube for a) REH b) DAH and c) HC

## 6.2 Finite Element Analysis: Details

### 6.2.1 Beam models, Beam types, Analysis type etc

For each configuration, two CAD models were created in CATIA v5 (Dassault Systèmes SE, Vélizy-Villacoublay, France) as beam models; one full-tube and one half-tube, except for the hexachiral configurations where only the full-tube versions were created, for the standard configurations see Figure 41. The models were then imported into, processed, and analysed with MSC Marc/Mentat (MSC Software Corporation, Newport, CA, U.S.A./Hexagon AB, Stockholm, Sweden), a non-linear implicit finite element software.

To perform the finite element analysis, the complex full models were subdivided into smaller components with simpler geometries, the finite elements which are used to perform the mathematical analysis on, by meshing the structure. The line mesh was chosen as 12 beam elements per strut for the maximum number of beams in the circumferential direction for the REH and DAH cases, as this is used in several of the sources. In the convergence analysis, the force variation between models using 10 and 12 elements per beam was only 0.3% and reduced to 0.2% when comparing models using 12 and 14 elements per beams. Further refinement of the mesh would also significantly slow down the computing time. For the hexachiral case an equivalent arrangement was made taking into account the beam length that the nodes contributed with in the circumferential direction. Hence for a case of  $N_c = 12$ , with two beams for each cell in the circumferential direction divided into 12 elements, there would be a total number of 288 elements in the circumferential direction. For the equivalent case of  $N_c = 4$ , the beams would be divided into 36 elements each to achieve the same number of elements in the circumferential direction.

The geometric properties were set as a solid section beam, beam element 98, which is an elastic straight beam element which incorporates transversal shear. Linear interpolation was used for displacements and rotations [145].

The material properties were chosen as linear elastic, similarly to the analytical study, with a Young's modulus equivalent to steel (210 GPa). The latter is of irrelevant to our study as it is normalised when comparing to the analytical study. The Poisson's ratio was chosen to be 0.3 as this is similar to that of engineering metals suitable and commonly used for stents, like stainless steel, chromium-cobalt and nitinol [146], [147]. However, this may have some impact on accuracy of the models as influences the deformation of the beams [148], and in turn might make the deformation of the beam a larger contributor than the deformation of the auxetic unit cell to the deformation of the structure as a whole.

### 6.3 Modes of deformation and associated boundary conditions

The pre-requisites of the boundary conditions vary greatly between each configuration due to different degrees of symmetry and anti-symmetry, see Figure 42. The re-entrant hexagonal honeycomb is symmetric in two directions, the double arrowhead in one direction and anti-symmetrical in the other. The hexachiral configuration have a rotational symmetry, however it is harder to define in two directions. One direction can be defined as anti-symmetrical, while the other one direction is treated as non-symmetry due to the rotational element of the deformation, even though it may be anti-symmetry from an image point of view. The boundary conditions also vary according to the different types of loading, resulting in different combinations for each structure and loading.

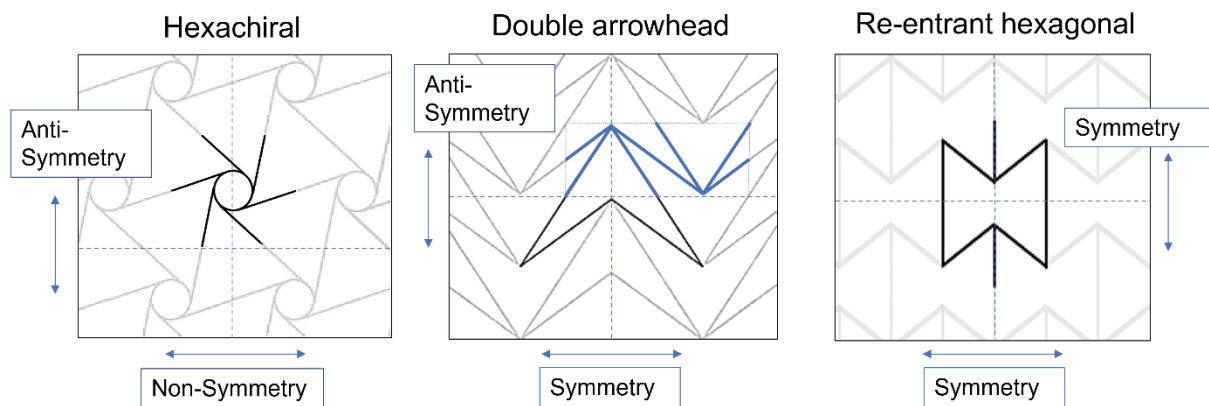


Figure 42: Symmetry evaluation of the different configurations, from the left: hexachiral, double arrowhead and re-entrant hexagonal honeycombs.

In cases where symmetry planes could be used, they were used in the axial direction along the tube, taking advantage of the symmetry of the double arrowhead and re-entrant hexagonal in that direction, allowing for reducing the analysis to half of a tube. For the hexachiral configuration, a full tube was used in all cases as that direction is non-



symmetrical. For unifying the boundary conditions of the open end of the tubes, and to reduce the dependency of tube length which is important as the number of cells in the axial direction varies greatly between the different geometrical combinations, periodic, or matching, boundaries were used when possible. These matching boundaries, see Figure 43, work by creating ties between the nodes at the top and bottom of the tubes, for which a set number of degrees of freedoms were linked, forcing the nodes at the bottom and top to behave in a similar way, for example by aligning the rotation or displacement in certain directions depending on type of loading.

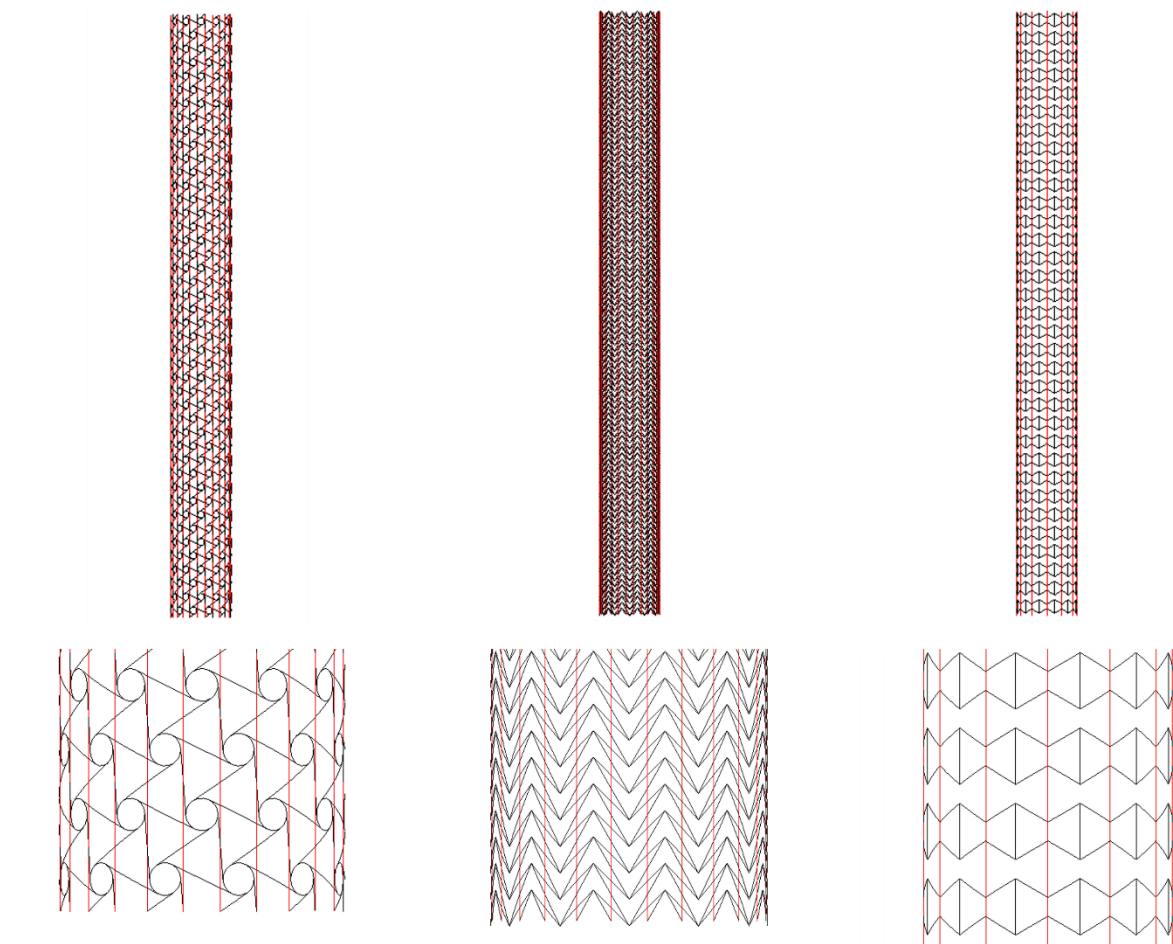


Figure 43: Matching boundary links: The red lines mark the connection between the node on the bottom and top of the tube. The pictures below are of the bottom ends of the tubes.

### 6.3.1 Circumferential expansion

The first mode of deformation selected for the tube investigation was circumferential expansion. A radial displacement was imposed on the structure of the nominal tube, which results into a circumferential stretching of the structure, see Figure 44.

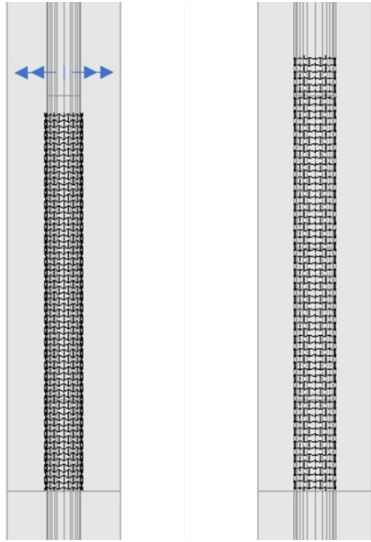


Figure 44: The circumferential expansion of an inner tubular surface expands the auxetic structure. For those cases where possible, a symmetry plane is added (see rectangle behind).

For the REH and DAH models, a longitudinal symmetry plane was placed along the axis of the tube to replicate a full tube, and a full cylinder was expanded inside, by setting a 'growth factor'. The reaction forces were then extracted from the longitudinal planes to calculate the nominal Young's modulus of the stents.

For the HC models, the circumferential models were all created as full-tube versions as there is only one way to cut the hexachiral structure and achieve anti-symmetry, and no way to cut it to achieve symmetry, as shown in Figure 42.

A tube sector of 60 degrees was analysed for the estimation of the hoop nominal Young's modulus,

as for this portion the hoop force is identical to the resultant of the radial forces acting on the model, simplifying calculations.

For the edges of the tube, to avoid a dependency on the tube length, the degrees of freedom except axial displacement were connected between the corresponding nodes at each end of the tube: Displacement in the circumferential direction, since in a cartesian coordinate system, consisted of two degrees of freedom, and all three rotational degrees of freedom. Therefore the stresses along the tube were uniform along the whole length of the tube.

The internal cylinder expanded the tube from a diameter of 20 mm to a diameter of 22 mm, hence an increase in diameter of 10 %.

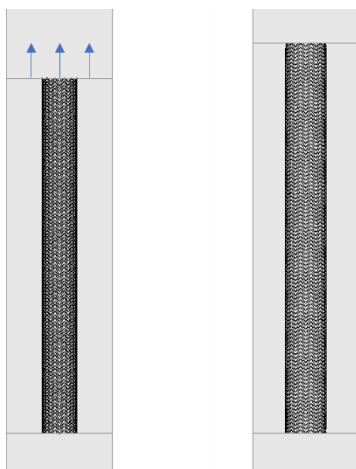


Figure 45: Longitudinal expansion of the tubular structure with the aid of a moving plane (moving line on top).

### 6.3.2 Longitudinal expansion

The longitudinal expansion of the models was carried out by the imposing a displacement in the axial direction to one of the edge planes. For the REH and the DAH configurations, a half tube was used with a symmetry plane along the axis of the tube to create a full tube. For the HC the same solution of using a full tube like discussed above for the circumferential expansion was used.

The moving plane was displaced to extend the tube by 10% for the longitudinal displacement, see Figure 45.

Just as for the circumferential expansion, to avoid a dependency on length of tube, all degrees of freedom except axial displacement were linked between the two edges of the tube for each set of corresponding nodes: displacement in the circumferential direction, which due to the use of a cartesian coordinate system consisted of two degrees of freedom, and all three rotational degrees of freedom. Due to this the stresses along the tube were uniform along the whole length of the tube.

### 6.3.3 Twist – Shear

The shear models were treated using full tube structures for all models, as no longitudinal symmetry would be possible for the type of deformation imposed. Initially, the same configuration with a plane at each edge of the tube was used, just as for the case of the longitudinal expansion, but the end nodes to the surface were glued to the plane (this boundary condition still allows rotations). The plane was then rotated around the axis of the tube, hence the need for the full tube and not an axially split half-tube like the previous cases. However, it was found that the structure did not rotate, even at high separation forces imposed through the rotating planes. The actual rotational displacement of the tubular structure around the axis were minimal in comparison to the rotation of the planes, indicating sliding between the two contact bodies.

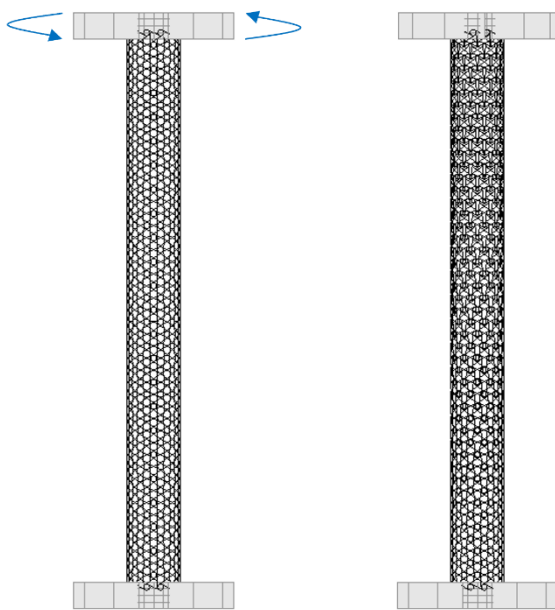


Figure 46: Twisting of tubular structure with the aid of rotating planes.

In alternative, a setup of a series of plates was used to rotate the structure, where the structure could freely expand in axial and circumferential direction. After having observed the behaviour of the deforming tube, it was noted that since the auxetic structures have a high shear modulus, the tube would only be able to shear for a small deformation and then local buckling of the struts connected to the rotating plates would occur. To counter this and allow the study of tubes of an 'infinite' length under larger shear, a small cylinder was introduced at the edges where the tube

was connected to the rotating plates, see Figure 46. This allowed the tubes to undergo a twist of 0.1 radians (around 5.7 degrees). Further numerical investigation of higher degrees of shearing would require more computing power and time. A potential further path of investigation could be to be able to determine what properties of the structure vs material

would cause this buckling under the global shearing load. Due to the challenges in the simulation and the unsuitable length of the processing time for each model, the further numerical investigation of this is not included in the project.

To minimise a dependency on length of tube, the degrees of freedom except axial displacement and rotation was connected between the two sides for each set of corresponding nodes: Displacement in the circumferential direction, which again due to the use of a cartesian coordinate system consisted of two degrees of freedom, and two out of three rotational degrees of freedom. Axial displacement could potentially be connected since a tube should not theoretically expand axially during torsion, but as it was decided not to over-restrict the deformations of the tube in case of unusual behaviour stemming from the auxetic cellular structure.

Due to the rotational symmetry of the hexachiral structure, for due diligence, the structures were investigated with both clockwise and anti-clockwise rotations, with the expectation that both should yield the same result.

## 7. Results: Tubular structures

Presented here are the results from the numerical study of the tubular structures described above. The numerical results for each combination of geometrical parameters and each beam thickness are displayed along with the analytically calculated equivalent for flat plane structure of identical parameters. The numerical results are displayed as dots and the analytical as lines. Each graph presents one elastic mechanical property as a result of variation in one structural geometrical component, for different beam thickness. For the re-entrant structures the elastic property is displayed in different graphs for different directions, so the Poisson's ratio in the circumferential direction,  $\nu_{cz}$ , is displayed in a separate graph to the Poisson's ratio in the axial direction,  $\nu_{zc}$ . Similarly for the Young's moduli, the graphs are separate for the Young's modulus in the circumferential direction,  $E_c$  and for the Young's modulus in the axial direction,  $E_z$ . For the hexachiral structures, both are displayed on the same graph due to the isotropic behaviour of the structure.

### 7.1 Re-entrant hexagonal

The elastic behaviour of the re-entrant hexagonal honeycomb relating to the geometric parameters in Figure 47 is presented below.

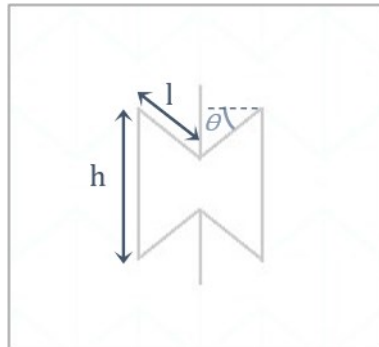


Figure 47: Re-entrant hexagonal geometric parameters referred to in results

#### 7.1.1 Poisson's ratio

For the re-entrant hexagonal honeycomb, the results for the Poisson's ratio were as seen below in Figure 48:

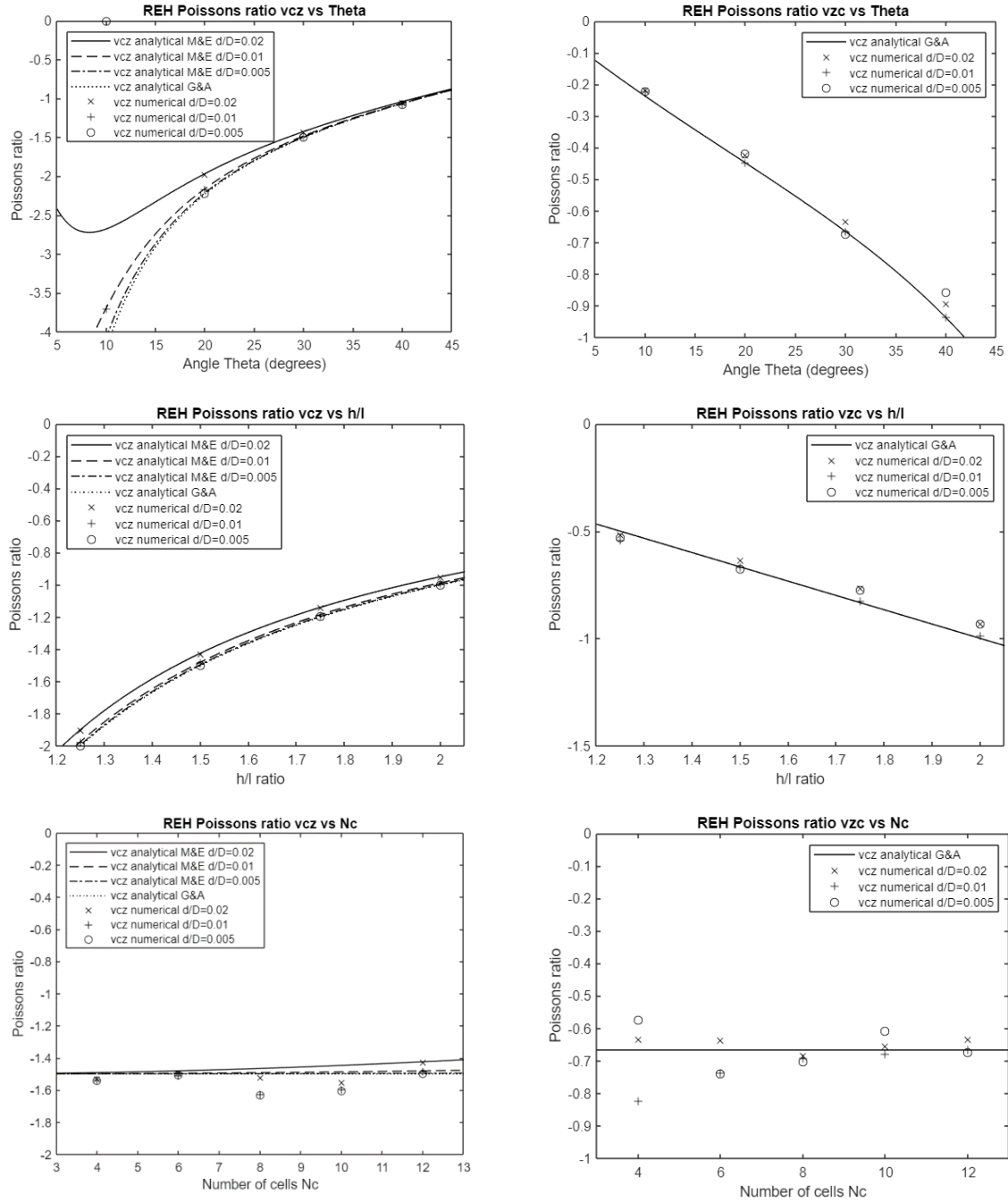


Figure 48: Poisson's ratio in relation to four different geometric parameters for the Re-entrant hexagonal honeycomb configuration, where M&E indicates analytical method derived by Masters & Evans and G&A Gibson & Ashby. Angle Theta ( $\theta$ ) is given in degrees.

The largest range of NPR observed was associated with changes in the angle  $\theta$ , as the largest NPR values were seen at very low angles of  $\theta$  which practically can pose a problem if the aim for the final structure is to undergo larger deformation. The structures with a smaller angle could not expand beyond a certain point well before the intended 10% total expansion and maintain its NPR, as the unit cell would approach a rectangle and then after that point either convert into a regular hexagonal honeycomb or change mode of deformation depending on the direction of the force. A general expression for this maximum

point of deformation, only taking the pivoting of the beam into account and not any resultant local shearing at the intersection of the beams just for guidance, could be expressed as

$$\delta_{max} = 2l(1 - \cos \theta) \quad (7.1)$$

The deformation for the structures with  $\theta = 10^\circ$  was less than 10% for that reason.

With larger angles, the structure behaved more isotropically, with NPR approaching -1 in both directions when the angle  $\theta$  passed 40 degrees. When changing the ratio between  $h$  and  $l$ , the structure behaved highly anisotropic for lower ratios of  $h/l$  closer to 1 with a higher NPR in the circumferential direction, while the closer the ratio  $h/l$  came to 2 the more isotropic the structure became with the NPR getting close to -1 in both directions, indicating different ways of nudging the structure towards a more iso- or anisotropic behaviour. Looking at the graphs for the  $h/l$  ratio, it is interesting to note the slight difference in slope between the numerical and analytical analyses for the axial deformation, while the numerical results for the Poisson's ratio in the circumferential direction seems to follow the analytically predicted behaviour more closely. The number of cells in the circumferential direction,  $N_c$ , do not significantly have an impact on the Poisson's ratio theoretically, however the numerical results align better with the analytical results with an increase in the number of cells, especially in the longitudinal direction. The graph REH Poisson's ratio  $\nu_{zc}$  vs  $N_c$  is particularly interesting, as for the smaller beam thickness the numerical models behave very close to the analytical models for a larger number of cells, in comparison to larger deviations for fewer number of cells. This indicates that the curvature of the cells has a stronger impact on the result along the axial direction. In contrast, the larger beam thickness results in smaller deviation all along.

### 7.1.2 Young's modulus

For the re-entrant hexagonal honeycomb, the results of the numerical study and the analytical study looking at the nominal Young's modulus, the following was observed as shown in Figure 49:

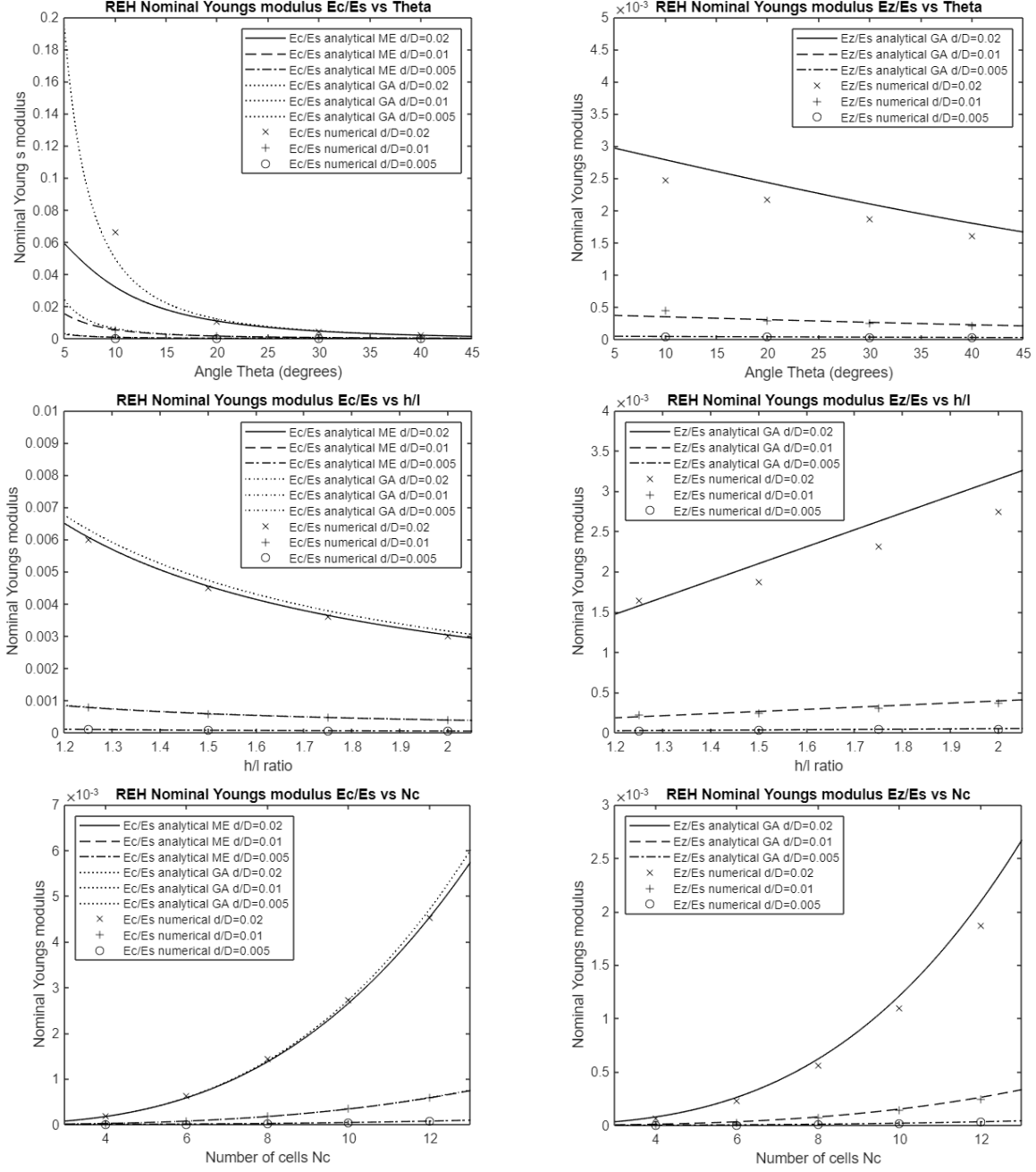


Figure 49: Nominal Young's Modulus  $E/E_s$  in relation to four different geometric parameters for the Re-entrant hexagonal honeycomb configuration

As expected, the same behaviour as for the Poisson's ratio was observed when it came to how anisotropic the system behaved in relation to which parameters changed, with an increase in anisotropic behaviour with a decrease in the angle  $\theta$  and a decrease the ratio  $h/l$ . The largest values of nominal Young's modulus was achieved at the largest values of NPR, for the lowest value of  $\theta$ , with an inverted relationship between the NPR and the nominal Young's modulus for both the relationship with a change in angle  $\theta$  and in ratio  $h/l$ . However, the nominal Young's modulus increases rapidly with the number of cells in

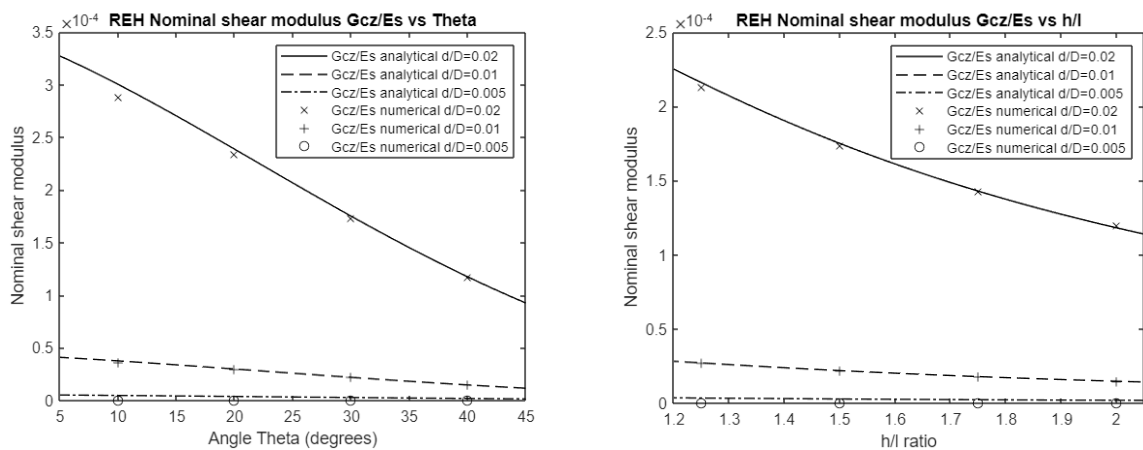


circumferential direction, despite the Poisson's ratio keeping stable. This is related to the increase in relative density, which is also seen with an increase in the Young's moduli with the beam diameter. The Poisson's ratio is not as affected as the Young's moduli, which with an increase in relative density slowly approaches the Young's modulus of the material of the beams. The same happens with the Poisson's ratio, which tends to the positive Poisson's ratio material, but far more slowly (in practice, the material Poisson's ratio becomes more and more relevant as its relative volume increases).

The notable difference between the analytical models and the numerical models is the deviations in behaviour for the Young's modulus in the axial direction,  $E_z$ . The Young's modulus is lower for the tubular structures, and the deviations in relation to the parameter  $h/l$  is particularly noteworthy.

### 7.1.3 Shear modulus

For the behaviour of the re-entrant hexagonal honeycomb under shear deformation, Figure 50, it can be observed that the numerical results are very close to the analytical predictions, with a decrease in the nominal shear modulus with an increase in the ratio  $h/l$ , the angle  $\theta$  and an increase in the shear modulus with an increase in the number of cells in the circumferential direction. Both the increase in angle  $\theta$  and the decrease of the ratio  $h/l$  leads to a higher relative density of the structure. The relative density increases to an even greater extent with the increase in the number of cells in the circumferential direction,  $N_c$ , which is a logical explanation to the increase in the shear resistance of the structure, just as can be seen with the increase in beam thickness. It is worth to note that the deformation of the numerical models shows that the shearing of the structure follows the analytically suggested behaviour of the majority of the twisting of the structure coming from the rotation of the beam joint and the flexure of the vertical beam with the length  $h$ .



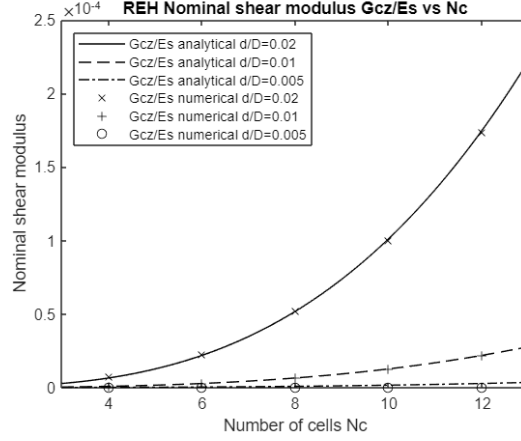


Figure 50: Nominal shear modulus for Re-entrant Hexagonal honeycombs

## 7.2 Double arrowhead

The elastic behaviour of the re-entrant hexagonal honeycomb relating to the geometric parameters in Figure 51 is presented below.

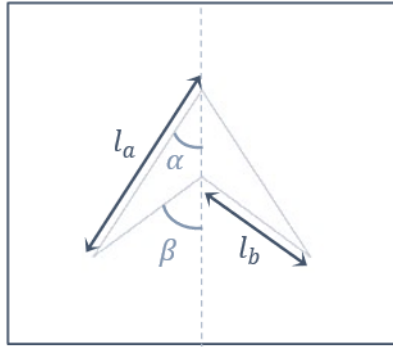


Figure 51: Double arrowhead geometric parameters referred to in results

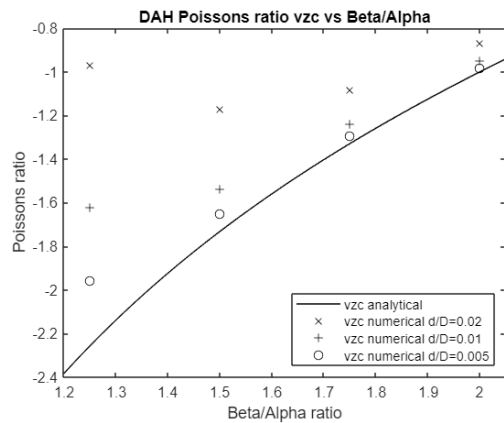
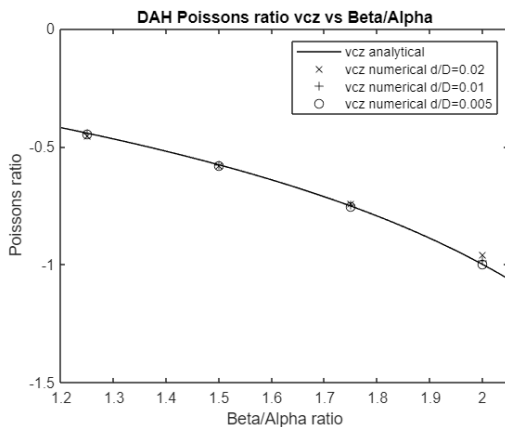
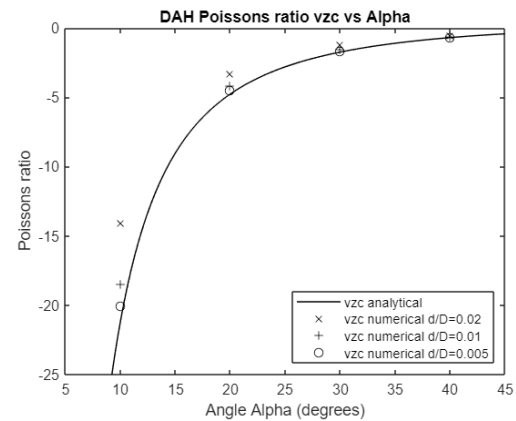
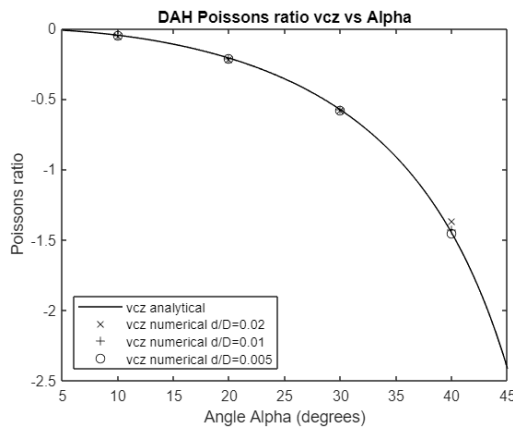
### 7.2.1 Poisson's ratio

The largest range of the Poisson's ratio is achieved by altering the angle  $\alpha$ , with very high NPR achieved when subjected by a load along the axial direction. As the structure gradually expands, the angle  $\alpha$  expands, which would indicate that the structure's Poisson's ratio gradually decreases with expansion. Looking at the results for 10% expansion of the structures in Figure 52, the NPR does not change significantly, especially for deformation in the circumferential direction, while it's noteworthy that the NPR in the axial direction is lower for a larger beam thickness

The other geometric parameter that has the second largest impact on the Poisson's ratio is the ratio between the angles of the beams  $\beta/\alpha$ . Just as for the angle  $\alpha$ , a smaller angle  $\beta$  results in a larger NPR. This indicates that the two angles are the most influential geometric parameters on the Poisson's ratio of the DAH, and the largest NPR would be achieved with the smallest angles so that all struts are approaching alignment with the direction of the

force. In the case of the structures studied here, the largest NPR are observed in the axial direction. As mentioned above, the NPR is lower for a larger beam thickness in the axial direction and follow a different pattern which could be more related to factors like the relative density of the structure.

The number of cells in the circumferential direction,  $N_c$ , do not significantly have an impact on the Poisson's ratio theoretically, however the numerical results align better with the analytical results with an increase in the number of cells, especially in the longitudinal direction. The graph DAH Poisson's ratio  $\nu_{zc}$  vs  $N_c$  is particularly interesting as for the smaller beam thickness the numerical models behave very close to the analytical models for a larger number of cells, likely indicating that the curvature of the cells has a stronger impact on the result along the axial direction. In contrast, the larger beam thickness results in a larger deviation, which is likely due to the increase in relative density of the structure with the number of cells in the circumferential direction  $N_c$ . The increased discrepancies between analytical and numerical models for  $\nu_{zc}$  as a function of  $\beta/\alpha$  as the beam thickness increases would need to be investigated further but could be related to the increase in relative density as well.



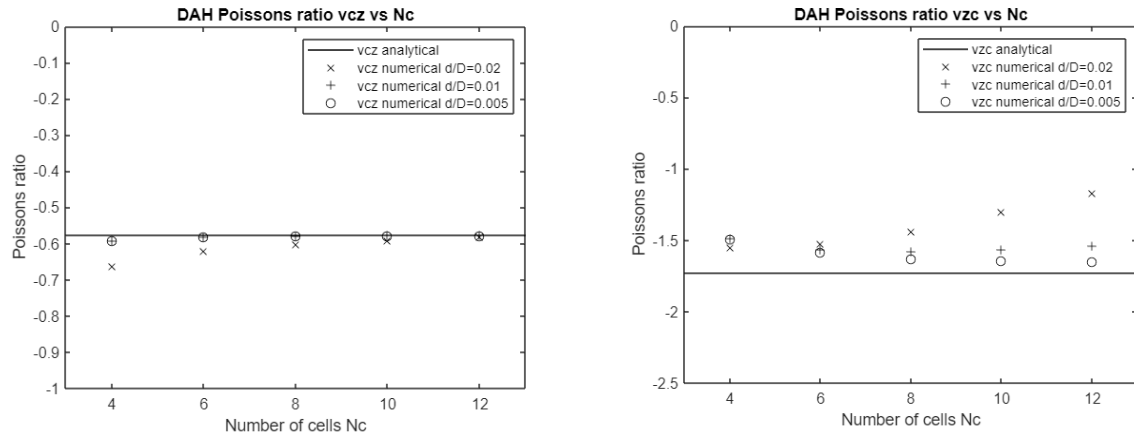
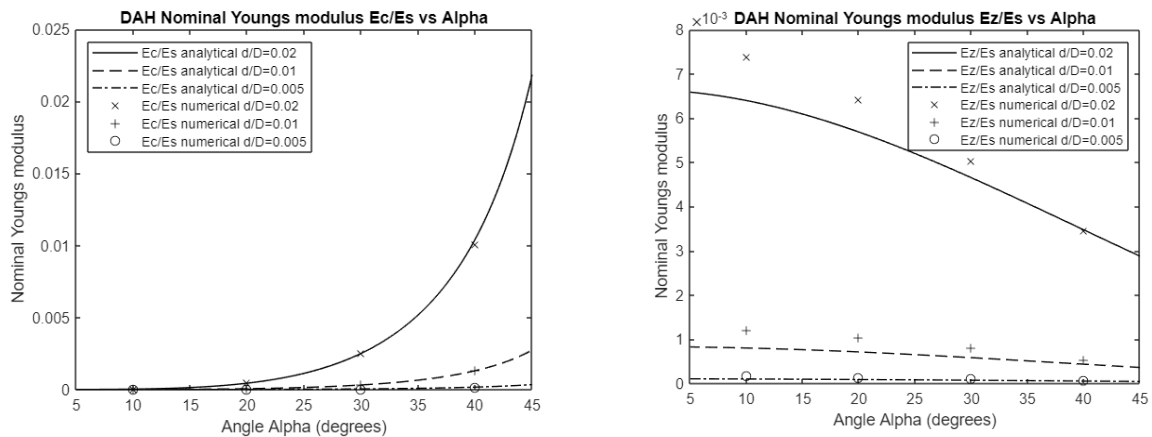


Figure 52: Poisson's ratio for the double arrowhead

### 7.2.2 Young's modulus

When varying the angle  $\alpha$  independently, see Figure 53, the effect on the nominal Young's modulus in the axial direction is far more gradual than the variation in Poisson's ratio and the difference between the axial and circumferential directions is smaller. The highest nominal Young's modulus was observed in the circumferential direction and stemmed from the highest angle  $\alpha$ , when the beams are approaching alignment with the direction of the force. When altering the ratio  $\beta/\alpha$  the nominal Young's modulus respond very differently in the circumferential and axial directions.



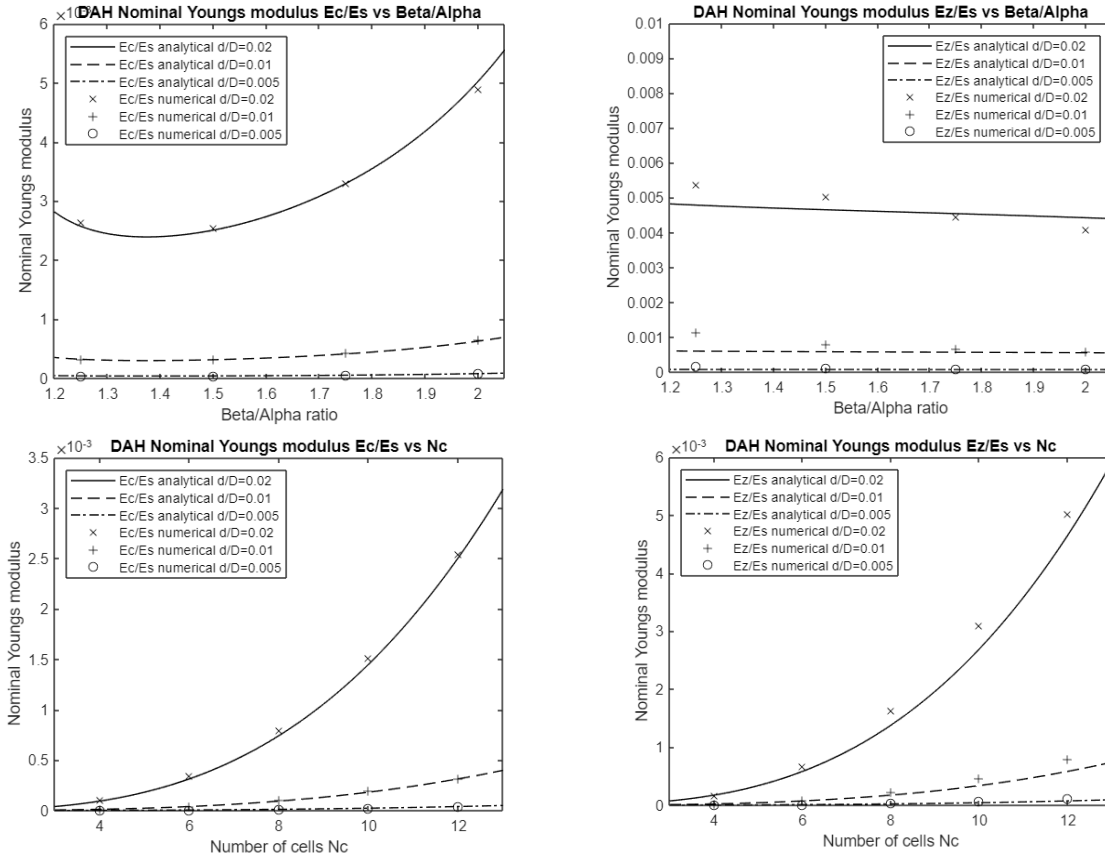


Figure 53: Nominal Young's moduli for the double arrowhead

The nominal Young's modulus varies significantly when altering the number of cells circumferentially,  $N_c$ . Again, in the axial direction the behaviour of the analytical models and the numerical models deviates. The beam thickness and, as a result, relative density of the structure, is consistently contributing to a higher stiffness of the structure.

The increase in strut diameter, which not cause major changes in the Poisson's ratio of the structure using the analytical approach, when referring to the numerical results appears subjected to a larger influence in the axial direction. Looking at the density of the structure, if the beam thickness is gradually increased, the structure will approach a solid wall instead of a beam lattice, where the Poisson's ratio would be determined not by the structure itself but by the material of the structure. Between the infinitely small theoretical beams and the solid surface, the Poisson's ratio of the object gradually transfers from being determined by the Poisson's ratio of the auxetic structure to that of the material. This can partially be observed from the numerical results as the NPR becomes significantly lower as the ratio  $d/D$  increases, indicating some limitations of the analytical models. For the more studied re-entrant hexagonal structures, there are models that have improved on the original equations done by Gibson and Ashby [77] and Masters and Evans [83] taking into account thicker ribs, like the one done by Grima et al [85]. Grima et al look at the joints of the ligaments, where

the effective length of the ligament becomes shorter when it ‘overlaps’ at the joint with the neighbouring ligaments due to the thickness of the ligaments. This type of approach could be a future improvement on the equations presented here for the double arrowhead structure. In contrast, for both the analytical and numerical results a major increase in nominal Young’s modulus is observed. This can again be related to the relative density of the structure.

### 7.2.3 Shear modulus

Observing the shear behaviour of the structure, Figure 55, there is a significant increase in shear stiffness with an increase in the angle  $\alpha$  and with an increase in the ratio between the angles,  $\beta/\alpha$ . There is a significant increase with an increase in the number of cells in the circumferential direction,  $N_c$ , and a similar increase in shear stiffness with an increase in beam diameter, indicating that an increase in the relative density of the structure increases the shear stiffness.

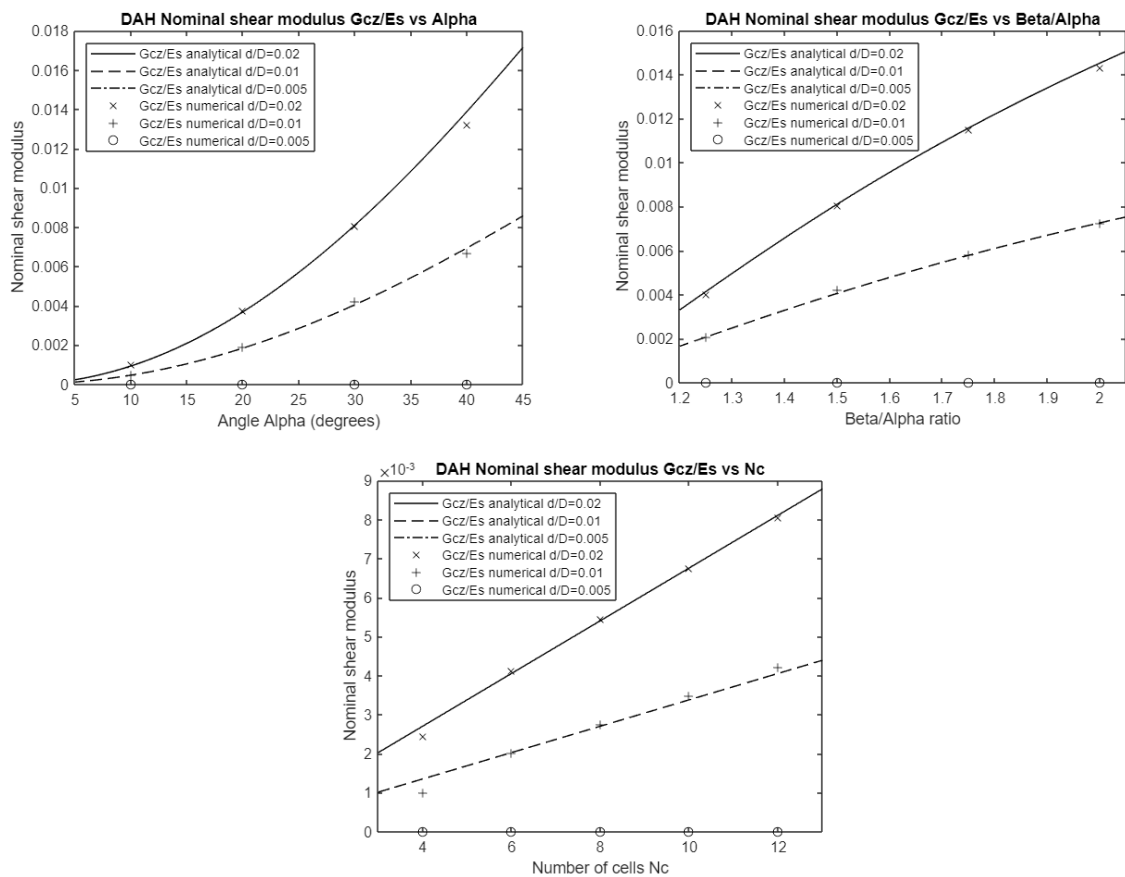


Figure 55: Shear moduli for the double arrowhead

Overall, the difference between the behaviour of the analytical and numerical models are very small for the shearing of the structure, with a stretching behaviour being observed in the

numerical models instead of a flexure dominated deformation mechanism, as initially assumed, resulting in the selection of stretching equations being used solely for the analytical expressions. This is demonstrated below in Figure 56, when comparing the numerical results to the different analytical approaches of pure stretching, pure flexure and the combination of the two. The numerical results align very well with the pure stretching model than either of the other options.

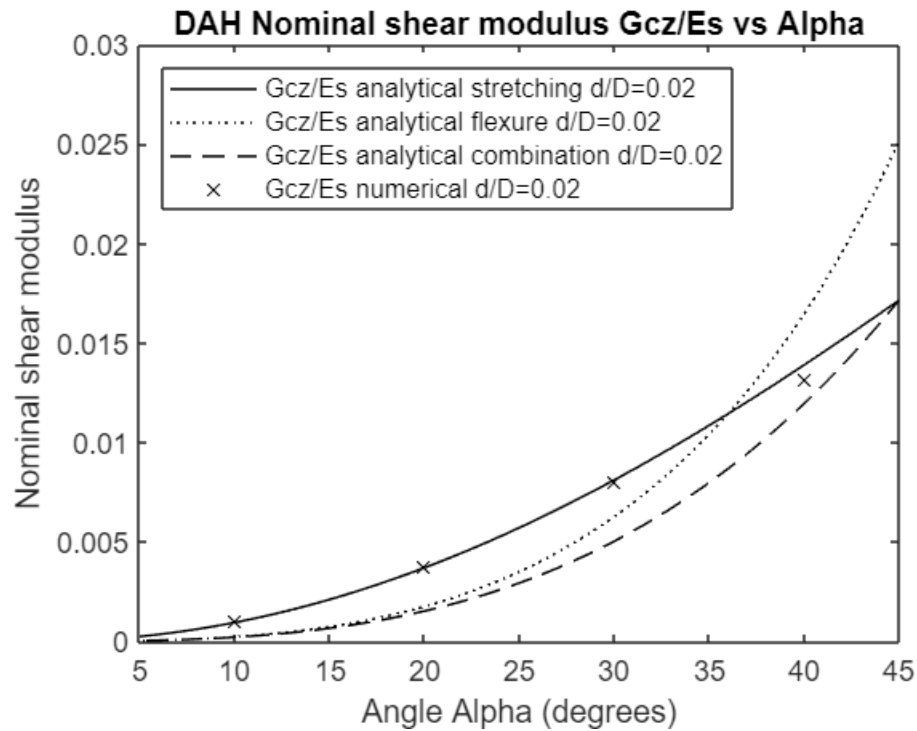


Figure 56: Double arrowhead shearing - comparing modes of deformation (flexure, stretching and a combination of both).

### 7.3 Hexachiral

The elastic behaviour of the re-entrant hexagonal honeycomb relating to the geometric parameters in Figure 57 is presented below.

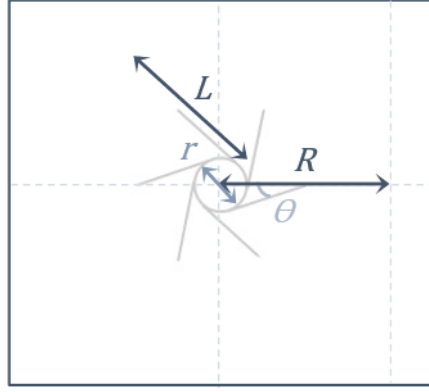


Figure 57: Hexachiral geometric parameters referred to in results, with  $R$  being the distance between the centre of two unit-cells and  $L$  the beam length of the connecting ligament

### 7.3.1 Poisson's ratio

For the hexachiral configuration, there are only three different geometrical parameters that could be altered to potentially affect the elastic properties of the structure. Due to the theoretical assumption that the hexachiral system is isotropic, there is only one analytically calculated Poisson's ratio which is to be valid for both directions, compared to two numerically investigated ones, one for each direction 'in-plane', see Figure 58.

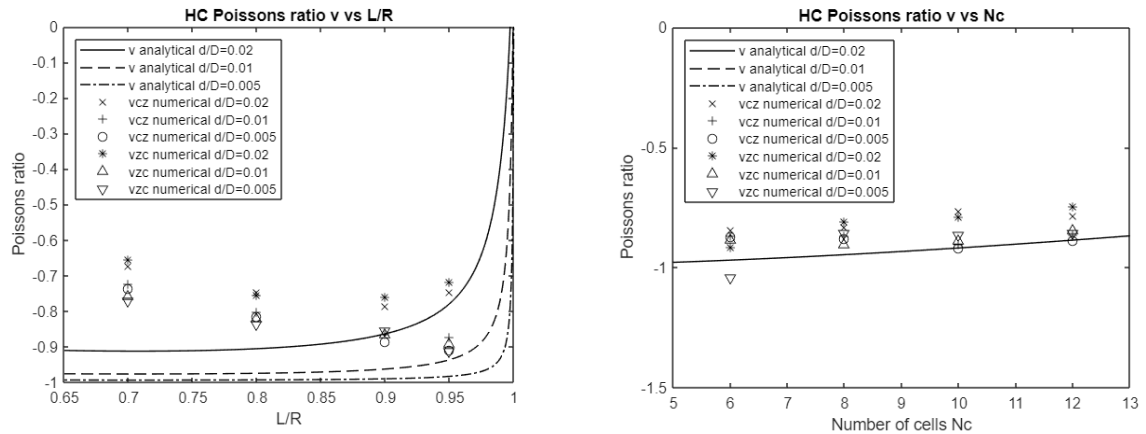


Figure 58: Poisson's ratio for the hexachiral configurations

The numerical results for the deformation in the axial and circumferential direction show an isotropic behaviour in line with the theoretical assumption, while the difference between the analytical and numerical models have been indicated by the authors of the analytical model to be related to the assumption of rigid nodes, while these numerical models use deformable nodes, as discussed for the Young's modulus below.

Like the other two structures, the change in number of cells in the circumferential direction does not have a major impact on the Poisson's ratio, although some increase in the NPR can be observed with both analytical and numerical models at lower number of cells in the



circumferential direction. The ratio  $L/R$ , or the degree of chirality (also sometimes written as the angle  $\beta$ ), have a much larger impact. The impact of the degree of chirality in the numerical models appears much larger than in the analytical prediction. This could be related to the relative density, as a higher angle means a shorter strut length of  $L$  and, in turn, a higher  $d/L$  ratio.

### 7.3.2 Young's modulus

Observing the Young's modulus of the hexachiral configurations, as seen in Figure 59, it increases with the number of cells in the circumferential direction, just as for the re-entrant structures. The Young's modulus in relation to the degree of chirality, or the parameter  $L/R$ , shows an interesting effect, with the lowest Young's modulus reached somewhere between 0.7 and 0.85. For the nominal modulus in relation to the change in thickness of the ribs, the analytical models give a far lower prediction than the numerical results.

This could be compared with the numerical results with deformable nodes from the paper that presented the analytical method with rigid nodes by Spadoni & Ruzzene [106], as seen in Figure 60. The nominal Young's modulus for the case of deformable nodes is marginally lower than that of the rigid nodes for the cases considered here, while the Poisson's ratio is higher and follow a similar curve to the results from this study. This highlights the importance of ensuring that the simplified analytical models really reflect the more complex systems they are meant to model. The higher the  $t/L$  ratio (where this work used  $d/L$ ), the further from the analytical models. As for the other structures, as the relative density increases, the elastic properties become closer to the material ones.

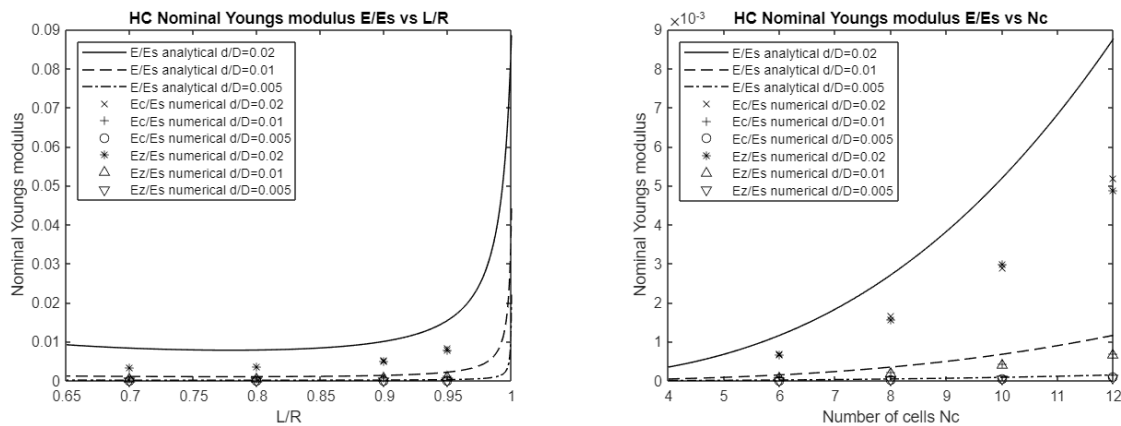


Figure 59: Nominal Young's moduli for hexachiral

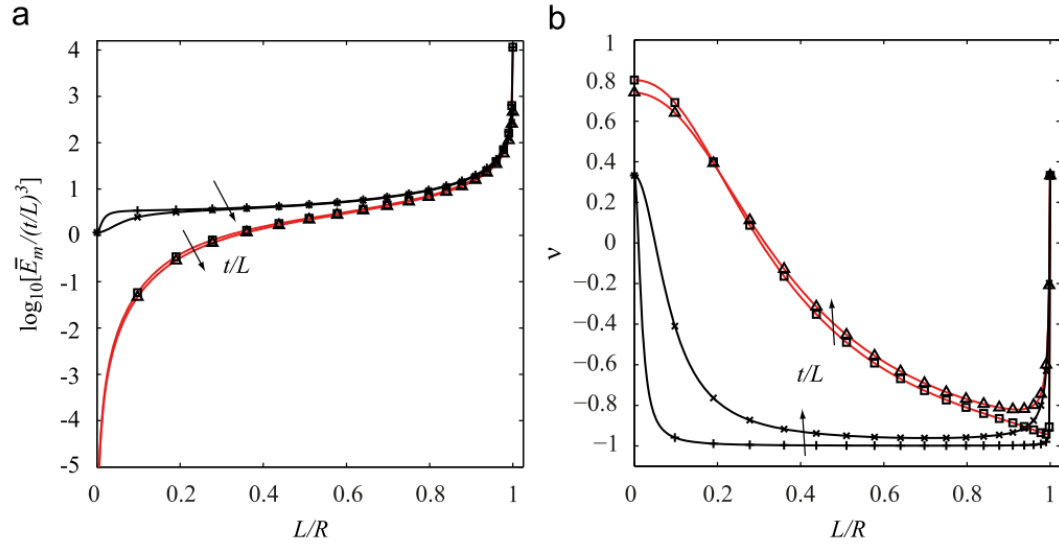


Figure 60: Micropolar constants with two values of ligament aspect ratio  $t/L = [1/100 \text{ and } 1/20]$  with rigid nodes (black lines, +, x symbols) and deformable nodes (red lines,  $\square$ ,  $\Delta$  symbols) for Nominal Young's Modulus and Poisson's ratio by Spadoni and Ruzzene for comparison. [106]

### 7.3.3 Shear modulus

In contrast to the other structures, the analytical predictions and the numerical results for the Hexachiral configurations differs greatly for the shear modulus, as seen in Figure 61.

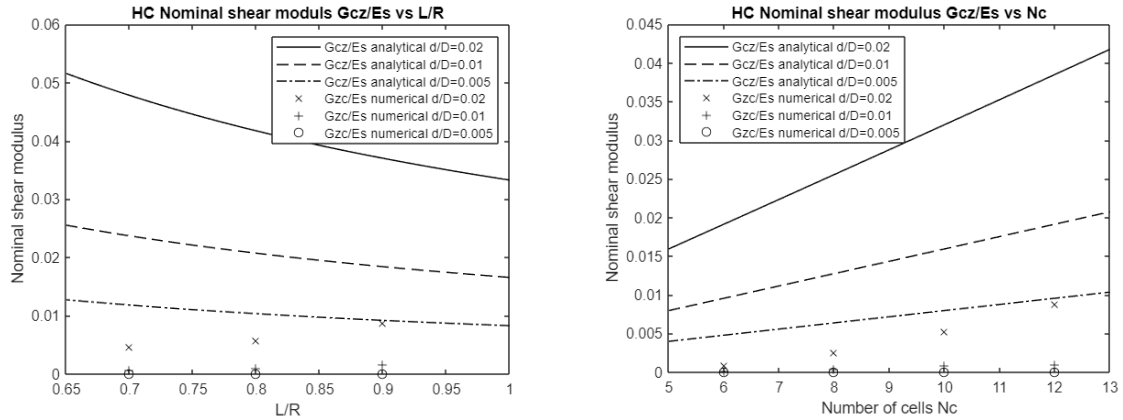


Figure 61: Nominal shear moduli for the hexachiral configurations

From the work of Spadoni & Ruzzene [106], it can be seen that the authors of the analytical method came across the same problem as seen in

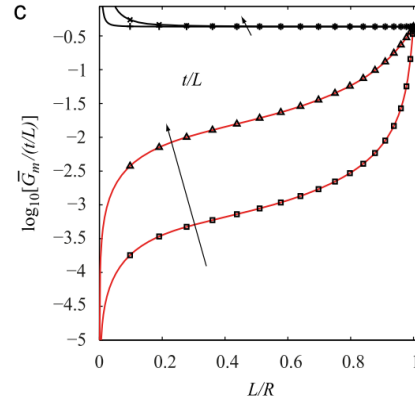


Figure 62. They concluded that the contribution of the deformation of the rings affects the results even more during shear deformation than in tension. The shear modulus observed in the case of deformable rings were significantly lower than the shear modulus observed in the case of ridged rings. The thickness of the ribs is hence a major influential parameter as it stiffens the nodes. An increase in  $L/R$  ratio increases the shear stiffness, and the results for the deformable and rigid nodes approaches each other, which is expected due to the deformation mechanism moving from being primarily of the deformation of the nodes to the deformation of the struts. Since the chiral structure is rotationally symmetrical and not axially, the simulations were run with both clockwise and anti-clockwise shear deformation for due diligence for a sample of 3 cases, and as expected, there is no significant difference shown in the result between the directions.

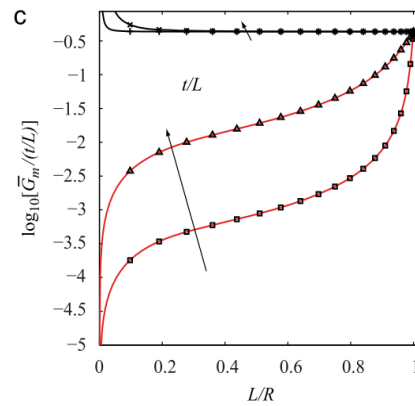


Figure 62: Micropolar constants with two values of ligament aspect ratio  $t/L = [1/100 \text{ and } 1/20]$  with rigid nodes (black lines, +, x symbols) and deformable nodes (red lines,  $\square$ ,  $\Delta$  symbols) for Nominal Shear Modulus by Spadoni and Ruzzene for comparison. [106]

## 7.4 Difference between analytical and numerical models

For the re-entrant and double arrowhead, the analytical prediction is generally consistent with the numerical results. Comparison between the two approaches indicates that

analytical description loses accuracy as the number of cells in the circumferential direction reduces and the ligaments thickness reduces the ability to adopt a beam model. Adapting the equations derived for a planar structure to predict the results for a tubular structure appears an acceptable approximation, which could be further improved by adding additional parameters considering eccentricity of load, when the number of circumferential cells becomes reduced. Though, the loss of accuracy appears to be significant when referring to the longitudinal direction, which is usually the less relevant in stent applications.

Another source of approximation is associated with the ligament thickness. Moreover, the ligaments being defined as uniformly circular in cross-section would also only be applicable to certain applications and manufacturing methods. The analytical equations leave room for the use of another shape of cross section by not simplifying the area  $A$  and second moment of area  $I$ , however there are several practical applications where the cross-section would be less than uniform. One example of source of more variation in the cross-section would be manufacturing methods. Either joining the ribs with welds or laser cutting would produce different kinds of unevenness in the cross-section, which would be more prominent the larger the relative rib thickness is. For the hexachiral structures, the analytical expressions, especially for shear, would need to be further developed to be more useful in guiding practical design, while the numerical analysis can in the meantime act as a guide on how the different parameters affect the performance.

## 7.5 Summary results

There is a large difference in outcome between the re-entrant structures, the re-entrant hexagonal (REH) honeycomb and the double arrowhead (DAH) honeycomb, and the hexachiral (HC) structure. The re-entrant structures have shown a mostly consistent result with the numerical models, while the chiral structure have shown less consistent results between analytical prediction and numerical models, especially in regard to shearing. The analytical chiral model is a continuum model focused on the deformation of the connecting ligaments, in contrast to the re-entrant models able to take the deformation of all components into consideration in their respective beam models. Since the analytical method for the hexachiral structure does not include the deformation of the nodes, and the numerical models do not restrict deformation of the nodes, this is likely a factor contributing to the discrepancy, which was also mentioned by the creators of the analytical model. Another difference worth noting is the effect of direction of deformation versus the direction of curvature for the anisotropic re-entrant structures in comparison to the isotropic hexachiral structure, where the effect of the axial deformation diverts more from the theoretical analytical values for plane beam structures than for circumferential deformation.

## 8. Discussion

### 8.1 Discussion of study of tubular structures

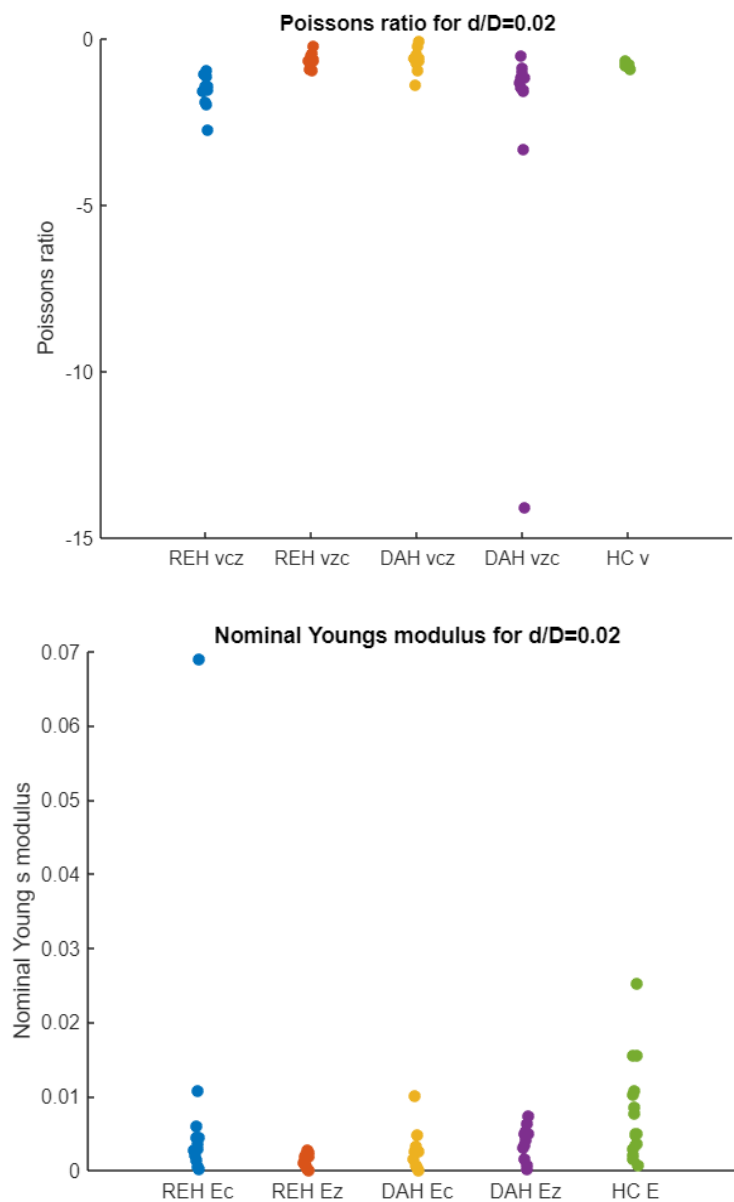
#### 8.1.1 General behaviour of the auxetic tubular structures

It can be observed that for all three different structures, the Young's modulus increases with the number of cells in the circumferential direction, although the Poisson's ratio remains largely the same, with some variation with curvature more noticeable for thinner ligaments, and some variation relating to increases in relative density more noticeable for thicker ligaments. Change in strut diameter resulted the parameter impacting the Young's modulus far more than any other for all three structures. This parameter had less geometric constraints than the others, with the only limit being that the structure should still be a cellular solid. In reality, in the case of laser cut or machined structures obtained from tubes, there are manufacturing constraints, but these will be neglected in the first instance. As the thickness increases, the structure slowly loses its auxetic behaviour as the dominant deformation mechanism, transitioning from being that of the structure which is auxetic to being that of the beam material. The analytical studies have indicated that their expressions are only valid for a very small strut diameter to length ratio or for small relative density of the structure. It is interesting that the Poisson's ratio still follows analytical models well up to a certain point for most re-entrant cases, with the notable exception of the Poisson's ratio in the axial direction for the double arrowhead. For the hexachiral structure, the difference between the numerical models and the analytical predictions can partially be attributed to the deformable centre rings, or nodes, and it is interesting to see how the result from the tubular structures here shows a similar pattern to the flat models from the study by Spadoni & Ruzzene [106].

One of the major takeaways from this is that it is possible to manipulate the Young's modulus of the structure without impacting much on the Poisson's ratio, while there are no geometric parameters that allows to change the Poisson's ratio without resulting in substantial changes in the Young's modulus. This has the implication that when designing an auxetic structure, the primary step should be to select which Poisson's ratio is desirable and after that the Young's modulus can be tailored to what is required. Another takeaway is the importance to identify in which direction the deformation is more prominent when planning to use an anisotropic structure, as the mechanical properties can differ greatly in the different directions and there is a constant trade-off when trying to achieve for example a higher Poisson's ratio in one direction, resulting in a lower one in the other direction. There are different options of structures which theoretically behave in an isotropic manner in both

in plane directions with a negative Poisson's ratio of about - 1, and which one to use can be selected based on other parameters, like shear behaviour or stiffness, or retention/change of that behaviour under large deformation.

Comparing the different ranges of Poisson's ratio, Youngs modulus and Shear modulus possible for the various configurations explored above without altering the diameter of the struts, Figure 63 can give an indication of the comparative magnitudes.



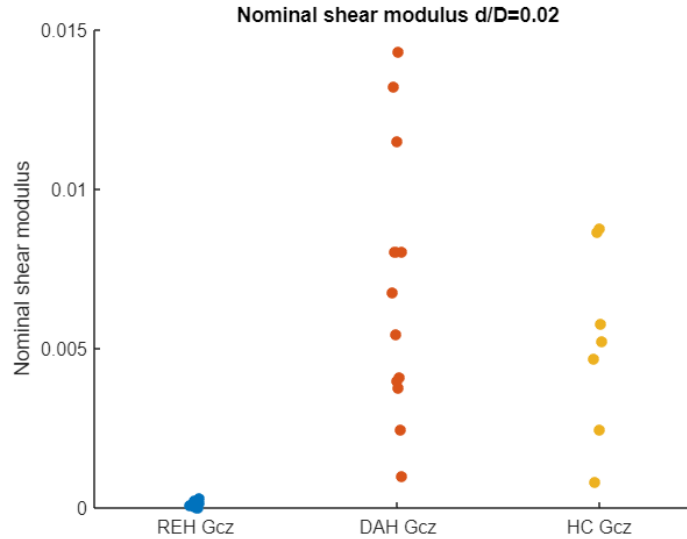


Figure 63: Direct quantitative comparison of the different ranges achievable for the different configurations without altering thickness of struts, for the circumferential (c) and the axial (z) directions for anisotropic parameters, with each dot representing the numerical result from one analysis for the reference  $d/D=0.02$ . Higher concentrations of dots indicate the property intervals more commonly achieved while outliers highlight extreme cases achieved only for a very small range of values for a parameter.

### 8.1.2 Comparison and suitability for different types of applications

Looking at the results above, some of the differences between the various structures which would be needed to take into account to inform the selection of which structure to use is the difference in behaviour between the underlying principal deformation mechanism: the re-entrant mechanisms, of both the re-entrant hexagonal cells and the double arrowhead cells, and the chiral mechanism. For the hexachiral structures, two of the main indications for use is the retention of elastic properties over larger range of deformation and the isotropic nature of the structure. Although it has been reported that the hexachiral structure retains its behaviour over larger range of deformations in experiments, the type of study that have been done numerically above has not confirmed this feature. Hence it is difficult to know the stipulations for which that applies to. The same goes for the isotropic behaviour of the hexachiral – there is a small difference in the numerical results between the deformations for the different directions, and further study on the extent of the isotropic behaviour in practical application would be needed. For the re-entrant hexagonal and the double arrowhead, the anisotropic behaviour can be leveraged to allow for a far larger range of Poisson's ratios. Again, since the properties of the two are not retained for large deformations, for practical applications it would be even more important to make sure that manufacturing constraints do not impact this further without taking their effect into consideration in the design stage. The

re-entrant hexagonal and the double arrowhead have a quite clear 'maximum' extension stage before the auxetic behaviour is compromised, so for larger deformations not only the change in elastic behaviour along the course of deformation need to be taken into account, but also how large maximum expansion is desired. The hexachiral have less clear definitions for this, so numerical and experimental modelling is more important in this case, early in the design stage.

### 8.1.3 Difference between analytical and numerical predictions – impact on design considerations, limitations, and further questions

There are clear distinctions between the analytical and numerical predictions of the elastic behaviour of the tubular structures. The curvature of the stent poses a challenge to analytical predictions, that should be taken into account when designing auxetic stents.

Another is the thickness of struts. In an actual design, the thin ligament needed to meet the analytical predictions highlight the importance to make adjustments based on the patterns observed when considering designing physical auxetic stents. The deviation shown in the numerical analysis should be incorporated in stent designs to ensure realistic expectations of elastic behaviour.

The third is the impact of manufacturing method on joints, and strut uniformity. As these numerical models of tubular structures were beam models, the joints were not specifically considered. Both the local deformations at the joints and the impact of the joints on the overall elastic behaviour of the stents were excluded from the analysis. If looking at two common stent manufacturing methods, laser cutting and knitting and welding of metal wires cause differences to both the struts and joints, that are not taken into consideration in the above numerical models. When obtaining the auxetic pattern from laser cutting of a metal tube, the cross section of the struts would be uneven along the struts. The knitted wires may have a more uniform beam cross section; however, the welded joints would be another factor to take into account instead.

Another limitation in respect to specific stent design is the factors that has been introduced to generalise the results: the lack of free edges. The tubular structures modelled above are designed to behave as if they are infinitely long, however in a real case the stents will be finite. Since the length of the stents are governed by anatomical considerations for the specific applications, some stents will be relatively long that only the ends of the stent behaves differently, while others are shorter and the stent length will have a more drastic impact on the elastic behaviour of the entire structure.



The above can be a good measure for the auxetic behaviours of bare stents, however for covered stents and stent-grafts, a covering or membrane would be needed. Membranes on top of auxetic structures have not been investigated in the literature and would likely impact the auxetic behaviour of the structure. So, additional investigation would be needed to address this aspect. In conclusion, the presented analytical and numerical investigation of auxetic tubular structures gives a good indication of the behaviour of the different configurations, and which type of structure may be more suitable for certain types of applications, but adjustments have to be made to any specific device design to take into account the device specific limitations.

#### 8.1.4 Summary tubular structures

All three structures exhibit distinctly different elastic behaviours. The analytical models for flat planes can to an extent be adapted and used for tubular structures, however there are differences which increase with factors like beam thickness and seems to be more pronounced in one direction than the other. The notable exception is the shear modulus for the hexachiral structures. The analytical plane structure model is made with the assumption of rigid nodes; however, the numerical models indicate that the shear behaviour might deviate more. Compared to the arrowhead structure, whose shear behaviour is dominated by stretching rather than flexure (which instead dominates for tension), it is possible that due to the triangular architecture of the structure, the shearing behaviour of the hexachiral structure might be dominated by different deformation mechanisms compared to those during tension.

The double arrowhead offers the largest range of Poisson's ratios, and the highest shear rigidity, while the re-entrant have a smaller range and the lowest shear rigidity. Both exhibit an anisotropic behaviour and have a similar range of Young's moduli. The hexachiral differs substantially from the two re-entrant configurations, with its isotropic and very limited range of Poisson's ratio. The Young's modulus is less isotropic in the context of tubular structures than the theoretical one for the plane structures with a thicker ligament, with a higher Young's modulus than the other two.

## 9. Specific issues in practical stent design

### 9.1 Manufacturing and deployment discussion

One of the popular stent manufacturing methods today is laser cutting which, especially in the case of TAVI, is typically done on a tube of the smallest size (in the case of transcatheter heart valves, the largest tube available commercially is substantially smaller than the operating valve size), which is then expanded, thermoset and polished to the final stent configuration. Here, an auxetic structure would have an advantage over a conventional one as it would not only be smaller in circumference but also shorter, resulting in a denser pattern and limiting the material which need to be cut out.

Another element of stent design that might benefit from using auxetic structures is the deployment mechanism used for implantation of minimally invasive devices like TAVI or PPVI. The stent is crimped to fit in a very narrow catheter which is then inserted through a vein in the body. When doing this with conventional stents, they elongate when in the crimped state, which is less ideal for the insertion and can also cause malpositioning as the stent foreshortens while expanding.

### 9.2 Membranes

In a number of cardiovascular applications, such as stent grafts and transcatheter valves, the stent needs to provide sealing at its nominal wall. This is commonly achieved by fixing to the structural cellular material a membrane made from fabric, soft tissue or polymer. The interaction of this membrane with the stent material may result in alterations of the auxetic behaviour. Here, this effect is investigated, in order to verify the effect of the covering component on the auxetic behaviour of the configurations identified as most suitable for stent applications.

There are several ways that membranes are attached to stents, with two examples being 'dip coating' in a polymer or suturing a sleeve onto the stent, with attachment to the metal frame in just a few places.

Membranes could theoretically be auxetic, as a form of knitted fabrics, however there are currently no clinically approved stent covers that are auxetic.

In the common case that the cover is not auxetic, it will have a restrictive impact on the otherwise auxetic behaviour of the structure. The option of different fastening mechanisms will play a role, because if the membrane is attached to the stent in a few localised regions, there might be the possibility of mutual sliding and that the fastening only restricts the motion in a limited way. For dipping in a polymer, the combined structures will need to be studied as one, to verify how the addition of a membrane impacts on the stent behaviour.

This effect will depend on which type of auxetic structure is being used, on beam and membrane thickness and on the rigidity of their materials (on the relation between the beam and membrane properties).

A preliminary study with membrane covered unit cells, for the three different auxetic structures investigated above is presented below.

### 9.2.1 Membrane modelling methodology

The preliminary study was done with a beam material like stainless steel with a Young's modulus of 210 GPa and a Poisson's ratio of 0.3, with a beam thickness of  $d = 0.3$  mm and a membrane with material properties similar to silicone with a Poisson's ratio of 0.49, a Young's modulus of 10 MPa, and a thickness of 0.1 mm.

In the case of the hexachiral configuration, the boundary conditions essentially act on the membrane component. This resulted into mechanical instability and out of plane deformations, transferred to the beams. To avoid this problem and obtain indicative results from the analysis, the beam thickness was increased to 3 mm. This should be kept in mind when interpreting the results and will be discussed further, as it has significant impact on the structures Poisson's ratio, even in absence of the membrane.

The Young's modulus of the beams, in relation to that of the membrane is 21,000 : 1, and the beam thickness to membrane thickness is 3:1.

The boundary conditions used were different for each structure, due to different degrees of symmetry on the membrane. It is important to note that the membrane unit cell can have different symmetry requirements than the beam unit cell, due to the movement of the membrane. The concept of 'Matching Boundaries' was used in MSC Marc: for each element the corresponding edges were marked (in Figure 64 below as pink and green), and the nodes 'tied' between these sides (marked with red lines). The deformation imposed on the structure was a simple expansion in one direction. For a more complete investigation of the structures, it would be of importance to investigate deformation in both directions.

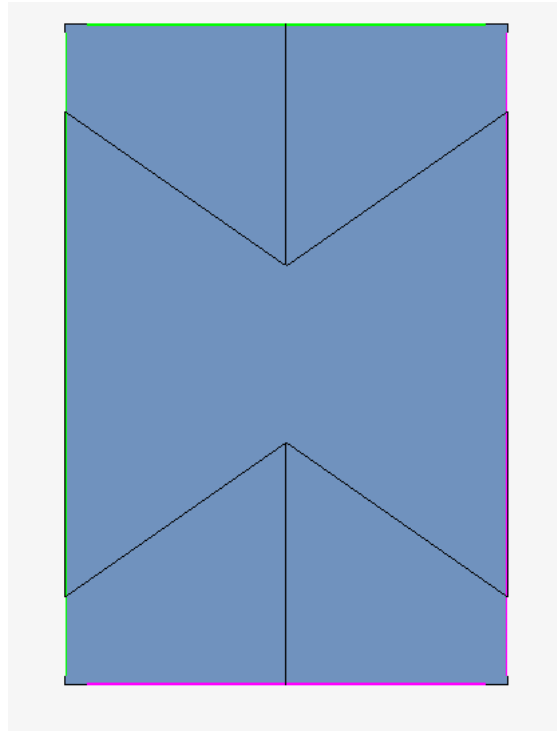


Figure 64: Re-entrant hexagonal membrane model, where the thin black lines represent the beams, the blue the membrane, and the pink and green the matching boundaries (where the pink side is tied to the mirrored green side, vertically and horizontally respectively).

Each structure required different configurations of number of cells, and boundary conditions. The re-entrant hexagonal is symmetrical in both directions for both the beam structure and the membrane, and hence a square of one unit cell in the x-direction and one in the y-direction with an additional half one in either direction to allow for membrane deformation to contribute on either side of the slanted beams, as seen in Figure 64.

For the double arrowhead, the structure is only symmetrical in one direction. Hence, to simulate the membrane on both side of the beams in the other direction, multiple stacked unit cells were used. This was also chosen as the direction of expansion, with 4 cells (3 full and two halves at each end) in the direction of the expansion, and one cell in the other, as shown in Figure 65.

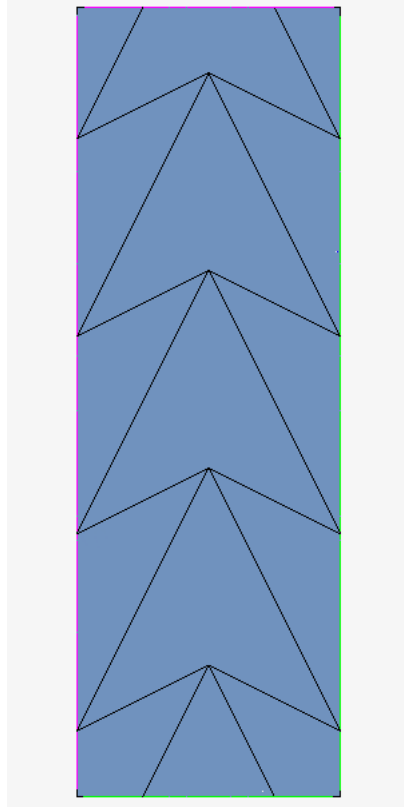


Figure 65: Double arrowhead membrane model, where the thin black lines represent the beams, the blue the membrane, and the pink and green the matching boundaries (where the pink side is tied to the mirrored green side, vertically and horizontally respectively).

For the hexachiral, the complex boundary conditions suffer not only from the lack of symmetry but is further complicated by the rotational nature of the structure. To compensate as much as possible from this, a much larger assembly of cells were used for simulations, with 4 number of cells in the direction of deformation, and 4 number of cells in the other, as shown in Figure 66.

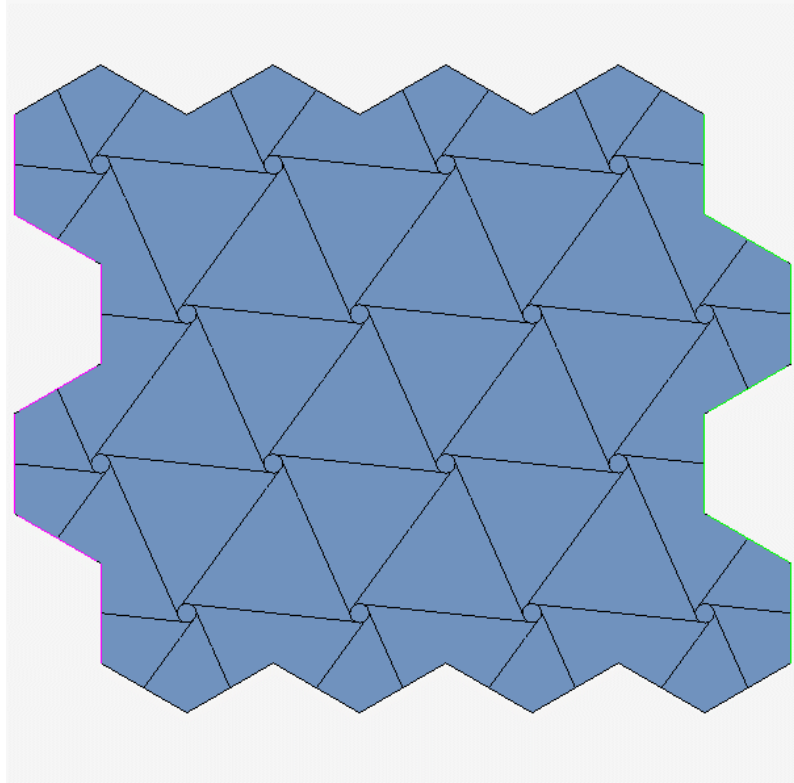


Figure 66: Hexachiral membrane model, where the thin black lines represent the beams, the blue the membrane, and the pink and green the matching boundaries.

Due to the differences between the configurations, different mesh densities were used. The re-entrant hexagonal uses quadratic, 4 node, structural 3D membrane cells (Element 18, MSC Marc) while the double arrowhead and hexachiral uses triangular 3 node elements (Element 158, MSC Marc). Both uses the same beam elements as for the tubular structures, element 98 (MSC Marc), a Structural 3D solid section linear beam element. For a more in-depth dedicated study, improving mesh uniformity between the three structures would be a point where to improve result comparability.

For consistency, the geometries of all three cell structures were chosen to exhibit a theoretical Poisson's ratio of -1, as that is the standard of the hexachiral and can be achieved by all three.

The size of the unit cells was unified with the unit cell width of 10 mm for both the re-entrant hexagonal and the double arrowhead, and a diameter of 15 mm for the hexachiral unit cell.

The height of the unit cell would be dependent on the different parameters, and for a more thorough examination, different combinations of those would be investigated.

All parameters can be seen below in Table 12.

*X1 is the direction of displacement and X2 is the other perpendicular in-plane direction*

Table 12: Membrane model parameters

	<i>Nr of cells</i> <i>X1</i>	<i>Nr of cells</i> <i>X2</i>	<i>Unit cell</i> <i>length X1</i> <i>(mm)</i>	<i>Unit cell</i> <i>length X2</i> <i>(mm)</i>	<i>Displacement in</i> <i>X1 direction</i> <i>(mm)</i>	<i>Displacement %</i> <i>of unit cell</i> <i>length in X1</i>
REH	2	1	15	20	3 (1.5 mm/cell)	10%
DAH	4	1	15	20	6 (1.5 mm/cell)	10%
HC	4	4	15	15	6 (1.5 mm/cell)	10%

### 9.2.2 Membrane elastic strain and stress results

For each structure is below a table and a stress and strain diagram of both the structure and the unit cells, with the latter taken from a central cell to exclude stress concentration effects at the edges.

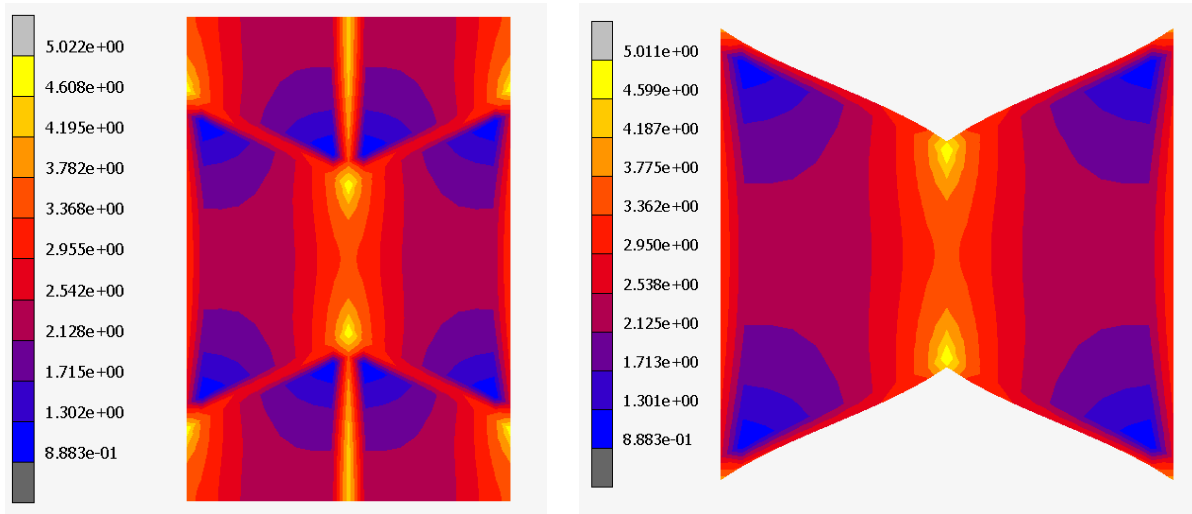
For the re-entrant model, geometries, test conditions and estimated Poisson's ratios with and without membrane are summarised in Table 13.

Table 13: Re-entrant hexagonal membrane results

<i>Cell width X2</i>	20 mm
<i>Cell height X1</i>	15 mm
<i>Beam length l</i>	12.2066 mm
<i>Beam length h</i>	22 mm
<i>Theta</i>	34.992 degrees
<i>Displacement X1</i>	3 mm (1.5 mm per unit cell) (30 mm to 33 mm) @10% real unit cell length X1 = 16.4967 mm Real unit cell displacement = 1.4967 mm
<i>Resultant displacement X2</i>	@10% 2.0769 mm (22.0769 mm new width)
<i>Nr of cells X1</i>	2
<i>Nr of cells X2</i>	1
<i>Analytically calculated Poisson's ratio for unit cell without membrane</i>	-1.09365
<i>Numerically calculated Poisson's ratio for unit cell with membrane</i>	-1.04074

Equivalent elastic strain and equivalent von Mises stress distribution for the re-entrant hexagonal membrane cell are represented in Figure 67.

## Equivalent Von Mises Stress



## Equivalent Elastic Strain

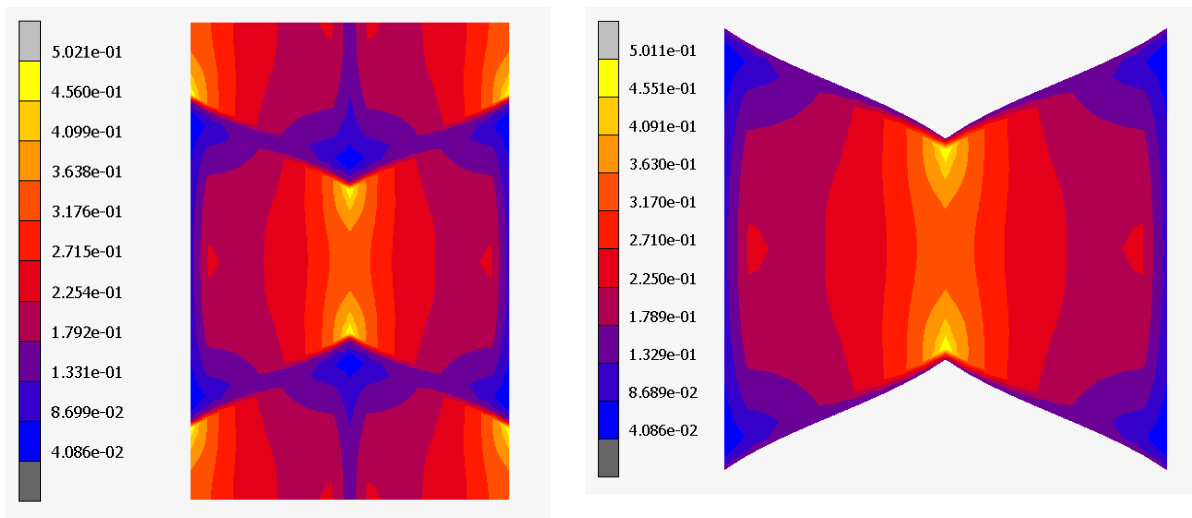


Figure 67: Re-entrant hexagonal membrane stresses and strains

For the double arrowhead, geometries, test conditions and estimated Poisson's ratios with and without membrane are summarised in Table 14.

Table 14: Double arrowhead membrane results

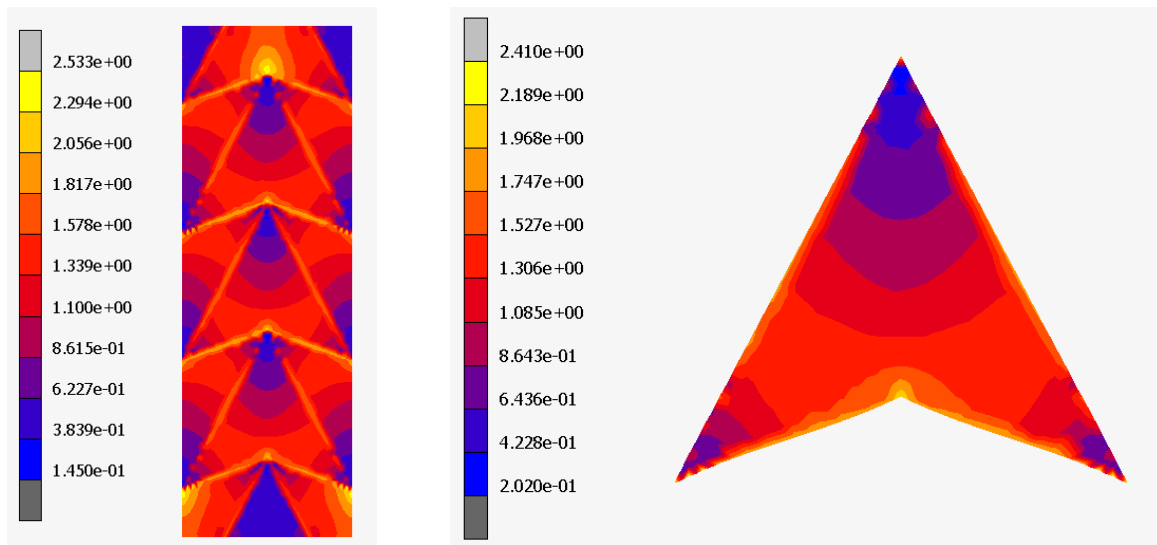
<i>Cell width X2</i>	20 mm
<i>Cell height X1</i>	15 mm
<i>Beam length la</i>	22.3607 mm
<i>Beam length lb</i>	11.1803 mm
<i>Alpha</i>	26.56505 Degrees
<i>Beta</i>	63.435 Degrees
<i>Displacement X1</i>	6 mm (1.5 mm per unit cell)
	New X1 length is 15.7502 mm
<i>Resultant displacement X2</i>	0.9841 mm (20.9841 mm new width)
<i>Nr of cells X1</i>	4



<i>Nr of cells X2</i>	1
<i>Analytically calculated Poisson's ratio for unit cell without membrane</i>	-1
<i>Numerically calculated Poisson's ratio for unit cell with membrane</i>	-0.98384

Equivalent of elastic strain and equivalent von Mises stress distribution for the double arrowhead membrane cell are represented in Figure 68.

#### Equivalent von Mises Stress



#### Equivalent Elastic Strain

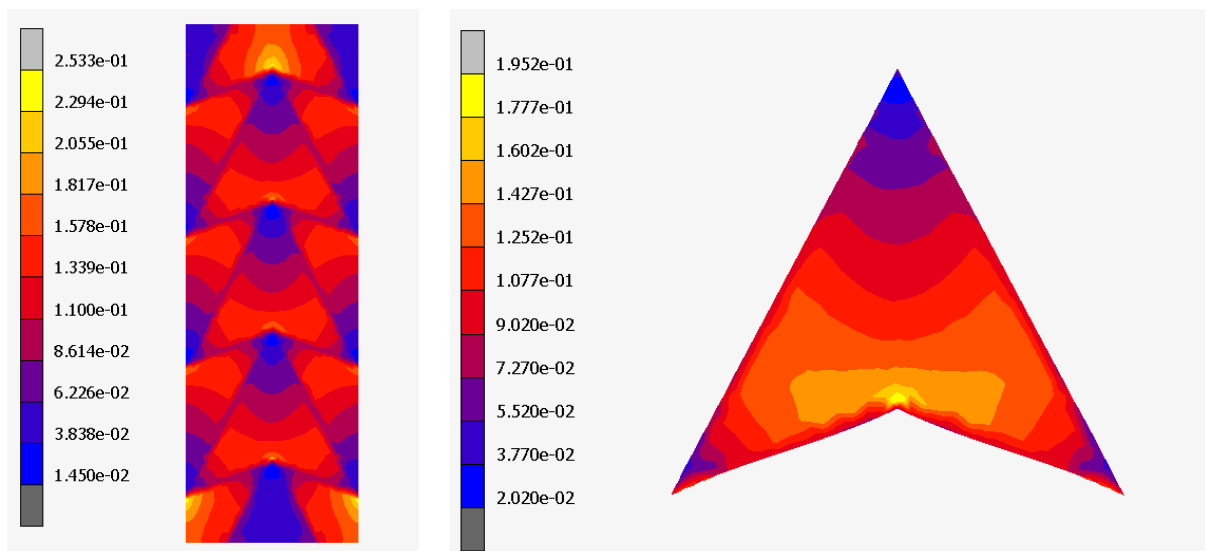


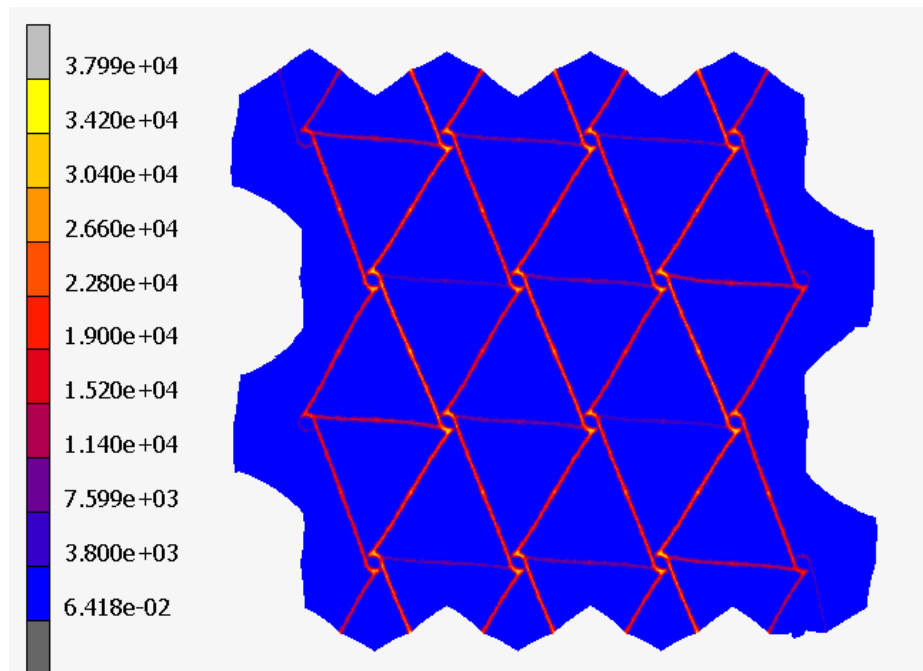
Figure 68: Double arrowhead membrane strain and stresses

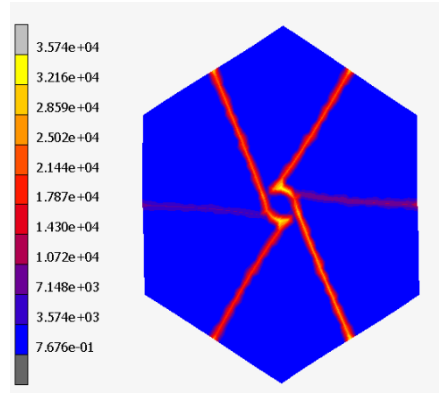
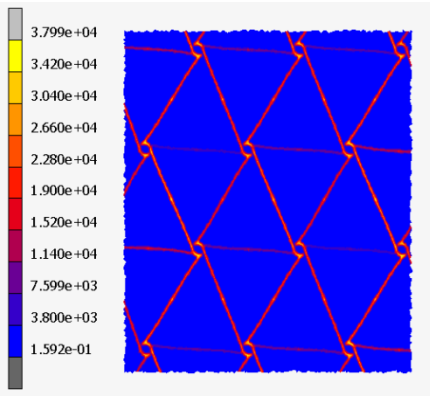
For the hexachiral model, geometries, test conditions and estimated Poisson's ratios with and without membrane are summarised in Table 15 and the resulting equivalent von Mises stresses and equivalent elastic strains are shown in Figure 69.

Table 15: Hexachiral membrane results

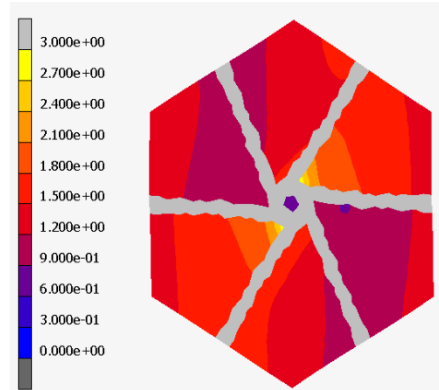
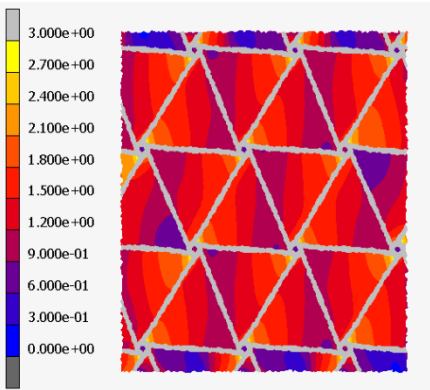
<i>Cell diameter <math>D</math></i>	15 mm
<i>Cell width <math>X2</math></i>	15 mm
<i>Cell height <math>X1</math></i>	17.3205 mm
<i>Beam length <math>L</math></i>	7.16437 mm
<i>Node diameter <math>2r</math></i>	1.67705 mm
<i>Displacement <math>X1</math></i>	1.5 mm (6 mm for all)
<i>Resultant displacement <math>X2</math></i>	19.293 mm Cell length $X1$
<i>Nr of cells <math>X1</math></i>	4
<i>Nr of cells <math>X2</math></i>	4
<i>Analytically calculated Poisson's ratio for unit cell without membrane</i>	0.04739
<i>Numerically calculated Poisson's ratio for unit cell with membrane</i>	0.113977

#### Equivalent Von Mises Stress





Equivalent Von Mises Stress with threshold excluding beam stresses



Equivalent Elastic Strain

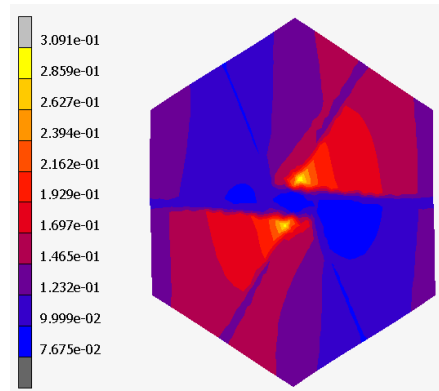
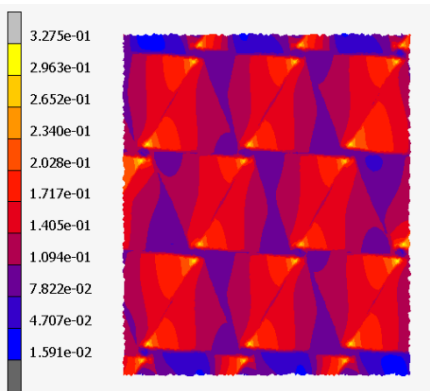


Figure 69: Top: Equivalent von Mises stress for the hexachiral configuration with membrane, Middle: Equivalent von Mises stress with threshold excluding beam stresses, Bottom: Equivalent elastic strain

In conclusion, results indicates that a thin silicone membrane would not impact the Poisson's ratio and auxetic behaviour significantly for the two re-entrant structures. For the chiral structure the results are more complex to interpret, as the results of any hexachiral structure that exhibits a NPR becomes unstable due to substantial out of plane deformation, see Figure 70, and the results hence are not necessarily accurate. Though, the deformation appears to be driven by the membrane rather than the beam structure mechanism in the cases where the beam structure was supposed to exhibit a NPR behaviour. This suggests that this structure is less suitable to be used in combination with membranes.

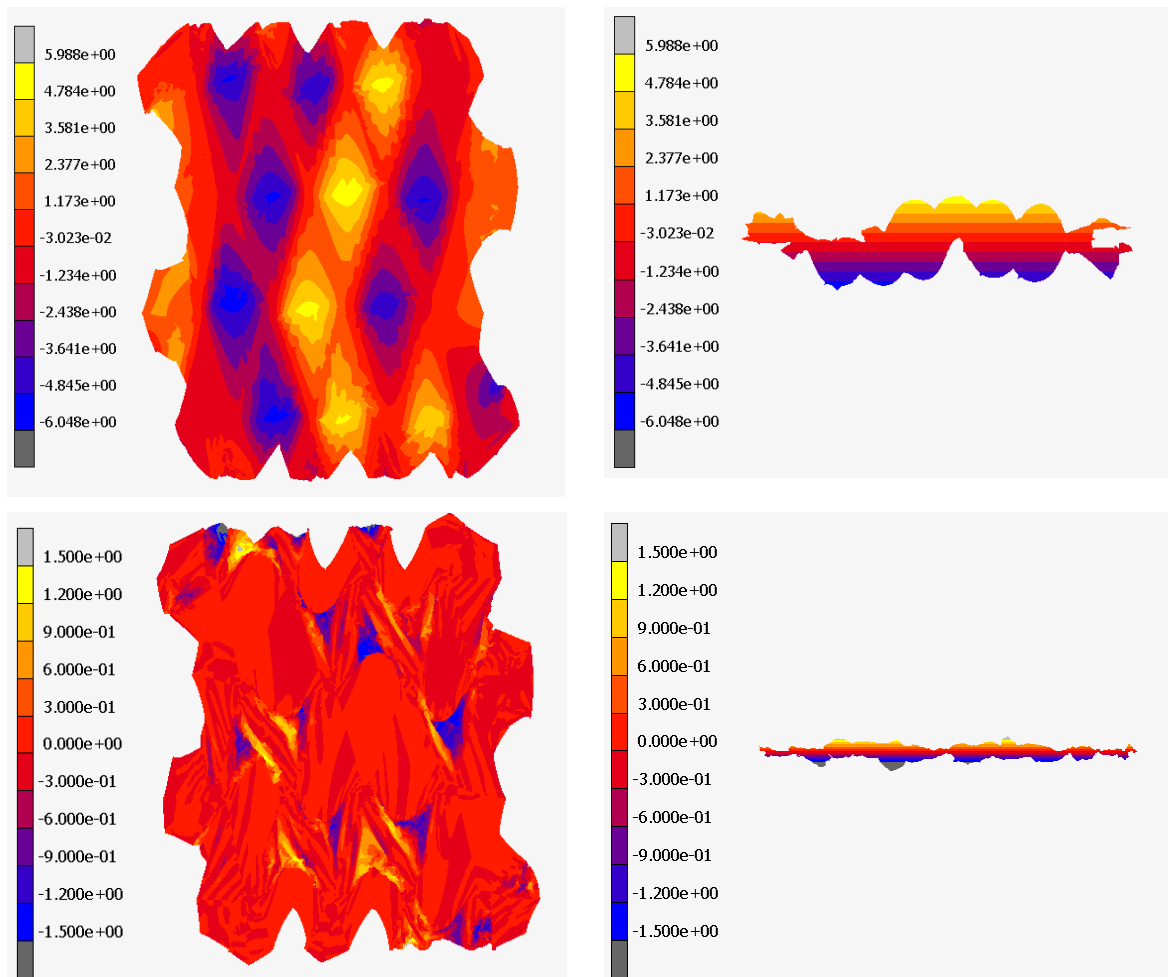


Figure 70: Instability of hexachiral membrane with struts of equivalent thickness to those for the double arrowhead and re-entrant hexagonal, with indications of out-of-plane deformations. To the left, in-plane view, to the right, out of plane view. At the top, the auxetic structure's struts were allowed to move out of plane, at the bottom the struts were restricted to in-plane movement (range of displacement shown in color narrowed for clarity).

### 9.3 Examples of cardiovascular applications possibly suitable for auxetic stents and design suggestions

For restoring the motion of a stiffened vessel, it would be more applicable to focus on surgical stent-grafts, as the native vessel around the endovascular stent graft would limit the motions and resist the dynamics of the implanted stent. For the case of an implantation site in an aneurysm, there is a possibility that the stent could impact on the dynamic pattern of the vessel, while reducing the strain on the vessel wall.

Examples of where this could be appropriate is the ascending aorta, for either endovascular grafting as treatment of ascending aorta aneurysm or surgical graft repair for stiffened, stenotic vessels. Auxetic configurations would allow, for example, to create a surgical stent-graft for the treatment of aneurysms of the ascending aorta, allowing to restore the optimum healthy dynamics of the native aortic root described in the clinical background.

Another suggested application would be in the area of non-invasive PPVI, Percutaneous Pulmonary Valve Implantation, device. As shown in the studies of the motion of the pulmonary artery, the simultaneous elongation and dilation is quite extreme, especially at the lower end of the vessel by the RVOT, right ventricular outflow tract, which expands greatly in diameter while having a simultaneous smaller elongation. The Poisson's ratio approaches zero around the valve, which is a naturally more rigid area, and then again turn negative at the upper end closer to the bifurcation. This variation of Poisson's ratio of the structure indicates that the ideal stent structure would be flexible at the ends and rigid in the middle, with a higher NPR at the lower end. This makes the hexachiral structure less suitable for the application. Since the NPR needed is larger than -1, and the pulmonary exhibits a very anisotropic behaviour, both the re-entrant hexagonal and the arrowhead structure could be considered.

To finetune the selection of parameters, a designated clinical study would be needed to make sure that needed measurements would be provided. Further indication of both the rigidity and shear rigidity of the native vessel, as well as the individual movement of the different sections of the vessels, would provide valuable guidance in tailored stent design.

#### 9.4 Case study: Design of auxetic stent graft for ascending aorta using re-entrant hexagonal honeycombs

To provide a proof-of-concept case study, the design of an auxetic stent for the ascending aorta a structure is presented below.

Since the observations of the motion of the ascending aorta have indicated an optimum Poisson's ratio of around -1 for the stent-graft, this theoretically gives the option of all the structures studied above. However, the observed motion of the healthy root also presents a twisting of the ascending aorta of about 6 degrees, which indicates that a structure with lower shear rigidity could be more suitable. Hence, the re-entrant hexagonal geometry would be, in this case, the most suitable configuration. In fact, the diagrams in chapter 7 indicate for this configuration a shear modulus lower for the double arrowhead of about one order of magnitude, and for the hexachiral of about 3 orders of magnitude. Moreover, the membrane exploration above indicates that re-entrant structures are more suitable to integrate sealing coverings, that in this application may be required.

##### 9.4.1 Introduction to Design Process

The initial base criteria for the design came from the anatomical data provided by George Tellides, a clinical collaborator at Yale University. The design process was divided into three stages.

The initial stage focused on designing a stent to suit the anatomical criteria of the ascending aorta as reported by Tellides, for a stent with diameter  $D = 23$  mm, using the analytical expressions presented earlier in the thesis.

The second stage focused on adapting this design to be able to be manufactured with laser cutting from a standard tube, 10 mm in diameter and 0.5 mm thickness, with a laser beam of diameter 0.5 mm.

The third stage consisted of numerically evaluating the designed shape using finite element analysis.

#### 9.4.2 Analytical design process

For the analytical design process, the equations and nomenclature presented in Chapter 5 [34] are used to relate the geometric variables of the stent structure to the mechanical properties of the stent.

The geometric variables of the stent are similar to the tubes above, with the length of the struts parallel to the length of the stent,  $h$ , the angled struts connecting them,  $l$ , the circular diameter of the struts,  $d$ , and the angle  $\theta$  between the angled struts and the direction perpendicular to the length of the stent. The other two geometrical variables are the number of cells of struts along the circumference of the stent,  $N_c$ , and the number of cells along the length of the stent,  $N_z$ .

The range of angles  $\theta$  considered were between  $0^\circ$  and  $40^\circ$ . The number of cells around the circumference of the stent,  $N_c$ , considered were between 4 and 12. The strut length  $l$  was dependent on this with the relationship:

$$l = \frac{D \pi}{2 N_c \cos \theta} \quad (\text{see 5.1})$$

where  $D = 23$  mm,  $4 < N_c < 12$ ,  $0 < \theta < 40$ .

The strut length  $h$  was studied in relation to the strut length  $l$ , where the  $h/l$  ratios were 1.25 to 2.0. The number of cells in the longitudinal direction,  $N_z$ , were dependent on the strut length  $h$ ,  $l$  and the angle  $\theta$ . To achieve the desired length of the stent,  $H$ , the number of cells in the longitudinal direction were adjusted to achieve the closest possible  $H$  for each combination, where:

$$H = N_z(h - l * \sin \theta) \quad (\text{see 6.4})$$

The most relevant mechanical properties to achieve are the Poisson's ratio and the radial compliance of the stent. The Poisson's ratio is calculated using the anatomical data, from the formula presented in Chapter 6:

$$\nu_{cz} = -\frac{\varepsilon_z}{\varepsilon_c} = -\frac{D(H'-H)}{(D'-D)H} \quad (\text{see 6.12})$$

where  $D'$  is the expanded systolic diameter,  $D$  the diastolic diameter,  $H'$  the expanded systolic length and  $H$  the diastolic length of the ascending aorta. To calculate the Poisson's ratio of the stent for different geometrical variables the following equation from Chapter 5 was used:

$$\nu_{cz} = -\frac{\varepsilon_z}{\varepsilon_c} = -\frac{\sin \theta}{\left(\frac{h}{l} - \sin \theta\right)} \times \frac{(\pi D)^2 - 3(dN_c \cos \theta)^2}{(\pi D \tan \theta)^2 + 3(dN_c \cos \theta)^2} \quad (\text{see 5.3})$$

For all angles below 28 degrees, the Poisson's ratio was too low for all combinations of  $h$  and  $l$ .

The manufacturing requirements of being able to make the stent out of a smaller, 10 mm diameter tube, put a limitation on maximum angle and minimum  $h/l$  ratio. To be able to have a 0.5 mm diameter gap (the size of the cutting laser beam) between the angular struts when the stent is crimped to 10 mm diameter, all angles above 32 degrees are excluded, as are all  $h/l$  ratios below 2.0, the maximum taken into consideration.

The Poisson's ratio for 30 degrees was the closest to the desired value of -1. The circumferential numbers of cells were selected to best approximate the desired radial compliance,  $C$ .

This is quantified as:

$$C = \frac{D' - D}{D P} * 100\% \quad (9.1) [49]$$

where  $P$  is the difference between the systolic and diastolic pressure, also known as pulse pressure. For these calculations, a typical systolic pressure of 120 mmHg and a typical diastolic pressure of 70 mm Hg were assumed, obtaining a pulse pressure of 50 mmHg, which corresponds to 6.6661 kPa.

To calculate the compliance of the theoretical shape of the stent, the equation used was:

$$C = \left( \frac{\pi^2 N_c \left( \frac{h}{l} - \sin \theta \right) \tan^2 \theta}{3 E_s \cos^2 \theta} \right) \left( \frac{D}{d N_c} \right)^4 * 100\% \quad (9.2) [49]$$

where  $E_s$  is the Young's Modulus of the material. The analytically calculated value for the radial compliance of the aorta was ca 1.82%/kPa.

For a beam diameter of 0.5 mm, only 4 cells around the circumference were possible, but when lowering the circular beam diameter to 0.45, the radial compliance necessary was possible to archive for 5 cells. For 6 cells however, the beams would be too small to allow practical manufacturing.

Since the structure was to be laser cut from a commercially available tube with a wall thickness of 0.5 mm, the beams are not circular, but about trapezoidal, with one dimension fixed at 0.5 mm. To accommodate for this, the second moment of area were calculated for a circular beam of diameter 0.45 mm, and this was used to find the width of the struts for a beam with the breath 0.5 mm and an equal second moment of area. This results in an 'in-plane' mean width of 0.25 mm. This is consistent with the requirement of a beam width smaller than the beam thickness (wall thickness) to avoid beam twisting during expansion and collapse of the stent.

#### 9.4.3 Numerical modelling process

Two CAD models were built using CATIA. One showing the larger structure, and one looking at the individual cells, which was used for the finite element analysis. Imported into the finite element program MSC Marc, they were subjected to an expansion imitating the thermal expansion used to enlarge the initial structure cut out from a 10 mm diameter tube, see Figure 71, to the final shape with a diameter of 23 mm. The material properties of Nitinol used for the model was a Poisson's ratio of 0.33 and a Young's Modulus of 70 MPa. The material was assumed as linear elastic.

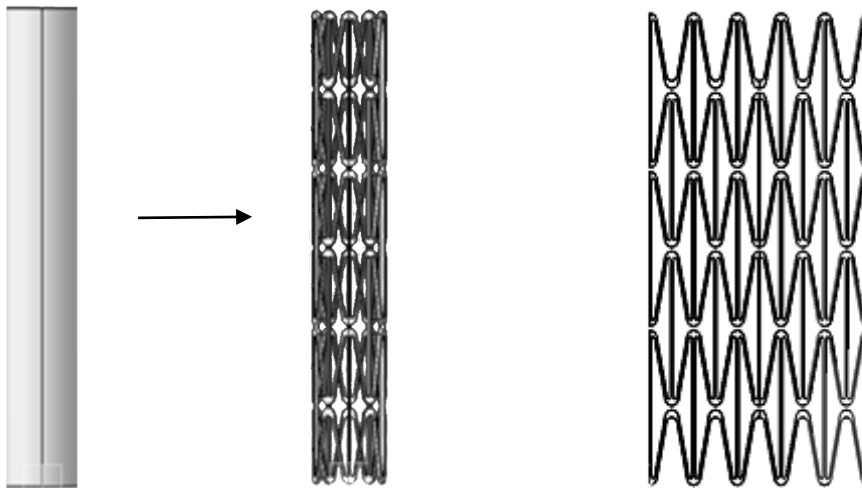


Figure 71: To the left, the pattern cut out from the tube; to the right, the unfolded pattern

It was decided to analyse a single cell to minimise computing time, while increasing accuracy of the analysis with a higher mesh density, see Figure 72. To account for the rest of the structure, symmetry planes were used, see



Figure 73. This allowed more elements being used for the single cell of the three-dimensional ten node tetrahedron element type, element number 127. [145]

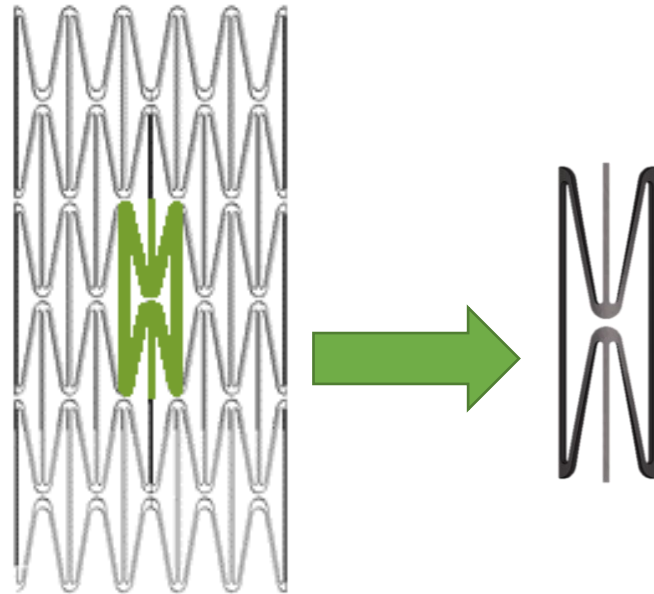


Figure 72: One cell cut out from the structure with the aid of symmetry plans to mark the presence of the other cells in the grid: cell marked in pattern on the left, isolated cell on the right.

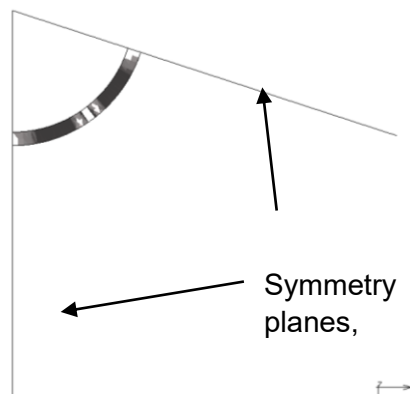


Figure 73: The cell flanked by symmetry planes marking the existence of the other cells, here around the circumference of the cylinder

The actual physical process of expanding a stent to the desired size would be to forcefully expand it and then thermally set it into the new shape. For the numerical model, the thermal expansion progress was simulated with the aid of an expanding inner cylinder. The stent unit cell was allowed to move along the circumferential symmetry planes, expanding without additional friction from those while mimicking the presence of further cells.

To validate the numerical models, the global mechanical properties exhibited by the model were compared to those calculated with the aid of the analytical study above. As already mentioned, the main global mechanical properties of interest were the Poisson's ratio ( $\nu_{cz}$ ) and the radial compliance ( $C$ ). These were determined using the expansion in the longitudinal direction, radial direction and the resultant forces acting on the stent.

#### 9.4.4 Resulting design

Table 16 reports the desired dimensions and global mechanical properties according to the anatomical data collected and analysed, and Table 17 show the resulting analytical design.

Table 16: Anatomical data

##### Anatomical study

<i>Asc Ao length <math>H</math></i>	66,2 mm
<i>Asc Ao length <math>H^*</math></i>	74,6 mm
<i>Asc Ao Diameter <math>D</math></i>	23,1 mm
<i>Asc Ao Diameter <math>D^*</math>, <math>D_p</math></i>	25,9 mm
<i>Poisson's ratio <math>\nu_{cz}</math></i>	-0,96
<i>Radial compliance <math>C</math></i>	1.82%/kPa

The radial compliance is calculated in %/kPa to better allow for comparison between the analytical analysis and the numerical models.

Table 17: Analytical design

##### Analytical design

<i>Global length <math>H</math></i>	63 mm
<i>Diameter <math>D</math></i>	23 mm
<i>Strut length <math>l</math></i>	8.35 mm
<i>Strut length <math>h</math></i>	16.7 mm
<i>Strut angle <math>\theta</math></i>	30°
<i>Number of cells <math>N_c</math></i>	5
<i>Number of cells <math>N_z</math></i>	5

Comparison of the analytical design to the numerical model is reported in Table 18.

Table 18: Comparison analytical design and numerical model

	Analytical design	Numerical model	% Difference
<i>Poisson's ratio <math>\nu_{cz}</math></i>	-1	-1,03	3%
<i>Radial compliance <math>C</math></i> %/kPa	1.83	1.87	2%

The final unit cell used in the numerical analysis is shown during ‘thermal’ expansion below in Figure 74 and Figure 75, and during ‘cardiac cycle’ in Figure 76. It is essential to observe that the departure from the analytical models maintains small and well acceptable, despite the geometrical alterations in the numerical 3D model to fit the manufacturing requirements of the stent. In fact, although the resulting non-uniform beam cross-sections and hinges have some effect, the analytically estimated elastic behaviour of an ideal structure still gives a good prediction for the more realistic unit cell studied here.

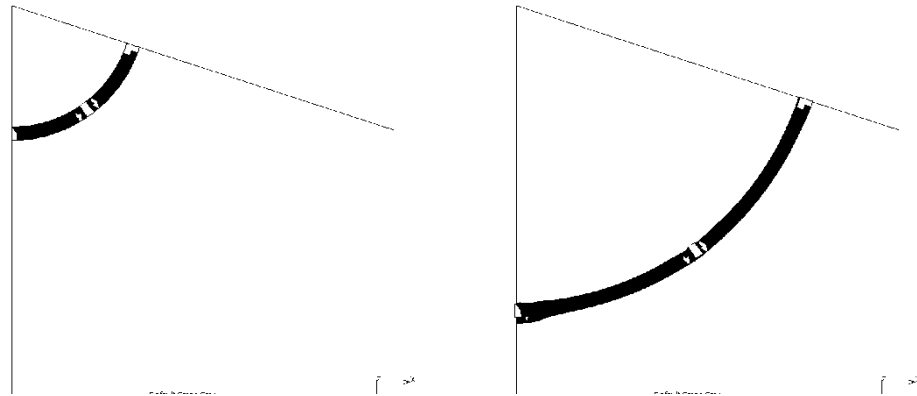


Figure 74: Expansion in the radial direction, symmetry planes shown, accounting for the rest of the cells around the circumference of the tube

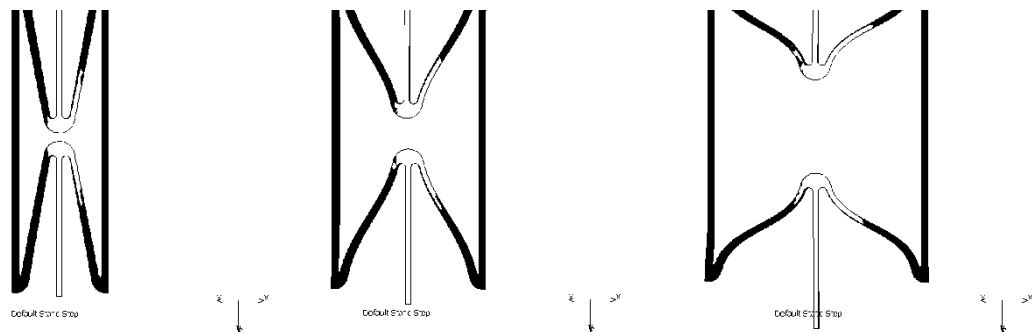


Figure 75: Expansion in the radial direction, view on cell showing expansion in both radial and longitudinal direction.

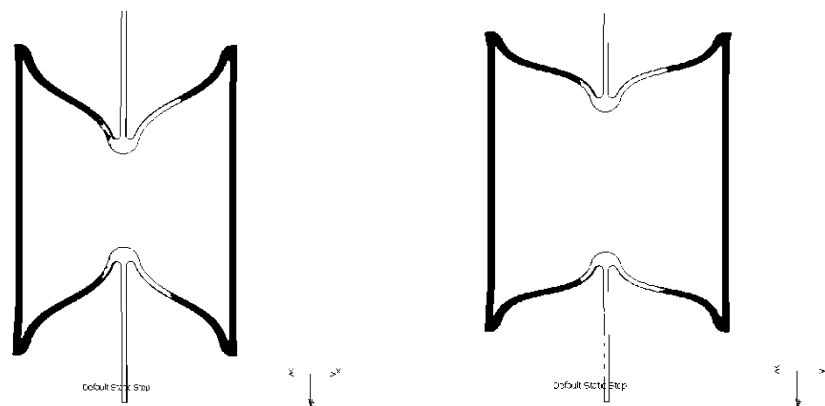


Figure 76: Shape of cell during the diastolic versus systolic phase of the cycle.

A view of the final device is shown in Figure 77.

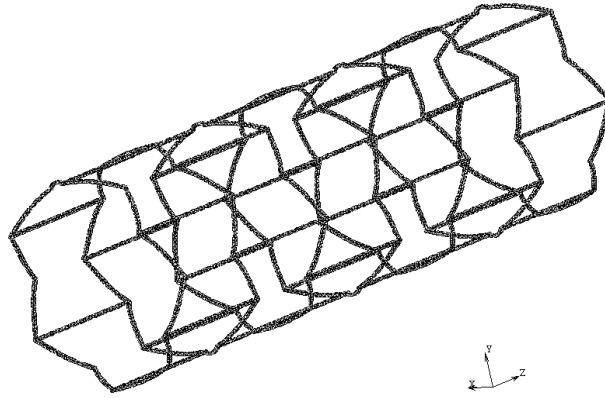


Figure 77: Final device in full

#### 9.4.5 General afternotes and concluding remarks

##### *Notes on kinking*

The factors affecting the kinking curvature, as observed by Karnessi & Burriesci [49], would be the  $h/l$  ratio, the number of cells in the circumferential direction and the angle between the stents  $\theta$ . The high  $h/l$  ratio of the design would lower the stents resistance to kinking but could not be avoided due to the manufacturing requirements. The low number of cells,  $N_c$ , in the circumferential direction works in favour for increasing the tolerance against kinking. The angle  $\theta$  could not have been altered greatly either due to the required specifications, though a slightly lower one could help, if required, to increase tolerance against kinking.

##### *Conclusion*

The behaviour of the more complex numerical model did not vary significantly from the analytical model predictions and the simpler idealised numerical models in earlier chapters. A design meeting the anatomical and physiological requirements was easily created, adopting the presented analysis, which allowed an immediate selection of a suitable auxetic configuration and its realistic dimensioning, taking into consideration a common manufacturing process. The approach provided an accurate design, despite the geometrical alterations in the numerical 3D model compared to the earlier idealised beam models, and due to the fact that the numerical 3D model had to be adjusted to fit the manufacturing requirements of the stent. The analytically estimated elastic behaviour of an ideal structure gives a good prediction for the more realistic unit cell studied here.

## 10. Conclusion and future works

After investigating the range of available auxetic structures to find potential ones for cardiovascular stent design, three auxetic cellular configurations were selected for further study. The comparison of the three structures, the re-entrant hexagonal, the double arrowhead and the hexachiral structures were done both analytically and numerically. To facilitate analytical comparison, original analytical expressions for the elastic behaviour of the double arrowhead were derived and proposed as part of the current work, as the available ones were incomplete. The three auxetic configurations were numerically investigated and adapted to tubular structures, and the effect of variation of the different geometrical properties of the structure on the mechanical response was studied for a range of parameters. The structures were subjected to axial tension, circumferential expansion, and twisting. These were then compared to each other to offer a guidance for selecting the most appropriate architecture for practical design application. The analysis indicates that the double arrowhead offers the largest range of Poisson's ratios, and the highest shear rigidity, while the re-entrant have a slightly smaller range of Poisson's ratios and by far the lowest shear rigidity of all three structures. Both exhibit an anisotropic behaviour and have a similar range of Young's modulus. The hexachiral differs much from the other two which have re-entrant deformation mechanisms, with its isotropic and very limited range of Poisson's ratio. The Young's modulus is less isotropic in the context of tubular structures with a thicker ligament than the theoretical one for the plane structures with a slightly higher Young's modulus than the other two. Finally, the mechanical behaviour of the structures was then analysed in relation to the clinical data available in respect to potential practical applications where auxetic configurations would allow stent designs more respectful of the physiological dynamics.

A new stent for the treatment of the stiffening of the ascending aorta was designed and presented as part of this work, exploiting the analysis of auxetic structures described in the first part of the thesis.

When looking at the limitations of the current models and practical implications of the suggested stent designs, there are a few areas that have been identified and partially analysed here, where further investigation would be useful.

The primary one for stent-graft design is the effect of membranes on an auxetic stent; the impact on the mechanical behaviour of the stent, and the possibility to mitigate this with selection of membrane type. Another is the potential effect of manufacturing methods on the mechanical properties, and to investigate if there is a preferred method to not negatively

impact the desired behaviour. A third is the effect of the length of the stent on the auxetic behaviour, and how the ends of the structure behaves.

From a clinical point of view more specific data would need to be collected, to optimally exploit the possibilities that auxetics can provide. Most clinical studies are incomplete from the auxetic stent design point of view, as all interesting factors are seldom included in studies using comparable methods.

Another device specific avenue for research is the impact of wall-device interactions. For this study, an ascending aortic stent-graft was discussed as a surgical option as most endovascular are used for stiffened aortas that would hamper the possible dynamics of a stent. However, similar principles could be a possibility for those with pathological changes associated with Marfans syndrome or hyper elastic vessels. In this case, maintaining the native aortic root might cause significant changes to the intended dynamics of a stent, and this would be important to study further.

## Bibliography

- [1] WHO, "WHO Health Topics Cardiovascular diseases," *Official WHO Website*, 2021. [https://www.who.int/health-topics/cardiovascular-diseases/#tab=tab\\_1](https://www.who.int/health-topics/cardiovascular-diseases/#tab=tab_1) (accessed Oct. 01, 2022).
- [2] British Heart Foundation, "UK Factsheet," *British Heart Foundation*, no. August. pp. 1–21, 2022. Accessed: Oct. 02, 2022. [Online]. Available: <https://www.bhf.org.uk/-/media/files/research/heart-statistics/bhf-cvd-statistics-uk-factsheet.pdf?rev=4b0be2cd03eb412f8f2703b63a3b4ebb&hash=E6965279D61DEA4CBD0C97E176CAA671>
- [3] British Heart Foundation, "Global Heart & Circulatory Diseases Factsheet," *British Heart Foundation*, no. August. pp. 1–12, 2022. Accessed: Oct. 02, 2022. [Online]. Available: <https://www.bhf.org.uk/-/media/files/research/heart-statistics/bhf-cvd-statistics-global-factsheet.pdf?rev=1ec126bd94344f8cade4d86df6f0598c&hash=7E7D15FC4B59B6544C92A19DCF8F4B9E>
- [4] WHO International, "WHO Fact Sheet The top 10 causes of death," <https://www.who.int/news-room/fact-sheets/detail/the-top-10-causes-of-death>, Dec. 09, 2020. <https://www.who.int/news-room/fact-sheets/detail/the-top-10-causes-of-death> (accessed Oct. 02, 2022).
- [5] D. A. Rubenstein, W. Yin, and M. D. Frame, "The heart," in *Biofluid Mechanics*, Elsevier, 2022, pp. 157–205. doi: 10.1016/B978-0-12-818034-1.00005-0.
- [6] "Disease: Anatomy & Physiology. [Online]. Available: <http://www.micardia.com/CHF-Congestive-Heart-Failure/Structural-heart-disease-and-mitral-prolapses.php>." 2010.
- [7] J. M. Kuijpers and B. J. M. Mulder, "Aortopathies in adult congenital heart disease and genetic aortopathy syndromes : management strategies and indications for surgery," 2017, doi: 10.1136/heartjnl-2015-308626.
- [8] F. Terms, "Chapter VI : Deformation of the Ascending Aorta During One Heart Cycle," 2010. doi: 10.3109/00016926209173871.
- [9] T. Plonek, B. Rylski, P. Nawrocki, F. Beyersdorf, M. Jasinski, and W. Kulickowski, "Systolic stretching of the ascending aorta," in *Archives of Medical Science*, 2021, pp. 25–30. doi: 10.5114/aoms.2019.82997.
- [10] C. J. Beller, M. R. Labrosse, M. J. Thubrikar, and F. Robicsek, "Role of Aortic Root Motion in the Pathogenesis of Aortic Dissection," pp. 763–769, 2004, doi: 10.1161/01.CIR.0000112569.27151.F7.
- [11] T. Kru, A. Oikonomou, D. Schibilsky, M. Lescan, K. Bregel, and L. Vo, "Aortic elongation and the risk for dissection: the Tübingen Aortic Pathoanatomy (TAIPAN) project," *European Journal of Cardio-thoracic Surgery*, vol. 51, no. February, pp. 1119–1126, 2017, doi: 10.1093/ejcts/ezx005.
- [12] S. Z. Pagoulatou, M. Ferraro, B. Trachet, V. Bikia, G. Rovas, and L. A. Crowe, "The effect of the elongation of the proximal aorta on the estimation of the aortic wall distensibility," *Biomech Model Mechanobiol*, vol. 20, no. 1, pp. 107–119, 2021, doi: 10.1007/s10237-020-01371-y.

- [13] C. J. Beller, M. R. Labrosse, M. J. Thubrikar, G. Szabo, F. Robicsek, and S. Hagl, "Increased aortic wall stress in aortic insufficiency: Clinical data and computer model," in *European Journal of Cardio-thoracic Surgery*, Feb. 2005, pp. 270–275. doi: 10.1016/j.ejcts.2004.11.011.
- [14] J. Ferruzzi, P. Di Achille, G. Tellides, and J. D. Humphrey, "Combining in vivo and in vitro biomechanical data reveals key roles of perivascular tethering in central artery function," *PLoS One*, vol. 13, no. 9, pp. 1–21, 2018, doi: 10.1371/journal.pone.0201379.
- [15] V. Bell *et al.*, "Longitudinal and circumferential strain of the proximal aorta," *J Am Heart Assoc*, vol. 3, no. 6, pp. 1–11, 2014, doi: 10.1161/JAHA.114.001536.
- [16] D. Muraru *et al.*, "Ascending aorta diameters measured by echocardiography using both leading edge-to-leading edge and inner edge-to-inner edge conventions in healthy volunteers," *Eur Heart J Cardiovasc Imaging*, vol. 15, no. 4, pp. 415–422, 2014, doi: 10.1093/ehjci/jet173.
- [17] J. Huang, Y. Wang, L. Lin, Z. Li, Z. Shan, and S. Zheng, "Comparison of dynamic changes in aortic diameter during the cardiac cycle measured by computed tomography angiography and transthoracic echocardiography," *J Vasc Surg*, vol. 69, no. 5, pp. 1538–1544, 2019, doi: 10.1016/j.jvs.2018.07.083.
- [18] A. T. Cheung and S. J. Weiss, "Diseases of the Aorta," in *Intraoperative Echocardiography*, D. C. Oxorn, Ed., Elsevier, 2012, pp. 161–182. doi: 10.1016/B978-1-4377-2698-5.00007-X.
- [19] J. D. Humphrey and S. Na, "Elastodynamics and arterial wall stress," *Ann Biomed Eng*, vol. 30, no. 4, pp. 509–523, 2002, doi: 10.1114/1.1467676.
- [20] I. D. Breslavsky and M. Amabili, "Fitting mechanical properties of the aortic wall and individual layers to experimental tensile tests including residual stresses," *J Mech Behav Biomed Mater*, vol. 138, no. December 2022, p. 105647, 2023, doi: 10.1016/j.jmbbm.2022.105647.
- [21] S. Pejdic, S. M. Ali Hassan, D. E. Rival, and G. Bisleri, "Characterizing the mechanical properties of the aortic wall," *Vessel Plus*, vol. 3, pp. 1–12, 2019, doi: 10.20517/2574-1209.2019.18.
- [22] C. Bellini, J. Ferruzzi, S. Roccabianca, E. S. di Martino, and J. D. Humphrey, "A microstructurally motivated model of arterial wall mechanics with mechanobiological implications," *Ann Biomed Eng*, vol. 42, no. 3, pp. 488–502, 2014, doi: 10.1007/s10439-013-0928-x.
- [23] S. Roccabianca, C. A. Figueroa, G. Tellides, and J. D. Humphrey, "Quantification of regional differences in aortic stiffness in the aging human," *J Mech Behav Biomed Mater*, vol. 29, pp. 618–634, 2014, doi: 10.1016/j.jmbbm.2013.01.026.
- [24] S. Avril, "Aortic and Arterial Mechanics," in *Cardiovascular Mechanics*, Boca Raton, FL : CRC Press/Taylor & Francis Group, [2018]: CRC Press, 2018, pp. 183–226. doi: 10.1201/b21917-6.
- [25] L. H. Timmins, Q. Wu, A. T. Yeh, J. E. Moore, and S. E. Greenwald, "Structural inhomogeneity and fiber orientation in the inner arterial media," *Am J Physiol Heart Circ Physiol*, vol. 298, no. 5, pp. 1537–1545, 2010, doi: 10.1152/ajpheart.00891.2009.



- [26] G. V. Guinea *et al.*, “Factors influencing the mechanical behaviour of healthy human descending thoracic aorta,” *Physiol Meas*, vol. 31, no. 12, pp. 1553–1565, 2010, doi: 10.1088/0967-3334/31/12/001.
- [27] A. N. Azadani *et al.*, “Comparison of mechanical properties of human ascending aorta and aortic sinuses,” *Annals of Thoracic Surgery*, vol. 93, no. 1, pp. 87–94, 2012, doi: 10.1016/j.athoracsur.2011.08.002.
- [28] M. Alreshidan *et al.*, “Obtaining the biomechanical behavior of ascending aortic aneurysm via the use of novel speckle tracking echocardiography,” *J Thorac Cardiovasc Surg*, vol. 153, no. 4, pp. 781–788, Apr. 2017, doi: 10.1016/j.jtcvs.2016.11.056.
- [29] S. Schievano *et al.*, “Four-dimensional computed tomography: A method of assessing right ventricular outflow tract and pulmonary artery deformations throughout the cardiac cycle,” *Eur Radiol*, vol. 21, no. 1, pp. 36–45, 2011, doi: 10.1007/s00330-010-1913-5.
- [30] Q. A. Truong *et al.*, “Reference Values for Normal Pulmonary Artery Dimensions by Noncontrast Cardiac Computed Tomography The Framingham Heart Study,” 2011, doi: 10.1161/CIRCIMAGING.111.968610.
- [31] C. Capelli, A. M. Taylor, F. Migliavacca, and S. Schievano, “Patient-specific reconstructed anatomies and computer simulations are fundamental for selecting medical device treatment : application to a new percutaneous pulmonary valve,” no. January, 2014, doi: 10.1098/rsta.2010.0088.
- [32] F. Cuomo, S. Roccabianca, D. Dillon-Murphy, N. Xiao, J. D. Humphrey, and C. A. Figueroa, “Effects of age-associated regional changes in aortic stiffness on human hemodynamics revealed by computational modeling,” *PLoS One*, vol. 12, no. 3, pp. 1–21, 2017, doi: 10.1371/journal.pone.0173177.
- [33] C. Martin, W. Sun, C. Primiano, R. McKay, and J. Elefteriades, “Age-dependent ascending aorta mechanics assessed through multiphase CT,” *Ann Biomed Eng*, vol. 41, no. 12, pp. 2565–2574, 2013, doi: 10.1007/s10439-013-0856-9.
- [34] T. M. Morrison, G. Choi, C. K. Zarins, and C. A. Taylor, “Circumferential and longitudinal cyclic strain of the human thoracic aorta: Age-related changes,” *J Vasc Surg*, vol. 49, no. 4, pp. 1029–1036, 2009, doi: 10.1016/j.jvs.2008.11.056.
- [35] M. D. Martin B. Leon, M.D., Craig R. Smith, M.D., Michael Mack, M.D., D. Craig Miller, M.D., Jeffrey W. Moses, M.D., Lars G. Svensson, M.D., Ph.D., E. Murat Tuzcu, M.D., John G. Webb, M.D., Gregory P. Fontana, M.D., Raj R. Makkar, M.D., David L. Brown, M.D., Pe and for the P. T. I. Augusto D. Pichard, M.D., Joseph E. Bavaria, M.D., Howard C. Herrmann, M.D., Pamela S. Douglas, M.D., John L. Petersen, M.D., Jodi J. Akin, M.S., William N. Anderson, Ph.D., Duolao Wang, Ph.D., and Stuart Pocock, Ph.D., “Transcatheter Aortic-Valve Implantation for Aortic Stenosis in Patients Who Cannot Undergo Surgery,” *N Engl J Med*, vol. 363, no. 17, pp. 1597–1607, 2010.
- [36] BHF, “BHF Coronary Angioplasty and Stents Treatment Information and Support,” <https://www.bhf.org.uk/informationsupport/treatments/coronary-angioplasty-and-stents>, 2020.

- [37] Jim Ritter (Loyola University Health System), "More aortic chest aneurysms being treated with less-invasive stents," 26-Aug-2008.  
[https://www.eurekalert.org/pub\\_releases/2008-08/luhs-mac082608.php](https://www.eurekalert.org/pub_releases/2008-08/luhs-mac082608.php) (accessed Jan. 27, 2020).
- [38] D. Stoeckel, A. Pelton, and T. Duerig, "Self-expanding Nitinol stents: Material and design considerations," *Eur Radiol*, vol. 14, no. 2, pp. 292–301, 2004, doi: 10.1007/s00330-003-2022-5.
- [39] D. Kapoor, "Nitinol for Medical Applications: A Brief Introduction to the Properties and Processing of Nickel Titanium Shape Memory Alloys and their Use in Stents," *Johnson Matthey Technology Review*, vol. 61, no. 1, pp. 66–76, 2017, doi: 10.1595/205651317X694524.
- [40] L. Petrini and F. Migliavacca, "Biomedical Applications of Shape Memory Alloys," *Journal of Metallurgy*, vol. 2011, no. Figure 1, pp. 1–15, 2011, doi: 10.1155/2011/501483.
- [41] S. Tzamtzis, J. Viquerat, J. Yap, M. J. Mullen, and G. Burriesci, "Numerical analysis of the radial force produced by the Medtronic-CoreValve and Edwards-SAPIEN after transcatheter aortic valve implantation (TAVI)," *Med Eng Phys*, vol. 35, no. 1, pp. 125–130, 2013, doi: 10.1016/j.medengphys.2012.04.009.
- [42] C. Moretti *et al.*, "Meta-Analysis of Comparison Between Self-Expandable and Balloon-Expandable Valves for Patients Having Transcatheter Aortic Valve Implantation," *Am J Cardiol*, vol. 115, no. 12, pp. 1720–1725, 2015, doi: 10.1016/j.amjcard.2015.03.015.
- [43] B. M. Jones, A. Krishnaswamy, E. M. Tuzcu, and S. Mick, "Matching patients with the ever - expanding range of TAVI devices," *Nature Publishing Group*, vol. 14, no. 10, pp. 615–626, 2017, doi: 10.1038/nrcardio.2017.82.
- [44] N. Demanget, A. Duprey, P. Badel, C. Geindreau, J. Favre, and L. Sols-solides-structures-risques, "Finite Element Analysis of the Mechanical Performances of 8 Marketed Aortic Stent-Grafts," *Journal of Endovascular Therapy*, vol. 20, no. 4, pp. 523–535, 2013.
- [45] T. C. Poerner, K. K. Haase, and S. Duda, "Impact of stent design on clinical outcome after coronary stent implantation," *Minimally Invasive Therapy and Allied Technologies*, vol. 11, no. 4, pp. 203–209, 2002, doi: 10.1080/136457002760273421.
- [46] B. Peters, P. Ewert, and F. Berger, "The role of stents in the treatment of congenital heart disease: Current status and future perspectives," *Ann Pediatr Cardiol*, vol. 2, no. 1, pp. 3–23, 2009, doi: 10.4103/0974-2069.52802.
- [47] S. Shukla and B. K. Behera, "Auxetic fibrous materials and structures in medical engineering—a review," *Journal of the Textile Institute*, vol. 0, no. 0, pp. 1–12, 2022, doi: 10.1080/00405000.2022.2116549.
- [48] R. Gatt *et al.*, "On the properties of real finite-sized planar and tubular stent-like auxetic structures," *Physica Status Solidi (B)*, vol. 251, no. 2, pp. 321–327, 2014, doi: 10.1002/pssb.201384257.
- [49] N. Karnesis and G. Burriesci, "Uniaxial and buckling mechanical response of auxetic cellular tubes," *Smart Mater Struct*, vol. 22, no. 8, 2013, doi: 10.1088/0964-1726/22/8/084008.

- [50] C. Luo, C. Zhen, X. Yu, X. Gang, X. Ren, and Y. Min, "Thin-Walled Structures Design , manufacturing and applications of auxetic tubular structures : A review," vol. 163, no. December 2020, 2021, doi: 10.1016/j.tws.2021.107682.
- [51] X. Ren, J. Shen, A. Ghaedizadeh, H. Tian, and Y. M. Xie, "A simple auxetic tubular structure with tuneable mechanical properties," *Smart Mater Struct*, vol. 25, no. 6, 2016, doi: 10.1088/0964-1726/25/6/065012.
- [52] W. Wu, X. Song, J. Liang, R. Xia, G. Qian, and D. Fang, "Mechanical properties of anti-tetrachiral auxetic stents," *Compos Struct*, vol. 185, no. July 2017, pp. 381–392, 2018, doi: 10.1016/j.compstruct.2017.11.048.
- [53] R. Hamzehei, S. Rezaei, J. Kadkhodapour, A. P. Anaraki, and A. Mahmoudi, "2D triangular anti-trichiral structures and auxetic stents with symmetric shrinkage behavior and high energy absorption," *Mechanics of Materials*, vol. 142, p. 103291, Mar. 2020, doi: 10.1016/j.mechmat.2019.103291.
- [54] L. C. Geng, X. L. Ruan, W. W. Wu, R. Xia, and D. N. Fang, "Mechanical Properties of Selective Laser Sintering (SLS) Additive Manufactured Chiral Auxetic Cylindrical Stent," *Exp Mech*, vol. 59, no. 6, pp. 913–925, Jul. 2019, doi: 10.1007/s11340-019-00489-0.
- [55] J. Liu *et al.*, "A flexible porous chiral auxetic tracheal stent with ciliated epithelium," *Acta Biomater*, vol. 124, pp. 153–165, Apr. 2021, doi: 10.1016/j.actbio.2021.01.044.
- [56] K. Kuribayashi *et al.*, "Self-deployable origami stent grafts as a biomedical application of Ni-rich TiNi shape memory alloy foil," *Materials Science and Engineering: A*, vol. 419, no. 1–2, pp. 131–137, Mar. 2006, doi: 10.1016/j.msea.2005.12.016.
- [57] M. N. Ali and I. U. Rehman, "An Auxetic structure configured as oesophageal stent with potential to be used for palliative treatment of oesophageal cancer; development and in vitro mechanical analysis," *J Mater Sci Mater Med*, vol. 22, no. 11, pp. 2573–2581, Nov. 2011, doi: 10.1007/s10856-011-4436-y.
- [58] F. Amin, M. N. Ali, U. Ansari, M. Mir, M. A. Minhas, and W. Shahid, "Auxetic coronary stent endoprosthesis: Fabrication and structural analysis," *J Appl Biomater Funct Mater*, vol. 13, no. 2, pp. E127–E135, Apr. 2015, doi: 10.5301/jabfm.5000213.
- [59] C. Lin, L. J. Zhang, Y. J. Liu, L. W. Liu, and J. S. Leng, "4D printing of personalized shape memory polymer vascular stents with negative Poisson's ratio structure: A preliminary study," *Sci China Technol Sci*, vol. 63, no. 4, pp. 578–588, 2020, doi: 10.1007/s11431-019-1468-2.
- [60] Z. Wu *et al.*, "Radial Compressive Property and the Proof-of-Concept Study for Realizing Self-expansion of 3D Printing Polylactic Acid Vascular Stents with Negative Poisson's Ratio Structure," *Materials*, vol. 11, no. 8, p. 1357, Aug. 2018, doi: 10.3390/ma11081357.
- [61] T. Vydts, A. Marinakis, P. Sinnaeve, C. Dubois, and W. Desmet, "Stents can jump!," *Int J Cardiol*, vol. 122, no. 1, pp. 93–95, Oct. 2007, doi: 10.1016/j.ijcard.2006.11.047.
- [62] A. Seth and A. Dhall, "Longitudinal stent shortening: The long and short of it!," *Catheterization and Cardiovascular Interventions*, vol. 81, no. 5. John Wiley and Sons Inc, pp. 818–819, Apr. 01, 2013. doi: 10.1002/ccd.24899.

- [63] P. Vogt, E. Eeckhout, J. -C Stauffer, J. -J Goy, and L. Kappenberger, "Stent shortening and elongation: Pitfalls with the wiktcor coronary endoprosthesis," *Cathet Cardiovasc Diagn*, vol. 31, no. 3, pp. 233–235, 1994, doi: 10.1002/ccd.1810310315.
- [64] K. E. Evans, M. A. Nkansah, I. J. Hutchinson, and S. C. Rogers, "Molecular Network Design," *Nature*, vol. 353. p. 124, 1991.
- [65] K. W. Wojciechowski, "Constant thermodynamic tension monte carlo studies of elastic properties of a two-dimensional system of hard cyclic hexamers," *Mol Phys*, vol. 61, no. 5, pp. 1247–1258, 1987.
- [66] J. N. Grima, A. Alderson, and K. E. Evans, "An Alternative Explanation for the Negative Poisson ' s Ratios in Auxetic Foams," *J Physical Soc Japan*, vol. 74, no. 4, pp. 1341–1342, 2005, doi: 10.1143/JPSJ.74.1341.
- [67] K. E. Evans, "The design of doubly curved sandwich panels with honeycomb cores," *Compos Struct*, vol. 17, no. 2, pp. 95–111, 1991, doi: 10.1016/0263-8223(91)90064-6.
- [68] L. J. Gibson and M. F. Ashby, *Cellular solids: Structure and properties, second edition*. Cambridge: Cambridge University Press, 1997. doi: 10.1017/CBO9781139878326.
- [69] L. J. Gibson, M. F. Ashby, G. S. Schajer, and C. I. Robertson, "The Mechanics of Two-Dimensional Cellular Materials," *Proceedings of the Royal Society A: Mathematical, Physical and Engineering Sciences*, vol. 382, no. 1782, pp. 25–42, 1982, doi: 10.1098/rspa.1982.0087.
- [70] A. Alderson and K. L. Alderson, "Auxetic materials," *Proc Inst Mech Eng G J Aerosp Eng*, vol. 221, no. 4, pp. 565–575, 2007, doi: 10.1243/09544100JAERO185.
- [71] K. E. Evans, "Auxetic polymers," *Membrane Technology*, no. 137, p. 9, 2001, doi: 10.1016/s0958-2118(01)80300-1.
- [72] R. S. Lakes, "Negative-Poisson's-Ratio Materials : Auxetic Solids," *Annu Rev Mater Res*, no. 47, pp. 63–81, 2017, doi: 10.1146/annurev-matsci-070616-124118.
- [73] P. Ma, Y. Chang, A. Boakye, and G. Jiang, "Review on the knitted structures with auxetic effect," *Journal of the Textile Institute*, vol. 108, no. 6, pp. 947–961, 2017, doi: 10.1080/00405000.2016.1204901.
- [74] K. Alderson, A. Alderson, S. Anand, V. Simkins, S. Nazare, and N. Ravirala, "Auxetic warp knit textile structures," *Phys Status Solidi B Basic Res*, vol. 249, no. 7, pp. 1322–1329, 2012, doi: 10.1002/pssb.201084216.
- [75] M. Sanami, N. Ravirala, K. Alderson, and A. Alderson, "Auxetic materials for sports applications," *Procedia Eng*, vol. 72, pp. 453–458, 2014, doi: 10.1016/j.proeng.2014.06.079.
- [76] F. C. Smith, F. L. Scarpa, and G. Burriesci, "Simultaneous optimization of the electromagnetic and mechanical properties of honeycomb materials," *Smart Structures and Materials*, vol. 4701, no. July 2002, pp. 582–591, 2002, doi: 10.1117/12.474693.
- [77] L. J. Gibson, M. F. Ashby, G. S. Schajer, and C. I. Robertson, "The mechanics of two-dimensional cellular materials," *Proc. R. Soc. Lond. B.*, vol. 42, no. 382, pp. 25–42, 1982, doi: 10.1098/rspa.1974.0120.

- [78] R. F. Almgren, "An isotropic three-dimensional structure with Poisson's ratio  $=-1$ ," *J Elast*, vol. 15, no. 4, pp. 427–430, 1985, doi: 10.1007/BF00042531.
- [79] U. D. Larsen, O. Sigmund, and S. Bouwstra, "Design and fabrication of compliant micromechanisms and structures with negative Poisson's ratio," *Journal of Microelectromechanical Systems*, vol. 6, no. 2, pp. 99–106, 1997, doi: 10.1109/84.585787.
- [80] J. N. Grima, R. Gatt, A. Alderson, and K. E. Evans, "On the potential of connected stars as auxetic systems," *Mol Simul*, vol. 31, no. 13, pp. 925–935, 2005, doi: 10.1080/08927020500401139.
- [81] P. S. Theocaris, G. E. Stavroulakis, and P. D. Panagiotopoulos, "Negative Poisson's ratios in composites with star-shaped inclusions: A numerical homogenization approach," *Archive of Applied Mechanics*, vol. 67, no. 4, pp. 274–286, 1997, doi: 10.1007/s004190050117.
- [82] J. N. Grima, R. Caruana-Gauci, K. W. Wojciechowski, and K. E. Evans, "Smart hexagonal truss systems exhibiting negative compressibility through constrained angle stretching," *Smart Mater Struct*, vol. 22, no. 8, 2013, doi: 10.1088/0964-1726/22/8/084015.
- [83] I. G. Masters and K. E. Evans, "Models for the elastic deformation of honeycombs," *Compos Struct*, vol. 35, no. 4, pp. 403–422, 1996, doi: 10.1016/S0263-8223(96)00054-2.
- [84] S. Malek and L. Gibson, "Effective elastic properties of periodic hexagonal honeycombs," *Mechanics of Materials*, vol. 91, no. P1, pp. 226–240, 2015, doi: 10.1016/j.mechmat.2015.07.008.
- [85] J. N. Grima, D. Attard, B. Ellul, and R. Gatt, "An improved analytical model for the elastic constants of auxetic and conventional hexagonal honeycombs Joseph N. Grima, Daphne Attard, Brian Ellul and Ruben Gatt," *Cellular Polymers*, vol. 30, no. 6, pp. 287–310, 2011.
- [86] S. Balawi and J. L. Abot, "A refined model for the effective in-plane elastic moduli of hexagonal honeycombs," *Compos Struct*, vol. 84, no. 2, pp. 147–158, 2008, doi: 10.1016/j.compstruct.2007.07.009.
- [87] S. Balawi and J. L. Abot, "The effect of honeycomb relative density on its effective in-plane elastic moduli: An experimental study," *Compos Struct*, vol. 84, no. 4, pp. 293–299, 2008, doi: 10.1016/j.compstruct.2007.08.009.
- [88] L. J. Gibson, "The elastic and plastic behaviour of cellular materials," University of Cambridge, 1981. [Online]. Available: <https://www.repository.cam.ac.uk/handle/1810/244863%0Ahttps://doi.org/10.17863/CAM.14049>
- [89] S. Gonella and M. Ruzzene, "Homogenization and equivalent in-plane properties of two-dimensional periodic lattices," *Int J Solids Struct*, vol. 45, pp. 2897–2915, 2008, doi: 10.1016/j.ijsolstr.2008.01.002.
- [90] I. E. Berinskii, "In-plane elastic properties of auxetic multilattices," *Smart Mater Struct*, vol. 27, 2018.

- [91] J. N. Grima, R. Gatt, T. G. C. Bray, A. Alderson, and K. E. Evans, "Empirical modelling using dummy atoms ( EMUDA ): an alternative approach for studying ' auxetic ' structures," *Mol Simul*, vol. 31, no. 13, pp. 915–924, 2005, doi: 10.1080/08927020500401121.
- [92] S. Chen and S. C. Ryu, "Design and characterization of rounded re-entrant honeycomb patterns for lightweight and rigid auxetic structures," *Smart Mater Struct*, vol. 26, no. 11, 2017, doi: 10.1088/1361-665X/aa8d3c.
- [93] H. Wan, H. Ohtaki, S. Kotosaka, and G. Hu, "A study of negative Poisson's ratios in auxetic honeycombs based on a large deflection model," *European Journal of Mechanics, A/Solids*, vol. 23, no. 1, pp. 95–106, 2004, doi: 10.1016/j.euromechsol.2003.10.006.
- [94] I. Ali and Y. J. Jun, "Mathematical models for in-plane moduli of honeycomb structures - A review," *Research Journal of Applied Sciences, Engineering and Technology*, vol. 7, no. 3, pp. 581–592, 2014, doi: 10.19026/rjaset.7.294.
- [95] L. Mizzi, D. Attard, R. Gatt, K. K. Dudek, B. Ellul, and J. N. Grima, "Implementation of periodic boundary conditions for loading of mechanical metamaterials and other complex geometric microstructures using finite element analysis," *Eng Comput*, vol. 37, no. 3, pp. 1765–1779, 2020, doi: 10.1007/s00366-019-00910-1.
- [96] J. Zhang and M. F. Ashby, "The out-of-plane properties of honeycombs," *Int J Mech Sci*, vol. 34, no. 6, pp. 475–489, 1992, doi: 10.1016/0020-7403(92)90013-7.
- [97] F. Scarpa, F. Smith, B. Chambers, and G. Burriesci, "Mechanical and electromagnetic behaviour of auxetic honeycomb structures," *The Aeronautical Journal*, vol. 107, no. 1069, pp. 175–183, 2003, doi: 10.1017/S0001924000013269.
- [98] R. Brighenti, A. Spagnoli, M. Lanfranchi, and F. Soncini, "Nonlinear deformation behaviour of auxetic cellular materials with re-entrant lattice structure," *Fatigue Fract Eng Mater Struct*, vol. 39, no. 5, pp. 599–610, 2016, doi: 10.1111/ffe.12381.
- [99] L. Mizzi *et al.*, "Mechanical metamaterials with star-shaped pores exhibiting negative and zero Poisson's ratio," *Mater Des*, vol. 146, pp. 28–37, 2018, doi: 10.1016/j.matdes.2018.02.051.
- [100] L. Ai and X. L. Gao, "An analytical model for star-shaped re-entrant lattice structures with the orthotropic symmetry and negative Poisson's ratios," *Int J Mech Sci*, vol. 145, no. June, pp. 158–170, 2018, doi: 10.1016/j.ijmecsci.2018.06.027.
- [101] G. W. Milton, "Composite materials with poisson's ratios close to - 1," *J Mech Phys Solids*, vol. 40, no. 5, pp. 1105–1137, 1992, doi: 10.1016/0022-5096(92)90063-8.
- [102] R. S. Lakes, "Deformation mechanisms in negative Poisson's ratio materials: structural aspects," *J Mater Sci*, vol. 26, pp. 2287–2292, 1991.
- [103] D. Prall and R. S. Lakes, "Properties of a chiral honeycomb with a poisson's ratio of — 1," *Int J Mech Sci*, vol. 39, no. 3, pp. 305–314, 1997, doi: 10.1016/S0020-7403(96)00025-2.
- [104] A. Spadoni, M. Ruzzene, and F. Scarpa, "Global and local linear buckling behavior of a chiral cellular structure," *Physica Status Solidi (B)*, vol. 242, no. 3, pp. 695–709, 2005, doi: 10.1002/pssb.200460387.

- [105] A. Alderson *et al.*, “Elastic constants of 3-, 4- and 6-connected chiral and anti-chiral honeycombs subject to uniaxial in-plane loading,” *Compos Sci Technol*, vol. 70, no. 7, pp. 1042–1048, 2010, doi: 10.1016/j.compscitech.2009.07.009.
- [106] A. Spadoni and M. Ruzzene, “Elasto-static micropolar behavior of a chiral auxetic lattice,” *J Mech Phys Solids*, vol. 60, no. 1, pp. 156–171, 2012, doi: 10.1016/j.jmps.2011.09.012.
- [107] A. Spadoni, M. Ruzzene, S. Gonella, and F. Scarpa, “Phononic properties of hexagonal chiral lattices,” *Wave Motion*, vol. 46, no. 7, pp. 435–450, 2009, doi: 10.1016/j.wavemoti.2009.04.002.
- [108] X. N. Liu, G. L. Huang, and G. K. Hu, “Chiral effect in plane isotropic micropolar elasticity and its application to chiral lattices,” *J Mech Phys Solids*, vol. 60, no. 11, pp. 1907–1921, 2012, doi: 10.1016/j.jmps.2012.06.008.
- [109] A. Bacigalupo and L. Gambarotta, “Homogenization of periodic hexa- and tetrachiral cellular solids,” *Compos Struct*, vol. 116, no. 1, pp. 461–476, 2014, doi: 10.1016/j.compstruct.2014.05.033.
- [110] J. Chung and A. M. Waas, “The inplane elastic properties of circular cell and elliptical cell honeycombs,” *Acta Mech*, vol. 144, pp. 29–42, 2000, doi: <https://doi.org/10.1007/BF01181826>.
- [111] D. Mousanezhad, B. Haghpanah, R. Ghosh, A. M. Hamouda, H. Nayeb-Hashemi, and A. Vaziri, “Elastic properties of chiral, anti-chiral, and hierarchical honeycombs: A simple energy-based approach,” *Theoretical and Applied Mechanics Letters*, vol. 6, no. 2, pp. 81–96, 2016, doi: 10.1016/j.taml.2016.02.004.
- [112] Y. J. Chen, F. Scarpa, Y. J. Liu, and J. S. Leng, “Elasticity of anti-tetrachiral anisotropic lattices,” *Int J Solids Struct*, vol. 50, no. 6, pp. 996–1004, 2013, doi: 10.1016/j.ijsolstr.2012.12.004.
- [113] R. Gatt *et al.*, “A realistic generic model for anti-tetrachiral systems,” *Phys Status Solidi B Basic Res*, vol. 250, no. 10, pp. 2012–2019, 2013, doi: 10.1007/s11192-017-2578-5.
- [114] J. N. Grima, R. Gatt, and P. S. Farrugia, “On the properties of auxetic meta-tetrachiral structures,” *Phys Status Solidi B Basic Res*, vol. 245, no. 3, pp. 511–520, 2008, doi: 10.1002/pssb.200777704.
- [115] L. Mizzi, D. Attard, R. Gatt, P.-S. Farrugia, and J. N. Grima, “On the mechanical properties of irregular hexachiral honeycombs,” *Smart Mater Struct*, vol. 27, no. 10, p. 105016, 2018.
- [116] F. Scarpa, S. Blain, T. Lew, D. Perrott, M. Ruzzene, and J. R. Yates, “Elastic buckling of hexagonal chiral cell honeycombs,” *Compos Part A Appl Sci Manuf*, vol. 38, no. 2, pp. 280–289, 2007, doi: 10.1016/j.compositesa.2006.04.007.
- [117] W. Miller, C. W. Smith, F. Scarpa, and K. E. Evans, “Flatwise buckling optimization of hexachiral and tetrachiral honeycombs,” *Compos Sci Technol*, vol. 70, no. 7, pp. 1049–1056, 2010, doi: 10.1016/j.compscitech.2009.10.022.
- [118] A. Lorato *et al.*, “The transverse elastic properties of chiral honeycombs,” *Compos Sci Technol*, vol. 70, no. 7, pp. 1057–1063, 2010, doi: 10.1016/j.compscitech.2009.07.008.

- [119] C. W. Smith, J. N. Grima, and K. E. Evans, "A Novel mechanism for generating auxetic behaviour in reticulated foams: Missing rib foam model," *Acta Mater*, vol. 48, no. 17, pp. 4349–4356, 2000, doi: 10.1016/S1359-6454(00)00269-X.
- [120] P.-S. Farrugia, R. Gatt, E. Zammit Lonardelli, J. N. Grima, and K. E. Evans, "Different Deformation Mechanisms Leading to Auxetic Behavior Exhibited by Missing Rib Square Grid Structures," *Physica Status Solidi (B)*, vol. 256, no. 1800186, 2019, doi: 10.1002/pssb.201800186.
- [121] J. N. Grima and K. E. Evans, "Auxetic behavior from rotating squares," *J Mater Sci Lett*, vol. 19, no. 17, pp. 1563–1565, 2000, doi: 10.1023/A:1006781224002.
- [122] J. N. Grima and K. E. Evans, "Auxetic behavior from rotating triangles," *J Mater Sci*, vol. 41, no. 10, pp. 3193–3196, 2006, doi: 10.1007/s10853-006-6339-8.
- [123] J. N. Grima, A. Alderson, and K. E. Evans, "Auxetic behaviour from rotating rigid units," *Phys Status Solidi B Basic Res*, vol. 242, no. 3, pp. 561–575, 2005, doi: 10.1002/pssb.200572706.
- [124] J. N. Grima, R. Gatt, A. Alderson, and K. E. Evans, "On the Auxetic Properties of 'Rotating Rectangles' with Different Connectivity," *J Physical Soc Japan*, vol. 74, no. No. 10, October, pp. 2866–2867, 2005, doi: 10.1098/rspa.2011.0273.
- [125] D. Attard and J. N. Grima, "Auxetic behaviour from rotating rhombi," *Phys Status Solidi B Basic Res*, vol. 245, no. 11, pp. 2395–2404, 2008, doi: 10.1002/pssb.200880269.
- [126] J. N. Grima, P. S. Farrugia, R. Gatt, and D. Attard, "On the auxetic properties of rotating rhombi and parallelograms: A preliminary investigation," *Phys Status Solidi B Basic Res*, vol. 245, no. 3, pp. 521–529, 2008, doi: 10.1002/pssb.200777705.
- [127] J. N. Grima, V. Zammit, R. Gatt, A. Alderson, and K. E. Evans, "Auxetic behaviour from rotating semi-rigid units," *Physica Status Solidi (B) Basic Research*, vol. 244, no. 3, pp. 866–882, 2007, doi: 10.1002/pssb.200572706.
- [128] J. N. Grima, P. S. Farrugia, C. Caruana, R. Gatt, and D. Attard, "Auxetic behaviour from stretching connected squares," *J Mater Sci*, vol. 43, no. 17, pp. 5962–5971, 2008, doi: 10.1007/s10853-008-2765-0.
- [129] Y. Ishibashi and M. Iwata, "A microscopic model of a negative Poisson's ratio in some crystals," *J Physical Soc Japan*, vol. 69, no. 8, pp. 2702–2703, 2000, doi: 10.1143/JPSJ.69.2702.
- [130] A. A. Vasiliev, S. V. Dmitriev, Y. Ishibashi, and T. Shigenari, "Elastic properties of a two-dimensional model of crystals containing particles with rotational degrees of freedom," *Phys Rev B Condens Matter Mater Phys*, vol. 65, no. 9, pp. 1–7, 2002, doi: 10.1103/PhysRevB.65.094101.
- [131] J. N. Grima, R. Gatt, A. Alderson, and K. E. Evans, "An alternative explanation for the negative Poisson's ratios in  $\alpha$ -cristobalite," *Materials Science and Engineering A*, vol. 423, no. 1–2, pp. 219–224, 2006, doi: 10.1016/j.msea.2005.08.230.
- [132] A. Alderson and K. E. Evans, "Molecular Origin of Auxetic Behavior in Tetrahedral Framework Silicates," *Phys Rev Lett*, vol. 89, no. 22, pp. 1–4, 2002, doi: 10.1103/PhysRevLett.89.225503.



- [133] J. N. Grima, R. Jackson, A. Alderson, and K. E. Evans, "Do Zeolites Have Negative Poisson ' s Ratios ?," *Advanced Materials*, vol. 12, no. 24, pp. 1912–1918, 2000.
- [134] J. N. Grima *et al.*, "On the auxetic properties of generic rotating rigid triangles," *Proceedings: Mathematical, Physical and Engineering Sciences by Royal Society*, vol. 468, no. 2139, pp. 810–830, 2012.
- [135] A. Alderson, K. L. Alderson, G. Chirima, N. Ravirala, and K. M. Zied, "The in-plane linear elastic constants and out-of-plane bending of 3-coordinated ligament and cylinder-ligament honeycombs," *Compos Sci Technol*, vol. 70, no. 7, pp. 1034–1041, 2010, doi: 10.1016/j.compscitech.2009.07.010.
- [136] M. Sanami, N. Ravirala, K. Alderson, and A. Alderson, "Auxetic materials for sports applications," *Procedia Eng*, vol. 72, pp. 453–458, 2014, doi: 10.1016/j.proeng.2014.06.079.
- [137] R. Gatt *et al.*, "Hierarchical Auxetic Mechanical Metamaterials," *Sci Rep*, vol. 5, pp. 1–6, 2015, doi: 10.1038/srep08395.
- [138] X. Ren, J. Shen, P. Tran, T. D. Ngo, and Y. M. Xie, "Auxetic nail: Design and experimental study," *Compos Struct*, vol. 184, no. September 2017, pp. 288–298, 2018, doi: 10.1016/j.compstruct.2017.10.013.
- [139] K. W. Wojciechowski, "Remarks on 'Poisson ratio beyond the limits of the elasticity theory,'" *J Physical Soc Japan*, vol. 72, no. 7, pp. 1819–1820, 2003, doi: 10.1143/JPSJ.72.1819.
- [140] J. X. Qiao and C. Q. Chen, "Impact resistance of uniform and functionally graded auxetic double arrowhead honeycombs," *Int J Impact Eng*, vol. 83, pp. 47–58, 2015, doi: 10.1016/j.ijimpeng.2015.04.005.
- [141] X. Li, Q. Wang, Z. Yang, and Z. Lu, "Novel auxetic structures with enhanced mechanical properties," *Extreme Mech Lett*, vol. 27, pp. 59–65, 2019, doi: 10.1016/j.eml.2019.01.002.
- [142] F. K. Abd El-Sayed, R. Jones, and I. W. Burgess, "A theoretical approach to the deformation of honeycomb based composite materials," *Composites*, vol. 10, no. 4, pp. 209–214, 1979, doi: 10.1016/0010-4361(79)90021-1.
- [143] W. C. Young, R. G. Budynas, A. M. Sadegh, and R. J. Roark, *Roark's formulas for stress and strain*, 8th ed. New York: McGraw-Hill Professional, 2012.
- [144] L. J. Gibson and M. F. Ashby, *The structure of cellular solids*. 1997. doi: 10.1017/CBO9781139878326.004.
- [145] MSC Marc, "MSC Marc B - Element Library." pp. 527–532, 2017.
- [146] F. Cardarelli, *Materials Handbook: A concise desktop reference*, Second edi. Springer London, 2008.
- [147] A. International, "Co-20Cr-15W-10Ni," *Materials and Coatings for Medical Devices: Cardiovascular ASM Materials for Medical Devices Database Committee*, pp. 69–73, 2009.
- [148] R. S. Lakes, "Design considerations for materials with negative poisson's ratios," *Journal of Mechanical Design, Transactions of the ASME*, vol. 115, no. 4, pp. 696–700, 1993, doi: 10.1115/1.2919256.

## Appendix

### A.1 Stretching equations

In the case of the double arrowhead configuration, exploring the stretching equations as defined by Masters and Evans' for the Poisson's ratio and Young's modulus in the main text. In fact, their definition of the stretching approach is '*This model assumes that the cell walls are only able to deform by stretching along their axes with no change in angle*'. Due to the configuration of the double arrowhead, this just forces the cell to scale up (in the case of tension), expanding equally in both in-plane directions, resulting in a Poisson's ratio of -1. Although this is expected, here are included the equations as per Masters and Evans' approach, which confirm this (resulting Poisson's ratios are equal to -1).

#### A.1.1 Uniaxial loading of double arrowhead cell in direction 1

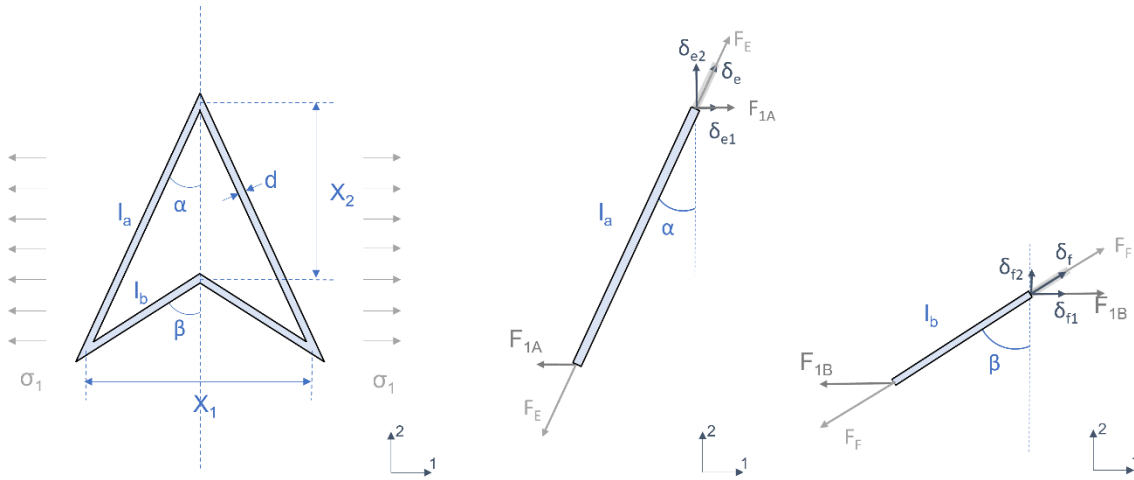


Figure 78: a) Uniaxial loading in 1-direction and resulting b) long beam and c) short beam free body diagram, respectively

Submitting the unit cell to uniaxial loading by a far field nominal stress  $\sigma_1$ , where

$$F_1 = \sigma_1(l_a \cos \alpha - l_b \cos \beta)b \quad (\text{see 4.3})$$

The force  $F_E$  along the long beam of length  $l_a$  is expressed as a function of the part of the force  $F_1$  acting on the long beam,  $F_{1A}$ .

$$F_E = F_{1A} \sin \alpha \quad (\text{A.1})$$

The displacement  $\delta_E$  along the long beam of length  $l_a$  is calculated using eq.4.2:

$$\delta_E = \frac{F_E l_a}{AE_s} = \frac{F_{1A} l_a \sin \alpha}{AE_s} \quad (\text{A.2})$$

where the component of deformation along the 1-axis is

$$\delta_{E1} = \frac{F_{1A} l_a \sin^2 \alpha}{AE_s} \quad (\text{A.3})$$

and the component of deformation along the 2-axis is

$$\delta_{E2} = \frac{F_{1A} l_a \sin \alpha \cos \alpha}{AE_s} \quad (\text{A.4})$$

The force  $F_F$  along the short beam of length  $l_b$  is expressed as a function of the part of the force  $F_1$  acting on the short beam,  $F_{1B}$ .

$$F_F = F_{1B} \sin \beta \quad (\text{A.5})$$

and the displacement  $\delta_F$  along the short beam of length  $l_b$  is calculated using eq.4.2

$$\delta_F = \frac{F_F l_b}{AE_s} = \frac{F_{1B} l_b \sin \beta}{AE_s} \quad (\text{A.6})$$

The component of deformation along the 1-axis is

$$\delta_{F1} = \frac{F_{1B} l_b \sin^2 \beta}{AE_s} \quad (\text{A.7})$$

and the component of deformation along the 2-axis is

$$\delta_{F2} = \frac{F_{1B} l_b \sin \beta \cos \beta}{AE_s} \quad (\text{A.8})$$

Due to geometry constrains,  $\delta_{E1} = \delta_{F1}$ , the relation between  $F_{1A}$  and  $F_{1B}$  can be determined as

$$\frac{F_{1A} l_a \sin^2 \alpha}{AE_s} = \frac{F_{1B} l_b \sin^2 \beta}{AE_s}$$

Since  $F_1 = F_{1A} + F_{1B}$

$$F_{1A} l_a \sin^2 \alpha = F_1 l_b \sin^2 \beta - F_{1A} l_b \sin^2 \beta$$

$$F_{1A} = \frac{F_1 l_b \sin^2 \beta}{l_a \sin^2 \alpha + l_b \sin^2 \beta} \quad (\text{A.9})$$

$$F_{1B} = F_1 \left( 1 - \frac{l_b \sin^2 \beta}{l_a \sin^2 \alpha + l_b \sin^2 \beta} \right) = \frac{F_1 l_a \sin^2 \alpha}{l_a \sin^2 \alpha + l_b \sin^2 \beta} \quad (\text{A.10})$$

### A.1.2 Uniaxial loading of unit cell in direction X2

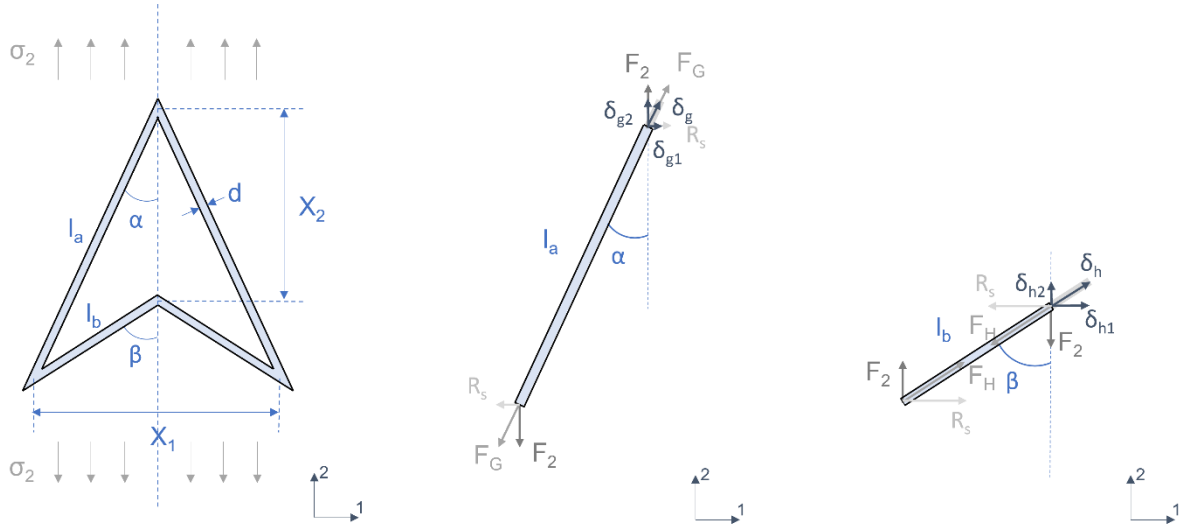


Figure 79: a) Uniaxial loading in 2-direction and resulting b) long beam and c) short beam free body diagram, respectively

Submitting the double arrowhead cell to uniaxial loading by a far field nominal stress  $\sigma_2$ , where

$$F_2 = \sigma_2 l_a b \sin \alpha = \sigma_2 l_b b \sin \beta \quad (\text{see 4.14})$$

The force  $F_G$  along the long beam of length  $l_a$

$$F_G = F_2 \cos \alpha + R_s \sin \alpha \quad (\text{A.11})$$

Where  $R_s$  is the horizontal reaction force from the shorter beam.

The displacement  $\delta_G$  along the long beam of length  $l_a$  is calculated using eq.4.2:

$$\delta_G = \frac{F_G l_a}{AE_s} = \frac{(F_2 \cos \alpha + R_s \sin \alpha) l_a}{AE_s} \quad (\text{A.12})$$

Where the component of deformation along the 1-axis is

$$\delta_{G1} = \frac{(F_2 \cos \alpha + R_s \sin \alpha) l_a \sin \alpha}{AE_s} \quad (\text{A.13})$$

And the component of deformation along the 2-axis is

$$\delta_{G2} = \frac{(F_2 \cos \alpha + R_s \sin \alpha) l_a \cos \alpha}{AE_s} \quad (\text{A.14})$$

The force  $F_H$  along the short beam of length  $l_b$  can be written as

$$F_H = F_2 \cos \beta + R_s \sin \beta \quad (\text{A.15})$$

where  $R_s$  is the horizontal reaction force from the longer beam.

The displacement  $\delta_H$  along the short beam of length  $l_b$  is calculated using eq.4.2

$$\delta_H = -\frac{F_H l_b}{AE_s} = \frac{-(F_2 \cos \beta + R_s \sin \beta) l_b}{AE_s} \quad (\text{A.16})$$

Where the component of deformation along the 1-axis is

$$\delta_{H1} = \frac{(-F_2 \cos \beta - R_s \sin \beta) l_b \sin \beta}{AE_s} \quad (\text{A.17})$$

And the component of deformation along the 2-axis is

$$\delta_{H2} = \frac{(-F_2 \cos \beta - R_s \sin \beta) l_b \cos \beta}{AE_s} \quad (\text{A.18})$$

Due to geometric constrains,  $\delta_{G1} = \delta_{H1}$ , an expression for  $R_s$  can be developed

$$\frac{(F_2 \cos \alpha + R_s \sin \alpha) l_a \sin \alpha}{AE_s} = \frac{(-F_2 \cos \beta - R_s \sin \beta) l_b \sin \beta}{AE_s}$$

$$R_s = -F_2 \frac{l_a \sin \alpha \cos \alpha + l_b \sin \beta \cos \beta}{l_a \sin^2 \alpha + l_b \sin^2 \beta} \quad (\text{A.19})$$

Calculating the elastic properties for pure stretching deformation

For expansion in 1-direction

$$\varepsilon_{1s} = \frac{\delta_{E1}}{X_1} = \frac{\delta_{F1}}{X_1} = \frac{\frac{F_1 \sin^2 \beta l_b}{\sin^2 \alpha l_a + \sin^2 \beta l_b} \sin^2 \alpha l_a}{\frac{AE_s}{l_a \sin \alpha}} = \frac{F_1 \sin \alpha \sin^2 \beta l_b}{(\sin^2 \alpha l_a + \sin^2 \beta l_b) E_s A} \quad (\text{A.20})$$

$$\varepsilon_{2s} = \frac{\delta_{E2} - \delta_{F2}}{X_2} = \frac{\frac{F_1 \sin^2 \beta l_b}{\sin^2 \alpha l_a + \sin^2 \beta l_b} \sin \alpha l_a \cos \alpha - F_1 \left( 1 - \frac{\sin^2 \beta l_b}{\sin^2 \alpha l_a + \sin^2 \beta l_b} \right) \sin \beta l_b \cos \beta}{\frac{AE_s}{(l_a \cos \alpha - l_b \cos \beta)}} =$$

$$F_1 \frac{l_a l_b \sin \alpha \sin \beta (\sin \beta \cos \alpha - \sin \alpha \cos \beta)}{E_s A (l_a \cos \alpha - l_b \cos \beta) (\sin^2 \alpha l_a + \sin^2 \beta l_b)} \quad (\text{A.21})$$

Leading to

$$E_{1\text{stretching}} = \frac{\sigma_1}{\varepsilon_{1s}} = \frac{\sigma_1}{\frac{\sigma_1 (l_a \cos \alpha - l_b \cos \beta) b \sin \alpha \sin^2 \beta l_b}{(\sin^2 \alpha l_a + \sin^2 \beta l_b) E_s A}} = \frac{E_s A (\sin^2 \alpha l_a + \sin^2 \beta l_b)}{b (l_a \cos \alpha - l_b \cos \beta) \sin \alpha \sin^2 \beta l_b} \quad (\text{A.22})$$

$$\nu_{12stretching} = -\frac{\varepsilon_{2s}}{\varepsilon_{1s}} = -\frac{F_1 \frac{l_a l_b \sin \alpha \sin \beta (\sin \beta \cos \alpha - \sin \alpha \cos \beta)}{E_s A (l_a \cos \alpha - l_b \cos \beta) (\sin^2 \alpha l_a + \sin^2 \beta l_b)}}{\frac{F_1 \sin \alpha \sin^2 \beta l_b}{(\sin^2 \alpha l_a + \sin^2 \beta l_b) E_s A}} = -\frac{l_a (\sin \beta \cos \alpha - \sin \alpha \cos \beta)}{\sin \beta (l_a \cos \alpha - l_b \cos \beta)} \quad (A.23)$$

For expansion in 2-direction

$$\begin{aligned} \varepsilon_{1s} &= \frac{\delta_{G1}}{X_1} = \frac{\delta_{H1}}{X_1} = \frac{\frac{(F_2 \cos \alpha + R_s \sin \alpha) l_a \sin \alpha}{A E_s}}{l_a \sin \alpha} = \frac{F_2 \left( \cos \alpha - \frac{(\sin \alpha \cos \alpha l_a + \sin \beta \cos \beta l_b)}{(\sin^2 \alpha l_a + \sin^2 \beta l_b)} \sin \alpha \right)}{A E_s} \quad (A.24) \\ \varepsilon_{2s} &= \frac{\delta_{G2} - \delta_{H2}}{X_2} = \frac{\frac{(F_2 \cos \alpha + R_s \sin \alpha) l_a \cos \alpha}{A E_s} - \frac{(-F_2 \cos \beta - R_s \sin \beta) l_b \cos \beta}{A E_s}}{(l_a \cos \alpha - l_b \cos \beta)} = \\ &= \frac{F_2 \left( (l_a \cos^2 \alpha + l_b \cos^2 \beta) - \frac{(\sin \alpha \cos \alpha l_a + \sin \beta \cos \beta l_b)^2}{(\sin^2 \alpha l_a + \sin^2 \beta l_b)} \right)}{A E_s (l_a \cos \alpha - l_b \cos \beta)} \quad (A.25) \end{aligned}$$

Leading to

$$E_{2stretching} = \frac{\sigma_2}{\varepsilon_{2s}} = \frac{A E_s (l_a \cos \alpha - l_b \cos \beta)}{b l_a \sin \alpha \left( (l_a \cos^2 \alpha + l_b \cos^2 \beta) - \frac{(\sin \alpha \cos \alpha l_a + \sin \beta \cos \beta l_b)^2}{(\sin^2 \alpha l_a + \sin^2 \beta l_b)} \right)} \quad (A.26)$$

$$\nu_{21stretching} = -\frac{\varepsilon_{1s}}{\varepsilon_{2s}} = -\frac{\left( \cos \alpha - \frac{(\sin \alpha \cos \alpha l_a + \sin \beta \cos \beta l_b)}{(\sin^2 \alpha l_a + \sin^2 \beta l_b)} \sin \alpha \right) (l_a \cos \alpha - l_b \cos \beta)}{\left( (l_a \cos^2 \alpha + l_b \cos^2 \beta) - \frac{(\sin \alpha \cos \alpha l_a + \sin \beta \cos \beta l_b)^2}{(\sin^2 \alpha l_a + \sin^2 \beta l_b)} \right)} \quad (A.27)$$

4.3.5 Rewritten in the format  $l_a = L$  and  $l_b = L \frac{\sin \alpha}{\sin \beta}$

$$\nu_{12stretching} = -1 \quad (A.28)$$

$$\nu_{21stretching} = -1 \quad (A.29)$$

$$E_{1stretching} = \frac{E_s A (\sin \alpha + \sin \beta)}{b L \left( \cos \alpha - \frac{\sin \alpha}{\sin \beta} \cos \beta \right) \sin \alpha \sin \beta} \quad (A.30)$$

$$E_{2stretching} = \frac{A E_s \left( \cos \alpha - \frac{\sin \alpha}{\sin \beta} \cos \beta \right)}{b L \sin \alpha \left( \left( \cos^2 \alpha + \frac{\sin \alpha}{\sin \beta} \cos^2 \beta \right) - \frac{\sin \alpha (\cos \alpha + \cos \beta)^2}{(\sin \alpha + \sin \beta)} \right)} \quad (A.31)$$

Combining Flexure and Stretching to a complete model

For expansion in X1-direction

$$\varepsilon_1^T = \varepsilon_{1f} + \varepsilon_{1s} \quad (A.32)$$

$$\varepsilon_{1f} = \frac{F_1 l_a^2 \cos^2 \alpha}{12 E_s I \sin \alpha} = \frac{\frac{F_1 l_b^3 \cos^2 \beta}{(l_a^3 \cos^2 \alpha + l_b^3 \cos^2 \beta)} l_a^2 \cos^2 \alpha}{12 E_s I \sin \alpha} = \frac{F_1 l_a^2 l_b^3 \cos^2 \alpha \cos^2 \beta}{12 E_s I \sin \alpha (l_a^3 \cos^2 \alpha + l_b^3 \cos^2 \beta)} \quad (\text{A.33}) \text{ (see 4.54 and 4.12)}$$

$$\varepsilon_{1s} = \frac{F_1 l_b \sin \alpha \sin^2 \beta}{E_s A (l_a \sin^2 \alpha + l_b \sin^2 \beta)} \quad (\text{see A.20})$$

$$\varepsilon_2^T = \varepsilon_{2f} + \varepsilon_{2s} \quad (\text{A.34})$$

$$\varepsilon_{2f} = \frac{\frac{F_1 l_b^3 \cos^2 \beta}{(l_a^3 \cos^2 \alpha + l_b^3 \cos^2 \beta)} l_a^3 \cos \alpha \sin \alpha - \frac{F_1 l_a^3 \cos^2 \alpha}{(l_a^3 \cos^2 \alpha + l_b^3 \cos^2 \beta)} l_b^3 \cos \beta \sin \beta}{12 E_s I (l_a \cos \alpha - l_b \cos \beta)} = \frac{F_1 l_a^3 l_b^3 \cos \alpha \cos \beta (\cos \beta \sin \alpha - \cos \alpha \sin \beta)}{12 E_s I (l_a \cos \alpha - l_b \cos \beta) (l_a^3 \cos^2 \alpha + l_b^3 \cos^2 \beta)} \quad (\text{A.35}) \text{ (see 4.55, 4.12 and 4.13)}$$

$$\varepsilon_{2s} = \frac{\delta_{E2} - \delta_{F2}}{X_2} = \frac{F_1 l_a l_b \sin \alpha \sin \beta (\sin \beta \cos \alpha - \sin \alpha \cos \beta)}{E_s A (l_a \cos \alpha - l_b \cos \beta) (l_a \sin^2 \alpha + l_b \sin^2 \beta)} \quad (\text{see A.21})$$

Stress, derived from eq 4.3

$$\sigma_1 = \frac{F_1}{(l_a \cos \alpha - l_b \cos \beta) b} \quad (\text{A.36})$$

Young's modulus

$$E_1 = \frac{\sigma_1}{\varepsilon_1^T} = \frac{\frac{F_1}{(l_a \cos \alpha - l_b \cos \beta) b}}{\frac{\frac{F_1 \cos^2 \beta l_b^3}{(\cos^2 \alpha l_a^3 + \cos^2 \beta l_b^3)} \cos^2 \alpha l_a^2}{12 E_s I \sin \alpha} + \frac{F_1 \sin \alpha \sin^2 \beta l_b}{(\sin^2 \alpha l_a + \sin^2 \beta l_b) E_s A}} = \frac{E_s}{\frac{l_b (l_a \cos \alpha - l_b \cos \beta) b}{\sin \alpha} \left( \frac{l_a^2 l_b^3 \cos^2 \alpha \cos^2 \beta}{12 I (l_a^3 \cos^2 \alpha + l_b^3 \cos^2 \beta)} + \frac{\sin^2 \alpha \sin^2 \beta}{A (l_a \sin^2 \alpha + l_b \sin^2 \beta)} \right)} \quad (\text{A.37})$$

Poisson's ratio

$$\nu_{12} = -\frac{\varepsilon_2^T}{\varepsilon_1^T} = -\frac{\frac{F_1 \cos \alpha \cos \beta}{12 E_s I (l_a \cos \alpha - l_b \cos \beta) (\cos^2 \alpha l_a^3 + \cos^2 \beta l_b^3)} l_a^3 l_b^3 (\cos \beta \sin \alpha - \cos \alpha \sin \beta) + F_1 \frac{l_a l_b \sin \alpha \sin \beta (\sin \beta \cos \alpha - \sin \alpha \cos \beta)}{E_s A (l_a \cos \alpha - l_b \cos \beta) (\sin^2 \alpha l_a + \sin^2 \beta l_b)}}{\frac{F_1 \cos^2 \beta l_b^3}{(\cos^2 \alpha l_a^3 + \cos^2 \beta l_b^3)} \cos^2 \alpha l_a^2}{12 E_s I \sin \alpha} + \frac{F_1 \sin \alpha \sin^2 \beta l_b}{(\sin^2 \alpha l_a + \sin^2 \beta l_b) E_s A}$$

$$= - \frac{\frac{l_a \sin \alpha (\sin \alpha \cos \beta - \sin \beta \cos \alpha)}{(l_a \cos \alpha - l_b \cos \beta)(l_a^3 \cos^2 \alpha + l_b^3 \cos^2 \beta)} \left( \frac{l_a^2 l_b^2 \cos \alpha \cos \beta}{12I} - \frac{\sin \alpha \sin \beta}{A} \right)}{\left( \frac{l_a^2 l_b^2 \cos^2 \alpha \cos^2 \beta}{12I(l_a^3 \cos^2 \alpha + l_b^3 \cos^2 \beta)} + \frac{\sin^2 \alpha \sin^2 \beta}{A(l_a \sin^2 \alpha + l_b \sin^2 \beta)} \right)} \quad (\text{A.38})$$

For expansion in X2-direction

Deformation

$$\varepsilon_1^T = \varepsilon_{1f} + \varepsilon_{1s} \quad (\text{See A.32})$$

$$\varepsilon_{1f} = \frac{(R_{f1} \cos \alpha + F_2 \sin \alpha) l_a^2 \cos \alpha}{12 E_s I \sin \alpha} = \frac{F_2 \left( \sin \alpha - \frac{(\sin \alpha \cos \alpha l_a^3 + \sin \beta \cos \beta l_b^3)}{(\cos^2 \alpha l_a^3 + \cos^2 \beta l_b^3)} \cos \alpha \right) l_a^2 \cos \alpha}{12 E_s I \sin \alpha} \quad (\text{A.39}) \quad (\text{See 4.58 and 4.23})$$

$$\varepsilon_{1s} = \frac{F_2 \left( \cos \alpha - \frac{(\sin \alpha \cos \alpha l_a + \sin \beta \cos \beta l_b)}{(\sin^2 \alpha l_a + \sin^2 \beta l_b)} \sin \alpha \right)}{A E_s} \quad (\text{See A.24})$$

$$\varepsilon_2^T = \varepsilon_{2f} + \varepsilon_{2s} \quad (\text{See A.34})$$

$$\varepsilon_{2f} = \frac{(R_{f1} \cos \alpha + F_2 \sin \alpha) l_a^3 \sin \alpha - (-F_2 \sin \beta - R_{f1} \cos \beta) l_b^3 \sin \beta}{12 E_s I (l_a \cos \alpha - l_b \cos \beta)} = \frac{F_2 \left( (\sin^2 \alpha l_a^3 + l_b^3 \sin^2 \beta) - \frac{(\sin \alpha \cos \alpha l_a^3 + \sin \beta \cos \beta l_b^3)^2}{(\cos^2 \alpha l_a^3 + \cos^2 \beta l_b^3)} \right)}{12 E_s I (l_a \cos \alpha - l_b \cos \beta)} \quad (\text{A.40}) \quad (\text{See 4.59 and 4.23})$$

$$\varepsilon_{2s} = \frac{F_2 \left( (l_a \cos^2 \alpha + l_b \cos^2 \beta) - \frac{(\sin \alpha \cos \alpha l_a + \sin \beta \cos \beta l_b)^2}{(\sin^2 \alpha l_a + \sin^2 \beta l_b)} \right)}{A E_s (l_a \cos \alpha - l_b \cos \beta)} \quad (\text{See A.25})$$

Stress, derived from eq. 4.14, is

$$\sigma_2 = \frac{F_2}{l_a \sin \alpha b} \quad (\text{A.41})$$

Young's modulus

$$E_2 = \frac{\sigma_2}{\varepsilon_2^T}$$



$$\begin{aligned}
&= \frac{\frac{F_2}{l_a \sin \alpha b}}{\left\{ \frac{F_2 \left( (\sin^2 \alpha l_a^3 + l_b^3 \sin^2 \beta) - \frac{(\sin \alpha \cos \alpha l_a^3 + \sin \beta \cos \beta l_b^3)^2}{(\cos^2 \alpha l_a^3 + \cos^2 \beta l_b^3)} \right)}{12E_s I (l_a \cos \alpha - l_b \cos \beta)} + \frac{F_2 \left( (l_a \cos^2 \alpha + l_b \cos^2 \beta) - \frac{(\sin \alpha \cos \alpha l_a + \sin \beta \cos \beta l_b)^2}{(\sin^2 \alpha l_a + \sin^2 \beta l_b)} \right)}{AE_s (l_a \cos \alpha - l_b \cos \beta)} \right\}} \\
&= \frac{E_s (l_a \cos \alpha - l_b \cos \beta)}{l_a \sin \alpha b \left[ \frac{1}{12I} \left( (l_a^3 \sin^2 \alpha + l_b^3 \sin^2 \beta) - \frac{(l_a^3 \sin \alpha \cos \alpha + l_b^3 \sin \beta \cos \beta)^2}{(l_a^3 \cos^2 \alpha + l_b^3 \cos^2 \beta)} \right) + \frac{1}{A} \left( (l_a \cos^2 \alpha + l_b \cos^2 \beta) - \frac{(l_a \sin \alpha \cos \alpha + l_b \sin \beta \cos \beta)^2}{(l_a \sin^2 \alpha + l_b \sin^2 \beta)} \right) \right]} \quad (\text{A.42})
\end{aligned}$$

Poisson's ratio

$$\begin{aligned}
\nu_{21} &= -\frac{\varepsilon_1^T}{\varepsilon_2^T} = \\
&= \frac{\left[ \frac{F_2 \left( \sin \alpha - \frac{(\sin \alpha \cos \alpha l_a^3 + \sin \beta \cos \beta l_b^3)}{(\cos^2 \alpha l_a^3 + \cos^2 \beta l_b^3)} \cos \alpha \right) l_a^2 \cos \alpha}{12E_s I \sin \alpha} + \frac{F_2 \left( \cos \alpha - \frac{(\sin \alpha \cos \alpha l_a + \sin \beta \cos \beta l_b)}{(\sin^2 \alpha l_a + \sin^2 \beta l_b)} \sin \alpha \right)}{AE_s} \right]}{\left\{ \frac{F_2 \left( (\sin^2 \alpha l_a^3 + l_b^3 \sin^2 \beta) - \frac{(\sin \alpha \cos \alpha l_a^3 + \sin \beta \cos \beta l_b^3)^2}{(\cos^2 \alpha l_a^3 + \cos^2 \beta l_b^3)} \right)}{12E_s I (l_a \cos \alpha - l_b \cos \beta)} + \frac{F_2 \left( (l_a \cos^2 \alpha + l_b \cos^2 \beta) - \frac{(\sin \alpha \cos \alpha l_a + \sin \beta \cos \beta l_b)^2}{(\sin^2 \alpha l_a + \sin^2 \beta l_b)} \right)}{AE_s (l_a \cos \alpha - l_b \cos \beta)} \right\}} \\
&= \frac{(l_a \cos \alpha - l_b \cos \beta) \left[ \frac{l_a^2 \cos \alpha}{12I \sin \alpha} \left( \sin \alpha - \frac{(\sin \alpha \cos \alpha l_a^3 + \sin \beta \cos \beta l_b^3)}{(\cos^2 \alpha l_a^3 + \cos^2 \beta l_b^3)} \cos \alpha \right) + \frac{1}{A} \left( \cos \alpha - \frac{(\sin \alpha \cos \alpha l_a + \sin \beta \cos \beta l_b)}{(\sin^2 \alpha l_a + \sin^2 \beta l_b)} \sin \alpha \right) \right]}{\left\{ \frac{1}{12I} \left( (\sin^2 \alpha l_a^3 + l_b^3 \sin^2 \beta) - \frac{(\sin \alpha \cos \alpha l_a^3 + \sin \beta \cos \beta l_b^3)^2}{(\cos^2 \alpha l_a^3 + \cos^2 \beta l_b^3)} \right) + \frac{1}{A} \left( (l_a \cos^2 \alpha + l_b \cos^2 \beta) - \frac{(\sin \alpha \cos \alpha l_a + \sin \beta \cos \beta l_b)^2}{(\sin^2 \alpha l_a + \sin^2 \beta l_b)} \right) \right\}} \\
&\quad (\text{A.43})
\end{aligned}$$

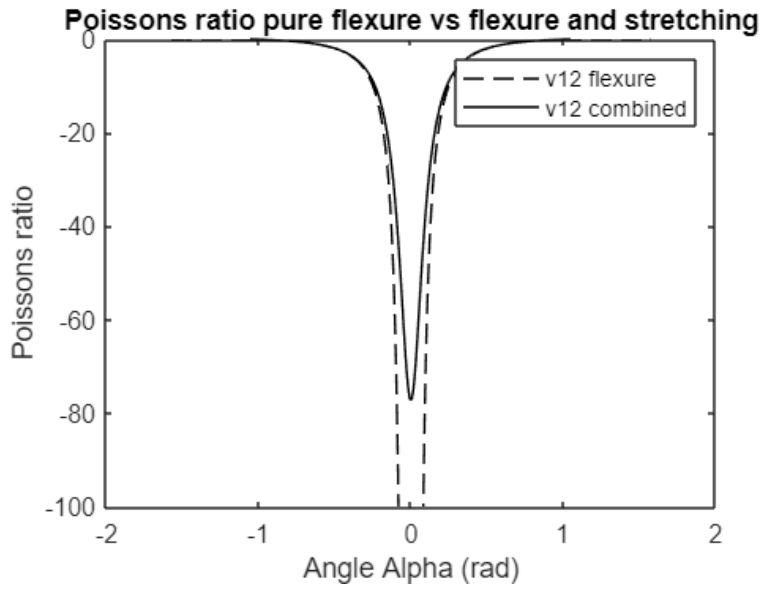
Rewritten in the format  $l_a = L$  and  $l_b = L \frac{\sin \alpha}{\sin \beta}$

$$\nu_{12} = \frac{\frac{L^2}{12I \sin^3 \beta} \frac{\cos \alpha \cos \beta \sin^2 \alpha}{(\cos^2 \alpha \sin^3 \beta + \cos^2 \beta \sin^3 \alpha)} - \frac{\sin \beta}{A(\sin \alpha + \sin \beta)}}{\left( \frac{L^2}{12I(\cos^2 \alpha \sin^3 \beta + \cos^2 \beta \sin^3 \alpha)} + \frac{\sin \beta}{A(\sin \alpha + \sin \beta)} \right)} \quad (\text{A.44})$$

$$\begin{aligned}
\nu_{21} &= -\frac{\left[ \frac{L^2 \cos \alpha}{12I} \left( 1 - \frac{(\cos \alpha + \cos \beta \frac{\sin^2 \alpha}{\sin^2 \beta})}{(\cos^2 \alpha + \cos^2 \beta \frac{\sin^3 \alpha}{\sin^3 \beta})} \cos \alpha \right) + \frac{1}{A} \left( \cos \alpha - \frac{(\cos \alpha + \cos \beta)}{(\sin \alpha + \sin \beta)} \sin \alpha \right) \right]}{\left\{ \frac{L^2 \sin^2 \alpha}{12I \left( \cos \alpha - \frac{\sin \alpha}{\sin \beta} \cos \beta \right)} \left( 1 + \frac{\sin \alpha}{\sin \beta} - \frac{(\cos \alpha + \cos \beta \frac{\sin^2 \alpha}{\sin^2 \beta})^2}{(\cos^2 \alpha + \cos^2 \beta \frac{\sin^3 \alpha}{\sin^3 \beta})} \right) + \frac{(\cos \alpha \cos \beta)}{A \left( \frac{1}{\sin \alpha} + \frac{1}{\sin \beta} \right)} \right\}} \quad (\text{A.45})
\end{aligned}$$

$$E_1 = \frac{E_s}{bL \left( \cos \alpha - \frac{\sin \alpha}{\sin \beta} \cos \beta \right) \left( \frac{L^2 \cos^2 \beta \sin^2 \alpha \cos^2 \alpha}{12I(\cos^2 \alpha \sin^3 \beta + \cos^2 \beta \sin^3 \alpha)} + \frac{\sin \beta}{(\sin \alpha + \sin \beta)A} \right)} \quad (\text{A.46})$$

$$E_2 = \frac{E_s(\cot \alpha - \cot \beta)}{\frac{bL^3 \sin^2 \alpha}{12I} \left( 1 + \frac{\sin \alpha}{\sin \beta} \frac{\left( \cos \alpha + \cos \beta \frac{\sin^2 \alpha}{\sin^2 \beta} \right)^2}{\cos^2 \alpha + \cos^2 \beta \frac{\sin^3 \alpha}{\sin^3 \beta}} \right) + \frac{bL}{A} \left( \cos^2 \alpha + \frac{\sin \alpha}{\sin \beta} \cos^2 \beta - \frac{\sin \alpha (\cos \alpha + \cos \beta)^2}{\sin \alpha + \sin \beta} \right)} \quad (\text{A.47})$$



Example of comparison between pure flexure and combined flexure and stretching according to Masters & Evans